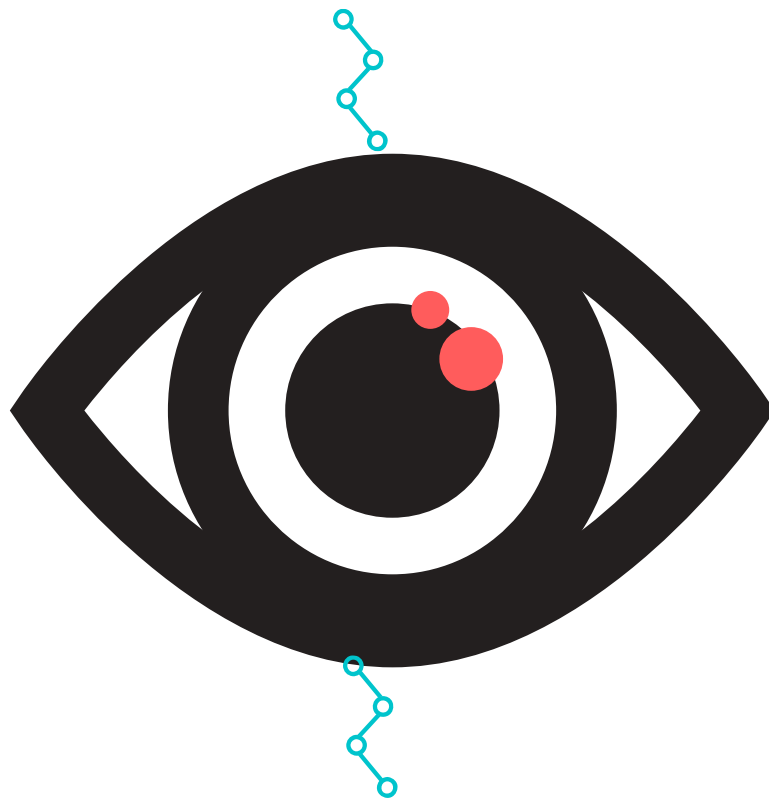


Calibration Methodology of Near-Field Wellbore Stress and Strength to Predict Failure Severity in Deep Geothermal Boreholes: From Theory to Industrial Applications



ASMAE DAHRABOU

UNIVERSITY OF NEUCHÂTEL, SWITZERLAND
FACULTY OF SCIENCE
CENTER FOR HYDROGEOLOGY AND GEOTHERMICS (CHYN)

Calibration methodology of near-field wellbore stress and strength to predict failure severity in deep geothermal boreholes: From theory to industrial applications

A THESIS PRESENTED FOR THE DEGREE OF
DOCTOR OF SCIENCES

BY

Asmae DAHRABOU

Accepted on the recommendation of:

Directeur de thèse :	Prof. Benoît VALLEY	University of Neuchâtel, Switzerland
Rapporteurs :	Prof. Philip BRUNNER	University of Neuchâtel, Switzerland
	Prof. Thomas KOHL	KIT, Karlsruhe, Germany
Examineur :	Dr. Andrés ALCOLEA	Geo-Energie Suisse, Zürich, Switzerland

Defended on September 23rd, 2021

IMPRIMATUR POUR THESE DE DOCTORAT

**La Faculté des sciences de l'Université de Neuchâtel
autorise l'impression de la présente thèse soutenue par**

Madame Asmae DAHRABOU

Titre:

**“Calibration methodology of near-field wellbore
stress and strength to predict failure severity in
deep geothermal boreholes: from theory to
industrial applications”**

sur le rapport des membres du jury composé comme suit:

- Prof. Benoît Valley, directeur de thèse, Université de Neuchâtel, Suisse
- Prof. Philip Brunner, Université de Neuchâtel, Suisse
- Prof. Thomas Kohl, Karlsruhe Institute of Technology, Allemagne
- Dr Andres Alcolea Rodriguez, Geo-Energie Suisse

Neuchâtel, le 13 septembre 2021



*"You cannot always control what goes on
outside. But you can always control what
goes on inside"*

— Wayne Dyer

Contents

List of Figures	v
List of Tables	ix
Nomenclature	xi
Abstract	xv
Acknowledgements	xxiii
1. Introduction	1
1.1. Context and motivations	1
1.2. Objectives	4
1.2.1. Industrial application objectives	4
1.2.2. Fundamental science developments	5
1.3. Thesis organization	5
2. Background	7
2.1. Deep geothermal energy	7
2.1.1. Hydrothermal Systems Vs. Petrothermal Systems	7
2.1.2. Stimulation techniques and reservoir creation	8
2.2. Stress and wellbore failure concept in crystalline rocks	11
2.3. Handling uncertainty in a probabilistic manner for a reliable geomechanical design	14
2.3.1. Uncertainties in geomechanical design	14
2.3.2. Natural variability	15
2.3.3. Quality of predictions and reduction of uncertainty	15
3. A systematic methodology to calibrate wellbore failure models, estimate the in-situ stress tensor and evaluate wellbore cross-sectional geometry	19
3.1. Introduction	22
3.2. Methodology	23
3.2.1. Calculation of the near-field state of stress	24
3.2.2. Strength models	27
3.2.3. Estimation of breakout width	28
3.2.4. Estimation of breakout extent	29

3.2.5.	Estimation of DITFs occurrence	31
3.2.6.	Parameter estimation	31
3.3.	BS-1 data description	34
3.3.1.	BS-1 failure data	35
3.3.2.	BS-1 stress state from previous studies	38
3.4.	Parametric and sensitivity analyses	39
3.4.1.	Relationship between breakout width and breakout extent in the BS-1 well	39
3.4.2.	Sensitivity analyses	41
3.4.3.	Illustration of solution non-uniqueness	44
3.5.	Calibration of the developed geomechanical model on observed failure in the BS-1 well	47
3.5.1.	First order calibration approach	47
3.5.1.1.	Non-uniqueness	48
3.5.1.2.	Reducing the solutions uncertainty	51
3.5.2.	2 nd order calibration	53
3.6.	Discussions	56
3.6.1.	Failure models evaluation	56
3.6.2.	Sensitivity analyses	57
3.6.3.	Stresses trends with depth	57
3.6.4.	Failure variability and implication for rock mass models	59
3.6.5.	Limitations and applicability of the methodology	61
3.7.	Conclusions	64
4.	A computational stochastic methodology to predict failure severity in deep geothermal boreholes	67
4.1.	Introduction	70
4.2.	Methodology	71
4.2.1.	1 st and 2 nd order calibration in the shallower section of the well	72
4.2.2.	Forecasting borehole failure in the deepest section of the well	74
4.3.	Application to the BS-1 well	75
4.3.1.	Failure prediction based on the 1 st order calibration	75
4.3.2.	Failure predictions based on the 2 nd order calibration	75
4.3.2.1.	2 nd order calibration results	75
4.3.2.2.	Parameters forecast and borehole failure prediction	80
4.4.	Discussion	82
4.4.1.	Forecasting calibrated parameters and accounting for variability	82
4.4.2.	Quality of the prediction	83
4.5.	Conclusions	83

5. Application of the calibration and prediction approaches to synthetic cases	85
5.1. Introduction	86
5.2. Methodology	88
5.2.1. Generating synthetic cases	89
5.2.2. Failure models calibration	93
5.2.2.1. 1 st order calibration	93
5.2.2.2. 2 nd order calibration	94
5.2.3. Borehole failure severity prediction	94
5.2.3.1. 1 st order prediction and quantification indicators	94
5.2.3.2. 2 nd order prediction and quantification indicator	95
5.2.4. Well optimization path	96
5.3. Results	97
5.3.1. Illustration of the relationship between borehole deviation and failure using stereographic projections	97
5.3.2. Generating synthetic failure data	101
5.3.3. 1 st order calibration	102
5.3.4. Failure prediction	103
5.3.4.1. 1 st order prediction	103
5.3.4.2. 1 st order predictions shift	104
5.3.4.3. Explaining the observed shifts	109
5.3.4.4. Dispersion of the 1 st order predictions	112
5.3.5. Dispersion of the 2 nd order predictions	114
5.4. Discussions	116
5.4.1. Quality of 1 st order calibration	116
5.4.2. Failure predictions quantification	117
5.4.2.1. Failure prediction in a vertical well	117
5.4.2.2. Failure prediction in a deviated well	118
5.5. Conclusions	119
6. Deep Geothermal Well Optimization Workflow (DG-WOW) application	121
6.1. Introduction	121
6.1.1. Scope and objectives of the 'DG-WOW' application	121
6.1.2. Guiding principles	122
6.2. Overview and implementation of the workflow	123
6.2.1. Workflow overview	123
6.2.2. DG-WOW-app implementation	123
6.3. Presentation of the DG-WOW application using the BS-1 borehole data	127
6.3.1. Data pre-processing - UBI data synthesis	127
6.3.2. Failure models calibration	128
6.3.2.1. 1 st order calibration	128
6.3.2.1.1. Zone and data definition:	128

6.3.2.1.2.	Starting points and calibrations:	129
6.3.2.1.3.	1 st calibrated profiles	130
6.3.2.1.4.	1 st calibrated histograms	131
6.3.2.2.	2 nd order calibration	132
6.3.2.2.1.	Second order calibration evaluation	133
6.3.2.3.	Natural fractures analyses	134
6.3.2.3.1.	Feedzones analyses:	135
6.3.2.3.2.	Slip-tendency analyses	136
6.3.2.3.3.	Fracture frequency analyses	136
6.3.3.	Failure severity prediction	137
6.3.3.1.	Well trajectory scenario selection	137
6.3.3.2.	Well trajectory scenario evaluation	138
6.4.	Summary and outlook	139
7.	Application of the workflow to two real test cases	141
7.1.	Introduction	141
7.2.	Brief site description	141
7.2.1.	CB-1 borehole (Bedretto)	141
7.2.2.	GPK3 borehole (Soultz-sous-Forêt)	143
7.3.	UBI data synthesis	144
7.4.	Failure models calibration	146
7.4.1.	1 st order calibration	146
7.4.2.	2 nd order calibration	150
7.5.	Natural fractures analyses	153
7.6.	Failure severity prediction	155
7.7.	Summary	160
8.	Conclusions and outlook	161
	Bibliography	169
	Bibliography	184
	Appendices	185
A.	Stresses transformation to a local borehole Cartesian coordinate system	187
B.	Stress perturbation induced by a cylindrical opening (Kirsch solution)	191
C.	Overview of the minimization algorithm implemented in PEST	193

List of Figures

2.1. Schematic diagrams illustrating HSs and PSs.	9
2.2. The evolution and classification of the deep geothermal reservoir concepts.	11
2.3. Hypothetical distribution curves of the uncertainty reduction.	17
3.1. Schematic description of the proposed methodology	25
3.2. Interpreted failure data along borehole BS-1	36
3.3. Geometry of the BS-1 borehole at 3509 m MD	37
3.4. Constraints on S_{hmin} and S_{Hmax} in the BS-1 well inferred from hydraulic data, FIT test and RACOS	39
3.5. BS-1 borehole failure data and failure models	41
3.6. Illustration of the effect of stress conditions controlling the relationship between breakout width and extension	42
3.7. Tornado diagram summarizing the sensitivity analyses	44
3.8. Illustration of non-uniqueness after the calibration process at the cross-section at 3509 m MD	46
3.9. 1 st order calibration results using the Mohr–Coulomb failure criterion	49
3.10. Prior and posterior cumulative density functions in the absence and in the presence of an estimate of S_{hmin} at a depth 4632 m MD	50
3.11. 1 st order calibration outputs while using Mogi–Coulomb failure criterion	50
3.12. Correlation matrix between the 1 st order calibrated parameters and the borehole failure indicators	51
3.13. 1 st order calibration outputs in the presence of a new measurement of S_{hmin} considering the Mohr–Coulomb failure criterion	53
3.14. 1 st order calibration outputs in the presence of a new measurement of S_{hmin} considering the Mogi–Coulomb failure criterion	54
3.15. Calibrated failure profiles using pilot points method from 3 to 5 km	55
3.16. Calibrated input parameters profiles using pilot points method from 3 to 5 km	55
3.17. 1 st order calibration from 2578 m MD to 4000 m MD using the Mohr–Coulomb failure criterion	59
3.18. Histograms of the calibrated parameters	60
3.19. Calibrated failure profiles for the first scenario	61
3.20. Calibrated failure profiles for the second scenario	62
3.21. Histograms of parameters variability, $\epsilon_{i,zi}$, for three different scenarios	62

4.1. Sketch of the prediction methodology.	73
4.2. Outputs of the 1 st order calibration and corresponding predictions.	76
4.3. 2 nd order calibrated failure profiles against data from 3 to 3.6 km.	78
4.4. 2 nd order calibrated parameter profiles along the section 3 to 3.6 km.	79
4.5. Correlation matrix of both calibrations and predictions.	79
4.6. Predicted depth profiles of failure indicators.	81
4.7. Cumulative distribution functions of predicted failure indicators.	82
5.1. Overview of the main steps of the proposed methodology	90
5.2. Stereoplot showing the generated different borehole trajectories.	92
5.3. Generalized stress transformation system for a deviated borehole.	97
5.4. Stereographic projection of breakout width and breakout extent for a given depth.	98
5.5. Set of calibrated stresses and Shen's parameters at a given depth.	99
5.6. Prediction of breakout width and extent for different borehole deviation azimuth.	100
5.7. Breadth of the envelop of all calibrated models for breakout width and breakout depth.	100
5.8. Factors influencing the coherence of the width and extent estimation from calibrated models and the base model.	101
5.9. An example of the generated stresses and strength profiles in depth for two synthetic cases.	103
5.10. Computed borehole failure for two synthetic cases.	104
5.11. Outputs of the 1 st order calibration that was carried out using two synthetic cases.	105
5.12. Outputs of the 1 st order calibration and prediction that were carried out using Scenario 1 (vertical borehole).	106
5.13. Outputs of the 1 st order calibration and prediction that were carried out using Scenario 1 (borehole deviation of 30°).	107
5.14. Computed first order shift, I_s , for breakout width.	108
5.15. Computed first order shift, I_s , for breakout extent	109
5.16. The difference between the mean of predicted and observed DITFs in the deepest section of the well, Vs. borehole trajectory	110
5.17. Stress anisotropy function, Φ , Vs. the optimum well path, γ	111
5.18. Computed dispersion of the 1 st order predictions Vs. borehole trajectory for all scenarios	114
5.19. Computed dispersion of the 2 nd order predictions Vs. borehole trajectory for all scenarios	115
5.20. Examples where breakout do not occur, but with stress conditions and distance to failure significantly different	117

6.1. Overview of the entire workflow	124
6.2. Summary of the main required initial data for each phase of the implemented workflow.	125
6.3. View of the interface of the application	127
6.4. UBI data synthesis panel	128
6.5. Definition of the zones where calibration will be performed	129
6.6. An example of prior distributions (displayed as histograms) of the input parameters to be calibrated	130
6.7. Outputs of the 1 st order calibration of 20 starting points	131
6.8. Prior and posterior distributions of initial and calibrated input parameters .	132
6.9. Required parameters to perform the 2 nd order calibration process	133
6.10. Evaluation of the outputs of the 2 nd order calibration	134
6.11. Screenshot displaying the fractures sets in BS-1	135
6.12. Screenshot of the GUI where fracture true spacing statistics are performed .	135
6.13. Screenshot illustrating slip tendency analyses performed on the natural fractures in BS-1.	136
6.14. Example of total fracture frequency analyses as a function of drilling directions performed in the BS-1.	137
6.15. 3D view of the borehole trajectory and sections along which calibrations and prediction were performed	138
6.16. Predicted failure severity from 4000 to 5000 m	138
7.1. Geological cross-section of the Bedretto tunnel	142
7.2. Screenshot of the CB1 UBI data synthesis panel	145
7.3. Screenshot of the UBI data synthesis panel of GPK3	146
7.4. Screenshot of the "Data and Zone Definition" panel of the DG-WOW-app tested on CB1 borehole	147
7.5. Screenshot of the "Data and Zone Definition" panel of the DG-WOW-app tested on GPK3 borehole	147
7.6. Screenshot of the '1 st order calibrated profiles' tab for CB1 borehole	148
7.7. Screenshot of the '1 st order calibrated profiles' tab for GPK3 borehole . . .	149
7.8. Prior and posterior parameters histograms for CB1	150
7.9. Prior and posterior parameters histograms for GPK3	151
7.10. Evaluation of the outputs of the 2 nd order calibration performed for CB1 borehole	152
7.11. Evaluation of the outputs of the 2 nd order calibration performed for GPK3 borehole	152
7.12. Fractures sets in CB-1	153
7.13. Fractures sets in GPK3	154
7.14. Total fracture frequency analyses for CB-1 borehole	154
7.15. [Total fracture frequency analyses for GPK3 borehole	155

7.16. 3D view of the CB1 borehole trajectory	156
7.17. 3D view of the GPK3 borehole trajectory	156
7.18. Predicted failure severity from 200 to 300 m MD for CB1 borehole	157
7.19. Predicted failure severity from 2700 to 3700 m MD for GPK3 borehole	157
7.20. Predicted failure severity from 200 to 300 m MD for CB1 borehole	158
7.21. Predicted failure severity from 2700 to 3700 m MD for GPK3 borehole	158
7.22. Predicted failure severity from 200 to 300 m MD for CB1 while accounting for stochastic variability	159
7.23. Predicted failure severity from 2700 to 3700 m MD for GPK3 while ac- counting for stochastic variability	159
A.1. Euler angles rotations	189
A.2. The various coordinate systems for stress tensor transformation	189

List of Tables

3.1. Statistical parameters of key breakout indicators.	38
3.2. Lower and upper bounds of calibrated S_{Hmax} and S_{hmin} using Mohr-coulomb and Mogi-Coulomb failure criteria.	48
4.1. Parameter values corresponding to the three chosen 1 st order calibrated models	77
5.1. Description of the generated synthetic scenarios	92
5.3. Parameters values of the base case	98
5.4. Common input parameters to all the generated synthetic scenarios.	102
5.5. The most favorable drilling trajectories	112
5.6. The least favorable drilling trajectories	113
7.1. Parameters values of the well calibrated 13 th and 3 rd models of CB1 and GPK3, respectively.	149

Nomenclature

Physical quantities

$\sigma_1, \sigma_2, \sigma_3$	Maximum, intermediate and minimum principal effective stresses, respectively.	MPa
S_{Hmax}, S_{hmin}, S_v	Maximum and minimum horizontal and vertical total stresses, respectively.	MPa
E	Young Modulus	GPa
α	Coefficient of linear expansion	K^{-1}
ν	Poisson ratio	—
α, β, γ	Euler angles	$^\circ$
P_p	Pore pressure	MPa
S	Total stress tensor	MPa
σ	Effective stress tensor	MPa
β	Biot coefficient	—
C_o	Uniaxial compressive strength	MPa
q	Material constant related to the internal friction angle	—
ψ	Internal friction angle	$^\circ$
c	Cohesion	MPa
τ_{oct}	Octahedral stress	MPa
$\sigma_{m,2}$	Mean stress	MPa
w_{BO}	Breakout width	$^\circ$

e_{BO}	Breakout extent/penetration depth	mm
θ_b	Breakout orientation	°
D	Computed value corresponding to presence or absence of drilling induced tensile fractures.	
a	Nominal borehole radius	mm
$\sigma_{\theta\theta}^{max}$	Maximum hoop stress	MPa
A, B	Regression parameters of Shen	
σ_{app}	Apparent wellbore strength	MPa
T_o	Tensile strength	MPa
F	Objective function	–

Coordinate Systems

(u, v, w)	Local and orthonormal borehole Cartesian coordinate system
(r, θ, w)	Cylindrical coordinate system centered on the borehole; r : radial, θ : tangential, w : axial

Acronyms

SFOE	Swiss Federal Office of Energy
GES	Geo-Energie Suisse AG
GLV-1	Name of the deep borehole of the Haute-Sorne project which is planned to be drilled in the canton of Jura
BS-1	Name of the deep borehole of the Deep Heat Mining project in Basel
CB1	Name of the borehole in Bedretto (BULG)
GPK3	Name of the deep geothermal borehole of Soultz-Sous-Forêt project
MD	Measured Depth measured along hole from ground level
TVD	True Vertical Depth

PEST	Parameter ESTimation software
EGS	Enhanced or Engineered Geothermal System
HS	Hydrothermal System
PS	Petrothermal System
HDR	Hot Dry Rock
HWR	Hot Wet Rock
HFR	Hot Fractured Rock
SGS	Stimulated Geothermal System
DHM	Deep Heat Mining
XLOTs	Extended Leak-off Tests
DITFs	Drilling Induced Tensile Fractures
A-DITFs	Axial Drilling Induced Tensile Fractures
E-DITFs	En-Echelon Drilling Induced Tensile Fractures
CHILE	Continuous, Homogeneous, Isotropic and Linearly Elastic
DS	Direct Sampling
MPS	Multiple-Point Statistics

Abstract

The economic viability of deep geothermal projects depends primarily on the extracted flow rate and thus its evaluation has to be made during its feasibility study stage. Borehole stability compromises sometimes the economic success of early stages of EGSs (Enhanced Geothermal Systems) and must therefore be comprehensively analysed. A stable borehole intersecting as many as possible hydraulically transmissive zones is the ideal target for a successful drilling. For instance, a highly irregular borehole cross-section involving deeply penetrating borehole breakouts or drilling induced tensile fractures (DITFs) may entangle the correct placing of packers used for a targeted stimulation of pre-existing fractures. As a consequence, the main challenge that drilling engineers usually encounter is the selection of an optimal borehole trajectory that will minimise borehole instabilities and maximise intersections with critically stressed fractures as they are favourably oriented to fail and exhibit very good fluid flow characteristics. For the aforementioned reasons, the accurate knowledge of the local state of stress and the rock strength is crucial to the success of deep geothermal projects.

State-of-the-practice methods estimate stresses and strength properties separately. Several approaches neglect to account for the interplay between stress and strength, a shortcoming this thesis addresses. Indeed, the interplay between the in-situ stresses and rock strength parameters (cohesion and friction angle) mainly controls the borehole stability. Additionally, there is still considerable controversy concerning the selection of an appropriate failure criterion and its parametrisation to compute borehole failure and most studies have only focused on estimating stress and strength from breakout width, ignoring as such other relevant borehole failure indicators such as breakout extent, breakout orientation and presence/absence of DITFs. This dissertation aims at filling this gap. A systematic, generic and novel methodology to calibrate jointly wellbore stress and strength in the shallowest section of a deep borehole and to predict failure severity in the deepest is presented. Beyond the theoretical development, practical tools are provided in order to facilitate knowledge transfer to the practice.

The calibration methodology was tested and developed with the extensive data set of the BS-1 borehole (from the Basel Deep Heat Mining project). The methodology aims at estimating jointly depth profiles of the local stress tensor (magnitudes and orientations) and rock strength properties (cohesion and friction). Emphasis is placed on better understanding the relationship between stress and strength, handling solution non-uniqueness and considering both depth trends (1st order characterization) and variability (2nd order) of key parameters. Regularized pilot points method were used to estimate model parameters as implemented in PEST software (Parameter ESTimation) from borehole cross-sectional characteristics (breakout width, breakout extent/penetration depth and breakout orien-

tation) and from the presence/absence of DITFs (including both axial and en-echelon tensile fractures, A-DITFs and E-DITFs). Results show consistency of the 1st order calibrated failure models with current knowledge of the stress in Basel. The reduction of parametric uncertainties was also investigated by including independent measurements of the minimum horizontal principal stress from hydraulic tests. It was concluded that this reduces drastically the range of calibrated parameters, which highlights the importance of collecting such data. Moreover, this methodology provides an effective and computationally efficient way of analysing extent of failure, which is potentially the most relevant parameter to assess packer sealing integrity. 2nd order calibrated models based on the pilot points technique allows reproducing the observed failure variability as well as most of the maxima/minima of breakout width and extent in addition to the small gaps without breakouts, which is critical to assess risk associated with packer placement. It provides also calibrated joint stress and strength profiles, including magnitude of all the stress components which gives a new insight into the source of stress variability in the earth crust. Our unique data set supports the idea that stress variability in the granitic basement of Basel arises primarily from fracture slip.

After estimating the stress and strength in the shallowest section of the well, prediction of failure severity is necessary for the selection of an optimal drilling trajectory. A stochastic methodology to perform predictions accounting for parameters uncertainty and variability in depth is proposed in this thesis. In this methodology, three elements are needed: (1) a borehole trajectory and section along which failure should be predicted, (2) a 1st order calibrated stress and strength model that can be extrapolated to a greater depth and finally (3) a 2nd order stress and strength model that can be used to generate stochastic variability and add it to the predictions. A key feature of the proposed prediction methodology is the possibility to perform predictions in a stochastic manner and to account for existing dependencies between all the parameters of interest. To validate our methodology, BS-1 data set were used. Results show the accurate goodness of fit between predictions and observations in the deepest section of BS-1. In addition to that, correlations between the failure model inputs and outputs were satisfactorily reproduced by using multivariate simulations that are based on direct sampling multi-point statistical approach as implemented in DeeSse software. These findings illustrate the robustness, completeness and accuracy of the developed workflow.

The applicability and limitation of the proposed workflow has been tested using synthetic cases covering a broad range of well trajectories, stress regimes and wellbore failure severity. In theory, the ability to predict failure in deviated boreholes with calibrated models based on data from a vertical well only is limited because the failure in the vertical hole is insensitive to the ratio between principal horizontal and vertical stresses which is important to assess stability of deviated wells. However, the proposed methodology in this work considers not only the data from borehole breakouts, but also from the drilling induced tensile fractures, DITFs. In addition, it accounts for depth trends of stress and strength and their variability in depth, which allows to mitigate these theoretical limita-

tions. Nevertheless, with calibration performed only on a vertical borehole section, the predictions carried out for deviated section show some divergences. The degree of dispersion of the predictions differ from one stress regime to another and depends mainly on the stress anisotropy ratio and the difference between failure severity in the calibration and prediction sections. This section of the thesis highlights and quantifies these limitations, guides the proper application of the proposed workflow and helps evaluating uncertainty and anticipating potential stability problems.

The significance of this thesis is that it enhances our theoretical understanding of borehole stability and optimal borehole trajectory selection by introducing a focus on the interplay between stress and strength and their stochastic variability in depth hitherto lacking, and informs our practical understanding of the importance of developing a set of versatile supporting software tool to quickly define the optimal borehole direction at a specific point during the drilling operations of deep geothermal wells. To that end, a graphical user interface was developed ('DG-WOW-app', Deep Geothermal Well Optimization Workflow application) and is presented in this dissertation bringing together the calibration and prediction developed methodologies into practice.

In addition, the proposed calibration and prediction methodologies as implemented in the DG-WOW application were tested on two real case studies in order to assess their versatility and robustness. For illustration purposes, the CB1 (Bedretto) and GPK3 (Souls-Sous-Foret) boreholes were used. Data from both boreholes were pre-processed, formatted and compiled. Then 1st and 2nd order calibrations were carried out in order to estimate depth trends of stresses and strength and to characterize their variability around these trends. Results outline the consistency of the calibration outputs with the literature.

The proposed methodology and associated tools call for their application on a wide range of new deep geothermal projects. This will allow them to be tested and improved so that they best meet the needs of the deep geothermal industry. Indeed, the research efforts deployed in this thesis are also aimed at transferring knowledge into practical and usable software tools with the ultimate objectives of making the extraction of deep geothermal energy possible and economical and thus assist with the energy transition.

Résumé

La viabilité économique des projets de géothermie profonde dépend principalement du débit extrait et son évaluation doit donc être effectuée au cours de l'étude de sa faisabilité. La stabilité des forages compromet parfois le succès économique des premières étapes des EGS (Enhanced Geothermal Systems - Systèmes Géothermiques Stimulés) et doit donc être analysée de manière exhaustive. Un forage stable, qui recoupe autant de zones hydrauliquement transmissibles que possible, est la cible idéale pour un forage réussi. Par exemple, une section transversale d'un forage très irrégulière impliquant des ruptures profondément pénétrantes ou des fractures de traction induites par le forage (DITF) peut empêcher le placement correct des packers utilisés pour une stimulation ciblée des fractures préexistantes. Par conséquent, le principal défi auquel les ingénieurs de forage sont généralement confrontés est la sélection d'une trajectoire optimale du puits qui minimisera les instabilités du forage et maximisera les intersections avec les fractures soumises à des contraintes critiques, car elles sont favorablement orientées pour se rompre et présentent de très bonnes caractéristiques d'écoulement des fluides. Pour les raisons susmentionnées, la connaissance précise de l'état local des contraintes et de la résistance de la roche est cruciale pour le succès de la géothermie profonde.

Les méthodes des pratiques de pointe estiment les contraintes et les propriétés de résistance séparément. Plusieurs approches négligent de prendre en compte l'interaction entre les contraintes et la résistance, une lacune à laquelle cette thèse remédie. En effet, l'interaction entre les contraintes in-situ et les paramètres de résistance de la roche (cohésion et angle de friction) contrôle principalement la stabilité du forage. De plus, il existe toujours une controverse considérable concernant la sélection d'un critère de défaillance approprié et sa paramétrisation pour calculer la défaillance d'un forage. La plupart des études se sont concentrées sur l'estimation des contraintes et de la résistance à partir de la largeur de la rupture, ignorant ainsi d'autres indicateurs de défaillance du forage tels que l'étendue de la rupture, son orientation et la présence/absence de DITFs. Cette thèse vise à combler cette lacune. Une méthodologie systématique, générique et nouvelle pour calibrer conjointement les contraintes et la résistance dans la section la moins profonde d'un forage profond et pour prédire la gravité de la défaillance dans la section la plus profonde est présentée. Au-delà du développement théorique, des outils pratiques sont fournis afin de faciliter le transfert des connaissances vers la pratique.

La méthodologie de calibration a été testée et développée avec l'ensemble de données complet du forage BS-1 (du projet Basel Deep Heat Mining). Cette méthodologie vise à estimer conjointement les profils en profondeur du tenseur de contraintes local (amplitudes et orientations) et les propriétés de résistance de la roche (cohésion et friction). L'accent est mis sur une meilleure compréhension de la relation entre les contraintes et la résistance,

sur le traitement de la non-unicité des solutions et sur la prise en compte des tendances en profondeur (caractérisation du premier ordre) et de la variabilité (caractérisation du second ordre) des paramètres clés. La méthode des points pilotes régularisés a été utilisée pour estimer les paramètres du modèle tels qu'ils sont implémentés dans le logiciel PEST (Parameter ESTimation) à partir des caractéristiques de la section transversale du forage (largeur de la rupture, son étendue ou sa profondeur de pénétration et son orientation) et de la présence/absence de DITF (y compris les fractures de traction axiales et en échelon, les A-DITF et les E-DITF). Les résultats montrent la cohérence des modèles de défaillance calibrés au 1^{er} ordre avec les connaissances actuelles des contraintes à Bâle. La réduction des incertitudes paramétriques a également été étudiée en incluant des mesures indépendantes de la contrainte principale horizontale minimale provenant d'essais hydrauliques. Il a été conclu que cela réduit considérablement la plage des paramètres calibrés, ce qui souligne l'importance de collecter de telles données. De plus, cette méthodologie fournit une méthode efficace et efficiente en termes de calcul pour analyser l'étendue de la défaillance, qui est potentiellement le paramètre le plus pertinent pour évaluer l'intégrité de l'étanchéité du packer. Les modèles calibrés du 2^d ordre basés sur la technique des points pilotes permettent de reproduire la variabilité observée de la défaillance ainsi que la plupart des maxima/minima de la largeur et de l'étendue de la rupture, en plus des petits intervalles sans rupture, ce qui est essentiel pour évaluer le risque associé au placement des packers. Il fournit également des profils de contraintes et de résistance calibrés conjointement, y compris la magnitude de toutes les composantes de la contrainte, ce qui donne un nouvel aperçu de la source de la variabilité de la contrainte dans la croûte terrestre. Notre ensemble de données unique soutient l'idée que la variabilité des contraintes dans le socle granitique de Bâle provient principalement du glissement des fractures.

Après avoir estimé les contraintes et la résistance dans la section la moins profonde du puits, la prédiction de la gravité de la rupture est nécessaire pour la sélection d'une trajectoire de forage optimale. Une méthodologie stochastique pour effectuer des prédictions tenant compte de l'incertitude des paramètres et de la variabilité en profondeur est proposée dans cette thèse. Dans cette méthodologie, trois éléments sont nécessaires : (1) une trajectoire de forage et une section le long de laquelle la rupture doit être prédite, (2) un modèle de contrainte et de résistance calibré du 1^{er} ordre qui peut être extrapolé à une plus grande profondeur et enfin (3) un modèle de contrainte et de résistance du 2^d ordre qui peut être utilisé pour générer une variabilité stochastique et l'ajouter aux prédictions. Une caractéristique clé de la méthodologie de prédiction proposée est la possibilité d'effectuer des prédictions d'une manière stochastique et de tenir compte des dépendances existantes entre tous les paramètres clés. Pour valider notre méthodologie, nous avons utilisé le jeu de données BS-1. Les résultats montrent la haute qualité de l'ajustement entre les prédictions et les observations dans la section la plus profonde de BS-1. De plus, les corrélations entre les entrées et les sorties du modèle de rupture ont été reproduites de manière satisfaisante en utilisant des simulations multivariées qui sont basées sur une approche statistique multi-point à échantillonnage direct telle qu'implémentée dans le logiciel

DeeSse. Ces résultats illustrent la robustesse, l'exhaustivité et la précision du workflow développé.

L'applicabilité et les limites du workflow proposé ont été testées à l'aide de cas synthétiques couvrant une large gamme de trajectoires de puits, de régimes de contraintes et d'intensité de rupture de puits de forage. En théorie, la capacité de prédire la rupture dans les forages déviés avec des modèles calibrés basés sur les données d'un puits vertical uniquement est limitée car la rupture dans le trou vertical est insensible au rapport entre les contraintes principales horizontales et verticale qui est important pour évaluer la stabilité des puits déviés. Cependant, la méthodologie proposée dans cette thèse prend en compte non seulement les données des ruptures de puits, mais aussi celles des fractures de traction induites par le forage (DITF). De plus, elle tient compte des tendances en profondeur de la contrainte et de la résistance et de leur variabilité en profondeur, ce qui permet d'atténuer ces limitations théoriques. Néanmoins, avec une calibration réalisée uniquement sur une section de forage verticale, les prédictions réalisées pour les sections déviées montrent quelques divergences. Le degré de dispersion des prédictions diffère d'un régime de contraintes à l'autre et dépend principalement du rapport d'anisotropie des contraintes et de la différence entre la sévérité de la rupture dans les sections de calibration et de prédiction. Cette section de la thèse met en évidence et quantifie ces limitations, guide l'application correcte du workflow proposé et aide à évaluer l'incertitude et à anticiper les problèmes potentiels de stabilité.

La pertinence de cette thèse réside dans le fait qu'elle améliore notre compréhension théorique de la stabilité des forages et de la sélection de la trajectoire optimale des forages en mettant l'accent sur l'interaction entre les contraintes et la résistance et leur variabilité stochastique en profondeur, jusqu'à présent inexistante. Elle éclaire aussi notre compréhension pratique de l'importance de développer un ensemble d'outils logiciels polyvalents pour définir rapidement la direction optimale du forage à un point spécifique pendant les opérations de forage des puits géothermiques profonds. À cette fin, une interface utilisateur graphique a été développée ('DG-WOW-app', Deep Geothermal Well Optimization Workflow application) et est présentée dans cette thèse réunissant les méthodologies de calibration et de prédiction développées dans la pratique.

En outre, les méthodologies de calibration et de prédiction proposées, telles que mises en uvre dans l'application DG-WOW, ont été testées sur deux études de cas réels afin d'évaluer leur polyvalence et leur robustesse. A titre d'illustration, les forages CB1 (Bedretto) et GPK3 (Soultz-Sous-Forêt) ont été utilisés. Les données des deux forages ont été prétraitées, formatées et compilées. Ensuite, des calibrations du premier et second ordre ont été effectuées afin d'estimer les tendances en profondeur des contraintes et de la résistance et de caractériser leur variabilité autour de ces tendances. Les résultats soulignent la cohérence des résultats de la calibration avec la littérature.

La méthodologie proposée et les outils associés appellent à leur application sur un grand nombre de nouveaux projets de géothermie profonde. Cela permettra de les tester et de les améliorer afin qu'ils répondent au mieux aux besoins de l'industrie de la géothermie

profonde. En effet, les efforts de recherche déployés dans cette thèse visent également à transférer les connaissances vers des outils logiciels pratiques et utilisables avec pour objectifs ultimes de rendre possible et économique l'extraction de l'énergie géothermique profonde et ainsi contribuer à la transition énergétique.

Keywords

Borehole failure; Calibration; Prediction; Uncertainties; Multiple-Point Statistics; Optimal borehole trajectory; Enhanced Geothermal Systems.

Mots-Clés

Rupture du forage; Calibration; Prédiction; Simulation multi-point; Trajectoire optimale du forage; Systèmes Géothermiques Stimulés;

Acknowledgements

I am really happy to finally be able to write this very important part of my thesis. My PhD was a life-changing journey. It took me 5 years of hard work at the Centre for Hydrogeology and Geothermics in Neuchâtel and collaboration with Geo-Energie Suisse in Zürich to give birth to this thesis. First, I would like to highlight a few things about this unique and unusual experience. My PhD is definitely more than just an academic or professional title. This was a real life experience, a journey with and within myself and a unique opportunity to ride a non-ending emotional rollercoaster of contentment/disappointment, enthusiasm/boredom, amusement/panic, hope/fear, gratitude/anger, patience/frustration, joy/sadness, calmness/stress, Being unaware of how this journey could be, I got stuck in the stress trap and caught in my own false and limited ways of thinking. This led me to a severe burnout and many other health issues, a very dark place where I was looking for only one reason not to give up. At that time, I was thinking I was unfortunate, but after a long healing journey and a deep reflection, I can just say that this was the best thing that ever happened to me. Hitting the rock bottom taught me valuable life lessons about courage, resilience, faith, persistence, tenacity, ambition, patience I don't even like to call it "rock bottom" because it was a new birth for me. Whoever is reading this, I want to say that failure and setbacks are ingredients for a rebirth, for a deep and unique self-exploration and self-discovery. No matter how hard you hit the bottom, the comeback is definitely greater than the setback.

Being able to bounce back couldn't have been possible without believing in myself even if everything was collapsing around me. It couldn't also have been possible without the people who supported me to make it to the end: my family, my husband, my supervisor, my friends and many other people who gave me a lift whenever I asked for help.

First, I would like to thank the University of Neuchâtel and Innosuisse for funding this project. I would also like to thank Geo-Energie Suisse for motivating the topic of this thesis and the Faculty of Science of the University of Neuchâtel for providing all the needed computational resources.

Special thanks to my supervisor, Prof. Benoît Valley, who was very patient with me in this journey and committed to the end of this project. I am so grateful that you believed in me from the beginning and chose me to work on this PhD project. Your guidance, support, and passion encouraged me to continue until the end. This project wouldn't have been possible without your tireless understanding and help.

I would like also to express my gratitude to Dr. Andrés Alcolea for always offering help and being available. Your trust helped me to do great things when it was getting harder and harder. Your jokes and good humor always made it fun to work with you. You showed the utmost commitment until the end.

I am also thankful for Dr. Peter Meier, Dr. Frédéric Guinot and Dr. Florentin Ladner

from Geo-Energie Suisse who were also involved in this project since the beginning. You have welcomed me and given me the chance to work with you. Every feedback you gave me was extremely important and helped me to improve constantly my work. I would like also to express my gratitude to Prof. Philip Brunner and Dr. John Doherty for their guidance, valuable and insightful feedback whenever it was needed.

I want to thank my friends who were a ray of sunshine even on my darkest days. They were always willing to listen, to grant me their love and trust.

Sara, words can't describe how truly grateful I am to have you in my life. We shared our darkest and brightest moments together, we laughed and cried together, we experienced life in all its ups and downs and still, we never left each other. This is one of the most beautiful gifts life gave me.

Dan, I can't thank you enough for how patient, open, loving, caring you were with me. You were always there to support me on all levels. You were one of the very few people who believed in me. Our laughs, jokes, secret stories, coffee breaks, and evening walks were precious and will remain timeless treasures. I really thank you for everything.

Maha, thank you for being the person I could rely on for many years. Our paths crossed together and we shared so many memories that can never be erased. Thank you for supporting me and sticking by me even when I had crazy ideas doomed to fail.

I also can't think of my PhD journey without thinking of Guillaume, Batoul, Thanushika, Maria, Kalliopi, Chencheng, Reza, Gunnar, Youssra, Alejandra, and Sandie. The time I spent with you was full of laughter and I knew that, at any moment, you were willing to cheer me up with your jokes. I want to thank you for your empathy, and for every moment you said that I will make it; these words lifted me up every time I was feeling down.

I can't thank enough my family. They offered me their endless support, they believed in me and kept me motivated in this journey. Thank you for embracing the toughest phases of my life, for always reminding me of the end goal, and for showing me that love is the most important thing in life. This makes me want to also thank my family-in-law for giving me the warmth I was missing and for creating a loving home for me. My soul was nurtured whenever I visited you.

To my precious husband and partner in life, I can't find the right words to describe my gratitude towards you. You are a rare and unique loving person who always backed me up. You watched me succeed. Seen me fail. Took my hand when I was drowning. Cheered me on. Patted me on the shoulder when I couldn't do it to myself and gave me all that you had. I am grateful and blessed to have you in my life. I just want to say that I love you.

Special thanks to the beautiful and creative, Zoé, who made the drawing below for me. It was three months before my PhD private defense when I had a small accident and broke my leg. Her drawing made me smile and somehow perceive what she could see: the sun always shines after the storm.

Last but not least, I want to thank myself for not giving up, for being courageous to



step into a very dark and scary place and see the light in it. I want to thank myself for always giving more than receiving even when my cup was empty. I want to thank myself for believing in me even when I felt lost, exhausted, useless, weak, scared, and unworthy. I want to pat myself on the shoulder now and say that I am proud and feeling blessed and grateful for this unique experience that opened many unlocked doors for me.

1. Introduction

1.1. Context and motivations

Around 80% of Switzerland's energy consumption is fed mainly by imported and non-renewable sources. Its main sources of energy are oil, nuclear, hydroelectric power and natural gas. Electricity is mainly generated by hydropower (59.9%), nuclear power (33.5%) and conventional thermal power plants (2.3%, non-renewable) as stated by the Swiss Federal Office of Energy (SFOE). Today, Switzerland consumes five times more energy than it did in 1950. The goal of the Swiss energy policy is to guarantee a secure, economical and ecological energy supply. To fulfil this mission, there is the Swiss Energy program, launched in 2001, which aims at achieving a 20% reduction in CO_2 emissions and energy consumption from 1990 levels by 2020, accompanied by a 50% increase in the share of renewables between 2010 and 2020. Following the nuclear reactor accident in Fukushima in 2011, Switzerland embarked on an energy transition process, which began with the launch of its national Energy Strategy 2050. The latter is based on three pillars: more energy-efficient buildings, machinery and transport, increased use of renewables, especially hydropower, and the phase-out of nuclear power. The aim of this new strategy is a 3% reduction in per capita energy consumption by 2020 and a 13% reduction on 2000 levels by 2035. This energy consumptions reduction target is accompanied by two other important objectives: (1) the decommissioning of Switzerland's five nuclear power plants by the end of their operating life and (2) the reduction of CO_2 emissions. The latter is a very active political topic with a new CO_2 law recently finalised but under the threat of referendum. This law aims at a zero net CO_2 emission in Switzerland by 2050, which is an enormous challenge as it requires a complete revolution of the energy system in Switzerland over a period of 20 to 30 years. This challenge must be addressed by (1) a massive increase in the use of all renewable and low-carbon energy sources and (2) the capture and storage of CO_2 (Carbon Capture and Storage, CCS). Within this push for renewable energy, the Swiss Energy Strategy targets for geothermal is a 4.4 TWh of power production by deep geothermal systems by 2050. This would mean that 50-100 geothermal power plants (with an electric power output of 5 - 10 MWe each) have to be realized by 2050. Using geothermal energy should also provide large heat production and contribute to the reduction of CO_2 emissions.

It is obvious that recovering geothermal heat requires deep drilling into the earth's crust (hence deep geothermal), possibly several kilometers deep. According to the TA-Swiss study on deep geothermal energy published in 2015 (Burgherr et al., 2015), an immense

amount of geothermal energy is potentially available in Switzerland's subsurface. The geothermal energy contained in the layer of rock between 4 km and 5 km depth (originally about 150 °C hot) is estimated to be 600.000.000 GWh or to be equivalent to 10.000 years of the current Swiss annual electricity consumption (SFOE). As a consequence, deep geothermal projects in crystalline basement are needed in order to recover geothermal heat. New drilling technologies developed in the oil and gas sector allow nowadays to vary and control the borehole trajectories. Directional drilling has been a game changer in the oil and gas industry. It can also play a key role in deep geothermal sector as it allows to access the rock mass in an optimal manner in terms of both intersection with potential feed zones (fracture and faults) and consideration of the in-situ stress state. Yet, the deeper we drill the greater are the subsurface unknowns controlling the stability of the Earth's crust. Wellbore instability is then one of the key problems that engineers encounter during drilling. The main causes of these instabilities can be grouped into three categories: (1) Mechanical failure of the rock around the hole due to high stresses and low rock strength, (2) erosion caused by fluid circulation or (3) chemical failure arising from damaging interactions between the rock and the drilling fluid. While (2) and (3) can be very important mechanisms in oil and gas industry where shales are crossed or targeted by boreholes, (1) is the most relevant mechanism for deep geothermal boreholes that are drilled in crystalline rocks.

Before drilling, the rock strength at some depth is in equilibrium with the in-situ rock stresses (effective overburden stress, effective horizontal confining stresses). When a volume of rock is excavated, however, for example by drilling it, the state of stress around the excavation is modified. The stresses that were carried out by the excavated rock have now to be supported by the neighboring rock leading to stresses redistribution and stresses concentrations and the balance between the rock strength and the in-situ stresses is disturbed. In addition, foreign fluids are introduced, and an interaction process begins between the formation and borehole fluids. This may result in hole-instability and thus, loss of drilling time, and sometimes, loss of drilling equipment. A growing body of literature has investigated borehole instabilities issues and there is a considerable amount of research sharing the same shortcoming of uncertainty in the input data needed to run borehole-stability analyses (in-situ stresses, pore pressure, rock mechanical properties, formation and drilling-fluids chemistry). Drillers recognise four different types of borehole instabilities: hole closure, hole enlargement or washouts, fracturing, and borehole collapse.

In deep geothermal wells, the most relevant type of instabilities are (1) fracturing — typically referred to as drilling induced tensile fractures (DITFs) — either due to high wellbore pressure or to thermo-elastic stresses that arise from cooling and (2) borehole collapse, referred to as borehole breakouts, when stresses at the borehole wall exceed the rock strength. For instance, investigations at the BS-1 borehole from the Deep Heat Mining (DHM) project in Basel (Håring et al., 2008) showed that borehole breakouts were pervasive and the crystalline section of the well was affected by approximately 80%. These features caused low drilling performance in the crystalline basement and highly

irregular hole shapes that may preclude a proper installation of any kind of completion system. Thus, deep geothermal projects require very good control on borehole stability. Several models in the literature address wellbore-stability analysis. These include very-simple models based on linear elastic analytical solutions to very-complex numerical simulations involving material models that require numerous parameters (Hale et al., 1993). In all cases, parameterizing the failure model is challenging because, in the context of deep geothermal project, the required data are either unavailable and/or encompass large uncertainties. For instance, in-situ stresses such as principal horizontal stresses and the rock parameters (cohesion, friction angle) are either unknown or estimated based on a limited number of measurements that are not representative. One path forward is the development of empirical relationships between strength and petrophysical parameters derived from sonic and density logs (Chang et al., 2006), but this approach is site specific and thus does not have a general scope. When cores are available, laboratory tests can be performed, but the question of their representativity of in-situ conditions is debated. Indeed, it is difficult to account for effects like core damage (Martin and Stimpson, 1994) that may hinder the estimation of strength properties. Also, estimating separately stresses and strength ignores the interplay between both of them, which mainly controls the shape of borehole failure. These are other challenges that motivate this thesis, which outlines the need for a new systematic methodology in order to fill this gap.

This thesis is a collaboration project between the University of Neuchâtel and Geo-Energy Suisse AG (GES) supported by InnoSuisse. One key feature of GES projects is an innovative borehole completion scheme, referred to as "multistage stimulation concept", which includes extensive zonal isolation using swellable packers allowing for reservoir stimulation and exploitation optimization and it aims at maximizing heat recovering and minimizing the seismic risk. The success of previous deep geothermal projects in Switzerland (for example the DHM project in Basel, Häring et al., 2008) was undermined in the critical project stage that is the reservoir creation. Thus, the enabling technology that is planned to be developed in this project will have a large impact as it has the potential to unlock the access to deep geothermal resources in Switzerland. The project is not limited to a theoretical development but it was planned that it will include a full scale application at the geothermal project of Haute-Sorne in the Canton of Jura. Unfortunately, due to a legal process initiated by opponents of the project in the Canton of Jura, the Haute-Sorne project was delayed. Additionally, shortly after the Pohang Mw 5.5 earthquake in November 2017, the Government of Jura requested GES to provide a report on the Pohang events and their possible implications on the Haute-Sorne project. Therefore, the latter could not be realized within the scheduled timeframe and was still not advanced at the completion date of this thesis. In order to develop the methodological aspects in this thesis, we used the extensive borehole data set along the 2.5 km crystalline section of the borehole BS-1 in Basel (Switzerland). We tested also our approach on newly acquired data by GES at the

Bedretto laboratory where the multistage stimulation approach is currently tested. We use also data from the Soultz-sous-Forêts project that are now available in public domain.

1.2. Objectives

This thesis has a strong application component as it is supported by the industry. New fundamental development on the manner to handle wellbore failure analyses were necessary to meet the industrial project objectives. These new methods provide also information on in-situ stress and strength that were not available and give thus new insights into the geomechanical conditions in the upper crust. In this Chapter, the objectives of the thesis are presented with two points of view: the industrial application objectives and the fundamental science development.

1.2.1. Industrial application objectives

The initial design of the project was based on a potential application in Haute-Sorne. Even if this project was not realised, the objectives are best illustrated with a potential application at Haute-Sorne as a template for any deep geothermal project. The first deep well in Haute-Sorne, GLV-1, is planned to be drilled as a J-hole (a deviated hole) to a depth of 4900 m TVD (true vertical depth) or 5800 m MD (measured depth). When GLV-1 reaches the depth of 3500 m following an essentially vertical trajectory, a decision has to be made in which direction the well has to be deviated in order to:

- Maximize the probability of intersection with potential feed zones (existing fractures and fracture zones).
- Maximize borehole stability in order (1) to limit drilling difficulties associated with borehole instability and (2) to obtain a hole which is sufficiently in gauge not to compromise a well completion with swellable packers for reservoir segmentation and subsequent staged stimulation.

Both criteria are not necessarily compatible and an optimum must be determined in order to decide of the best well path. According to these two criteria, this project is developed as the basis for decision making. It comprises:

1. A workflow to optimize well trajectory planning that enables a decision making process in a comprehensive and structured way within a short time period. This workflow will guide through the required processes to integrate existing and newly acquired data from the vertical open hole section within the crystalline basement, to forecast borehole failure and fracture intersection for potential hole trajectories and to select the most favorable one.
2. A software toolbox that allows expediting the processes required in the workflow above so that non-productive time of the drill rig is minimized. This software solution includes read-in/write-out routines for data collected in the vertical section

of the borehole, processing toolboxes for specific steps in the developed workflow and visualization of the analyses output to enable decision making. These software solutions will allow exchanging data between available software solutions for well-log analyses (WellCadTM) and parameters estimation (PEST).

1.2.2. Fundamental science developments

In order to achieve the industrial objectives cited above, some fundamental developments are needed. The main scientific questions to answer are the following:

1. How to jointly calibrate stress and strength parameters against borehole failure observations without imposing a priori constraints on these parameters? How to handle non-uniqueness of the calibrated solutions?
2. What failure model and failure estimation approach are suitable for such calibration process?
3. How do we account for natural variability in our calibration approach?
4. How do we use our calibrated parameter sets to make robust borehole failure predictions? Will different sets of calibrated parameters allow for consistent predictions? What is the uncertainty associated with these predictions? Can we reproduce natural variability in our predictions? What are the limits of applicability of our prediction approach?
5. What are the main factors that control natural stress variability in the crystalline basement? Can we bring new evidences on this topic from our calibrated stress and strength models?

The objective of this research is to develop new methodologies that answer these questions by combining geomechanical modeling, parameter estimation and geostatistical approaches.

1.3. Thesis organization

The thesis contains a main part composed of 8 chapters and appendix part containing the supplementary materials. Chapters 3, 4 and 5 constitute the base of three scientific papers that are in preparation for submission to the 'International journal of rock mechanics and mining sciences' at the time of compilation of this thesis. The latter is organized as follows:

- Chapter 1 gives a general introduction and highlights the motivations and objectives of my research work.
- Chapter 2 reviews fundamental principles of deep geothermal systems. It discusses stress and wellbore failure concept in deep boreholes drilled to the crystalline basement and outlines uncertainties encountered in geomechanical designs and how to

deal with them. All these concepts are at the root of the methodologies proposed in this thesis.

- Chapter 3 presents a new systematic methodology to estimate depth profiles of the characteristics of the local stress tensor (both magnitudes and orientations of all three principal stresses) and rock strength properties together. This chapter focuses particularly on breakout geometrical characteristics relevant to assess suitability for zonal isolation techniques deployment and uses the exceptional failure data set from the deep geothermal borehole BS-1.
- Chapter 4 deploys a generic methodology for borehole failure prediction and carries out its application to the prediction of the final section of the Basel borehole, BS-1, in order to validate the applicability and robustness of the developed methodology.
- In Chapter 5, the calibration and prediction methodologies proposed in Chapter 3 and 4 are tested systematically on synthetic cases covering a broad range of stress regimes and wellbore trajectory. The objective of this work is to test the applicability, robustness and limitations of our methodology.
- Chapter 6 presents the developed software tool that supports the developed methodology. The latter is presented in the form of a systematic workflow in order to speed-up data processing and enable decision making in a timely manner.
- In Chapter 7, additional real case studies are presented by applying the methodology to real data sets: Soultz-Sous-Forêts (France) and Bedretto (Switzerland).
- Finally, Chapter 8 summarizes the main contributions of this thesis and gives some perspectives for future research.

2. Background

2.1. Deep geothermal energy

A large part of the of earth is at temperature above 1000°C and, at drillable depth, the temperature can reach up to $\approx 350^\circ\text{C}$ in areas with special geothermal conditions, and up to $\approx 200^\circ\text{C}$ in areas with normal geothermal conditions. Deep geothermal energy is then defined as the natural heat found beneath the earth's surface. This energy source is of interest to mitigate global warming as it has a low carbon footprint and is available in essentially unlimited quantities. It arises primarily from the initial heat resulting from the early earth time gravity collapse, the latent heat of the earth core and the decay of radioactive elements in the earth's crust (Jaupart et al., 2007). Deep geothermal energy involves deep drilling more than 400 m below the earths surface. The depth range from 400 to 1000 m is sometimes referred to as middle-deep geothermal. The term 'deep geothermal energy' is usually used for depths of at least 1000 m and temperatures of more than 60°C . Note that deep geothermal systems are commonly divided into Hydrothermal Systems (HSs) and Petrothermal Systems (PSs). The distinction between these two concepts will be addressed next.

2.1.1. Hydrothermal Systems Vs. Petrothermal Systems

A hydrothermal system includes fluid, heat and permeability in a naturally occurring geological formation such as an aquifer (Fig. 2.1), which is exploited by a production and injection well (Bertani, 2012). Schulz (2008) showed that the permeability of the productive horizon in HSs should be at least $1 \times 10^{-14} \text{ m}^2$ and the productivity index at least $1 \times 10^{-2} \text{ m}^3/\text{MPa} \cdot \text{s}$ in order to ensure high enough flow rate and thus high productivity of the well. Note that the most prototypical of HSs worldwide are volcanic systems in addition to some standard hydrothermal reservoir rocks like sedimentary porous aquifers (sandstones) or secondary fractured rocks (limestones). In Switzerland, hydrothermal systems are targetting either hot water from natural aquifers or faulted and fractured zones at depths of 3-5 km. According to the TA-Swiss study on deep geothermal energy (Burgherr et al., 2015), only limited contribution from hydrothermal systems to future geothermal electric power production is expected in Switzerland due to the scarcity of naturally sufficiently permeable deep target and the difficulty to identify them.

An alternative to HSs, which mainly depends on the presence of fluid and high permeability, involves human intervention to engineer these reservoirs in hot rocks for commercial use. For instance, the impermeable rock can be fractured sufficiently so that water can

flow more freely. This technique is called Enhanced or Engineered Geothermal Systems (EGS). The heat of the rock at depth is extracted by advective transport driven by fluid circulation between two or more boreholes. Once the water reaches the surface, it passes through a power plant where electricity is generated. Then the loop is completed when water is returned to the reservoir through injection wells. This closed-loop system has the advantage of not releasing any fluids to the atmosphere and not emitting any greenhouse gas. Petrothermal Systems (PSs) refer also to EGSs, where the permeability of the rock is permanently increased by rock mass modification using various types of stimulation techniques. In order to be economically attractive, a commercial petrothermal system should provide approximately 50 to 200 liters of water per second with a temperature of 150°C to 180°C (Fig. 2.1), although development in power plant technology may allow nowadays to produce power from water as low as 90°. The advantage of the EGS technology is that by applying engineering to the reservoir, rock mass without sufficient initial permeability could still be exploited, reducing the prospection and exploration risk. EGS approach has been applied to a variety of geological settings (e.g., sedimentary rocks: Gross Schonebeck, Germany (Blöcher et al., 2015); igneous rock: Krafla, Iceland (Mortensen et al., 2010); metamorphic rock: Larderello, Italy (Parri and Lazzeri, 2016)). However, preferred locations for EGSs are deep granitic bodies covered by a 35 km layer of insulating sediments that slow heat loss. An EGS plant is expected to have an economical lifetime of 2030 years using current technology (Tester et al., 2006). PSs or EGSs have a much higher resource potential in Switzerland (Burgherr et al., 2015). However, it must first be demonstrated that the EGS technology, that heavily relies on the reservoir creation procedure, is a viable option in order to complete a meaningful assessment of deep geothermal resources. When considering past nomenclature, PSs could also fall into other categories (Breede et al., 2015) such as: engineered geothermal systems (EGSs), hot dry rock (HDR), hot wet rock (HWR), deep heat mining (DHM) and stimulated geothermal systems (SGSs). Some of these concepts will be further explained in the next section.

2.1.2. Stimulation techniques and reservoir creation

The development of a safe and robust permeability creation methodology in order to allow flow rate at economical levels is central to the deployment of the EGS approach. The permeability creation methodologies, often referred to as reservoir stimulation, can be primarily based on thermo-mechanical processes activated by cold fluid injection (thermal stimulation), mineral dissolution by acids injection (chemical stimulation) or the modification of the fracture network by massive fluid injections (hydraulic stimulation). The latter is believed to be the most likely to have an effect that is not limited on the well-bore near field. During massive hydraulic injections, different processes leading to the enhancement of the hydraulic properties of the rock mass can be activated by using (1) hydro-fracturing (also called fracking or hydro-fracking) and (2) hydro-shearing. Hydro-fracturing is a well stimulation technique mainly used in the oil & gas industry (Sutton

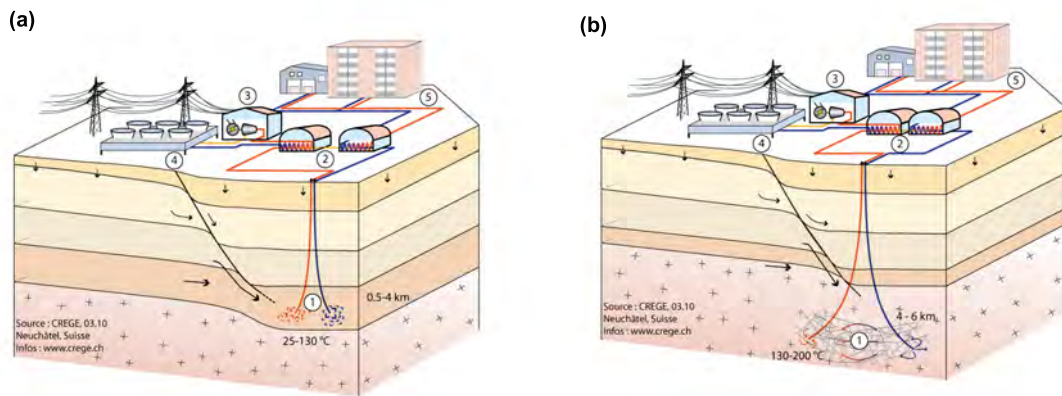


Figure 2.1.: Schematic diagrams illustrating (a) hydrothermal systems and (b) petrothermal systems. (1) corresponds to production and reinjection drilling, (2) heat exchanger, (3) power plant, (4) air cooling system, (5) district heating network (after CREGE, 2010).

et al., 2010; King, 2012) involving the injection of 'fracking fluid' (typically water that contains viscosity modifiers, sand or other proppants) under high pressure into a bedrock formation in order to create new fractures and increase the size and the connectivity of existing fracture through which natural gas and oil will flow more freely. During the 'fracking' process, the injection pressure is usually brought above the minimum principal stress, σ_3 , in the ground to open the joints which are already in the right orientation. In case of a pre-existing fracture oriented normal to σ_3 , the fracture can be opened by exceeding σ_3 only. On the contrary, during the hydro-shearing process, the injection pressure is maintained by pumping continuously closely to σ_3 in the ground (perhaps 95 to 99% of its value). Hydro-shearing aims at increasing the fluid pressure in the naturally fractured rock and inducing shear failure or slip events, which can enhance the systems permeability through permanent dilatational opening of the sheared fractures. This process was shown to be very important for permeability development by hydraulic stimulation during the geothermal reservoir operations in 1985 at the Rosemanowes test site in Cornwall (Pine and Batchelor, 1984; Richards et al., 1994) or the one created in 1987 at Soultz-sous-Forets test site (Evans et al., 2005).

The evolution of deep geothermal reservoir terminology and concepts is presented by conceptual end-members in Fig. 2.2. It is relevant to review this terminological evolution in terms of the implied wellbore trajectories and their relation to the in-situ stress. The Hot Dry Rock (HDR) concept was developed in the early 1970s when a team from Los Alamos National Laboratories began the hot dry rock (HDR) project at Fenton Hill (Cummings and Morris, 1979; Tester et al., 1989; Brown, 1997; Duchane, 1998). In this early concept, the heat from a dry rockmass was to be exploited by hydraulic fractures placed between two wells in order to establish a closed-loop circulation of pressurized fluid (Fig. 2.2a). This concept is fully described in Potter et al. (1974). The terminology evolved by realizing that

the crust at target depth is always water saturated even if permeability does not allow for large flow rates. This led to the emergence of the Hot Wet Rock (HWR) concept (Duchane, 1998) (Fig. 2.2b). HDR and HWR neglected an important characteristic of natural rock masses: the pervasive presence of natural fractures that have a dominating impact on the fluid flow. When these fractures carried natural fluid flow, the minerals in the fractures are altered by these hydrothermal fluid circulation. The terminology 'Hot Fractured Rock' (HFR) (Wyborn et al., 2004; Goldstein et al., 2011) and 'fractured hydro-thermally altered reservoir' (Genter et al., 2003, 2010) emphasise the importance of these natural fractures in the hydraulic behaviour of deep seated rock masses (Fig. 2.2c-d). However, the natural transmissivity of the fractures is often not sufficient to permit economical flow rate and thus must be enhanced. This led to the terminology Enhanced Geothermal System (EGS) (Tester et al., 2006), that has been largely and conceptually developed based on the experiment performed at the Soultz-sous-Forêt geothermal site. At this site, reservoir enhancement was primarily achieved by massive fluid injection in long open hole sections. The combined effect of the in-situ stresses and natural fracture network led to stimulated volumes imaged by microseismic monitoring with an oblate shape extending in the plane perpendicular to the minimum principal stress direction. After stimulation, the subsequent borehole was placed in the continuity of this stimulated volume, leading to a wellbore alignment in the direction of the maximum principal stress direction. Directional drilling was used to steer the well from the same drill pad. Drilling trajectory was essentially decided upon the geometry of the previous well stimulated volume.

The same concept applied in Basel led to the abandonment of this project due to induced seismicity and a reservoir with volumetric and hydraulic properties likely insufficient for economical exploitation. This led to a review of the stimulation concept and the realisation of the need for more control on the stimulation processes and the possibility to swap a larger rock mass volume between the injection and production well (Meier et al., 2015). Such approach needs more engineering of the wellbore in order to improve control on the reservoir. We introduce here a terminological nuance and call this approach Engineered Geothermal System (EGS), a term that was often used as a synonym to Enhanced Geothermal System, although we believe that the terminology emphasises an important difference. One possibility to increase control is the 'multi-stage stimulation' concept, derived from the O&G technical developments in the last decades, that includes extensive zonal isolation by using for example swellable packers within a highly engineered borehole completion. This idea changes the paradigm on the optimal drilling trajectory of the wells. In this case, long sub-horizontal lateral well section should be oriented in a direction close to the minimum stress so that the stimulated volumes growing perpendicular to minimum stress permit to establish hydraulic links between the wells (Fig. 2.2f). This evolution in concepts illustrated by the terminology that evolves over time calls for the complete rethinking of the optimal wellbore trajectories that is at the core of this thesis. In this latest concept, an optimal trajectory is one that allows complex completion and thus requires a stable borehole, that intercepts as many as possible potential feed-zones to seed

the reservoir creation operations and that is oriented favorably to the stress state in order to promote hydraulic linkage between the wells and maximize swapped rock mass volume.

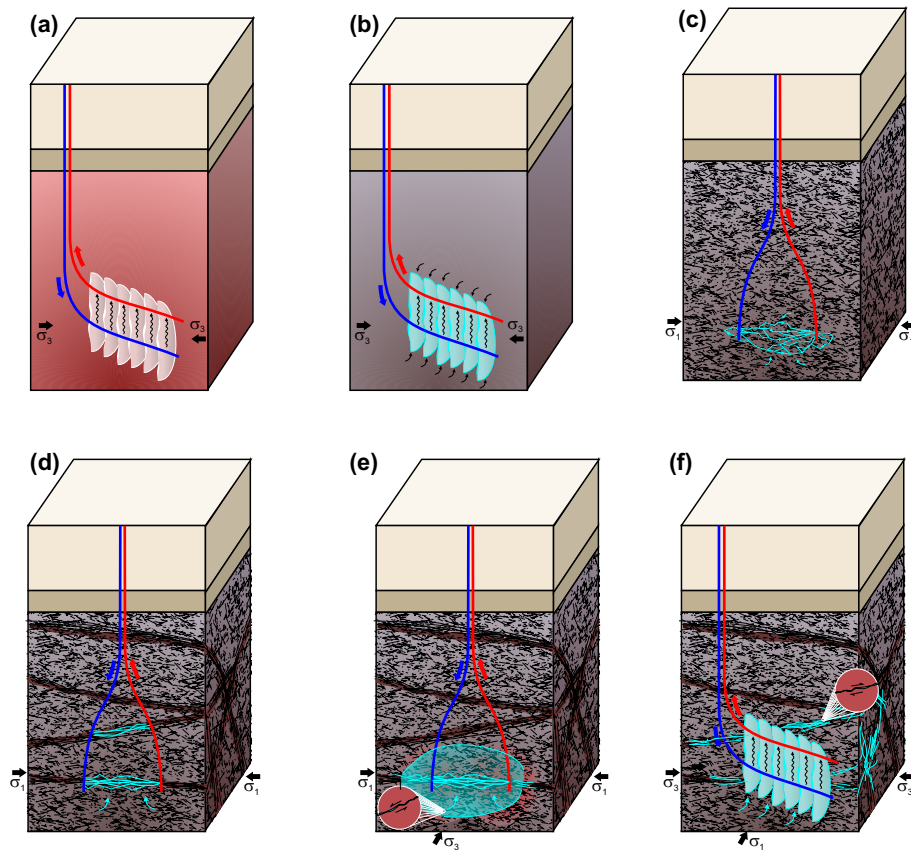


Figure 2.2.: The evolution and classification of the deep geothermal reservoir concepts: (a) Hot dry rock (HDR), (b) hot wet rock (HWR), (c) hot fractured rock (HFR), (d) fractured hydrothermally altered geothermal reservoir (HFR), (e) enhanced geothermal reservoir (EGS) and (f) engineered geothermal reservoir (EGS; e.g., multi-stage fractured geothermal reservoirs) (after Dutler, 2020).

2.2. Stress and wellbore failure concept in crystalline rocks

A growing body of literature has studied the stability of boreholes in the Oil and Gas (O&G) industry. However, these findings are not representative of the rock failure around deep boreholes in crystalline rocks because (1) the failure mode is fundamentally different and (2) the geological environment of O&G projects and the type of reservoir rocks encountered (sedimentary rocks: shale, sandstones and carbonates) are very different from the conditions in deep geothermal projects (crystalline rocks: granites, gneiss). For instance, deep wells in crystalline basement are affected by borehole breakouts, which are mainly controlled by the in-situ stresses acting on the borehole and dominated by brittle failure mode that differs from shear failure usually assumed for borehole stability analy-

ses. These features may entangle, or even preclude, the correct placing of packers, whose sealing is mandatory for a correct stimulation of pre-existing fractures.

The other problem arises from the difficulty to characterize stresses in deep wells. The latter are often poorly constrained, particularly at early project stage and the estimation of the in-situ strength is usually lacunar (Valley and Evans, 2019). This is also due to a gap in understanding the processes at play at the borehole wall during initiation and accumulation of damage leading to the formation of borehole breakouts. Thus, the initiation, extension and final shape of borehole breakouts cannot be reliably predicted. So far, the standard methods estimate stresses and strength properties separately, thus ignoring the interplay between them, which actually controls the shape of borehole failure. For instance, hydraulic tests (e.g. XLOTs, Extended Leak-off tests, Lin et al., 2008) can be used to estimate the minimum horizontal principal stress, S_{hmin} . Borehole failure in compression or tension are excellent estimates of the orientation of the horizontal principal stresses. For instance, Bell and Gough (1979) used stress induced failure – as it is the cause of deep borehole elongation – to characterize stress orientation. At the time, breakouts were largely identified with multi-arm caliper logs, but very little was known about the details of their geometry. Afterwards, borehole wall imaging techniques such as the acoustic televiewer (Zemanek et al., 1970) were invented and widely used since the 1990s (Luthi, 2001) in addition to the development of high temperature tools as described in Asm (2014).

These innovative tools gave us the opportunity to precisely describe the shape of breakouts in deep geothermal boreholes. However, the magnitude of the maximum horizontal principal stress, S_{Hmax} , is particularly difficult to constrain. In 1988, Barton et al. (1988a) studied the Fenton Geothermal well *EE3* in New Mexico and proposed a relationship between the angular opening of breakouts (also named as 'breakout width') and the magnitude of the maximum horizontal principal stress, S_{Hmax} , assuming that the strength of the rock at the borehole wall is given by its uniaxial compressive strength, UCS , and that breakout deepens after failure initiation but does not widen (i.e., the initial and final width of the breakouts are the same). Although, some modification of breakout width with time have been reported in-situ (Azzola et al., 2019), this approach is widely accepted. Moreover, in crystalline rocks, the failure is progressive with an accumulation of damage starting at the so-called crack initiation level ($0.4 \cdot UCS$), which leads to a variation in the cohesive and frictional strength components (Martin, 1997; Diederichs, 2007). Martin et al. (1999) reported also that failure occurs when the maximum tangential stress is about $0.4 \cdot UCS$ and this result was confirmed by Andersson et al. (2009b) at the Aspö underground rock laboratory. As such, these findings show that the opening wall stress is significantly lower than the UCS , which highlights a contradiction with theoretical and experimental arguments stating that the intermediate principal stress has a strengthening effect (Colmenares and Zoback, 2002; Haimson, 2006; Al-Ajmi and Zimmerman, 2005).

The estimation of S_{Hmax} magnitude from borehole breakouts (see Zoback et al., 2003, for a review) has the advantage to allow to assess variability along the borehole. There are several examples where stress magnitudes were constrained by wellbore failure. For

instance, stress magnitudes were constrained in the KTB borehole in Germany (Mastin et al., 1991; Brudy and Zoback, 1993; Borm et al., 1997) by using both breakouts and drilling-induced tension fractures (DITFs) and in the Habanero geothermal project in Australia (Fernández-Ibáñez et al., 2009) and Pohang in South-Korea, (Alcolea et al., 2020). However, such approach is very sensitive to the used failure criterion used to compute borehole failure. Indeed, different failure criteria lead to different estimates of S_{Hmax} magnitude depending on whether they are taking into account the effect of the intermediate principal stress, σ_2 , or not (Valley and Evans, 2019). Moreover, independently of the subjectively chosen failure model, it is difficult to parametrize the failure criteria from deep well data. The choice of an appropriate failure criterion and characterization that captures borehole wall strength remains controversial. In their study of the BS-1 deep borehole in Basel, Valley and Evans (2019) used results from a single triaxial test on a core plug to parametrize their failure models and they acknowledged the inherent and high uncertainties. Another approach is to estimate in-situ strength by developing empirical relationships between strength and petrophysical parameters derived from sonic and density logs (Chang et al., 2006). Such relationship can be calibrated using results from laboratory tests on cores. However, rarely sufficient tests on cores are available from deep wells to calibrate such relationships. It is also difficult to account for effects like core damage (Martin and Stimpson, 1994) that may mislead the in-situ strength estimation. In a nutshell, methods developed for the O&G industry to characterize the stress state from borehole failure (Zoback, 2007) or approaches to predict borehole failure intensity and to optimize borehole trajectory and other drilling parameters (Ottesen et al., 1999; Moos et al., 2003) cannot be applied directly for deep geothermal wells in crystalline rocks.

Moreover, in state-of-the-practice approaches stress and strength are not estimated jointly, i.e. one has to be determined independently (often with large uncertainty) in order to evaluate the second one. In addition, such approaches are applied in a deterministic manner without systematic evaluation of the uncertainties. It is also worth noting that specific effects like the influence of the borehole size, time dependencies and the impact of thermo-elastic contrasts and grain structure in the constitutive mineral of the rock are not well understood. This leads to uncertainty in the model outputs that need to be integrated when making a prediction of the expected borehole shape. In addition, the specificity of the well design intended by Geo-Energie Suisse AG has not been studied in detail. A systematic parameters analysis is lacking. The drilling sequence proposed in such projects allows for solutions to be developed, i.e., calibrating a failure model on the vertical borehole section and applying the calibrated model on the deviated section. However this approach must be developed and tested in order to verify its practicality and robustness. The main motivation behind this thesis is to show that, despite all of the aforementioned limitations, it is nevertheless possible to calibrate the geomechanical parameters that are difficult to constrain (stresses and rock properties) on existing data sets (e.g., vertical hole section already drilled) and to use these models to predict borehole failure in other conditions (e.g., deviated borehole). As such, the failure models are used

as predictive tool for failure intensity. The solutions are not unique (multiple combination of stress/strength parameters match equally the observed data). It would be valuable, however, to evaluate how different or similar will be the prediction using equally well calibrated but different models or in other words what constraints on the borehole shape can be given despite the uncertainties on the processes and model parameters.

2.3. Handling uncertainty in a probabilistic manner for a reliable geomechanical design

2.3.1. Uncertainties in geomechanical design

Uncertainty in geomechanics engineering is a broad term that accounts for natural variability, lack of data and limited knowledge. In order to manage geomechanical risk and to ensure the robustness and resilience of the rock design, it is crucial to account for and reduce these uncertainties and to evaluate the probability of occurrence of a given scenario. One of the main challenges in reservoir geomechanics is that data concerning rock mass properties is usually scarce. Note that estimating geomechanical parameters such as Young modulus, rock strength and in-situ stresses is extremely important in reservoir simulation and for borehole stability analysis (Papanastasiou and Zervos, 2004; Sarris and Papanastasiou, 2012). However, this is very challenging as these geomaterials are inherently anisotropic, heterogeneous, and discontinuous. The combination of these factors leads to large uncertainties in practical engineering situations. Therefore, it is necessary to develop a proper framework for dealing with these uncertainties. In recent years, there has been considerable interest in studying this topic as uncertainties are typically present in all the stages of a reservoir geomechanics project. Different classifications of uncertainties can be found in the literature. They can usually be divided into two groups (Lacasse and Nadim, 1996; Helton et al., 2007):

- Aleatory uncertainty, also known as stochastic, active or type A uncertainty, which includes natural variability of a property (spatial and temporal variability).
- Epistemic uncertainty, also called subjective, passive or type B uncertainty, which consists of statistical uncertainty, model uncertainty and measurement uncertainty. They are associated with the lack of knowledge about a system and/or its properties. This uncertainty can be reduced by collecting additional data in order to narrow the uncertainty range.

In reservoir geomechanics, both uncertainties are encountered. Indeed, limited information are available in terms of material properties and in-situ stresses and rock masses are most of the case very heterogeneous leading to strong natural variability of parameters (strength and stresses).

2.3.2. Natural variability

Wellbore failure variability measurements are one of the best sources of information to characterize stress heterogeneity as it provides continuous profiles of some stress components contrary to most stress measurements techniques that are time-consuming and do not permit a proper sampling of heterogeneities (Shamir and Zoback, 1992; Valley and Evans, 2010; Afshari Moein et al., 2018; Valley and Evans, 2014b; Schoenball and Davatzes, 2017). It is worthy underlining that the intensity of borehole failure with depth varies, reflecting both depth trends and local variability in the in-situ stresses and strength (both being related to the presence of fault zones). When characterising stress and/or strength at depth, it is important to differentiate between a 1st and a 2nd order characterisation. The first one yields practical insights on the general trends of both stress and strength along the borehole. However, these trends are only representative of the mean conditions along the borehole, but are not capturing the variation around the mean. As a consequence, 2nd order characterisation must be carried out to quantify this variability for the design of completion schemes including packers because such variability can cause locally severe conditions and thus may lead to completion problems. This is one of the main aspects addressed in this thesis.

Another aspect to highlight is investigating the potential source of observed borehole breakouts variability and quantification in-situ of the potential magnitude of stress and strength variability. Two general hypotheses are proposed to potentially explain the observed failure variability in granitic basement. The first one consists of assuming that failure variability arises mainly from the variability in stress orientation and magnitudes with relatively constant strength. This can be attributed to the stress perturbations associated with fracture slip (Shamir and Zoback, 1992; Valley, 2007). Conversely, the second rock mass model assumes that the failure variability arises primarily due to variability in rock strength likely to be linked with lithological variations and alterations. In addition to these hypothesis, it is likely that both stress and strength variations occur concomitantly. This is another important aspect that was addressed in this PhD thesis.

2.3.3. Quality of predictions and reduction of uncertainty

As borehole stability analysis and predictions of rock mass are based on very restricted information, the degree of uncertainty and risk remain higher while predicting the quality of rock mass at planning phase. Consequently, both rock quality knowledge and level of uncertainty are time dependent and project stage based as illustrated in Fig. 2.3 and stated in Hoek (1991) and Panthi (2006). Indeed, the ability to enhance understanding of the rock mass conditions increases as project development stage moves on. This is mainly due to the fact that site explorations, in-situ and laboratory testing activities increase steadily. It is worthwhile noting that basic design and economic viability evaluation of deep geothermal projects (and any underground project) has to be made during its feasibility study stage, whereas the actual rock mass condition of an underground structure is fully known only

after the completion of its excavation work (Panthi, 2006). Thus, the degree of uncertainty related to the geological condition is much higher at an early stage of planning, which leads to high risk of large variations on the estimated and actual rock mass condition. Therefore, the real challenge is on how to minimize this level of uncertainty and reduce possible risk of large discrepancies between predicted and actual rock mass condition. To that end, one needs to develop a reliable design approach by using methods to deal with the parameters uncertainties and the design criteria (Harr, 1987, 1989).

Although various approaches have been put forward to deal with this issue in geomechanics, the traditional empirical and numerical approaches (e.g., Finite Element Analyses, FEM) of rock mass quality evaluation and stability analysis are usually deterministic. They are indeed based on single point estimate that give a single answer. As a consequence, the possibility for considerable discordance between predictions and reality is very high. In addition to that, these tools are usually time consuming. Clearly, it is very challenging to carry out enough geological, geotechnical and geomechanical investigation and design analysis to be able to fully account for all existing types of uncertainties. However, one can use a simple and computing efficient probabilistic approach to reduce large discrepancies. Note that the aforementioned uncertainties are usually evaluated and reduced by acquiring repeated measurements during the development of a project (Fig. 2.3). In the general geomechanical probabilistic risk analysis approach, one uses a probability density function (PDF) as illustrated in Fig. 2.3. Design parameters such as the loads or stresses are identified as 'Demand'. The rock strength, often the shear strength, is identified as 'Capacity'. Fig. 2.3 shows how our knowledge of the design parameters improves while progressing from the preliminary to the detailed and then the final design stage, leading to a considerable reduction of failure probability. In this thesis, we have been interested in studying how to reduce the uncertainty on the failure intensity during the calibration process. Some of the ideas developed in this thesis can be summarized in three main aspects: (1) calibrating many failure models in order to span the entire parameters space, (2) selecting only representative calibrated models and (3) using available measurements (e.g., estimate of minimum principal horizontal stress from extended leak-off test, XLOT) to reduce the range of the calibrated parameters. This step is crucial as predictions quality relies mainly on the representativity of the calibrated models. Another key aspect is to select an appropriate model and efficient calibration process. Using very complex models with a large number of model parameters is likely inefficient. These approaches require computationally demanding numerical solvers and they would be difficult to implement in the massive calibration framework proposed in this thesis. Finally, the quality of failure prediction, in the deepest section of the well, depends also on whether or not they account for existing correlations between stress and strength and on their ability to mimic the observed variability patterns. This is also a key aspect that was investigated in this thesis by performing stochastic multivariate simulations using the Direct Sampling Multi-Point Statistical (DS-MPS) approach as implemented in DeeSse (Straubhaar, 2019).

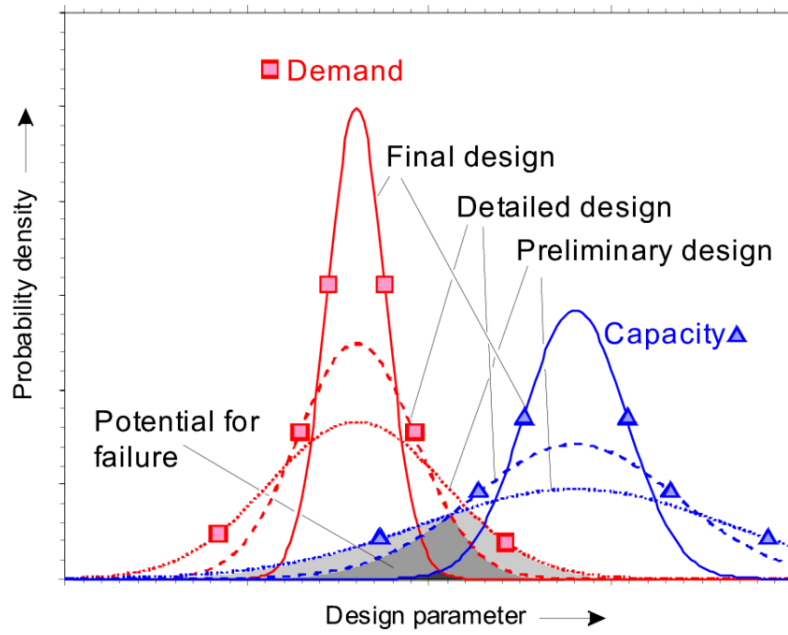


Figure 2.3.: Hypothetical distribution curves of the uncertainty reduction during different stages in the design of a structure until failure's potential is reduced to an acceptable level (grey area) (Valley et al., 2010, modified after Hoek (1991)).

3. A systematic methodology to calibrate wellbore failure models, estimate the in-situ stress tensor and evaluate wellbore cross-sectional geometry

This chapter was published on the 'International Journal of Rock Mechanics and Mining Sciences' as:

A. Dahrabou, B. Valley, P. Meier, P. Brunner, J. Doherty, and A. Alcolea. A systematic methodology to calibrate wellbore failure models, estimate the in-situ stress tensor and evaluate wellbore cross-sectional geometry, International Journal of Rock Mechanics and Mining Sciences, ISSN 1365-1609.

Asmae Dahrabou performed the analysis and provided the structure of the main text. Benoît Valley and Andrés Alcolea contributed to the development of the methodology, the discussion of the results and the writing of the manuscript. Philip Brunner, Peter Meier and John Doherty gave insights on the calibration part.

Abstract

Deep geothermal boreholes, often drilled to the crystalline basement, suffer from borehole breakouts that compromise borehole stability and/or lead to low drilling performance. These issues increase the cost of deep geothermal projects and lead to irregular cross-sectional geometries that may entangle well completion (e.g., packer isolation for zonal stimulation, cementing, etc.). Thus, the proper knowledge of rock strength, state of stress and their interactions at the closest vicinity of the borehole is key to the success of deep geothermal drilling. Traditionally, the magnitudes of the vertical and minimum horizontal principal stresses, S_v and S_{hmin} , respectively, can be estimated while S_{Hmax} is difficult to constrain. This paper presents a systematic methodology to jointly evaluate the heterogeneous distributions of the stress tensor principal components and orientations, and the rock strength properties (e.g. cohesion, friction). Model parameters are estimated from measurements available during or shortly after drilling, i.e., breakout width, breakout extent/depth of penetration, breakout orientation and drilling induced tensile fractures. Additionally, measurements of estimated parameters or transformations of them can be considered in the calibration in a generic manner (e.g., S_{hmin} interpreted from XLOT). For illustration purposes, the methodology is applied to the extensive borehole data set along the crystalline section of the borehole BS-1, in Basel (Switzerland). The methodology allows us (1) to derive plausible sets of stress and strength parameters reproducing the complex distribution of breakouts along BS-1, and (2) to unveil the paradox of having high density of natural fractures at sections without borehole breakouts.

3.1. Introduction

Deep geothermal boreholes of an Enhanced Geothermal System (EGS) are drilled to hot and low permeable rock masses, most often in the crystalline basement (BS-1 in Basel, Häring et al. (2008), Soultz-sous-Forêts site, Rummel and Baumgärtner (1991), Habanero well in Australia, Fernández-Ibáñez et al. (2009) or Pohang in South-Korea, Alcolea et al. (2020), amongst others), to depths between 3000 and 5000 m. Drilling performance, i.e., the first critical factor to the economic success of an EGS, borehole stability and the regularity of the borehole cross-section are controlled by the interplay between rock strength and the state of stress around the borehole. If drilling was successful, a second critical factor to the installation of the EGS is well completion, which most often includes the stimulation of pre-existing fractures. An irregular borehole cross-section involving deeply penetrating borehole breakouts or drilling induced tensile fractures (DITFs) may entangle, or even preclude, the correct placing of packers, whose sealing is mandatory for a targeted stimulation of pre-existing fractures. This issue becomes critical when stimulating so-called multi-stage EGSs, in which natural fractures are individually isolated with packers and stimulated sequentially. For the aforementioned reasons, the accurate knowledge of the interplay between the local state of stress and the rock strength is crucial to the success of an EGS.

Methods to characterize stresses in deep boreholes are described in the literature (Zoback et al., 2003; Zoback, 2007) and can be classified into two groups, namely 1st order and 2nd order methods. 1st order methods aim at estimating linear depth trends, whereas 2nd order methods characterize the perturbations around the trend arising from the presence of faults, fractures or other sources of rock heterogeneity. Due to the dominant effect of gravity on the stress state and the relatively small range of density variations in most rocks, it is common to consider that one principal stress is vertical and to estimate its magnitude, S_v , as the weight of the overburden by integrating the linear trends observed in density logs. The assumption of a vertical principal stress may not be accurate due to the effects of (1) topography (e.g., at shallow boreholes in hilly zones, Evans K.F. (1995)), (2) nearby excavations (e.g., at the monitoring boreholes of a tunnel, Martin et al. (2003)), or (3) even due to the drilling of the borehole itself. In a 1st order approximation, the magnitudes of horizontal stress are also approximated by depth linear trends (Zoback et al., 2003). Hydraulic tests (e.g. XLOTs) (Lin et al., 2008) can be used to estimate the minimum horizontal principal stress, S_{hmin} . The direction of penetration of borehole breakouts is usually an accurate estimate of the orientation of S_{hmin} . As suggested by Zoback et al. (2003), the geometry of breakouts along the borehole can be used to infer a linear trend of S_{Hmax} .

The aforementioned 1st order characterization method is standard and currently applied in geothermal boreholes (e.g. Häring et al., 2008; Valley and Evans, 2019; Mastin et al., 1991; Borm et al., 1997; Brudy and Zoback, 1993; Fernández-Ibáñez et al., 2009). However, it is very sensitive to the failure criterion used to compute borehole failure. Different

failure criteria lead to different estimates of S_{Hmax} magnitude, depending on whether or not the effect of the intermediate principal stress, σ_2 , is considered. Moreover, the rock strength properties defining the subjectively chosen failure criterion are hard to estimate from available borehole data. The choice of an appropriate failure criterion remains controversial. For example, Valley and Evans (2019) used results from a single triaxial test on a core plug to parametrize their failure models and acknowledged the inherent and high uncertainties. Another approach consists of estimating rock strength properties by means of empirical relationships between strength and petrophysical parameters derived from sonic and density logs (Chang et al., 2006). Such empirical relationships can be constrained by laboratory measurements on cores. Unfortunately, laboratory tests are time-consuming, expensive (and therefore often disregarded or, at best, carried out at one given depth) and rarely representative of in-situ conditions. Furthermore, It is also difficult to account for effects like core damage (Martin and Stimpson, 1994) that may hinder the estimation of strength properties.

State-of-the-art methods estimate stresses and strength properties separately relying heavily on very uncertain strength estimates. This work is aimed at filling this gap. We propose a systematic methodology to estimate depth profiles of the characteristics of the local stress tensor (both magnitudes and orientations of all three principal stresses) and rock strength properties (cohesion and friction) together. Both trends (1st order approximation) and/or variations around the trend (2nd order) can be estimated for each unknown. Model parameters are estimated via the regularized pilot points method (Doherty, 2003; Alcolea et al., 2006) as implemented in PEST (Parameter ESTimation, Doherty, 2015) from borehole cross-sectional characteristics (breakout width, breakout extent/depth of penetration and breakout orientation at different depths) and from the presence/absence of DITFs (including both axial and en-echelon drilling induced tensile fractures, referred to as A-DITFs and E-DITFs, respectively, (Brudy and Zoback, 1993)) using the Kirsch analytical solution (Kirsch, 1898) to estimate the stress state around the borehole and appropriate failure parameter estimation approaches. All stress components around the borehole, including the remnant thermal stresses arising from the cooling of the borehole wall are accounted for. The inherent uncertainty on the choice of a failure criterion is taken into account through a sensitivity analysis, whose results allow to validate or discard failure models. For illustration purposes, the suggested methodology is applied to assess the variability of stress and strength along the 2.5 km crystalline section of the borehole BS-1 in Basel (Switzerland, Häring et al., 2008).

3.2. Methodology

The methodology suggested here is based on the five blocks sketched in Fig. 3.1, which are carried out in an iterative manner and at each borehole cross-section. The main steps of the algorithm are described in detail in the following subsections and itemized next:

- Step 1: given a set of initial parameters (e.g. depth trends of magnitudes, stress

orientation, wellbore orientation, Poisson's ratio, thermo-elastic parameters, etc.), calculate stresses around the borehole using Kirsch analytical solution (Kirsch, 1898).

- Step 2: evaluate failure conditions. So far, Mohr-Coulomb and Mogi-Coulomb criteria have been implemented. Nonetheless, any other failure criterion can be implemented without loss of generality.
- Step 3: evaluate breakout width, extent and orientation, and the presence of DITFs.
- Step 4: evaluate an objective function (i.e., a penalty function) measuring the departure of the obtained solution from available measurements. Measurements include geometric features (i.e., borehole shape and presence/absence of DITFs), prior estimates of estimated parameters (e.g., a linear depth trend of a given parameter) or direct parameter measurements (e.g., of S_{hmin} after the interpretation of XLOTs).
- Step 5: modify parameters and go back to Step 1, until a minimum of the objective function is attained. This step is the so-called parameter estimation, optimization or, in broad sense, inverse problem (Ramírez et al., 2005). The aforementioned workflow is carried out by the generic parameter estimation software PEST (Doherty, 2015; Doherty et al.).

3.2.1. Calculation of the near-field state of stress

The stress redistribution caused by drilling and thermal effects can be calculated analytically or numerically. Analytical solutions are often preferred to complex numerical borehole models because they are (1) well established as standard practice in borehole design, (2) computationally faster, and (3) relatively simple to implement. The methodology presented here aims at obtaining fast and reliable near real-time calculations, which aids in-situ decision-makings based on previously collected data (e.g., the direction and inclination of the deviated section of a borehole from data collected along the vertical initial section). In this work, we have chosen an elastic analytical solution (Kirsch, 1898; Schmitt et al., 2012) to compute the stress redistribution around the borehole. Our implementation of the Kirsch closed-form solution takes into account situations where the borehole is not aligned with one of the principal stresses. It further includes a thermo-elastic stress component to simulate the remnant stresses arising from the cooling of the borehole wall caused by the presence of warm water in the formation and of (generally) cold mud in the borehole during drilling. The stress distribution is computed in two main steps, presented in detail in Appendices A and B of the supplementary materials. First, the stress tensor is expressed in a local and orthonormal borehole Cartesian coordinate system (u,v,w) . Next, Kirsch equations are solved to compute the stress redistribution around the borehole in a cylindrical coordinate system with its origin at the center of the borehole, $(r,\theta,w$; r : radial, θ : tangential, w : axial).

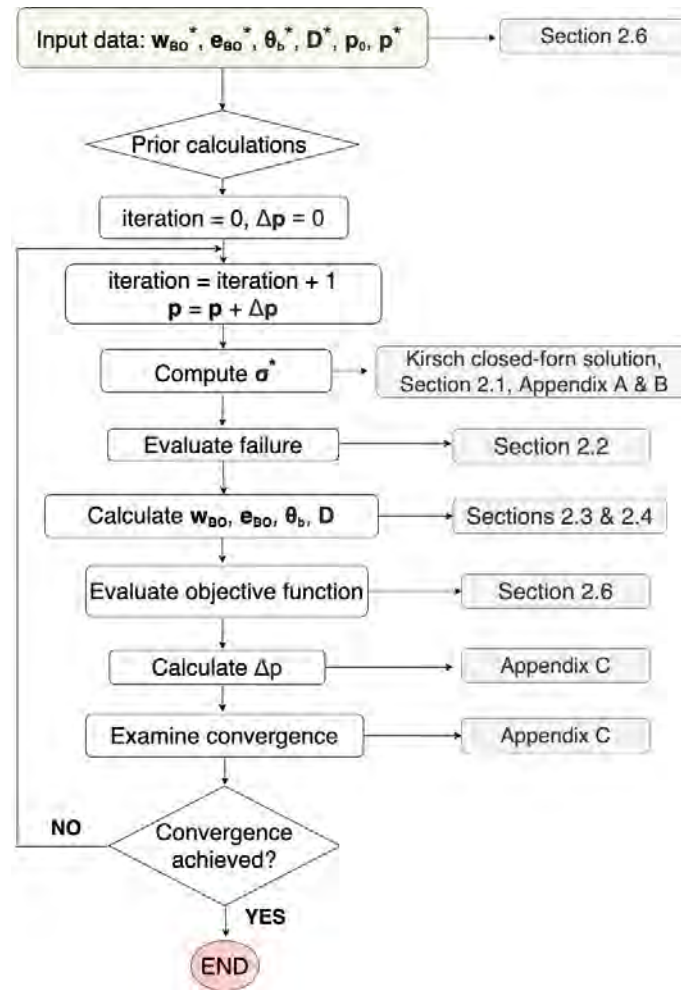


Figure 3.1.: Schematic description of the proposed methodology. In the insets, p_0 and p are the initial and sequentially updated sets of parameters, respectively; w , e and θ are vectors containing calculated breakout width, extent/depth of penetration and orientation; vector D represents the presence or absence of DITFs; the corresponding magnitudes with asterisk represent the measured counterparts.

The thermal stress components, $S_r^{\Delta T}$, $S_\theta^{\Delta T}$ and $S_w^{\Delta T}$ arising from any deviation from ambient temperature, ΔT , at the borehole wall are (Stephens and Voight, 1982):

$$S_r^{\Delta T} = 0 \quad (3.1)$$

$$S_\theta^{\Delta T} = S_w^{\Delta T} = \frac{\beta E \Delta T}{1 - \nu} \quad (3.2)$$

where E is the Young modulus, β is the coefficient of linear expansion and ν is the Poisson ratio. $\Delta T \geq 0$ denotes a temperature gain inside the borehole. These stress components are added to the corresponding components arising solely from the stress redistribution in response to excavation of the borehole (Appendix B).

Failure is computed from effective stresses, which are calculated from total stresses and pore pressure, P_p (Terzaghi et al., 1925):

$$\boldsymbol{\sigma} = \mathbf{S} - \gamma \delta_{ij} P_p \quad (3.3)$$

where P_p is fluid pressure, \mathbf{S} and $\boldsymbol{\sigma}$ are the total and effective stress tensors, respectively, $\gamma \in [0 \ 1]$ is the Biot coefficient (Biot, 1941, 1955; Biot and Willis, 1957) and δ_{ij} is the Kronecker δ which applies Terzaghi's correction to the isotropic components of \mathbf{S} only. The Biot coefficient controls the degree of hydromechanical coupling (Zimmerman, 2000) and its value is not excluded from debate because it depends not only on the type of rock, but also on rock microstructure (Tan and Konietzky, 2014). In addition, it varies with time during failure (Tan et al., 2015). Laboratory experiments evidence that Terzaghi's correction is valid for compressive failure even for low permeability rocks (Brace and Martin, 1968). Recent experiments in the Grimsel Granite report Biot coefficients in the range 0.5 to 0.7 (Suvorov and Selvadurai, 2019). In our work, we have chosen $\beta = 1.0$ because this value indicates the strongest possible hydromechanical coupling (Zimmerman, 2000) regardless of the failure type (i.e., under compression or under tension).

The Kirsch closed-form solution is computationally attractive and is easy to implement. However, one must bear in mind the following assumptions and limitations:

1. It assumes CHILE material conditions (Continuous, Homogeneous, Isotropic and Linearly Elastic), which is generally not strictly true for rocks.
2. It assumes that the stresses are redistributed around a perfect cylinder. In other words, progressive failure is not considered.
3. It assumes an infinite cylindrical hole in a infinite medium. The stress rotations and magnitude changes associated with borehole drilling are neglected.
4. The scale effect is not taken into account as stresses at the borehole wall are independent of the borehole diameter.

These limitations can be tackled by means of numerical models or more complex closed-form solutions. For instance, transient failure can be modelled by analytical solutions including continuum plasticity with non-associated flow rules and strain softening (Hajiabdolmajid et al., 2002) or continuum damage mechanics (Sahara et al., 2017) or by hybrid continuum-discontinuum models (Shen et al., 2002; Alcolea et al., 2016; Marschall et al., 2017). Unfortunately, the aforementioned approaches are either hard to parameterize using standard data sets, involve a larger number of unknown parameter and are computationally intensive, which precludes parameter estimation (See Section 3.2.6).

3.2.2. Strength models

A main issue in the analysis of wellbore stability is the selection of an appropriate rock failure criterion. Without loss of generality, we focus here on two criteria: (1) the Mohr-Coulomb criterion (Coulomb, 1776; Mohr, 1900), because it is the most used in practice and (2) the Mogi-Coulomb (Mogi, 1971; Al-Ajmi and Zimmerman, 2005), which takes into account all principal stresses and has been shown to capture accurately true triaxial strength data.

The Mohr-Coulomb criterion assumes that σ_2 has no influence on rock strength, and is expressed in terms of principal stresses as:

$$\sigma_1 \geq C_o + q\sigma_3 \quad (3.4)$$

where C_o is the uniaxial compressive strength of the rock, and q is a material constant. Both C_o and q can be related to the internal friction angle, ψ , and the cohesion, c through:

$$q = \tan \left(\frac{\pi}{4} + \frac{\psi}{2} \right)^2 \quad (3.5)$$

$$C_o = \frac{2c \cos \psi}{1 - \sin \psi} \quad (3.6)$$

This failure criterion is standard in rock mechanics and its parameters are typically determined from conventional triaxial tests ($\sigma_1 > \sigma_2 = \sigma_3$). However, in practice, the Mohr-Coulomb criterion has been reported to be very conservative in predicting wellbore instability since it ignores the impact of σ_2 . In fact, it was recommended (Song and Haimson, 1997; Ewy, 1999) to use alternative failure criteria accounting for the influence of σ_2 on rock strength, such as the Mogi-Coulomb criterion to represent rock conditions more realistically. The latter relates the octahedral shear stress, τ_{oct} , to the mean stress, $\sigma_{m,2}$ as follows (Al-Ajmi and Zimmerman, 2005):

$$\tau_{oct} \geq m + p \cdot \sigma_{m,2} \quad (3.7)$$

where:

$$\tau_{oct} = \frac{1}{3} \sqrt{(\sigma_1 - \sigma_2)^2 + (\sigma_1 - \sigma_3)^2 + (\sigma_2 - \sigma_3)^2} \quad (3.8)$$

and:

$$\sigma_{m,2} = \frac{(\sigma_1 + \sigma_3)}{2} \quad (3.9)$$

The parameters m and p are material constants that are also related to the internal friction, ψ and cohesion, c , by:

$$m = \frac{2\sqrt{2}}{3} c \cos \psi \quad (3.10)$$

$$p = \frac{2\sqrt{2}}{3} \sin \psi \quad (3.11)$$

Regardless of their formulation, failure criteria are difficult to parameterize. Both friction and cohesion can be measured in the laboratory. Unfortunately, this is rarely the case in practice because (1) retrieving cores from deep boreholes is expensive and time-consuming, and (2) laboratory conditions rarely represent in-situ conditions due to scale effects. In traditional rock mechanical engineering analyses, the cohesion is set to zero because that represents the worst case scenario (i.e., closest to failure). However, the cohesion of crystalline rocks can be large (e.g. in Basel, cohesion ranges from 18.2 MPa to 35.5 MPa Valley and Evans, 2019). To make things worse, uncertainties become critical in what concerns friction. Traditionally, the friction coefficient is set to 0.6, value qualified as that of the critically stressed crust (Barton, 1976; Zoback, 2007). Such value has been criticized by many authors on the basis of experimental data. For instance, laboratory analysis in the context of the Pohang EGS report values ~ 1.7 (Kwon et al., 2019) for an intact granite. Instead, Alcolea et al. (2020) report low values in the range 0.4-0.45 for a fault zone in the same crystalline formation. Such relatively low values are not uncommon in faults (Reasenbergs and Simpson, 1992; Iio, 1997; Tanikawa and Shimamoto, 2009; Barth et al., 2013), especially if they have suffered from weakening after seismic or aseismic slip episodes (Houston, 2015). We consider the uncertainties inherent to strength parameters by means of model calibration (See Section 3.2.6).

3.2.3. Estimation of breakout width

The computation of breakout width, w_{BO} , consists of evaluating the failure criteria (Eq. 3.4 or 3.7) at the borehole wall (i.e. $r = a, \forall \theta$) using the stresses calculated by the Kirsch closed-form solution. The arc, measured as angle, along which the failure criterion is met provides an estimate of w_{BO} . The assumption behind such computation is that failure occurs at the cylindrical borehole wall spanning an initial maximum width and then the breakouts progressively extend (deepen) but do not widen. Thus, it is not necessary to simulate the progressive failure leading to the final breakout geometry. Although some modifications of breakout width with time have been reported in-situ (Azzola et al., 2019), the approach implemented in our methodology is widely accepted (Zoback et al., 2003).

It is worth noting that breakouts with initially small size deepen as they grow, but do not further widen (Zoback, 2007). Consequently, stable wells can still be drilled that tolerate a degree of wellbore failure. Instead, initially wide breakouts can lead to washouts caused

by the lack of intact material around the wellbore wall to withstand the applied stresses. In this work, it is important to highlight that the suggested method estimates model parameters from measurements available during or shortly after drilling, i.e., breakout width, breakout extent/depth of penetration, breakout orientation and drilling induced tensile fractures.

3.2.4. Estimation of breakout extent

Approaches to compute breakout extent, e_{BO} , are scarce in the literature. This is partly due to the fact that breakout width has been traditionally preferred to estimate the stress state. Breakout extent is the result of progressive failure successively shedding the stresses and pushing failure deeper until a stable section is reached (Cuss et al., 2003). Such processes are difficult to simulate and, as a by-product, breakout extent has been disregarded. However, we argue that the characterization of breakout extent is crucial towards proper well completion, e.g., to guarantee effective packer sealing. In the following, we investigate computationally feasible alternatives to carry out this characterization.

Unfortunately, the application of the same general principle as for the computation of breakout width, i.e., evaluating the failure criteria for $r \geq a$ using the Kirsch solution is not meaningful because progressive failure is neglected.

An empirical criterion has been developed for brittle failure at tunnels (Diederichs et al., 2004) and applied to borehole failure (Walton et al., 2015):

$$\frac{e_{BO}}{a} = 0.49 + 1.25 \frac{\sigma_{\theta\theta}^{max}}{C_o} \pm 0.1 \quad (3.12)$$

This criterion assumes (1) that the breakout extension, normalized by the nominal borehole radius, $\frac{e_{BO}}{a}$, is a linear function of the ratio of the maximum effective hoop stress, $\sigma_{\theta\theta}^{max}$, to the uniaxial compressive strength, C_o and that the wall strength is about half the uniaxial compressive strength. The wall strength can be estimated by the crack initiation level, which is typically about half the uniaxial compressive strength (Andersson et al., 2009a; Hoek and Martin, 2014). This relationship was developed using numerous field observations of enlargement of tunnel sections. Thus, its applicability to breakout in boreholes, with a radius of curvature of the open space much smaller than in the tunnel cases on which this empirical criterion has been developed, is not yet established. Valley (2007), analysing data from the well characterized deep geothermal project of Soultz-sous-Forêts concluded that Eq. 3.12 tends to largely overestimate breakout extent in boreholes. This approach has been tested at early stages of this work without generating acceptable results. Thus, it is no longer considered in this manuscript for the sake of conciseness.

An alternative empirical approach is proposed by Shen (2008). The relationship was established upon numerical simulation of borehole failure using the fracture mechanics code FRACOD (Shen and Stephansson, 1994). Shen's approach assumes a vertical borehole under plain strain conditions (FRACOD is a 2-dimensional code), i.e., one principal stress is aligned with the borehole axis, and dry conditions (no pore pressure, no borehole internal

pressure) and he derived the following relationships between stress conditions, strength parameters and breakout extent:

$$\frac{3\sigma_{Hmax} - \sigma_{hmin}}{C_o} = 1 + A \left(\frac{e_{BO}}{a} - 1 \right)^B \quad (3.13)$$

where $\frac{3\sigma_{Hmax} - \sigma_{hmin}}{C_o}$ represents the ratio of the maximum effective tangent stress to the uniaxial compressive strength. Under the constraints of Shen's relationship, the Kirsch solution simplifies and the maximum effective hoop stress becomes $\sigma_{\theta\theta}^{max} = 3\sigma_{Hmax} - \sigma_{hmin}$, σ_{Hmax} and σ_{hmin} being the maximum and the minimum effective principal horizontal stresses, respectively. A and B are regression parameters in the range (Shen, 2008):

- Upper limit curve: $A = 21.2$, $B = 3.33$.
- Average curve: $A = 15.2$, $B = 2.67$.
- Lower limit curve: $A = 12.6$, $B = 2.22$.

In spite of its non-linearity, Shen's approach is computationally affordable. However, the strength is defined as a Rankine criterion, i.e. the minimum and intermediate principal stresses are ignored, which neglects the important stabilizing effect of the internal wellbore pressure (mud pressure). In our analyses, we extend Shen's criterion by defining an apparent wellbore strength σ_{app} , which accounts for the strengthening effect of σ_2 and σ_3 , regardless of the chosen failure criterion. σ_{app} is evaluated at the borehole wall ($r = a$) and at an angle θ corresponding to the breakout centre, as calculated by the Kirsch closed-form solution. For the Mohr-Coulomb failure criterion, the apparent strength depends on the minimum principal effective stress, σ_3 :

$$\sigma_{app} = q \cdot \sigma_3 + C_o \quad (3.14)$$

For the Mogi-Coulomb criterion, the apparent strength depends on both intermediate σ_2 and minimum σ_3 effective principal stresses (Eqs. 3.7 to 3.9). Resolving the maximum effective principal, σ_1 , yields the estimate of the apparent strength σ_{app} :

$$\sigma_{app} = \frac{-(4\sigma_2 + 4\sigma_3 + 18mp + 9p^2\sigma_3)}{9p^2 - 8} + \frac{2\sqrt{6}\sqrt{12m^2 + 6mp\sigma_2 + 18mp\sigma_3 + 3p^2\sigma_2^2 + 9p^2\sigma_3^2 - 2\sigma_2^2 + 4\sigma_2\sigma_3 - 2\sigma_3^2}}{9p^2 - 8} \quad (3.15)$$

where m and p are the parameters of the Mogi-Coulomb failure criterion (Eqs. 3.10 and 3.11).

Once the apparent strength has been determined, the depth of failure can be evaluated using the following modified Shen formula:

$$\frac{\sigma_1}{\sigma_{app}} = 1 + A \left(\frac{e_{BO}}{a} - 1 \right)^B \quad (3.16)$$

where σ_1 is the maximum effective stress at the breakout center point ($\theta = \theta_b$, see Fig. 3.3) computed with the Kirsch equations. A and B are fitting parameters, whose estimation is included in our methodology. It can be demonstrated that our modified relationship reduces exactly to that of Shen (Eq. 3.13) when the internal wellbore pressure is ignored.

3.2.5. Estimation of DITFs occurrence

The occurrence of drilling induced tensile fracture is evaluated by the Rankine criterion:

$$\sigma_3 \leq T_o \quad (3.17)$$

where T_o is the tensile strength (negative meaning tension). The minimum effective principal stress at the borehole wall, σ_3 , is computed using the Kirsch solution presented in Appendices A and B and accounts for the wellbore internal pressure and the thermal stress arising from the cooling of the borehole wall. Note that both axial and en-echelon tensile fractures, A-DITFs and E-DITFs (Brudy and Zoback, 1993) are considered jointly in our implementation.

3.2.6. Parameter estimation

Our methodology, as any other stress characterization methodology, includes uncertain parameters (e.g., friction, cohesion, etc.). Traditionally, parameter uncertainties are taken into account through parametric sensitivity analysis or by manual trial-and-error calibration at best. Instead, we cast the estimation problem in the mathematical framework of automatic inverse modelling, which frees the modeller of the burden of having to deal with complex, tedious, and prone to error testing of different parameter combinations. In broad terms, inverse modelling refers to the process of gathering information about the model from measurements of what is being modelled (Ramírez et al., 2005).

Once a conceptual model represented by equations (Sections 3.2.1 to 3.2.5 and Appendices A and B), the inverse problem, also known as history matching, tomography or calibration, consists of estimating the set (or sets) of parameters that best fit observations through the aforementioned mapping equations. This is achieved by minimizing a penalty function F , so-called objective function, which measures the misfit between calculated and observed values, arranged in vectors \mathcal{O} and \mathcal{O}^* , respectively, with components $\mathcal{O}_i^* = \{w_{BO}^*, e_{BO}^*, \theta_b^*, D^*\}$. The set of calibrated parameters, described below, is arranged in vector \mathcal{M} . The objective function F can be expressed in a generic manner as:

$$F = \sum_{i=1}^4 \lambda_i (\mathcal{O}_i - \mathcal{O}_i^*)^t \mathbf{V}_i^{-1} (\mathcal{O}_i - \mathcal{O}_i^*) + \sum_{j=1}^{npar} \beta_j (\mathcal{M}_j - \mathcal{M}_j^*)^t \mathbf{V}_j^{-1} (\mathcal{M}_j - \mathcal{M}_j^*) \quad (3.18)$$

where subscripts i and j stand for type of measurement ($i = 1$ for w_{BO}^* , $i = 2$ for e_{BO}^* , etc.) and parameter, up to $npar$ ($j = 1$ for parameters characterizing S_{Hmax} , $j = 2$ for those of S_{hmin} , etc.). The scalars λ_i and β_j are global calibration weights

that balance the contribution of the individual pieces of information. Matrices V_i and V_j are the corresponding prior covariance matrices, which contain information about the initial uncertainty of each measurement/parameter type and the possible cross-correlations between them. Note that cross-correlation between measurements and parameters is not included in our calculations because these are already accounted for in the direct problem equations (e.g., in the Kirsch closed-form solution or in the expression of the chosen failure criterion). λ_i and β_j are global weights, whereas the inverse of matrices V_i and V_j can be viewed as a collection of individual, per-measurement, weights, δ . A more developed expression for the first term, of F , involving measurements only and assuming no correlation between measurements at different depths, can be written as:

$$F_m = \sum_{i=1}^n \lambda_{w_{BO,i}} \cdot \delta_{w_{BO,i}} \cdot (w_{BO,i} - w_{BO,i}^*)^2 + \sum_{i=1}^n \lambda_{e_{BO,i}} \cdot \delta_{e_{BO,i}} \cdot (e_{BO,i} - e_{BO,i}^*)^2 \\ + \sum_{i=1}^n \lambda_{\theta_i} \cdot \delta_{\theta_i} \cdot (\theta_{bi} - \theta_{bi}^*)^2 + \sum_{i=1}^{n_{DITF}} \lambda_{D_i} \cdot \delta_{D_i} \cdot (D_i - D_i^*)^2 \quad (3.19)$$

where $\delta = \frac{1}{\sigma^2}$ is the inverse of the variance of each individual measurement (i.e., reporting on the degree of the confidence) and n_{DITF} is the number of DITFs observations. The second term, of parameters, in Eq. 4.2 can be developed similarly. Note that the formulation of F in Eqs. 4.2 and 3.19 is none other than that of generalized least squares of the well-known maximum likelihood method, which consists of maximizing the probability of observing the measured data with respect to the parameters (i.e., maximizing the parameters likelihood). Both allow to account for prior information of parameters (Edwards, 1974). As observed, the first term in F accounts for the misfit between calculated and observed breakout geometries and DITFs. The second, so-called plausibility term (Alcolea et al., 2006), penalizes the departure between parameter estimates and the corresponding prior information, arising, e.g., from prior studies, laboratory analyses and/or field tests like XLOTs. As such, we aim at finding not only the typically displayed goodness of fit, but the goodness of fit achieved with reasonable, or plausible, parameter values. Note that w_{BO}^*, e_{BO}^* and θ_{BO}^* are direct measurements. However, the presence/absence of DITFs is a binary variable (yes/no), which does not favour mathematical parameter estimation. To tackle this problem, we generate an estimate of the minimum hoop stress at the borehole wall consistent with observed DITFs. To that end, prior estimates of the mean tensile strength and of its standard deviation are required, which define a statistical Gaussian distribution of tensile strength, T_o . The raw observation is the total length of the borehole where DITFs are present standardized by borehole length, $L_D/L \cdot 100$ (%). With these data, a statistical distribution of the maximum hoop stress yielding DITFs at the corresponding measured depths is generated and arranged in vector D^* . The parameterization of the problem depends on the desired characterization. 1st order characterization aims at

estimating depth trends. In such case, parameters are expressed in a generic manner as:

$$p = a \cdot TVD + b \quad (3.20)$$

Our methodology includes the segmentation of the borehole according to e.g., geological observations. Thus, parameters a and b can vary with depth in a step-wise manner, which allows us to consider, the presence of different strata yielding en-echelon parameter depth profiles. Uncertain parameters, at each borehole segment, are the slope, a , and the shift, b , of all parameters intervening in the direct problem equations (See Section 3.5.1, and Appendices A and B in the supplementary materials). If segmentation is applied, calibrating different shifts may lead to discontinuous parameter profiles caused by, e.g., abrupt changes in the petrology of the column or the presence of a prominent shear zone. If smooth parameter variations between segments are preferred, then only the shifts b at the shallowest segment should be calibrated to grant continuity.

2nd order characterization aims at estimating the deviations of a given parameter from its estimated mean (1st order characterization), which enables the analysis of variability at all scales. To that end, we used the regularized pilot points method (RPPM, Alcolea et al., 2006), originally devised by De Marsily (1984), as implemented in the free parameter estimation software PEST (Doherty, 2015). The generic parameterization now becomes:

$$p = a \cdot TVD + b + \epsilon(MD) \quad (3.21)$$

where ϵ is the perturbation of a parameters around its trend and it depends on measured depth to account for deviated boreholes. Note that the parameter a multiplies TVD instead, because most geomechanical parameters are expressed as depth gradients (e.g., principal stresses, Häring et al. (2008)). Indeed, MD and TVD are related univocally through the borehole trajectory.

Pixel-based methods have been developed for the continuum spatial estimation of parameters (Kitanidis and Vomvoris, 1983; Rubin and Dagan, 1987; Gutjahr and Wilson, 1989). These reduce to a particular case of our formulation in which the vertical discretization step tends to zero (Meier et al., 2001), which boosts the number of estimated parameters and precludes the targeted near real-time calibration. Instead, we estimate variability at selected so-called pilot points. The complete depth profile of a parameter is obtained by means of interpolation techniques. In our study, we use ordinary kriging (Krige, 1951; Matheron, 1963), which smooths parameter variations. To that end, a variogram is inferred from the corresponding estimates at pilot points (and possibly, measurements). Note that each parameter is defined by its own set of pilot points. Thus, finer or coarser characterizations can be obtained for different parameters, depending on the pilot point discretization. The total number of pilot points may be larger than the total number of observations. In that case, the solution may become unstable (Hadamard, 1902). To overcome this issue, two techniques are jointly used, i.e., singular value de-

composition (SVD; Doherty (2003)) and Tikhonov regularization (Tikhonov, 1963). SVD reduces the number of parameters being estimated, while regularization adds stability to the inverse problem solution by incorporating prior information on parameters (second term in Eq. 4.2).

A key question is the optimal location of pilot points. The density of pilot points should be larger in areas where a finer characterization is needed. Another, less pragmatic and subjective alternative consists of placing pilot points randomly (Alcolea et al., 2006; Hendricks-Franssen and Franssen, 2001); or according to adjoint sensitivity to identify the most sensitive/informative sections of the data sets (LaVenue and Pickens, 1992).

The vector \mathcal{M} , which includes first and/or second order coefficients (a and b , and ϵ at pilot points for all parameters) is updated by PEST in an iterative manner using the Levenberg-Marquardt algorithm (Marquardt, 1963). PEST also allows to include upper and lower bounds to each estimated parameter. As observed, the parameterization for the 2nd order characterization includes that for the 1st order characterization, and all parameters (a and b , and ϵ at pilot points) can be estimated together. However, prior studies in the context of this work reveal that depth trends estimated in this manner do not deviate much from those estimated as raw 1st order method (i.e., a and b only). Thus, our calibration is made in two steps. First, depth trends of parameters are estimated. Second, 1st order parameter values at pilot point locations are used as prior information for the 2nd order characterization. For illustration purposes, the suggested methodology is applied to the data set of borehole BS-1 in Basel, described next.

It is worth nothing that "characterisation" and "estimation/calibration" have two different meanings. On the one hand, characterisation refers to the conceptualisation of the stress field and the underlying parameterisation. On the other hand, calibration is the process of estimating the key parameters involved in the characterisation. This vicious circle causes that, in the inverse problem literature, both terms are used indistinctly.

3.3. BS-1 data description

In 2006, a 5 km deep borehole, termed BS-1, was drilled to the crystalline basement in Basel (Switzerland) as part of a planned EGS doublet (Häring et al., 2008). In the crystalline basement, from 2516 m MD, the wellbore diameter was 9 7/8" down to 4850 m MD. The borehole was then drilled to a total depth of 5009.4 m MD with a diameter of 8 1/2". The borehole is sub-vertical with a maximum deviation from the vertical of 8°. MD was measured from the rotary , located 9.14 m above ground level.

The crystalline basement was described on-site by observing cuttings (Kaesler et al., 2007), and only a 10 m long core was retrieved at a depth of 4909 m MD . The composition of the granitic basement rock is generally homogeneous with slight variations in quartz content from monzogranite to monzonite. Alteration associated with brittle shear zones is present locally along the borehole. Ziegler et al. (2015) obtained an average fracture frequency that decreases with depth (3.1, 1.3 and 0.3 fractures/m at depth ranges 2.62.65

km, 2.653.0 km, and below 3.0 km, respectively). The upper 400 m of the crystalline section of BS-1 are interpreted as influenced by paleo-exhumation during the Permo-Carboniferous prior the sedimentation of the Mesozoic and Cenozoic cover. Thus, this zone may be affected by a perturbed stress state, either as a remanence of pre-sedimentation exhumation and relaxation or in response to more recent tectonic loadings.

Ultrasonic borehole televiewer (UBI) logs with azimuthal resolution of 2° were run between 2578 and 5001 m MD shortly after drilling (Valley and Evans, 2009b). The fluid velocity in the borehole was measured during the trip in hole and used to compute wellbore geometry from transit time data. The open hole crystalline section was subject to an extensive logging program before setting a 7 5/8" casing with its shoe at a depth of 4638 m MD. A reservoir characterization phase was conducted in the open hole section below the 7 5/8" casing shoe. Finally, a hydraulic stimulation was performed in December 2006, which caused a felt 3.4 event magnitude and ultimately led to the abandonment of the project (Håring et al., 2008; Deichmann and Giardini, 2009).

3.3.1. BS-1 failure data

The borehole data used in our analysis and the procedure to infer borehole failure are described in Valley and Evans (2009b, 2019). Breakouts were identified along 81% of the logged section and are almost continuous except for a large gap from 2747 m TVD to 2899 m TVD and some other minor gaps at 3820-3856 m TVD, 4185-4221 m TVD and 4582-4631 m TVD (Fig. 3.2). The aforementioned borehole segments coincide with those of strong intensity of natural fractures. This paradox, involving the coalescent presence of natural fractures but the absence of borehole breakouts, occurs frequently in deep boreholes and is attributed to local stress heterogeneities and to the impact of thermal stresses as discussed in Section 3.6. Borehole geometry was averaged from the inferred breakouts at cross sections with a longitudinal spacing of 40 cm (5001 sections for each type of measurements, and, overall, 20004 sections; see an example in Fig. 3.3).

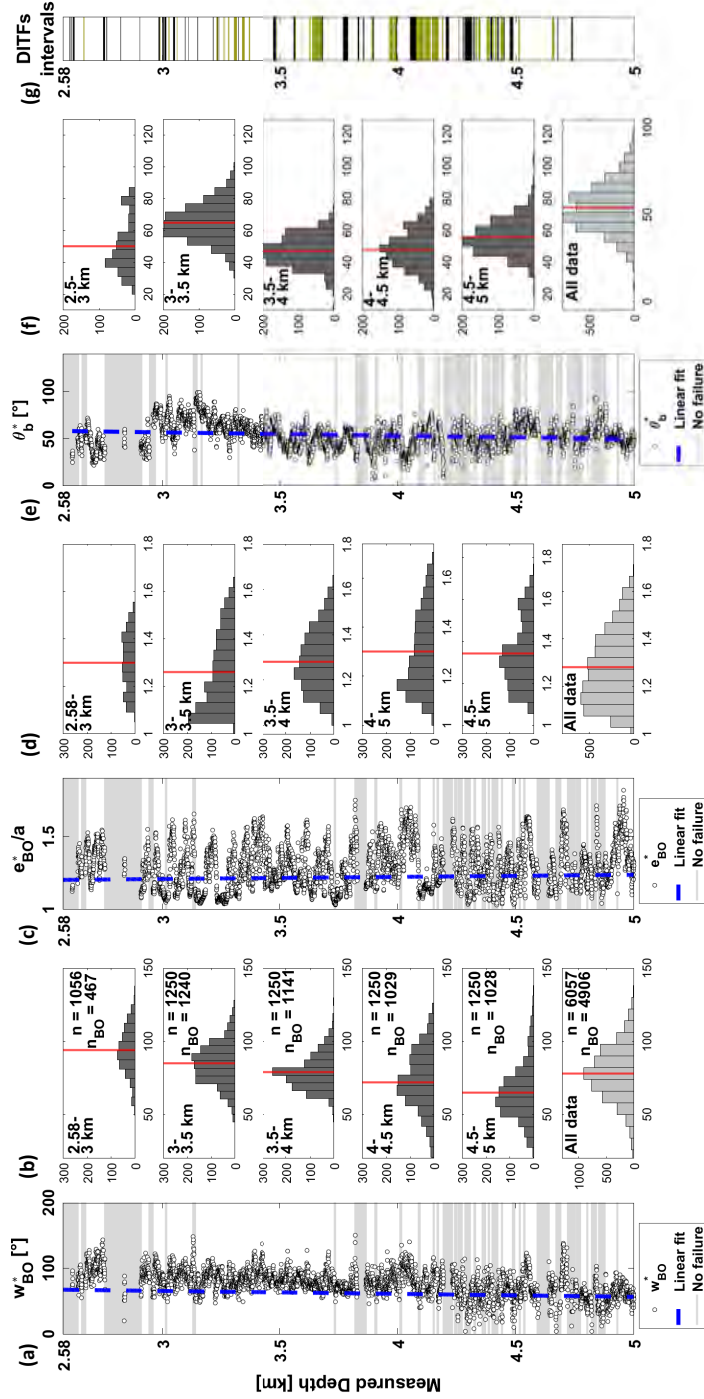


Figure 3.2.: Interpreted failure data along borehole BS-1 (modified from Valley and Evans (2009b)): (a, c and e) Spatial distribution of breakout width (w_{BO}), extent normalized by borehole radius (e_{BO}/a) and orientation (θ_b), respectively. The dashed lines represent linear depth trends and the horizontal grey shaded zones represent cross-sections without breakouts; (b, d and f) histograms of the aforementioned magnitudes along 500 m long borehole sections and considered altogether (panels on bottom). The insets report on the number of sections (n) and the number of sections where breakouts occur (n_{BO}). The red lines depict mean values; (g) Observed DITFs intervals (green = en-echelon; black = axial).

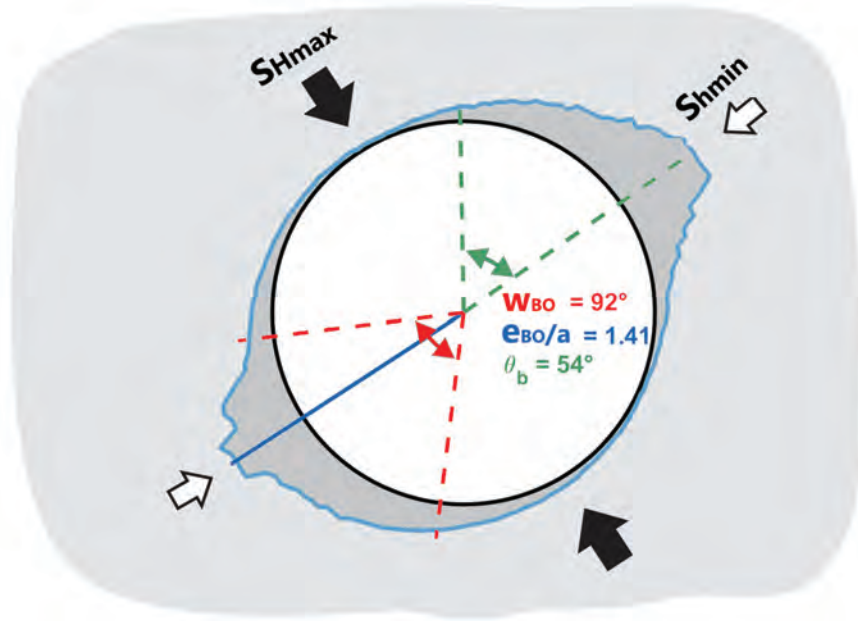


Figure 3.3.: Geometry of the BS-1 borehole at 3509 m MD. The black circle corresponds to the normal bit size ($a = 9 \frac{7}{8}$ ") and the blue envelop corresponds to the inferred geometry of the BS-1 borehole. A breakout width $w_{BO}=92^\circ$, a normalized breakout extent $\frac{e_{BO}}{a}=1.41$ and a breakout orientation $\theta_b=54^\circ$ were measured. Note that the two limbs defining the breakout at 2pm and 8pm clock positions are not necessarily symmetric because the borehole is not exactly vertical.

Table 3.1 summarizes the statistical description of borehole failure along BS-1. Breakouts are pervasive along BS-1 (81%), whereas DITFs are present along 20% of the borehole only. As already observed by Valley and Evans (2019), breakout width, w_{BO} decreases with depth from an average of 94° in the 2.58-3 km section to 65° in the 4.5-5 km section (Fig. 3.2b). Normalized failure extension, $\frac{e_{BO}}{a}$, remains relatively constant with depth (only a slight increase with depth is observed). The change of diameter from $9\frac{7}{8}$ " to $8\frac{1}{2}$ " at 4850 m MD does not impact significantly breakout geometry. Considering all data, the average of θ_b is 54° (Valley and Evans, 2009b). The variability of breakout orientation is shown to follow scaling laws (Valley and Evans, 2014a) and can differ significantly from the mean orientation at the local scale, which is typically attributed to the presence of natural fractures and other sources of local heterogeneity. Correspondingly, the standard deviation of breakout orientation is 14° (Valley and Evans, 2009b).

Overall, 20% of the logged section was affected by DITFs (A-DITFs and E-DITFs, Fig. 3.2g). As observed, there are not obvious depth trends in the distribution of DITFs. This suggests that, along the entire borehole length, σ_3^{min} at the wellbore wall is not far from tensile failure and additional hoop stresses caused by cooling of the borehole wall are sufficient to induce locally tensile failure. This is further discussed in Section 3.6.

DITFs observations are transformed into minimum hoop stress (in vector \mathbf{D} , Eq. 3.19).

In the presence of DITFs, the minimum hoop stress must be lower than tensile strength ($T_o = -4$ MPa, tension being negative), whereas the minimum hoop stress remains higher than the tensile strength in the presence of DITFs. In greater detail, 20% of the BS-1 profile is affected by DITFs. We generate a minimum hoop stress distribution respecting the observations of DITFs occurrences. This allows converting the boolean DITFs observations (occurrence or absence) into a continuous variable which is better suited for our calibration algorithm.

Table 3.1.: Statistical parameters of key breakout indicators.

Cross sections every 40 cm from 2.58 to 5 km MD:		$n=6057$		
Sections with identified breakouts:		$n_{BO} = 4906$		
Percentage of wellbore length affected by breakouts:		81%		
	min	max	mean	std
w_{BO} :	15°	150°	78°	19°
$\frac{e_{BO}}{a}$:	1.03	1.81	1.28	0.15
θ_{BO} :	7°	170°	54°	14°
Sections with identified DITFs:		$n_{DITFs} = 1211$		
Percentage of wellbore length affected by DITFs :		20%		

3.3.2. BS-1 stress state from previous studies

Häring et al. (2008) provided an initial assessment of the stress state. Valley and Evans (2009b) assessed the orientation of the maximum horizontal stress. Valley and Evans (2019) used breakout width data to estimate stress magnitudes. The analyses of microseismicity associated with the stimulation in BS-1 (Kastrup et al., 2004; Deichmann and Giardini, 2009; Kraft and Deichmann, 2014; Terakawa et al., 2012) gave some further insights on the stress state. A detailed discussion of the stress magnitudes at the Basel Geothermal site is given in Valley and Evans (2019) and we refer the interested reader to this publication for details out of the scope of this paper. We report here only on the so-called 1st order characterisation, i.e. linear depth trend of the magnitude of S_v , S_{hmin} , S_{Hmax} and P_p and of the azimuth of S_{Hmax} . Fig. 3.4 summarizes the published profiles.

The main discrepancies between prior studies concern the S_{hmin} and S_{Hmax} profiles. The profiles proposed by Valley and Evans (2019) share the commonality of a very low stress gradient that are required to explain the fact that breakout width decreases with depth and assuming that the borehole wall strength remains constant with depth, as supported by the homogeneity of the rock along the BS-1 basement section. The absolute value of S_{Hmax} is highly uncertain because it depends strongly on the chosen failure criterion and its parametrization, for which there are not robust evidences. The focal mechanism of induced seismic events indicate a mix of strike-slip and normal faulting regimes at the level of the reservoir. The stress profiles proposed by Valley and Evans (2019) are consistent

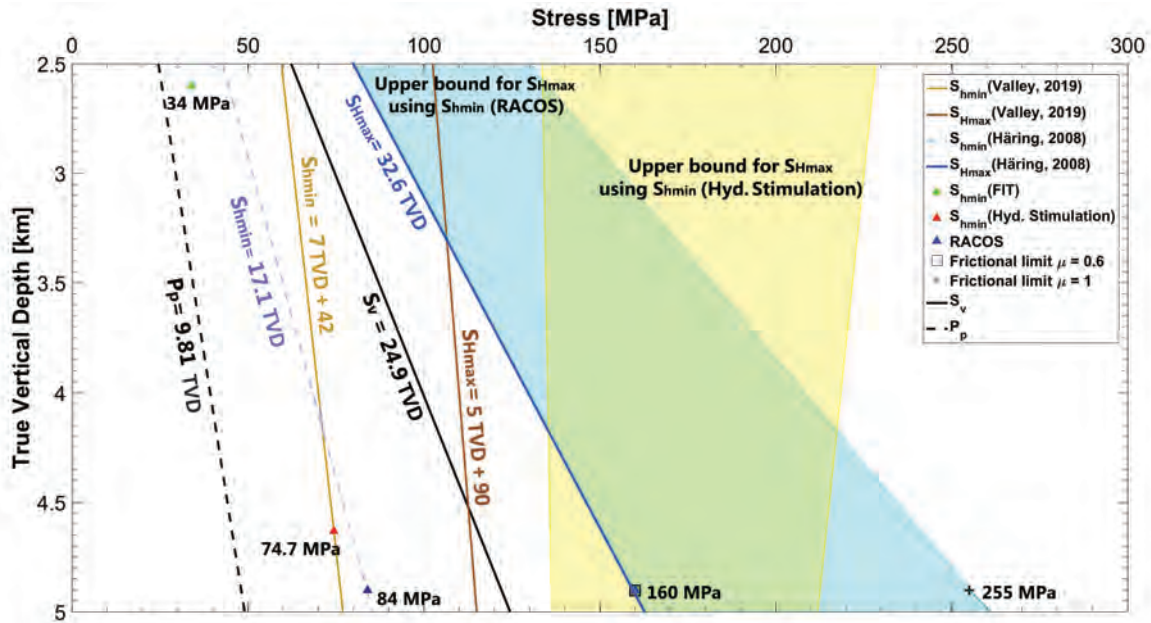


Figure 3.4.: Constraints on S_{hmin} and S_{Hmax} in the BS-1 well inferred from hydraulic data, FIT test and RACOS (Braun, 2007) as compiled by Häring et al. (2008). Profiles of S_{Hmax} and S_{hmin} from Valley and Evans (2019) are also presented. The colored areas depict upper bounds for S_{Hmax} considering frictional equilibrium (Zoback, 2007), friction coefficients between 0.6 and 1.0 and the two proposed profiles of S_{hmin} . The orientation of S_{Hmax} is common to all analyses, i.e., $144 \pm 14^\circ$ (Valley and Evans, 2009b).

with this observation. All proposed profiles are also consistent with the limits imposed by frictional strength of the earth crust (Zoback et al., 2003).

3.4. Parametric and sensitivity analyses

In this section, we summarize a series of parametric and sensitivity analyses carried out prior to parameter calibration, aimed at understanding the influence of each parameter intervening in the formulation of the stress and failure models. Identifying the critical parameters will help us to (1) reduce the parameterization, and (2) bound the parameter space. Furthermore, we illustrate the problem of non-uniqueness by calibrating parameters at the cross-section MD = 3509 m in Fig. 3.3.

3.4.1. Relationship between breakout width and breakout extent in the BS-1 well

Fig. 3.5 displays the cross plot of measurements of breakout width and extent along the BS-1 well. The data present the expected positive correlation, i.e., as borehole failure severity increases, both breakout width and extent increase. However, and in spite of

data scattering, some underlying non-linear trends can be identified. For instance, wide breakouts with limited extent are observed along the shallower section of the borehole (blueish dots in Fig. 3.5). Instead, breakouts are relatively narrower at greater depth (yellowish dots) for a similar extent. In order to identify what parameters control such trends, we explore first in a generic manner the conditions controlling the relative width and extent of breakouts.

An obvious condition influencing the relationship between width and extent of breakout is the difference between stresses in the plane normal to the borehole. To illustrate this effect, we consider the simple case of a vertical borehole in a stress field with one principal stress being vertical. The effect of the differential horizontal stress, $\Delta\sigma_h = \sigma_{Hmax} - \sigma_{hmin}$, is illustrated in Fig. 3.6a-b using arbitrary numerical values to facilitate comprehension and the reproducibility of our numerical experiment. In Fig. 3.6a, we present a case with $\Delta\sigma_h = 2$ MPa. The variation of the maximum principal stress at the borehole wall is 8 MPa (from 94 to 102 MPa). Assuming a borehole wall strength $C_o = 100$ MPa, the resulting breakout width is 60° and the normalized breakout extent is 1.08 (corresponding to a maximum stress at the borehole wall of 102 MPa, 2 MPa above C_o ; see Sections 3.2.3 and 3.2.4). Fig. 3.6b explores the same conditions using a highly anisotropic stress tensor with $\Delta\sigma_h = 20$ MPa. In this case, the variation of the maximum principal stress at the borehole wall is much larger ($4\Delta\sigma_h = 80$ MPa). We deliberately choose absolute value of the stress magnitude leading to the same breakout width of 60° . In this case, the normalized breakout extent is 1.2 (corresponding to a maximum stress at the borehole wall of 120 MPa, 20 MPa above C_o). We conclude from these two examples that (1) for larger $\Delta\sigma_h$, breakouts with identical width will have a larger extent, and (2) in broad terms, small $\Delta\sigma_h$ tend to generate wide and shallow breakouts whereas large $\Delta\sigma_h$ will tend to generate narrow and extended breakouts. Note that, for simplicity, we have chosen a simple situation in which the hoop stress is always the maximum principal stress and a failure criterion independent of the intermediate stress. Indeed, this is not always the case in practice, and more complex conditions would lead to less obvious computations of breakout width and extent according to the equations in Section 3.2, which are generic.

Another key point is the asymptotic behaviour of the equations governing breakout width (Valley, 2007), manifested in the so-called pivot points depicted as black triangles in Fig. 3.6c-d. The stress curves displayed in Fig. 3.6c-d are built by setting and increasing incrementally σ_{Hmax} . All the curves share a common pivot point corresponding to an angular opening of 120° . The stress magnitude at the pivot point is equal to $2\sigma_{hmin}$ (Eq. B.3 for isotropic stress conditions). When the pivot point is close to the failure line (Fig. 3.6c, $2\sigma_{hmin} = 96$ MPa), breakouts tend to be shallow. On the contrary, when the pivot point is far from the failure line (Fig. 3.6d, $2\sigma_{hmin} = 76$ MPa), extended breakouts are generated. As a direct comparison, the lower line in Fig. 3.6c and the upper line in Fig. 3.6d yield the same breakout width of 60° , relative breakout extent of 1.08 and 1.16 respectively. Thus, the ratio $\frac{\sigma_{hmin}}{C_o}$ has a strong impact on the relationship between

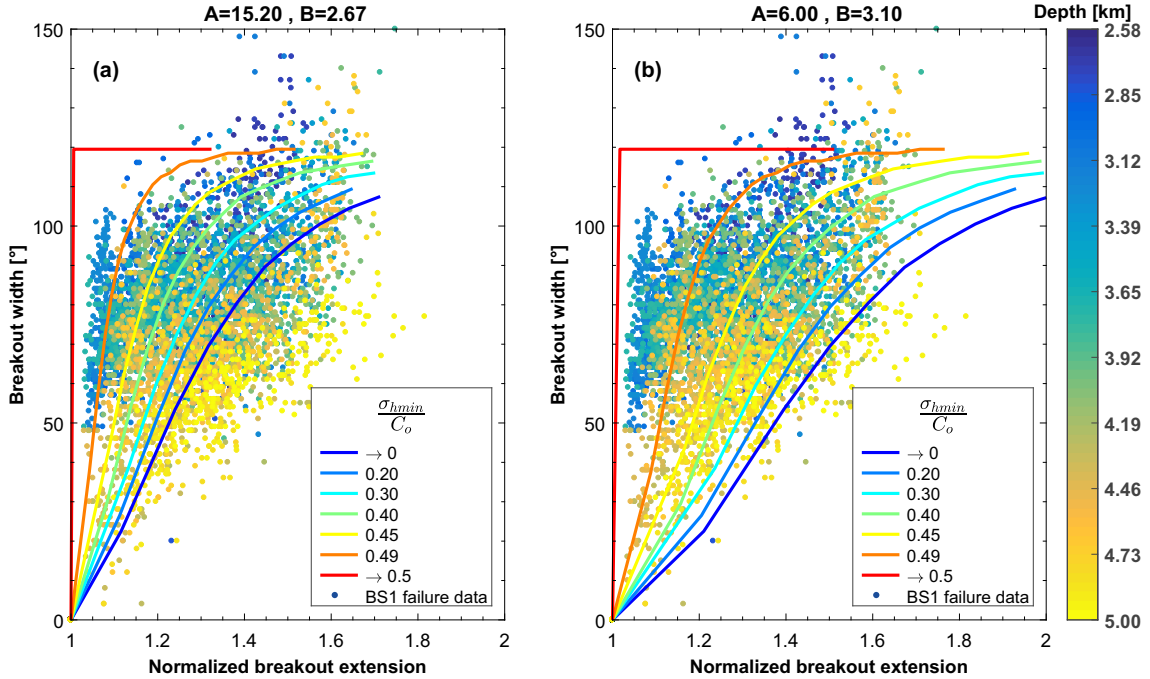


Figure 3.5.: BS-1 borehole failure data and failure models. Dots represent measurements and are colored according to TVD. Failure models are depicted for different values of the ratio σ_{hmin}/C_o and different values of the governing parameters: (a) mean values suggested by Shen (2008); (b) modified values after a preliminary calibration exercise.

breakout width and extension. When pivot points are located exactly at the failure line, i.e., when $\frac{\sigma_{hmin}}{C_o} = 0.5$, the breakout width is always 120° .

Failure models corresponding to different values of $\frac{\sigma_{hmin}}{C_o}$ are superimposed to the Basel breakout width-extent data set in Fig. 3.5. In broad terms, the suggested failure model explains well the dispersion of data observed along BS-1. Note that, in our failure model, the relationship between breakout width and extent is controlled by the parameters A and B in Eq. 3.13. The lines in Fig. 3.5a display the failure criterion using the average parameters suggested by Shen (2008), i.e., $A = 15.2$ and $B = 2.67$. As observed, the envelope of solutions obtained in the maximum possible ranges of $\frac{\sigma_{hmin}}{C_o} \in [0, 0.5]$ does not fully cover the breakout geometries at greatest depths (TVD > 4000 m). Fig. 3.5b displays the same setup, but now using $A = 6$ and $B = 3.1$, attained after a preliminary calibration exercise. The coverage of breakout geometries is now better regardless of depth, as expected. We attribute this to the fact that Shens parameters depend on rock type (and heterogeneity) and, therefore, must be calibrated.

3.4.2. Sensitivity analyses

Sensitivity analyses are useful to identify parameters with large impact on model outputs, i.e., those to be calibrated, and to bracket parameter ranges, thus reducing prior uncertainties and computational effort. We use as base case the breakout at 3509 m MD

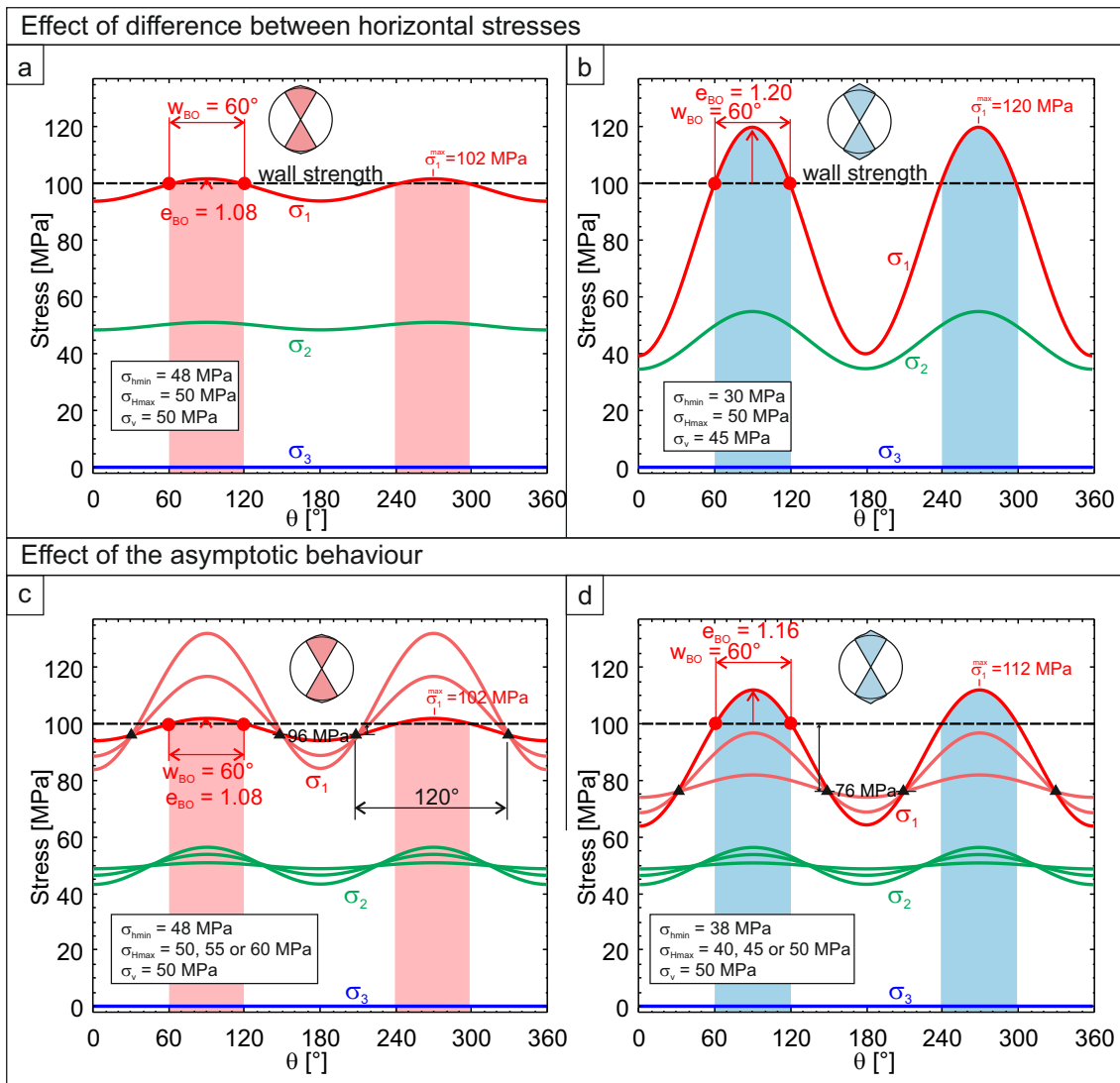


Figure 3.6.: Illustration of the effect of stress conditions controlling the relationship between breakout width and extension. The principal stresses (σ_1 , σ_2 and σ_3) at the wall of a vertical borehole are shown in red, green and blue, respectively, for conditions generating 60° breakout width but a variable breakout extent. In all cases, a vertical borehole is considered with far field stress σ_v aligned with the borehole axis and σ_{Hmax} and σ_{hmin} normal to it. Borehole internal fluid pressure, P_w , is taken as 0 MPa and borehole wall strength, C_o , as 100 MPa. a) Example with similar horizontal stresses ($\Delta\sigma_h = 2$ MPa) leading to shallow breakouts. b) Example with dissimilar horizontal stresses ($\Delta\sigma_h = 20$ MPa) leading to extended breakout. c) Example with the pivot point close to the borehole wall strength leading to shallow breakouts. d) Example with the pivot point low compared to the borehole wall strength leading to extended breakouts.

displayed in Fig. 3.3, which we consider as representative of the entire borehole length. A set of base case parameters (Fig. 3.7) is defined that leads to a good fit of either breakout width or breakout normalized extent. Note that different rock strength parameters are used in both cases, which allows us to identify the parameters controlling breakout geometric features separately. Incremental parametric variations of 1% are applied to each parameter in a range $\pm 20\%$ of the base value, while the remaining parameters are set to the base case value. The solution, either w_{BO} or e_{BO} is computed and represented as tornado plots in Fig. 3.7. Note that the shape of each bar is the result of an individual sensitivity analysis. A linear relationship between a parameter and an output (breakout width/extent) is seen as a perfect triangular bar (e.g., P_m). Instead, nonlinear relationships are seen as thorny or bulgy bars (e.g., S_{Hmax} and S_{hmin} , respectively) reflecting the nature of the correlation.

We have limited the analysis to w_{BO} and e_{BO} because breakout orientation is directly inferred from breakout geometry (and is therefore not parameterized) and the presence/absence of DITFs depends only on stresses and the cooling but not on the rock strength properties. As expected, the most influencing parameter in both cases is the internal well pressure, P_m . The second most influencing parameter is S_{Hmax} . Moreover, S_{hmin} plays a very important role at the global scale and must necessarily be calibrated. The apparent wall strength plays also an important role on breakout geometry. As such, it is not strange that model outputs are overly sensitive to both cohesion and friction (in fact, to a suitable combination of them). Last, Shen parameters A and B also play an important role in the final breakout extent. To make the long story short, the chosen parameterization for the calibration in Section 3.5 is as follows:

- It is assumed that the vertical stress, S_v , is principal and known, which greatly reduces the number of model parameters. This is justified by the observed small deviations of the density log around its linear depth trend and is attributed by the homogeneity of the crystalline section of the BS-1 borehole observed in the cuttings retrieved during drilling.
- In the same line of arguments, the azimuth of the maximum principal stress S_{Hmax} and the strength parameters (internal friction angle, ψ , cohesion c , and modified Shens parameters A and B) are considered constant in the 1st order approach. Nonetheless, our methodology is generic and linear depth trends can be accommodated for any of the aforementioned parameters. The parameters controlling thermal stresses, E and ν , are assumed constant and known. In fact, they are usually inferred after the dynamic to static correction of the sonic log in the best case or inherited from existing literature in most cases. The impact of stiffness variations is discussed in Section 3.6.
- In the absence of further information, the distribution of formation pressure is assumed to be hydrostatic, which further reduces the parameterization. Although for

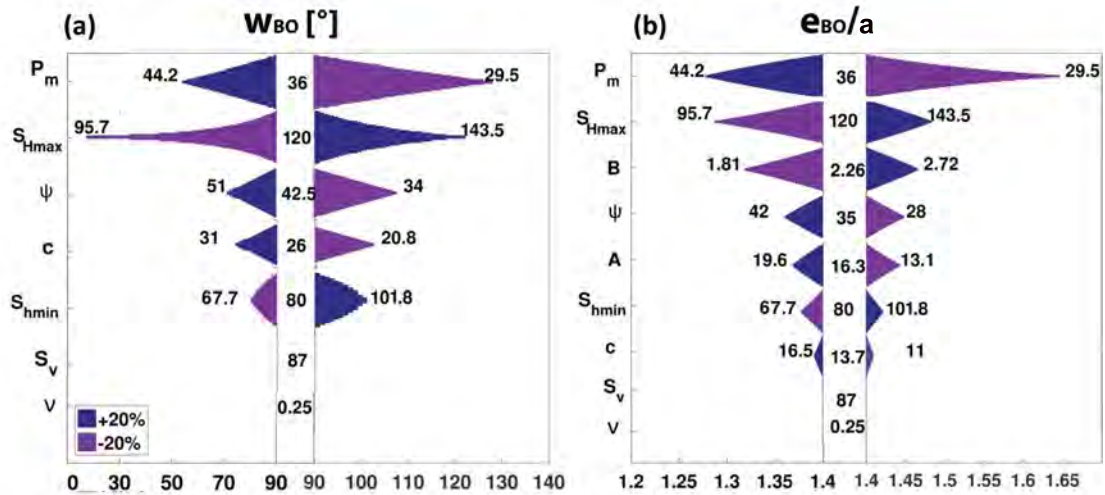


Figure 3.7.: Tornado diagram summarizing the sensitivity analyses: (a) breakout width [°]; (b) normalized breakout extent [-]. The analyzed parameters are: mud pressure, P_m [MPa], maximum and minimum principal horizontal stresses, S_{Hmax} and S_{hmin} , respectively [MPa], principal vertical stress, S_v [MPa], internal friction angle, ψ [°], cohesion, c [MPa], Poisson ratio, ν [-] and Shen's parameters, A [-] and B [-]. Base case values of analysed parameters are displayed at the centre of the tornado plot. Note that different values are used for the sensitivity analysis of width and extent. The minimum and maximum values of inputs (in the range $\pm 20\%$ with respect to the base values) are typed to the left and right of each diagram, respectively. Stress parameters are common to both cases ($S_v = 87$ MPa, $S_{Hmax} = 1.37S_v$, $S_{hmin} = 0.97S_v$). A common Poisson ratio $\nu = 0.25$ and Young modulus $E = 65$ GPa were used.

example at the BS1 site, a slightly artesian conditions are encountered, we argue that deviations from the hydrostatic distribution are small compared to uncertainties on other model parameters.

The chosen first order parameterization, summarized in vector \mathcal{M} is:

$$\mathcal{M} = \{a_{S_{Hmax}}, b_{S_{Hmax}}, a_{S_{hmin}}, b_{S_{hmin}}, \alpha, c, \psi, A, B\} \quad (3.22)$$

The parameter α in this first order parameterization refers to Euler's angle (see Appendix A). The second order characterization is carried out by estimating optimum parameters values at a set of pilot points (common to all parameter type, and is discussed in detail in Section 3.5.1.1).

3.4.3. Illustration of solution non-uniqueness

Inverse problem often suffers from instability, non-identifiability and non-uniqueness. Carrera and Neuman (1986) discuss extensively these concepts and show that they are closely related. Instability is present when small changes in the observations lead to

large changes in the estimated parameters, and is tackled by using model identification criteria (Akaike, 1974; Akaike et al., 1977; Rissanen, 1978; Schwarz, 1978; Hannan, 1980; Kashyap, 1982; Medina and Carrera, 2003; Alcolea et al., 2006). Non-identifiability occurs when more than one set of parameters leads to a given solution of the forward problem. Non-uniqueness is present when more than one set of parameters leads to a minimum of the objective function F . We illustrate non-uniqueness by calibrating only S_{Hmax} and C_o at the cross-section in Fig. 3.3. All other parameters are set to the corresponding base case values. Furthermore, the impact of the parameters of the modified Shens criterion is also evaluated by comparing the breakout extent attained with three different pairs of values (A,B) . Results are summarized in Fig. 3.8, which shows combinations of C_o and S_{Hmax} reproducing the geometry of the breakout. The first obvious observation is that for any given C_o , a value of S_{Hmax} exists that reproduces exactly the observations and that the calibrated pairs of C_o and S_{Hmax} are almost linearly correlated. This is consistent with Barton's equation (Barton et al., 1988b), developed for the estimation of S_{Hmax} based on breakout width observations. Unfortunately, C_o is usually unknown (or known at certain sections at best) and thus the problem is under-determined.

As expected, the calibrated pairs (S_{Hmax}, C_o) reproducing breakout width (red curve in Fig. 3.8) do not capture properly the breakout extent and vice versa. The only sets of parameters reproducing both geometric features are the intersections between the calibrated w_{BO} and $\frac{e_{BO}}{a}$ (squares in Fig. 3.8), which depends on the value of the Shen's empirical parameters A and B , not known a priori. Thus, considering simultaneously both breakout width and extension at a certain section does not allow to converge to a unique optimum parameter solution at a certain borehole cross-section. Fortunately, adding other sources of measurements (i.e., breakout orientation, DITFs and, especially, prior information on model parameters) helps to alleviate non-uniqueness (Ramírez et al., 2005; Alcolea et al., 2006).

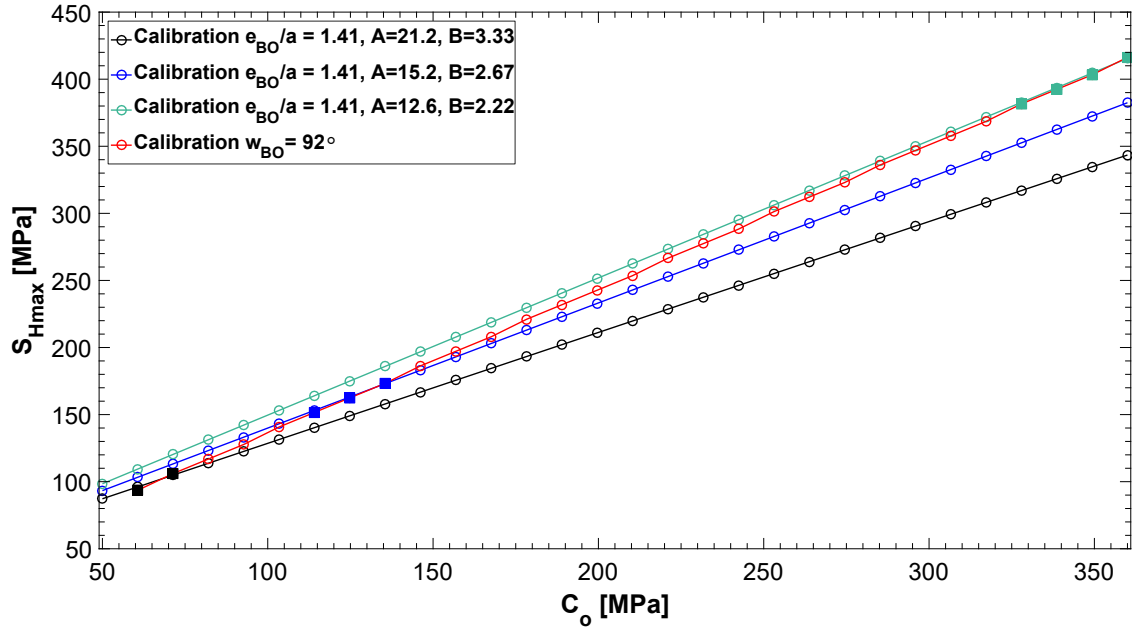


Figure 3.8.: Illustration of non-uniqueness after the calibration process at the cross-section at 3509 m MD. The curves depict the calibrated pairs (S_{Hmax}, C_o) capable of reproducing either a breakout width of 92° or a normalized breakout extent of 1.41. The latter is carried out using three different pairs of values of Shen's parameters A and B . The borehole is assumed to be vertical. The other parameters used for this basic calibration are: $S_{hmin} = 48.6$ MPa, $S_v = 87$ MPa, $P_p = 34.4$ MPa, $P_m = 1.07 \cdot P_p$, $\psi = 30^\circ$, $\nu = 0.25$, $E = 65$ GPa. The filled squares represent the calibrated pairs (S_{Hmax}, C_o) for which we reproduce jointly w_{BO} and e_{BO} at 3509 m MD.

3.5. Calibration of the developed geomechanical model on observed failure in the BS-1 well

In this section, we present the calibration results using measurements from 3 to 5 km MD. We first focus on the 1st order characterization, i.e., the estimation of linear trends of parameters with depth. We argue that 1st order characterization is necessary, but not sufficient to warrant proper completion (e.g., cementing or packer sealing). Thus, we analyse the variability of model parameters by calibrating the deviations with respect to the trend at 201 pilot points, whose location is common to all parameters (i.e., overall 1407 pilot points). We call this stage 2nd order calibration.

3.5.1. First order calibration approach

To reproduce BS-1 observations with our failure models, we focus on the model parameters that are the most influential and cannot be estimated otherwise. In this 1st order calibration, we use simplified profile with depth of these model parameters (Eq. 5.1). In summary our stress/strength model is parametrized by 9 parameters (Eq. 3.22). A number of starting points is used in the calibration to guarantee that a global optimum is achieved by the Levenberg-Marquardt algorithm (Alcolea et al., 2000). To that end, the prior distribution of each parameter is randomly sampled assuming a uniform distribution, which renders overall 200 initial parameterizations that explore the global parameter space. An initial rejection criterion, based on frictional equilibrium, is applied to the initial starting points, as follows:

1. Sample the parameter space.
2. Check coherency and frictional equilibrium (Zoback, 2007; Jaeger, 2007):

- $S_{Hmax} \geq S_{hmin}$
- $\frac{S_1 - P_p}{S_3 - P_p} \leq [\sqrt{\mu^2 + 1} + \mu]^2$

where S_1 and S_3 are the maximum and the minimum total principal stresses respectively, P_p is the pore pressure and μ is the friction coefficient ($\mu = \tan(\psi)$).

Initial sets of parameters not meeting the aforementioned constraints are rejected and new ones are generated until the target 200 initial coherent parameterizations is achieved. Note that initial sets of parameters may lead to different final optimum sets of calibrated parameters with similar final value of the objective function F . This is a common issue in inverse problem theory, known as non-uniqueness, and is discussed in detail in Section 3.5.1.1.

Assumptions are required for model parameters that are not calibrated. We use the following equations for S_v and P_p :

$$S_v[MPa] = 24.9 \cdot TVD[km] \quad (3.23)$$

$$P_p[\text{MPa}] = 9.81 \cdot \text{TVD}[\text{km}] \quad (3.24)$$

Based on the mud density measurements collected during the drilling of BS-1, we assume a hydrostatic mud pressure corresponding to an equivalent mud density, $\rho_{mud} = 1.07 \text{ g/cm}^3$. We use the actual BS-1 borehole trajectory in our computations. Different cooling profiles for breakouts and DITFs after Valley and Evans (2019) were used to estimate thermal stresses as well as the Young modulus ($E = 65 \text{ GPa}$) and the coefficient of linear expansion ($\beta = 10^{-5} \text{ K}^{-1}$). In addition, a set of bounding thresholds is implemented in PEST to minimize unwanted and large parameter oscillations.

3.5.1.1. Non-uniqueness

A posterior rejection criterion was defined by setting a maximum threshold for the objective function after calibration, and calibrated models with final objective function above the threshold were rejected. After this rejection process, only 136 and 95 well calibrated models were kept using the Mohr-Coulomb and Mogi-Coulomb failure criteria, respectively.

Fig. 3.9 shows failure observations (w_{BO}^* , $\frac{e_{BO}}{a}^*$, θ_b^* and D^*) and the 136 well calibrated horizontal principal stresses using the Mohr-Coulomb failure criterion. As observed, the breakout width tends to decrease with depth while breakout extent does not vary much, which is consistent with the BS-1 borehole observations in Fig. 3.2. This can be explained by the low slopes of calibrated stresses ($a_{S_{Hmax}}$ and $a_{S_{hmin}}$, with mean values 4.3 and 7.2 MPa/km, respectively; Fig. 3.10), which resemble well the experimental results in Valley and Evans (2019). All models converge towards a breakout orientation $\theta_b = 54^\circ$, which is precisely the orientation of S_{hmin} reported in Häring et al. (2008).

Fig. 3.11 shows the 95 calibrated stresses and breakout geometries attained by using the Mogi-Coulomb failure criterion. Despite the overall trends of calibrated principal stresses are similar to those attained by using Mohr-Coulomb failure criterion, the envelope of the calibrated S_{Hmax} is now broader due to the strengthening effect of σ_2 (not accounted for by the Mohr-Coulomb failure criterion). This negative finding, as well as the strengths and weaknesses of the tested failure models will be further discussed in Section 3.6.

Table 3.2.: Lower and upper bounds of calibrated S_{Hmax} and S_{hmin} using Mohr-coulomb and Mogi-Coulomb failure criteria.

	Mohr-Coulomb		Mogi-Coulomb	
	Lower bound	Upper bound	Lower bound	Upper bound
$a_{S_{Hmax}}$ [MPa/km]	5.4	6.5	4.8	7.6
$b_{S_{Hmax}}$ [MPa]	87	130.2	138.6	230.5
$a_{S_{hmin}}$ [MPa/km]	7.5	4.5	6.5	7.6
$b_{S_{hmin}}$ [MPa]	31.31	87.5	30.6	124.5

Fig. 3.12 shows the correlation at 3000 m MD between the input parameters S_{Hmax} ,

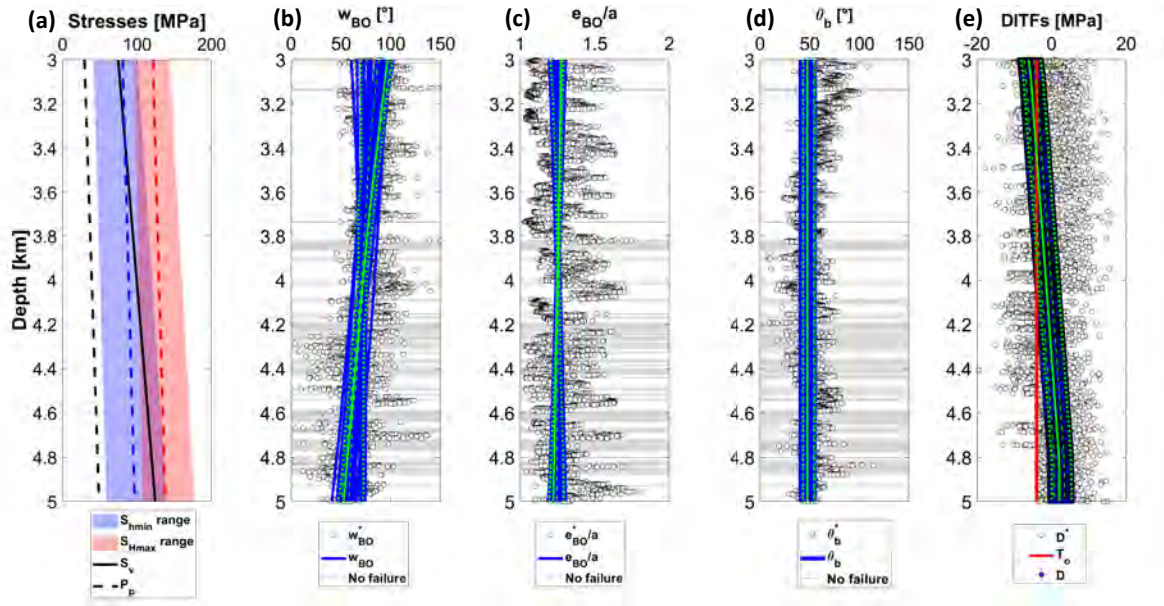


Figure 3.9.: 1st order calibration results using the Mohr-Coulomb failure criterion. (a) range of the calibrated S_{Hmax} (pink) and S_{Hmin} (purple) for 136 different starting points. S_v and pore pressure profiles are depicted by the solid and dashed black lines, respectively. The blue and red dashed lines depict the mean of the ranges of the calibrated S_{Hmin} and S_{Hmax} , respectively; (b) calibrated and measured breakout width; (c) normalized breakout extent; (d) breakout orientation; (e) DITFs. In panels (b) to (d), the black symbols depict measurements, whereas in panel (e), they depict the estimated minimum hoop stress derived from DITFs observations. In panels (b) to (e), the blue lines represent the outputs of the calibrated models. The grey shaded zones represent depth ranges without breakouts. The red line in panel (e) corresponds to tensile strength, $T_o = -4$ MPa. Finally, the solid green lines correspond to the mean of the outputs of the 136 accepted models, whereas the dashed lines represent the 25-75 and 5th-95th percentiles.

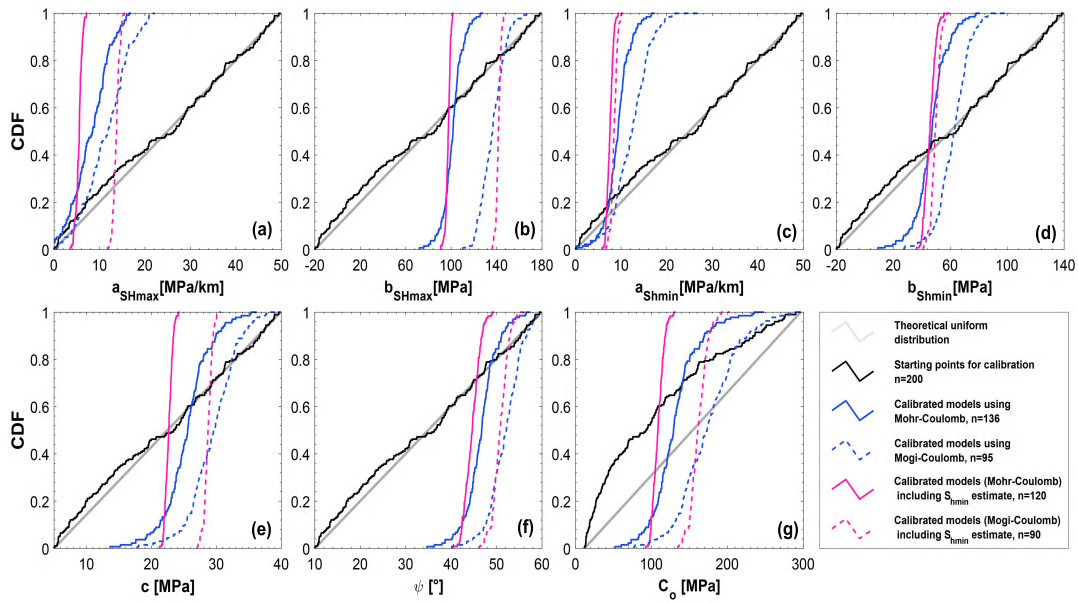


Figure 3.10.: Prior (black) and posterior cumulative density functions in the absence (blue lines) and in the presence (pink) of an estimate of S_{hmin} at a depth 4632 m MD: (a) slope of S_{Hmax} ; (b) intercept of S_{Hmax} ; (c) slope of S_{hmin} ; (d) intercept of S_{hmin} ; (e) cohesion, c ; (f) internal angle of friction, ψ and (g) uniaxial compressive strength, C_o .

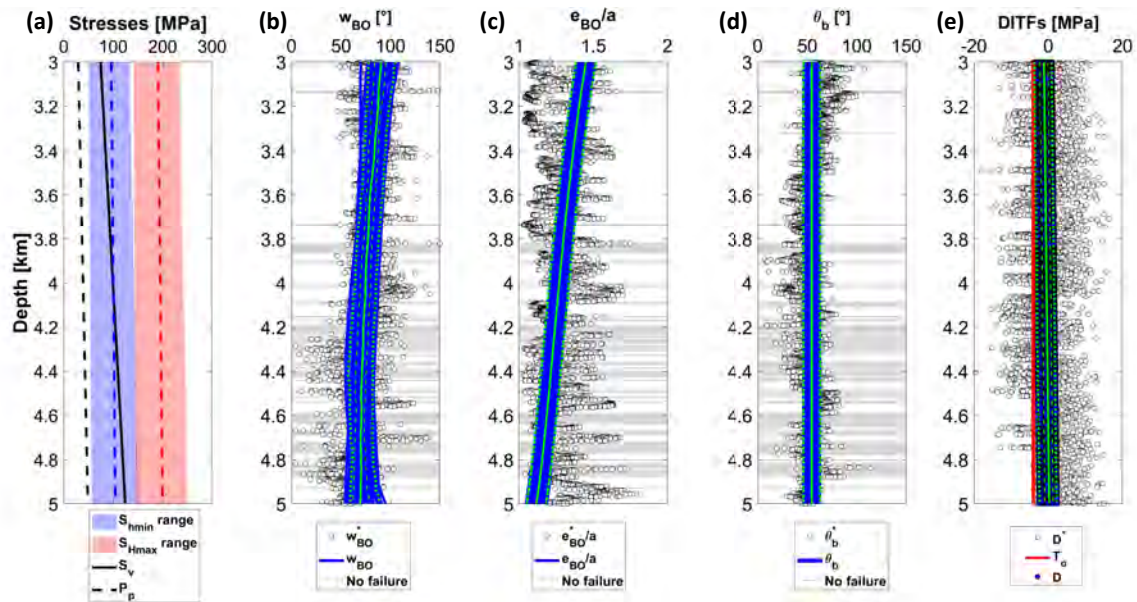


Figure 3.11.: 1st order calibration outputs while using Mogi-Coulomb failure criterion. See the caption of Fig. 3.9 for further details.

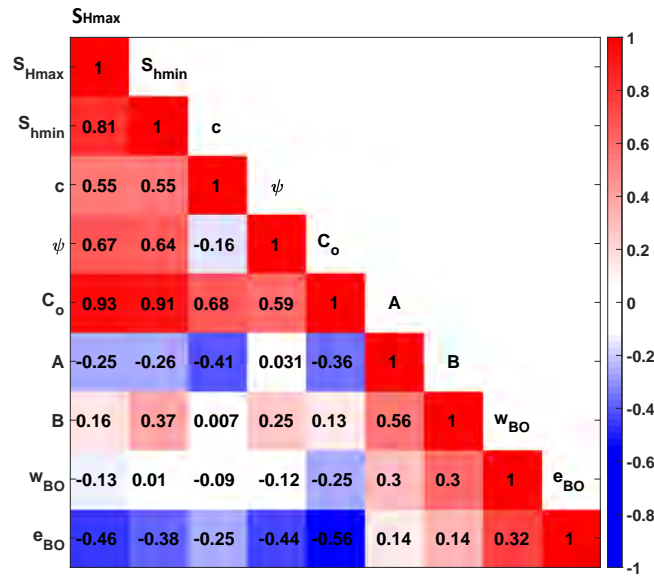


Figure 3.12.: Correlation matrix between the 1st order calibrated parameters S_{Hmax} , S_{hmin} , c , ψ , C_o , A and B and the borehole failure indicators w_{BO} and e_{BO} . Correlation coefficients are placed in the middle of each cell. The Mohr-Coulomb failure criterion and MD=3000 m were selected. Similar qualitative results are attained by using the Mogi-Coulomb failure criterion or any other given depth.

S_{hmin} , c , ψ , C_o , A and B and the borehole failure indicators w_{BO} and e_{BO} using the Mohr-Coulomb criterion. As observed, the correlation between S_{Hmax} , S_{hmin} and C_o is almost linear, which is consistent with the results shown in Section 3.4.3. As expected, the correlation between parameters and measurements is very low, which highlights the non-linearity of our formulation. As observed in Fig. 3.10, the initial sampling of the parameter space was nearly uniform (black versus grey lines), and the number of models fulfilling the posterior rejection criterion is large enough to draw meaningful statistical distributions regardless of the chosen failure criterion. The range of calibrated parameters is generally large, which again draws attention to the non-uniqueness of the inverse problem illustrated in Section 3.4.3. Non-uniqueness highlights the inherent parametric uncertainties and can be alleviated by adding either more measurements of a given kind, or more kinds of measurements. In the context of this work, the impact of the number of measurements was done by skipping cross-sections. This exercise led to results almost identical to those in Figs. 3.9-3.11. In the next section, we explore how non-uniqueness can be alleviated by adding an additional type of measurement, i.e., S_{hmin} after the interpretation of a XLOT.

3.5.1.2. Reducing the solutions uncertainty

The best estimate of S_{hmin} from hydraulic stimulation was considered as a measurement (Häring et al., 2008) at a depth of 4632 m MD. The new measurement was added

to the objective function F in Eq. 3.19. The first order calibration was carried out using the same 200 initial set of parameters as in the prior exercise. After applying the posterior rejection criterion based on the objective function value, only 120 and 90 models are selected when the Mohr-Coulomb and Mogi-Coulomb are used as failure criteria, respectively (136 and 95 in the absence of the S_{hmin} measurement). Figs. 3.13 and 3.14 show the dramatic reduction of uncertainty in the calibrated stress model parameters regardless of the considered failure criterion, as displayed by the narrower envelopes of plausible solutions. Interestingly, the use of the Mogi-Coulomb criterion leads to conceptually wrong stress profiles, which are inconsistent with the faulting regime data derived from the focal mechanisms of the microseismic events induced during hydraulic stimulation, i.e., not honoring the transitional regime at ca. 4800 m MD. Although this may be a plausible inference, we acknowledge that the kinematics of faulting represented by focal mechanisms is not always consistent with faulting mechanics represented by the stress state. Indeed, the Mohr-Coulomb criterion is, in the case of BS-1, more consistent, but this does not exclude the validity of the Mogi-Coulomb criterion. The Mogi-Coulomb failure criterion is nevertheless problematic in at least two other aspects. First, it yields calibrations that contravene bounds on admissible S_{Hmax} values imposed by frictional limits (Valley and Evans, 2019). Second, it is not capable of reproducing, in the case of BS-1, the simultaneous observation of a decrease in breakout width and constant breakout extension with depth when using the Mogi-Colomb criterion (Fig. 3.11). For these reasons, we use the Mohr-Coulomb criterion in further analyses.

The reduction of parametric uncertainties is best observed in Fig. 3.10. As observed, including one single measurement of S_{hmin} reduces drastically the range of calibrated parameters, as inferred from the steeper shape of all CDFs.

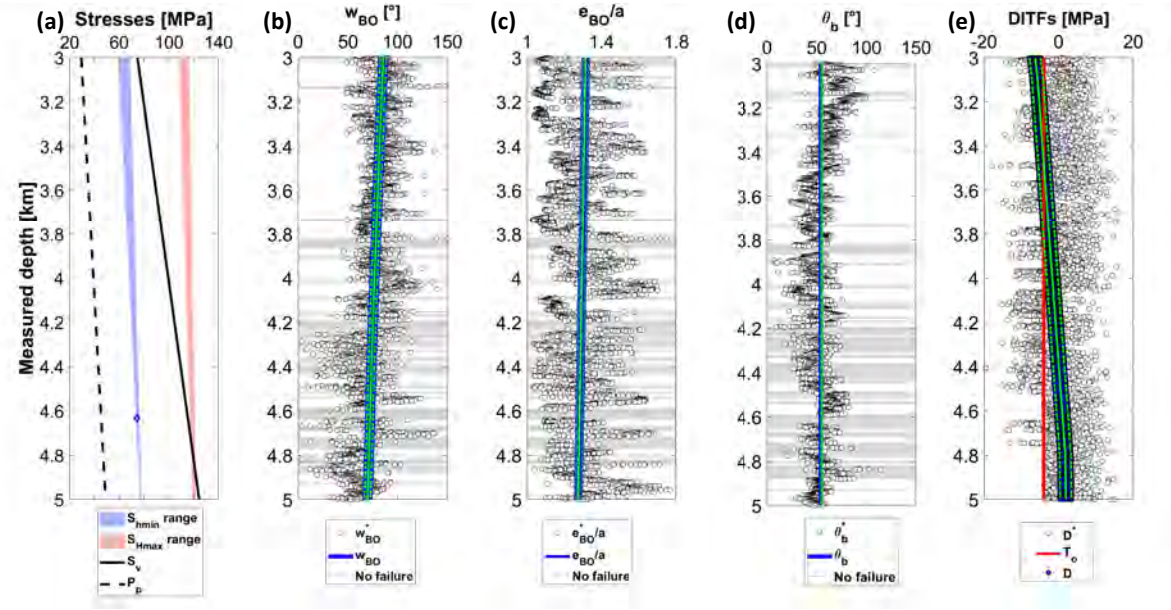


Figure 3.13.: 1st order calibration outputs in the presence of a new measurement of S_{hmin} considering the Mohr-Coulomb failure criterion. See the caption of Fig. 3.9 for further details.

3.5.2. 2nd order calibration

The 1st order calibration presented so far yields practical insights on the general trends of both stress and strength along the borehole. These trends are representative of the mean conditions along the borehole, but are not capturing the variation around the mean. In natural systems like rock masses, such variations can be locally large. It is important to quantify this variability for the design of completion schemes including packers because such variability can cause locally conditions that are much more severe than the average conditions and that can cause completion problems. To fill this gap, the 2nd order calibration is carried out using as starting parameterization and prior information the 1st order parameter values leading to the median profile of S_{Hmax} in Fig. 3.9. Only one calibration is presented here for the sake of brevity. For the reason stated in Section 3.5.1, only the Mohr-Coulomb failure criterion is used. Each parameter intervening in model equations is now parameterized with pilot points regularly spaced every 10 m. The pilot point discretization is common to all strength and stress parameter profiles, which leads to an overall parameterization involving 1407 pilot points. Ordinary kriging was used as spatial interpolation algorithm to render continuous profiles from values at pilot points.

The results in terms of goodness of fit and derived parameters are displayed in Figs. 3.15 and 3.16, respectively. The 2nd order calibrated outputs (Fig. 3.15) resemble not only the trends observed in measurements, but also the corresponding small scale variabilities. The goodness of fit is striking, the root mean square errors being 10°, 0.086, 9° and 4.6 MPa for

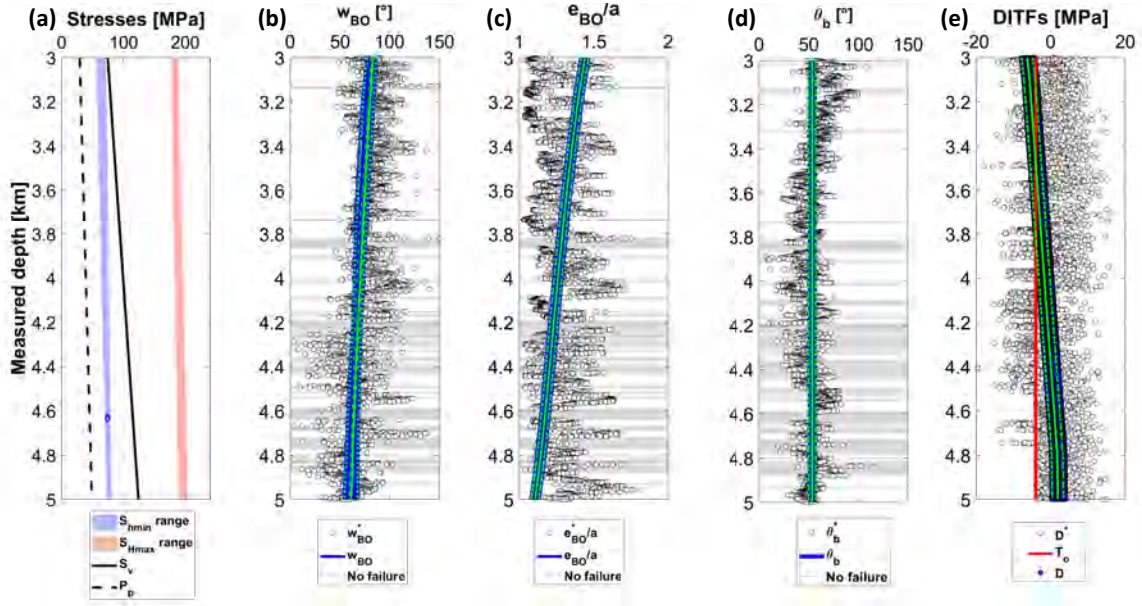


Figure 3.14.: 1st order calibration outputs in the presence of a new measurement of S_{hmin} considering the Mogi-Coulomb failure criterion. See the caption of Fig. 3.9 for further details.

breakout width, normalized extent, orientation and DITFs, respectively (the initial misfits corresponding to the 1st order calibration were 27°, 0.175, 25° and 11.5 MPa). The 2nd order calibrated outputs reproduce well most of the small gaps without breakouts (shaded blue areas in Fig. 3.15a) and most of the maxima/minima of normalized extent (Fig. 3.15b). The extreme values along measured profiles are not exactly captured because (1) the number of pilot points, which exerts major control on computation effort, is not enough for that purpose, and (2) capturing the variability at the smallest scale would lead to undesired large (although perhaps realistic) oscillations in the profiles of calibrated parameters in Fig. 3.16. The derived parameters stress/strength in Fig. 3.16 are all plausible. The stress profiles of S_{Hmax} and S_{hmin} reproduce well the transitional regime at ≈ 4800 m depth reported by Valley and Evans (2019). The profiles of strength parameters in panels b to d display values coherent with those in the literature (Valley and Evans, 2019). It is worth noting how the interplay between stress and strength is properly captured by the 2nd order model, i.e., there is a general negative correlation between the peaks of stress and strength at the gaps in the absence of breakouts (low stress/high strength or vice versa). The orientation of breakouts displays low departures ($\pm 5^\circ$) from the median value of 144°, as reported in Häring et al. (2008). Finally, Shens parameters defining our failure model are well within standard limits (Shen, 2008).

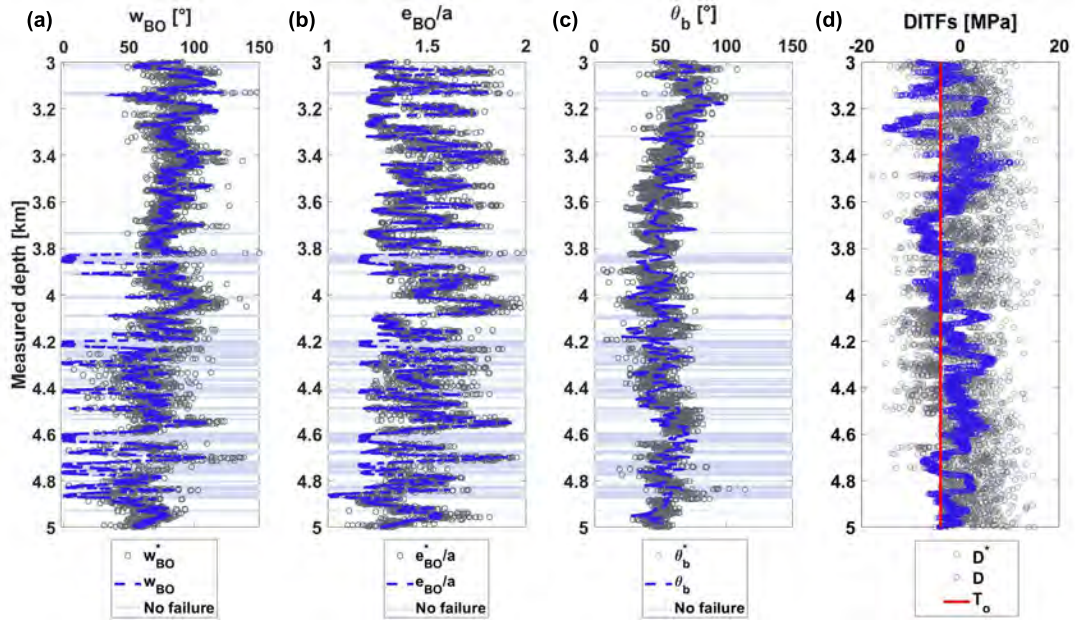


Figure 3.15.: Calibrated failure profiles using pilot points method from 3 to 5 km. (a) breakout width; (b) breakout extent; (c) breakout orientation; (d) Transformed and calibrated DITFs. In (a)-(c), the grey circles correspond to failure observations while in (e) they depict the estimated minimum hoop stress derived from DITFs observations. In (a)-(e), the dashed blue lines correspond to the calibrated failure using Mohr-Coulomb criterion. Light blue shaded areas in panels (a), (b) and (c) correspond to depths with no breakouts. The red line in panel (d) depicts the tensile strength, $T_o = -4$ MPa.

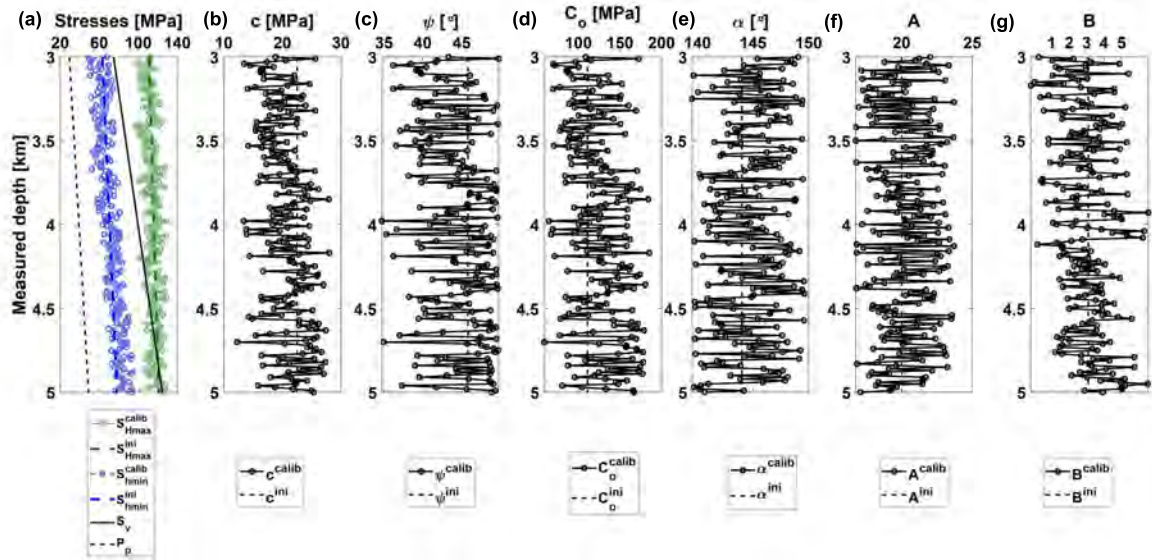


Figure 3.16.: Calibrated input parameters profiles using pilot points method from 3 to 5 km. (a) minimum and maximum principal horizontal stresses S_{Hmax} and S_{Hmin} ; (b) Cohesion; (c) internal friction angle; (d) uniaxial compressive strength; (e) the angle α of Euler and finally the regression parameters of Shen (f) A and (g) B . The dashed lines in all panels correspond to the initial depth profiles.

3.6. Discussions

3.6.1. Failure models evaluation

Our evaluation of failure models approach allows us to explore the validity of failure criteria and their ability to reproduce the borehole failure observations. In theory, models accounting for the strengthening effect of the intermediate principal stress – such as the Mogi-Coulomb criterion used in our study – capture more completely failure processes compared to models ignoring this effect (e.g. the Mohr-Coulomb criterion). However, our analyses show that calibration using the Mogi-Coulomb combined with an estimate of S_{hmin} magnitude from hydraulic tests leads to conceptually wrong stress profiles. Indeed, the obtained stress profiles (see Section 3.5.1.2) suggests a pure strike-slip stress regime ($S_{Hmax} > S_v$) while indications from focal mechanisms indicate a mix of strike-slip and normal faulting regimes ($S_{Hmax} \approx S_v$). Profiles obtained using the Mohr-Coulomb criterion are consistent with the stress regime observations, honoring the transitional regime at ca. 4800 m MD. These results are also in agreement with Valley and Evans (2019). Although this rationale is plausible, the kinematics of faulting represented by focal mechanisms is not always consistent with faulting mechanics represented by the stress state. Thus, choosing an "appropriate" failure criterion cannot be based solely on this observation.

When discussing the validity of the failure criterion, we shall recall that we used the Kirsch closed-form solution to compute stress because it is computationally attractive and is easy to implement. However, one must bear in mind its limitations. This analytical solution does not capture progressive failure and assumes that the initial breakout width remains constant once failure is initiated. Thus, this method tends to underestimate borehole failure parameters. Instead, the Mohr-Coulomb failure criterion tends to overestimate failure parameters because it neglects the strengthening effect of the intermediate stress effect. We assume that the Mohr-Coulomb criterion is performing well in our application because both conservative and non-conservative effects are compensating leading to stress and strength estimates that are consistent with independent stress observations, while combining the Mogi-Coulomb criterion with the analytical stress computation approach leads to an overestimation of the S_{Hmax} magnitude. Based on these results, we recommend to use the Mohr-Colomb criterion in combination with the simple analytical stress computation which is used as standard in practice. Note that the limitation of analytical solutions not being able to reproduce progressive failure impairs also the computation of breakout extension. To solve this issue, we combined the analytical stress computation with the empirical relationship proposed by Shen (2008). We extended this relationship for complex stress state where we took into account borehole trajectory, mud pressure and thermal stresses effect. When properly calibrated, this approach appears to be efficient at estimating breakout extension.

A path forward to develop the approach would be to make use of a more complex failure simulation, for example including continuum plasticity, continuum damage mechanics,

hybrid continuum-discontinuum models. However these approaches involve a large number of unknowns, they are computationally demanding and we anticipate that they would be difficult to implement in the massive calibration framework we propose here. The use of empirical relationship supported by numerical simulation – as we apply here using the approach proposed by Shen (2008) – is likely the most tractable and promising path forward to further develop our approach.

These limitations can be tackled by means of numerical models or more complex closed-form solutions. For instance, transient failure can be modelled by analytical solutions including continuum plasticity with non-associated flow rules and strain softening (Hajabdolmajid et al., 2002) or continuum damage mechanics (Sahara et al., 2017) or by hybrid continuum-discontinuum models (Shen et al., 2002; Alcolea et al., 2016; Marschall et al., 2017). Unfortunately, the aforementioned approaches are either hard to parameterize using standard data sets, involve a larger number of unknown parameter and are computationally intensive, which precludes parameter estimation (See Section 3.2.6).

3.6.2. Sensitivity analyses

Sensitivity analysis were carried out prior to parameter calibration. Sensitivity analyses are useful to identify parameters with a significant impact on model outputs, and to bracket parameter ranges, thus reducing prior uncertainties and computational effort. The sensitivity analysis can help in selecting the parameters used in calibration. One key outcome of the sensitivity analyses is that the main parameters that influence borehole failure are S_{Hmax} , S_{Hmin} , c , ψ , P_m in addition to Shen's parameters, A and B . We recognise that for practitioners, drilling mud density management is a primary tool to manage wellbore stability. However, mud weight is assumed to be constant in this paper ($\rho_m = 1.07g/cm^3$) and the consideration of mud pressure on borehole stability is beyond the scope of this study. The aforementioned parameters were calibrated using PEST in order to reproduce the BS-1 borehole failure data. However, sensitivity to parameters controlling thermal stresses (i.e., Young Modulus, E , the coefficient of linear expansion, β and the Poisson ratio, ν) was not studied. This is justified by the fact that the thermal stresses are small compared to the mechanical stress when considering borehole breakouts. Thermal stresses are however often necessary to consider for explaining DITFs. The estimation of the relevant cooling magnitude occurring during drilling is also subject to uncertainties. We used a value proposed by Valley and Evans (2019) to estimate thermal stresses and did not consider them as additional calibration parameters. The topic of the variability of thermo-elastic parameters on the wellbore failure could be further investigated.

3.6.3. Stresses trends with depth

Our 1st order model calibration provides insight into the depth trend of stress magnitudes. The outputs of the 1st order calibration are consistent with Valley and Evans (2019) but the probabilistic model calibration proposed here allows to investigate a much broader

possible solutions range and increases confidence in the stress characterization. A common feature of the calibrated S_{Hmax} and S_{hmin} profiles is the low gradient with depth. This explains why breakout width tends to decrease with depth in BS-1, although, solutions that reproduce equally the observations are non-unique. This problem was addressed by using regularization, information to bound and constrain input parameters as well as the available best estimate of S_{hmin} from hydraulic stimulation. The latter reduced significantly the solution uncertainty, which shows that it is very important to collect these data in order to constrain the posterior distribution of the calibrated parameters.

The geodynamic explanation of the observed low stress gradient remains uncertain. S_{hmin} also has a low gradient but this result is largely dependent on the assumed cooling profile for the formation of DITFs. Valley and Evans (2019) showed that considering a much lower cooling profile in the upper section of the well can increase the S_{hmin} gradient by to up to 12 MPa/km, but not more. Another possible explanation is that the stiffness contrast may affect the stress gradient. An alternate explanation hypothesized by Valley and Evans (2019) is that the observed reduction of horizontal stress gradient would require a tectonic strain gradient, with more intense straining at the cover basement interface and a reduction of the tectonic straining with depth.

In addition to the decrease in depth of breakouts width, we observe that they are continuous except for a large gap from 2747 m TVD to 2899 m TVD and some other minor gaps below (Fig. 3.2). These borehole segments coincide with those of strong intensity of natural fractures. We have been interested in studying this paradox. In order to get the stress and strength depth profiles in this fractured zone, we run a 1st order calibration from 2578 m MD to 4000 m MD. The studied depth interval were divided into 3 different zones: (1) from 2578 to 2758 m MD, (2) from 2758 to 2900 m MD and finally (3) from 2900 to 4000 m MD. In each zone, 7 parameters are calibrated (S_{Hmax} , S_{hmin} , α , c , ψ , A and B (Fig. 3.18) and the prior distribution of each parameter is randomly sampled assuming a uniform distribution, which renders overall 100 initial parameterizations that explore the global parameter space. Fig. 3.17 shows the calibrated stresses and failure depth profiles. We notice that stresses magnitudes in 'zone 2' are smaller than in 'zone 1' and 'zone 3' and more importantly, the conditions in 'zone 2' approaches isotropic stress conditions ($S_{hmin} \approx S_{Hmax} \approx S_v$). In unfractured zones (zone 1 and 3), S_{Hmax} varies between 102 and 113 MPa, S_{hmin} varies in the range [80.5-90.9 MPa] and S_v is approximately equal to 70 MPa. In the fractured zone (Zone 2), $S_{Hmax} \approx 88$ MPa, $S_{hmin} \approx 69$ MPa). The maximum stress difference thus decreases from 43 MPa (zone 1 and 3) to 18 MPa (zone 2). As we have almost no breakouts in zone 2, our calibration leads to a strength increase compared to the one in zones 1 and 3 (C_o varies between 115 and 119 MPa in zones 3 and 1 respectively, whereas it is around 137 MPa in zone 2). The fact that 'zone 2' is mainly affected by fractures and has almost no breakouts may be explained by a perturbed stress state in this zone, either as a remanence of pre-sedimentation exhumation and relaxation or in response to more recent tectonic loading. The fractured rock mass being softer,

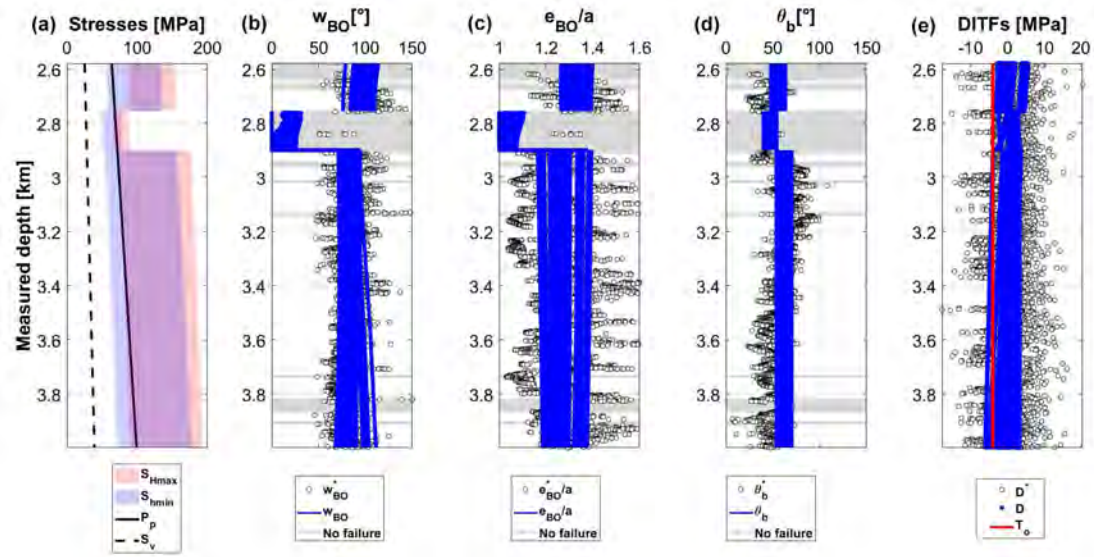


Figure 3.17.: 1st order calibration from 2578 m MD to 4000 m MD using the Mohr-Coulomb failure criterion performed for 100 different starting points. (a) the range of the calibrated S_{Hmax} (pink) and S_{Hmin} (purple), S_v is plotted in solid black line and the pore pressure in dashed black line; Observed (black circles) and calibrated (blue lines) (b) breakout width; (c) normalized breakout extent; (d) breakout orientation; (e) transformed and calibrated DITFs. Gray lines in (b), (c) and (d) correspond to depths with no breakouts. The red line in (e) depicts the tensile strength $T_o = -4$ MPa.

the stress level and differential stress may be lower which could explain the absence of breakouts.

3.6.4. Failure variability and implication for rock mass models

Wellbore failure variability is common and has been used to characterize stress heterogeneity (Shamir and Zoback, 1992; Valley and Evans, 2010; Afshari Moein et al., 2018; Valley and Evans, 2014b; Schoenball and Davatzes, 2017). Variations in breakout orientation gives a direct estimate of the stress orientation variability. However, an estimation of stress magnitude heterogeneity is more difficult to derive since it requires an independent estimate of strength. With our 2nd order calibration methodology, we can investigate the potential source of observed borehole breakouts variability and quantify in-situ the potential magnitude of stress and strength variability. Two end-members rock mass models can potentially explain the observed failure variability:

1. The failure variability arises primarily from the variability in stress orientation and magnitudes within a rock with relatively constant strength. A credible explanation for the stress variability is the stress perturbations associated with fracture slip. Studies of wellbore failure variation around fractures have been shown to be related to fracture slip (Shamir and Zoback, 1992; Valley, 2007).

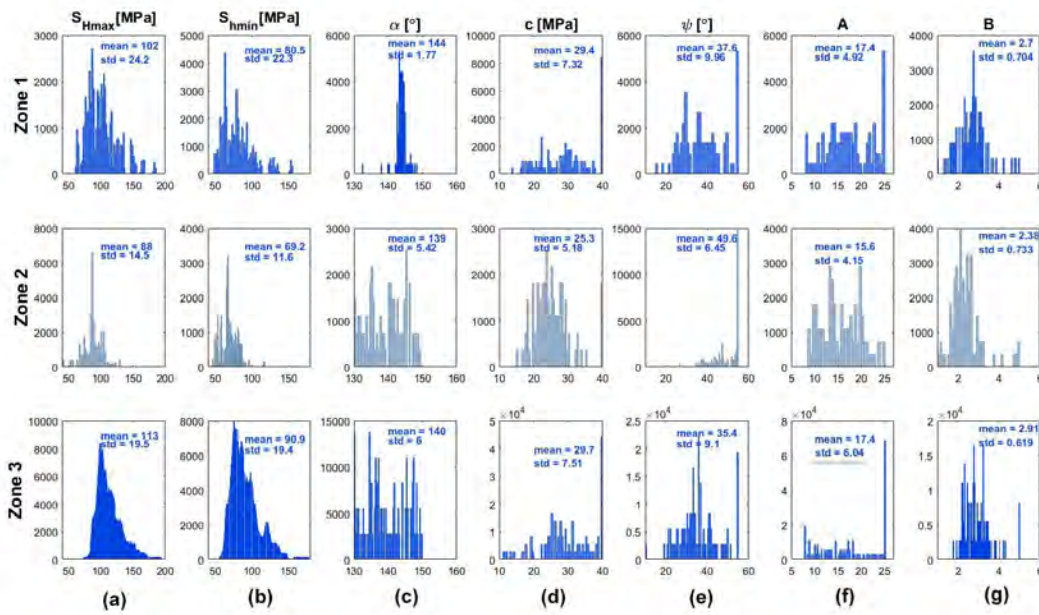


Figure 3.18.: Histograms of the calibrated parameters (plotted in columns) in each of the three considered zones (rows). (a) maximum horizontal principal stress, S_{Hmax} ; (b) minimum horizontal principal stress, S_{hmin} ; (c) Euler's angle, α ; (d) cohesion, c ; (e) internal friction angle, ψ ; (f) Shen's parameters, A and (g) B .

2. The failure variability arises primarily due to variability in rock strength. In crystalline basements, like in the BS-1 borehole, strength variability could be associated with alteration related to hydrothermal fluid circulations. Velocity profiles derived from sonic logging shows variability (Holliger, 1996) that could be related to strength and stiffness rock variability, although variation in stresses could also explain velocity variations.

These two rock mass models are not incompatible, and it is not unlikely that both stress and strength variations occurs concomitantly. We investigated these scenarios by performing 2nd order calibrations where only the stress parameters are calibrated while the strength parameters are assumed to be constant (Fig. 3.19) and here only strength parameters are calibrated and with no stress variability (Fig. 3.20). In both cases, the failure variability can be reproduced satisfyingly.

The histograms of Fig. 3.21 illustrate the variability distributions of stress and strength parameters for these two scenarios as well as for a case where both strength and stress parameters are calibrated concomitantly. The coefficient of variations (COV) for strength parameters are 20% and 13% for cohesion and friction, respectively. Such values are not surprising and correspond to the variability obtained from data compilation from testing programs on igneous rocks (Aladejare and Wang, 2017). A variability in stress of 7 to 8 MPa (1σ) is observed when strength parameters are assumed to be constant. Comparing these standard deviations with absolute stress magnitude in the range of 80 MPa for S_{hmin}

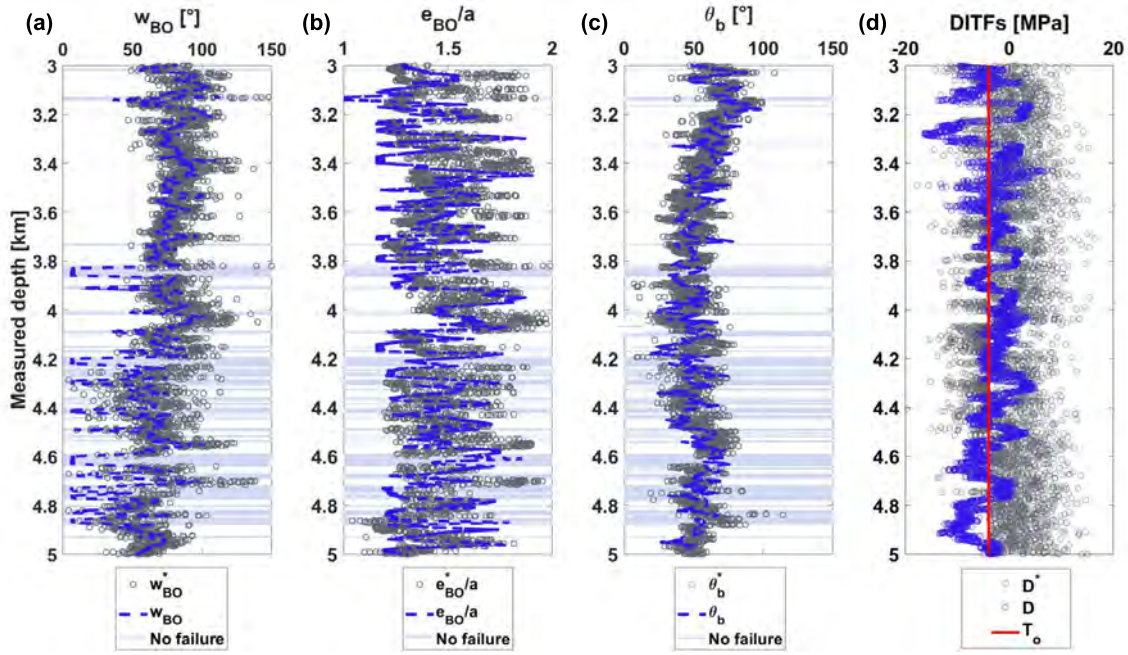


Figure 3.19.: Calibrated failure profiles for the first scenario where it is assumed that breakouts and DITFs variability comes from variability among stresses only. See the caption of Fig. 3.15 for further details.

and 105 MPa for S_{hmax} lead to a maximum COV for the stress parameters of about 10%. Such values can be easily explained by stress variability induced by fracture slip (e.g. Valley et al., 2014). Thus our observations and analyses are consistent with both the proposed source of failure variations (strength or stress heterogeneity) and it is likely that both sources act concomitantly at inducing failure parameters variability. However, it is important that considering only strength variability while assuming that stresses are linear trends in depth does not explain neither the variability of the breakout orientation nor the DITFs. Our analyses provide however a unique opportunity to quantify in-situ the magnitude of the stress and strength variability.

3.6.5. Limitations and applicability of the methodology

The novel methodology described above proved very efficient on the BS-1. Its mathematical formulation (see Section 3.2) is generic and applicable to any case study. However, as any new method, it suffers from some limitations. In this section, we summarize them and provide some ongoing footsteps to overcome them. One of the main novelties of our methodology is the inclusion of breakout extent in the calibration process. Breakout extent has been traditionally neglected because its computation is difficult. Theoretical considerations and experimental observations suggest that breakouts develop by progressive failure, i.e., incremental evolution of the borehole shape characterised by a fairly stable breakout width and an increasing extent (e.g., Zoback et al. (2003)). Solving progressive borehole failure requires complex numerical simulations including, e.g., viscoplastic con-

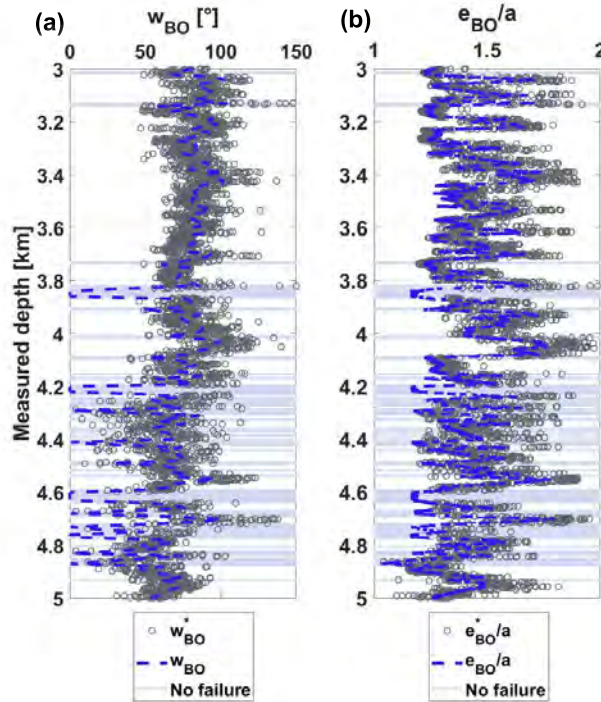


Figure 3.20.: Calibrated failure profiles for the second scenario where it is assumed that breakouts variability comes from variability among rock strength only. See the caption of Fig. 3.15 for further details.

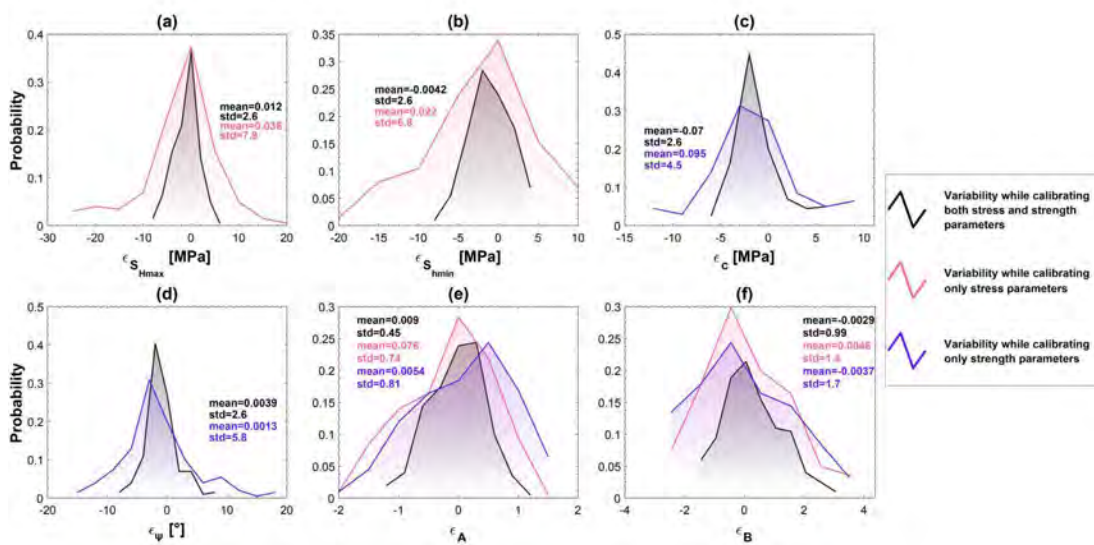


Figure 3.21.: Histograms of parameters variability, $\epsilon_{i,zi}$, for three different scenarios assuming that failure variability is due to (1) both stress and strength variability in depth (black shaded histograms), (2) stress variability only, (3) rock heterogeneity only. These shaded histograms show the probability on the y axis and the bins centers on the x axis of (a) S_{Hmax} ; (b) S_{Hmin} ; (c) cohesion, c ; (d) internal friction angle, ψ and finally Shen's parameters (e) A and (f) B .

stitutive laws, which are not tractable in a calibration process often demanding a large number of iterations. However, breakout extent is a very important parameter because it addresses the suitability of borehole segments for zonal isolation, i.e., for packer location.

To overcome this impasse, we use an empirical approach (see Section 3.2.4). Possible improvements involve more complex mathematical approaches, e.g., the semi-analytical approach proposed by Setiawan and Zimmerman (2020). Dealing with the absence of borehole breakouts is also difficult. The absence of breakouts indicates that failure conditions have not been met at the borehole wall, but do not provide insights on how far from failure is the stress-strength state. This often lead to difficulties in the calibration process, which tends to yield stress conditions at the borehole wall close to failure, even in the absence of breakouts. We did not encounter this problem in the case of the BS-1 dataset because breakouts are pervasive (81% of the borehole length) and sufficient information is available for constraining the calibrated solutions.

However, we envisage ill-posed inverse problems in case studies with limited occurrence of breakouts. A possibility to overcome this problem consists of adding a penalty criterion to the objective function (Eq. 4.2) that accounts for discontinuous or boolean variables (presence/absence of breakouts, i.e., failure or not). Unfortunately, boolean variables are not well-suited for constraining calibration and equivalent continuum criteria should be used instead. The same occurs with the evaluation of DITFs. In that case, we calculate the minimum hoop stresses leading to the presence/absence of DITFs. A similar criterion, taking into account stress and strength parameters can be used to account for the presence/absence of breakouts. The BS-1 borehole is essentially sub-vertical. In principle, the use of data out of deviated boreholes should not pose any additional difficulty. In fact, the combination of boreholes with different orientations should increase both quantitatively and qualitatively the calibration constraints and yield better solutions. In fact, the robustness and applicability of the suggested methodology is being tested at present.

The sensitivity to parameters controlling thermal stresses (i.e., the Young Modulus, the coefficient of linear expansion and the Poisson ratio) has not been analysed yet, which was justified by the relative low presence of DITFs in borehole BS-1. In this line of arguments, the impact of the heterogeneity of thermo-elastic parameters on wellbore failure should be further investigated. Finally, it is important to highlight that our approach is based on the inversion of principal stresses at the borehole wall. The concomitance of low internal well pressure (quasi hydrostatic) and the in-situ stresses in BS-1 favour the tangential stress as the maximum principal stress. However, this may not be the case in practice and particular breakout geometries may be generated (?) that are hard to cope with the suggested methodology. Similarly, stress-strength situations in which breakouts initiate with large width ($> 90^\circ$) often lead to total borehole collapse and the formation of washouts (Zoback et al., 2003). Such special situation would also lead to difficulties in applying our inversion approach.

3.7. Conclusions

In state-of-the-art wellbore failure analyses, stresses and strength properties are commonly estimated separately. Given the limitations of the traditionally used approaches, we proposed in this paper a new methodology to jointly evaluate the stress tensor components and orientations, and the rock strength properties (e.g. cohesion, friction) in a robust probabilistic framework. For this purpose, analytical and empirical solutions for estimating wellbore stresses and failure parameters were combined with the regularized pilot points method as implemented in the PEST software. We used measurements which are available during or shortly after drilling, i.e., breakout width, breakout extent and breakout orientation at different depths in addition to the presence/absence of DITFs (including both axial and en-echelon tensile fractures, A-DITFs and E-DITFs). In addition, measurements of estimated parameters can be easily included in a generic manner (e.g., S_{hmin} interpreted from XLOT, etc). Also, all stress components around the borehole, including the remnant thermal stresses arising from the cooling of the borehole wall were accounted for. For illustration purposes, the proposed methodology was applied to the extensive borehole data set along the 2.5 km crystalline section of the borehole BS-1, in Basel (Switzerland). Our failure analyses approach and its application to the data set from the BS-1 borehole allow us to improve our understanding of failure processes in boreholes, the relationship amongst failure parameters and to better understand the stress and strength conditions and their variability in the earth crust:

- Breakout width is commonly analyzed to estimate the in-situ stress state while breakout extension is considered to be ineffective for such purpose and thus largely neglected. In this paper, we investigated in more details borehole failure by using not only breakout width for stress and strength estimation but also breakout extent, breakout orientation and the presence or absence of DITFs. Using data from the deep geothermal well BS-1, shows that width and extent of failure are non-linearly related. This can be explained by considering the relationships between stress concentration at the borehole wall and material strength.
- Based on the observed relationships between width and extent of failure, we developed a new approach by extending Shen's empirical relationship (Shen, 2008) to cover wellbore conditions that include internal well pressure, pore pressure and thermo-elastic stress and apply it considering the Mohr-Coulomb and Mogi-Coulomb failure criteria. This approach provides an effective and computationally efficient way for analysing the extent of failure.
- The joint inversion of stress and strength parameters proposed in our approach lead to a non-unique solution for the strength and stress profiles. This problem was addressed by using singular value decomposition and regularization, information to bound input parameters and the available measure of S_{hmin} from hydraulic stimu-

lation. The latter reduced significantly the solutions uncertainty, which shows the importance of collecting such data.

- We show that in the framework of the simplified stress computation using an elastic solution around a cylindrical opening (Kirsch, 1898), the Mohr-Coulomb criterion provides the stress profiles the most consistent with independent observation.
- The obtained stress profiles present systematically low stress gradients which confirms the results of Valley and Evans (2019) obtained within a less systematic parameter estimation framework. The geodynamic explanation for such low stress gradients remains uncertain but could be attributed to non-uniform tectonic straining associated with decoupling at the basement-cover interface.
- The absence of breakouts along certain segments of BS-1 is consistently associated with increased natural fracturing. We analysed this situation with our parameter estimation approach and showed that the absence of failure requires a reduction of the differential stress with a stress state tending toward isotropic conditions. These stress conditions can be explained by stress relief and rock mass softening associated with fracturing. In the upper crystalline section of the borehole, near the basement-cover interface, such stress relief and fracturing could be associated with the near surface exhumation that took place in carboniferous and permian times.
- Our 2nd order analyses suggest that both strength and stress heterogeneity likely contribute concomitantly to the observed borehole failure variability. We provide a unique in-situ quantification of strength and stress parameters. The *COV* for frictional parameters is about 13% and 20% for cohesive strength parameters. The *COV* for stress magnitude variations is about 10%. However, the variability of the strength only while assuming that the stresses are linear functions of depth, is not sufficient to explain the variability in depth of both DITFs and breakout orientation.
- The wellbore failure analyses approach presented in this paper sets the base for quantitative wellbore failure prediction and risk analyses that are required for the design and deployment of innovative borehole completions enabling zonal isolation that are required for unlocking the potential of deep Engineered Geothermal Systems (EGS).

4. A computational stochastic methodology to predict failure severity in deep geothermal boreholes

This chapter is in preparation for submission to the 'International Journal of Rock Mechanics and Mining Sciences' as:

A. Dahrabou, B. Valley, P. Meier, P. Brunner, and A. Alcolea. A computational stochastic methodology to predict failure severity in deep geothermal boreholes, 2020.

Asmae Dahrabou performed the analysis and provided the structure of the main text. Benoît Valley and Andrés Alcolea contributed to the development of the methodology, the discussion of the results and the writing of the manuscript. Philip Brunner and Peter Meier gave general insights on the calibration part.

Abstract

Wellbore instability is a serious problem in well drilling that can lead to costly delays caused by stuck pipes and irregular cross-sectional geometries entangling well completion. The important developments made in the oil & gas industry, most often in the context of sedimentary rocks, are not readily applicable to geothermal projects because the failure mode is different, so is the quality and amount of available data. Most published studies are based on deterministic and decoupled estimations of the stress and strength parameters driving borehole stability, which is not appropriate for deep geothermal wells in which the amount of data is not sufficient to constrain such deterministic models with a sufficient level of confidence. In Chapter 3, we propose a novel and efficient methodology for the calibration of stress and strength parameters together. Once calibrated against available measurements, e.g. down a certain depth, the model can be used to generate stochastic simulations of the borehole geometry (breakout width, extent/penetration depth and orientation and the presence/absence of drilling induced tensile fractures) to be expected if the drilling progresses. The methodology includes a multiple-point statistical approach to yield a manifold of equally likely simulations, which allows us to cope with the inherent parametric uncertainties. The robustness of the proposed methodology is applied to the extensive borehole data set along the crystalline section of the borehole BS-1 in Basel (Switzerland). First, model parameters are calibrated with a data subset, down to 3.6 km depth. Next, simulations of the well down to 5 km are carried out. The methodology is proven to be accurate, fast and able to reproduce the observed variability of parameters, both in terms of ranges and patterns. The proposed methodology is a hopeful step forward in the path to minimizing risks derived from wellbore instability, as it may help drilling engineers and field planners to make right decisions during drilling operations.

4.1. Introduction

In recent years, the drilling of sophisticated and challenging well trajectories (i.e., multi-lateral, horizontal and highly deviated wells) has gained steam to enhance the productivity of oil and gas and geothermal fields. The main challenge that drilling engineers usually encounter is the choice of the optimal mud weight, borehole trajectory and completion scheme to guarantee borehole stability and facilitate further operations within the borehole. This is particularly important for Engineered Geothermal Systems (EGS), which are planned with zonal isolation with packers. Indeed, it can improve control during reservoir stimulation and optimize reservoir management. Borehole stability is a well-known issue in the oil and gas industry. Optimal drilling parameters are estimated by trial and error on many wells, developing an empirical and site specific know-how for selecting them. Instead, the conditions are radically different in deep geothermal industry. First, the geological conditions are very different and boreholes are drilled to deep crystalline rocks. Second, the failure mode is generally different (shear band in sedimentary rocks vs. spalling in crystalline rocks). Third, the heterogeneity of a crystalline reservoir is much affected by the presence of local features like fractures, shear zones, etc. Finally, the deep geothermal industry is still not mature and cannot rely on the experience gained from the drilling of many deep wells. In deep geothermal, only few wells are usually drilled in a site and the collected data cannot feed efficiently the empirical relationships required for optimizing drilling parameters.

Deep wells drilled to the crystalline basement are affected by borehole breakouts when the stress concentration at the borehole wall exceeds the rock strength. These features may cause low drilling performance and highly irregular borehole shapes that entangle, or even preclude, the proper installation of any kind of completion system. In fact, borehole instability compromises sometimes the economic success at early stages of EGSs and must therefore be comprehensively analysed. Borehole stability analyses rely strongly on the estimated stresses and strength parameters, which are usually highly uncertain. Deterministic analyses are doomed to fail to account properly for such uncertainties and a rigorous parameter estimation framework is required. A number of models have been developed to compute borehole failure in deviated wells. For instance, Al-Ajmi and Zimmerman (2006, 2009) developed a 3-D analytical model to study the behavior of the collapse pressure under different in-situ stress regimes and drilling trajectories. Russell et al. (2003) analyzed the stability of the Tullich field wells and concluded that boreholes drilled parallel to the maximum horizontal stress have minimum risk of instability. Last and McLean (1996) showed that highly deviated wells are more stable than vertical wells in an overthrust region by conventional stability analysis. Hassan et al. (1999) used logs and core data to evaluate the stability of boreholes with different deviations. Awal et al. (2001) found that the optimal wellbore trajectory can be either vertical, directional or horizontal depending on the in-situ stress regime.

The vast volume of literature on borehole stability analysis and optimal borehole tra-

jectory selection is mainly on deterministic analysis, specific to local conditions and fail at systematically integrate parameters uncertainties. In the first paper of this series, Dahrabou et al. (2022b) propose an efficient methodology to estimate wellbore failure parameter sets that reproduce the observations of cross-sectional borehole geometry. In this paper, we extend the methodology to failure prediction. The stress and strength model can be calibrated against measurements down to a certain depth, e.g., that of the kick-off point of a possible deviated trajectory, and stochastic forecasts of different boreholes trajectories (including diameter changes) can be carried out that account for (1) all available information, and (2) the inherent variability and uncertainty of model parameters. For illustration purposes, we apply the methodology to the prediction of the deepest part of the BS-1 well (Häring et al., 2008) in order to verify the applicability and robustness of the developed method. First, the parameters of the failure model described in Dahrabou et al. (2022b) are calibrated against data from the shallower part of the borehole in the crystalline rock (from 3 to 3.6 km depth). Second, a number of equally-likely stochastic simulations of the remaining 1.4 km, which include a severe change of diameter, is carried out. Finally, a comparison between predictions and actual observations along the deepest part of the well is established, which allows us to validate our methodology.

4.2. Methodology

The overall methodology presented in this paper consists of two main steps, i.e., calibration and prediction (Fig. 4.1). Calibration of stress and strength parameters of the proposed failure model is made against existing data, typically collected along the shallower section of the well (Dahrabou et al., 2022b). The calibrated failure model is then used to predict failure in the subsequent well sections. Note that the calibration can be updated at any stage of the drilling process as soon as additional data are available, which alleviates parametric uncertainties and improves predictions. The basic steps of the proposed methodology are described in greater detail in subsequent sections and itemized next:

1. Calibration of model parameters against observations along the shallower section of the well:
 - Step 1: jointly estimate the stress state and rock strength parameters by 1st order calibration (Dahrabou et al., 2022b). This fast calibration, involving a few parameters (those defining 1st order parameter linear trends), is carried out for N different starting points in order to span the entire parameter space and account for non-uniqueness of the solution.
 - Step 2: select a subset of M representative 1st calibrated models as starting points for the 2nd order calibration in order to evaluate local fluctuations around the previously computed 1st order trends. The 2nd order calibration is computationally intensive, which precludes using too many starting points.

- Step 3: perform 2nd order calibrations using the regularized pilot points method (RPPM, Alcolea et al., 2006), originally devised by De Marsily (1984), as implemented in the free parameter estimation software PEST (Doherty, 2015) using as starting points the 1st order trends selected in step 2.

2. Prediction of different borehole trajectories and geometries:

- Step 4: extrapolate linearly the calibrated parameter trends of the selected 1st order models (Steps 1 and 2) to a larger depth. This assumes that there is not a severe disruption of the lithological conditions precluding the extrapolation of the calibrated trends.
- Step 5: perform 1st order predictions using the extrapolated parameters and the failure model described in (Dahrabou et al., 2022b) in order to verify the consistency of the predictions. In this paper, we also carry out a verification analysis by comparing the predictions with available observations along the deepest section of the well, which allows us (1) to validate the methodology, and (2) to evaluate the accuracy of our predictions.
- Step 6: use the 2nd order calibrated models obtained in Step 3 as training data sets to generate synthetic variability for each parameter along the deepest section of the well using a Multiple-Point Statistics (MPS) technique. Several equally-likely realizations of parameter variability (and corresponding predictions) can be simulated for each 2nd order calibrated model.
- Step 7: use the ensemble of produced stochastic realizations to predict failure along the deepest part of the well, and analyze the consistency of the predictions.

4.2.1. 1st and 2nd order calibration in the shallower section of the well

Dahrabou et al. (2022b) proposed a systematic and rapid methodology to estimate depth profiles of the characteristics of the local stress tensor and strength parameters jointly. The methodology is summarized below for the sake of completeness. The 1st order characterization aims at estimating depth trends for each of the stress and strength parameters to be calibrated. 1st parameters are expressed in a generic manner as:

$$p = m \cdot TVD + n \quad (4.1)$$

where p is the parameter being calibrated, m and n are the slope and the offset of the parameter p , respectively, and TVD is the true vertical depth.

The calibration procedure using PEST starts from initial values (starting points) of the parameters to be calibrated and seeks a minimum (hopefully, but rarely, the minimum; see Dahrabou et al. (2022b) for the analysis of non-uniqueness) of an objective function F that measures the misfit between calculated and observed geometric features, arranged in the

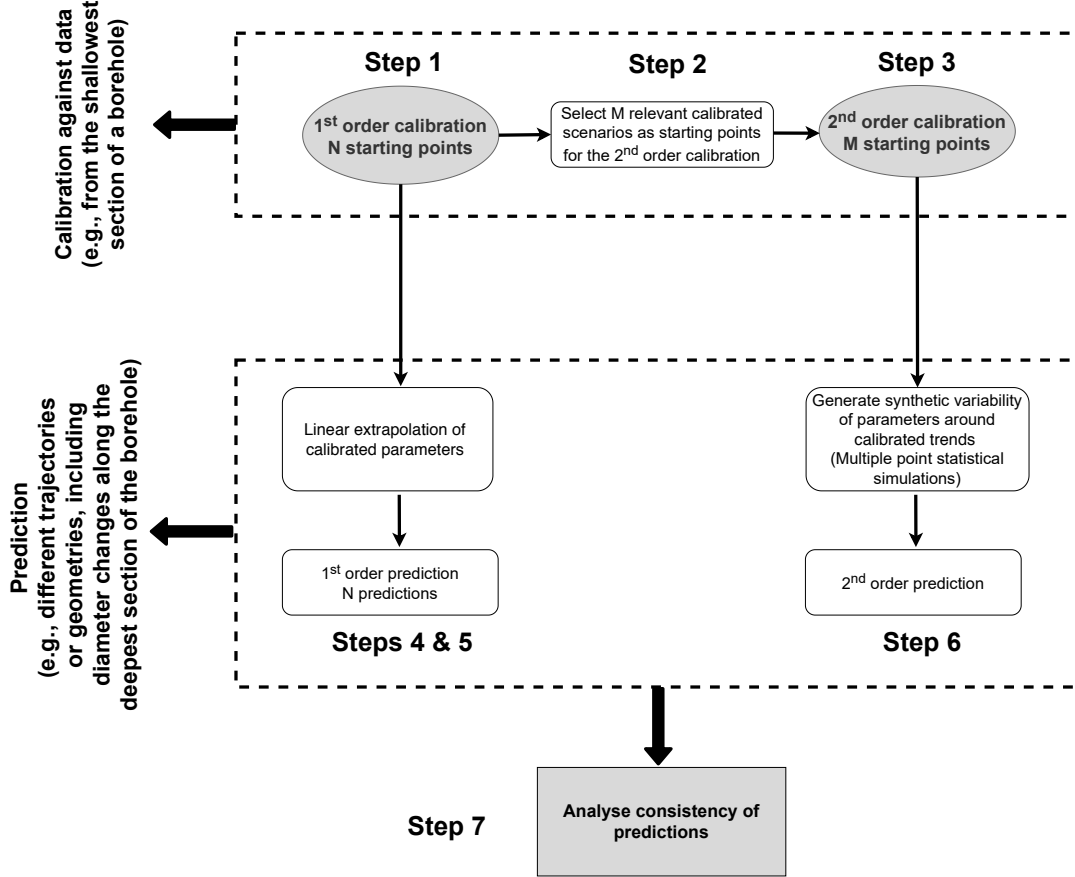


Figure 4.1.: Sketch of the prediction methodology.

vectors \mathcal{O} and \mathcal{O}^* , respectively, with components $\mathcal{O}_i^* = \{w_{BO}^*, e_{BO}^*, \theta_b^*, D^*\}$. $w_{BO}^*, e_{BO}^*, \theta_b^*$ and D^* represent failure observations, namely breakout width, breakout extent (often referred to as depth of failure), breakout orientation and the presence or absence of drilling-induced tensile fracture, DITFs. The set of parameters to be calibrated is arranged in vector \mathcal{M} . The objective function F can be expressed in a generic manner as:

$$F = \sum_{i=1}^4 \lambda_i (\mathcal{O}_i - \mathcal{O}_i^*)^t V_i^{-1} (\mathcal{O}_i - \mathcal{O}_i^*) + \sum_{j=1}^{npar} \beta_j (\mathcal{M}_j - \mathcal{M}_j^*)^t V_j^{-1} (\mathcal{M}_j - \mathcal{M}_j^*) \quad (4.2)$$

where subscripts i and j stand for type of measurement ($i = 1$ for w_{BO}^* , $i = 2$ for e_{BO}^* , etc.) and parameter respectively, up to $npar$ ($j = 1$ for parameters characterizing S_{Hmax} , $j = 2$ for those of S_{Hmin} , etc.). Matrices V_i and V_j are the corresponding prior covariance matrices representing an initial best guess of the correlation structure between measurements and measurements or measurements and parameters. The scalars λ_i and β_j are calibration weights that balance the relative contribution of each measurement type to the bulk objective function value. The 1st order calibration is performed for N different starting points in order to span the parameters space.

At the end of the calibration process (in this work, using data along the shallower section of the well from 3 to 3.6 km), a rejection criterion is applied (Dahrabou et al., 2022b) to retain calibrated models whose objective function is smaller than a given threshold (i.e., properly calibrated models only). This step removes models that either (1) did not converge to a minimum, or (2) converged to local minima, and alleviates the computational effort required in the second order calibration. We retain as starting points for the 2nd order calibration the calibrated models closest to the median, the 0.05 and the 0.95 quantiles. This insures spanning most of the parameter space while excluding extreme outliers. The 2nd order calibration aims at estimating the deviations of a given parameter from its calibrated mean. As such, the methodology allows to evaluate heterogeneity at any given scale supported by the underlying discretization. The Regularized Pilot Points Method (Alcolea et al., 2006), as implemented in PEST (Doherty, 2015), was used to that end. The generic parameterization now becomes:

$$p = m \cdot TVD + n + \epsilon(MD) \quad (4.3)$$

where ϵ is the perturbation around the mean and is a function of measured depth (MD).

4.2.2. Forecasting borehole failure in the deepest section of the well

Predictions are carried out using the outcomes of both 1st and 2nd order models. In the first case, the linear trends identified along the shallowest section of the borehole are linearly extrapolated to greater depths. Failure is then computed along the deepest section of the borehole using the failure model of (Dahrabou et al., 2022b).

The 2nd order calibration-prediction deals with the quantification of variability of the calibrated parameters and predicted variables around the estimated trends. Local scale variability has been shown to be typically large (Valley, 2007) in crystalline rocks and must be accounted for in meaningful predictions. The depth profiles of the 2nd order calibrated parameters exhibit patterns such as individual oscillations around the mean or sequences of oscillations of a given kind (e.g., positive-positive, negative-negative or positive to negative). Such patterns, which are expected to be found at further depth and in any given random order, are used as training data sets feeding a machine-learning multiple-point stochastic technique (MPS), the Direct Sampling algorithm (Mariethoz et al., 2010), as implemented in DeeSse (Straubhaar, 2019; Straubhaar et al., 2020). DeeSse can simulate multiple variables together similarly to the univariate case, provided that different training data sets (TDSs), one per variable, are available. As such, the coupled character of the relationships between stress and strength parameters and the non-linearity of the problem is maintained because all variables are simulated together. For example, the absence of breakouts may be associated to the co-existence of low stress and high strength, which are considered by DeeSse together. It also represents physically realistic spatial dependencies between variables (i.e., maximum and minimum horizontal principal stresses, S_{Hmax} and S_{Hmin} , respectively, Euler's angle, α , cohesion, c , internal friction

angle, ψ and finally Shen's parameters, A and B , (Shen, 2008)). The aforementioned correlations and joint simulations will be investigated below.

4.3. Application to the BS-1 well

4.3.1. Failure prediction based on the 1st order calibration

We use the extensive borehole data set along the 2.5 km crystalline section of the borehole BS-1, in Basel (Switzerland). Prior sensitivity analyses (Dahrabou et al. (2022b) and Chapter 3) revealed the most sensitive parameters, i.e., maximum and minimum horizontal principal stresses, S_{Hmax} , S_{Hmin} , respectively, mud pressure, P_m , cohesion, c , internal friction angle, ψ and the regression parameters, A and B (Shen, 2008). The mud weight was set to the actual value measured at the BS-1 borehole ($\rho_m \approx 1.07\text{g/cm}^3$). The remaining parameters were calibrated using PEST (Doherty, 2015) against data along the vertical shallower section from 3 to 3.6 km. The calibration was performed for $N=100$ starting points, which are combinations of model parameters \mathcal{M} randomly drawn from independent uniform distributions (see Dahrabou et al. (2022b) for further details). Constraints, e.g., based on frictional equilibrium were also imposed on the starting points. Only Mohr-Coulomb failure criterion was used in this analysis because it provided the most consistent calibrated sets of parameters (Dahrabou et al., 2022b). After the initial rejection process, $M=96$ well calibrated models were selected based on their objective function. These models are displayed in Fig. 4.2 along the calibration section (3-3.6 km) and extrapolated to the deepest part of the borehole (the prediction section, down to 5 km). Extrapolation is justified in the case of the BS-1 borehole, where the cuttings along the entire crystalline section of the borehole are relatively homogeneous and there is not a large tectonic disruptive feature identified in borehole images. The computed failure indicators are presented in Fig. 4.2.b-e along with the actual measurements.

The calibrated stress profiles of S_{Hmin} and S_{Hmax} span over a fairly wide range of stresses (Fig. 4.2a). However, the predictions, in terms of geometric features (panels b to e) are rather homogeneous and coherent with the mean profile of the available observations along the borehole. This validates the accuracy and reliability of the proposed methodology. However, the 1st order calibration approach does not account for the variations around the mean of the calibrated parameters (and correspondingly, of the calculated geometric features). In order to account for the variability, 2nd order calibration were carried out and is presented next.

4.3.2. Failure predictions based on the 2nd order calibration

4.3.2.1. 2nd order calibration results

Out of the $M=96$ calibrated and filtered 1st order models, three were selected corresponding to (actually those closest to) the median and 0.05 and 0.95 quantiles of the calibrated profiles of S_{Hmin} and S_{Hmax} . This minimizes the computational effort but still

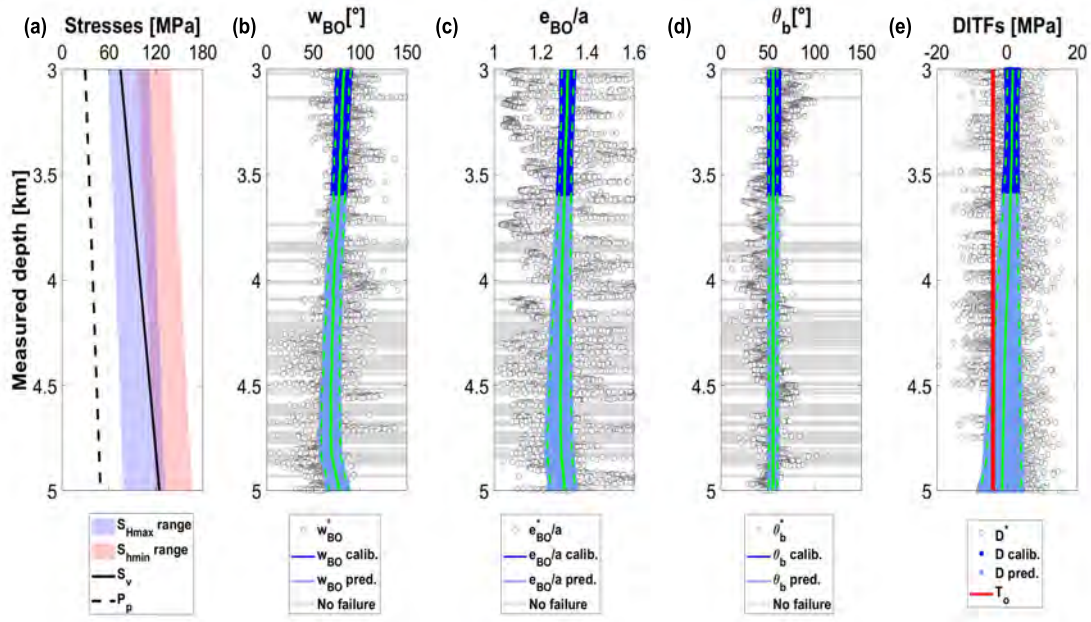


Figure 4.2.: Outputs of the 1st order calibration and corresponding predictions: (a) ranges of the calibrated profiles of S_{Hmax} (pink) and S_{hmin} (purple) from 3 to 3.6 km. These profiles were linearly extrapolated to a depth of 5 km to compute predicted failure all along the borehole. The solid and dashed black lines depict S_v and the pore pressure profiles, respectively; (b) to (e) computed failure indicators (dark and light blue lines along the calibration and prediction sections, respectively, and geometric features along with the observations (black circles). Note that only the measurements in the shallower section were used for calibration. The failure indicators are (b) breakout width; (c) breakout extent, i.e., depth of penetration, normalized by the nominal borehole radius; (d) breakout orientation and (e) DITFs. Gray lines in (b), (c) and (d) correspond to depths without breakouts. The red line in (e) depicts the tensile strength $T_o = -4$ MPa. Finally, the solid and dashed green lines in panels (b) to (e) correspond to the median and the 0.05 and 0.95 quantiles of the computed failure parameters based on our 96 calibrated models.

spans the range of uncertainty of the calibrated parameters. These models were used as starting points for the 2nd order calibration. The corresponding 1st order parameters for each model are summarized in Table 4.1. Model parameters, ϵ_{j,z_i} , are now the perturbation from the 1st calibrated trend (j represents either [S_{Hmax} , S_{hmin} , α , c , ψ , A and B]) at each pilot point at a given depth z_i . Pilot points were located at regular intervals (5 m) along the upper section (3-3.6 km).

Table 4.1.: Parameter values corresponding to the three chosen 1st order calibrated models, i.e., the starting points for the 2nd order calibration.

	0.05 quantile	Mean	0.95 quantile
$a_{S_{Hmax}}$ [MPa/km]	5.6	4.2	6.3
$b_{S_{Hmax}}$ [MPa]	74	97	131.2
$a_{S_{hmin}}$ [MPa/km]	5.3	7.5	6.8
$b_{S_{hmin}}$ [MPa]	19	51.5	79
α [°]	143	146	145
c [MPa]	13.5	21.8	28.1
ψ [°]	34.3	42.5	50
A [-]	19.9	20.3	21
B [-]	2.8	3.3	3.8

Fig. 4.3 shows the depth profiles of the calibrated breakout width, extent, orientation and DITFs along with borehole failure observations for the three considered models. The calibrated 2nd order profiles of geometric features reproduce the variability of observations with high accuracy regardless of the chosen model and corresponding initial parameterization (i.e., the 1st order calibrated model). The calibrated depth profiles of parameters are shown in Fig. 4.4. Two observations become apparent from Figs.4.2 and 4.3. First, a large range of calibrated parameters leads to similar calculated outputs, which brings out the problem of non-uniqueness illustrated in (Dahrabou et al., 2022b) and Chapter 3. Second, parameter correlations can be identified graphically (e.g., cohesion and internal friction angle). However, Shen's parameters A and B or, overall, stress and strength parameters, are anticorrelated. Correlations and anticorrelations between calibrated parameters are best observed by examining the posterior correlation matrix between the profiles of calibrated parameters and those of model outputs (Fig.4.5a; we focus here on w_{BO} and e_{BO} only, but similar conclusions can be established using other geometric descriptors). As expected, calibrated stress and strength parameters are anti-correlated. For example, for reproducing the presence of a breakout, the model must react either by reducing, or by increasing stress, or both (most likely). This desired effect is only possible if all parameters are estimated simultaneously, as in the proposed methodology. It is worthwhile noting that S_{Hmax} and S_{hmin} are not correlated and that strength parameters are positively correlated (surprisingly almost one to one), which reflects the fact that the calibration method reacts by increasing/decreasing both parameters at the same time. Finally, the correlation between calculated and observed geometric features is very high, which also reveals the goodness of fit attained by the model. The parameter correlations and anticor-

relations observed along the calibrated section must also be captured in the predictions. Otherwise, predictions will be generally incorrect because the variability estimates will be biased. This is achieved by using the calibrated parameter profiles as training data sets for the 2nd order prediction using DeeSse, presented next.

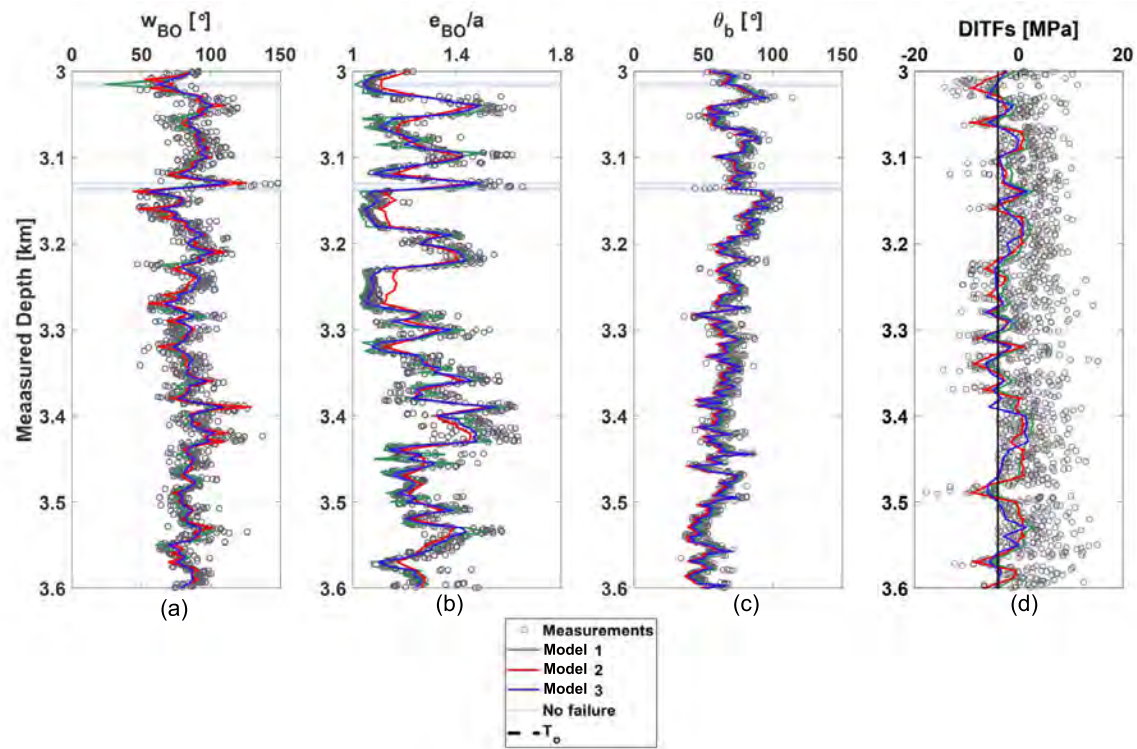


Figure 4.3.: 2nd order calibrated failure profiles against data from 3 to 3.6 km: (a) breakout width; (b) normalized breakout extent; (c) breakout orientation; (d) DITFs. The grey circles correspond to failure observations while the solid green, red and blue lines correspond to the calibrated failure for the analyzed models. The solid black line in panel (d) depicts the tensile strength, $T_o = -4$ MPa. Models 1, 2 and 3 correspond to 0.05 quantile, mean and 0.95 quantile models, respectively.

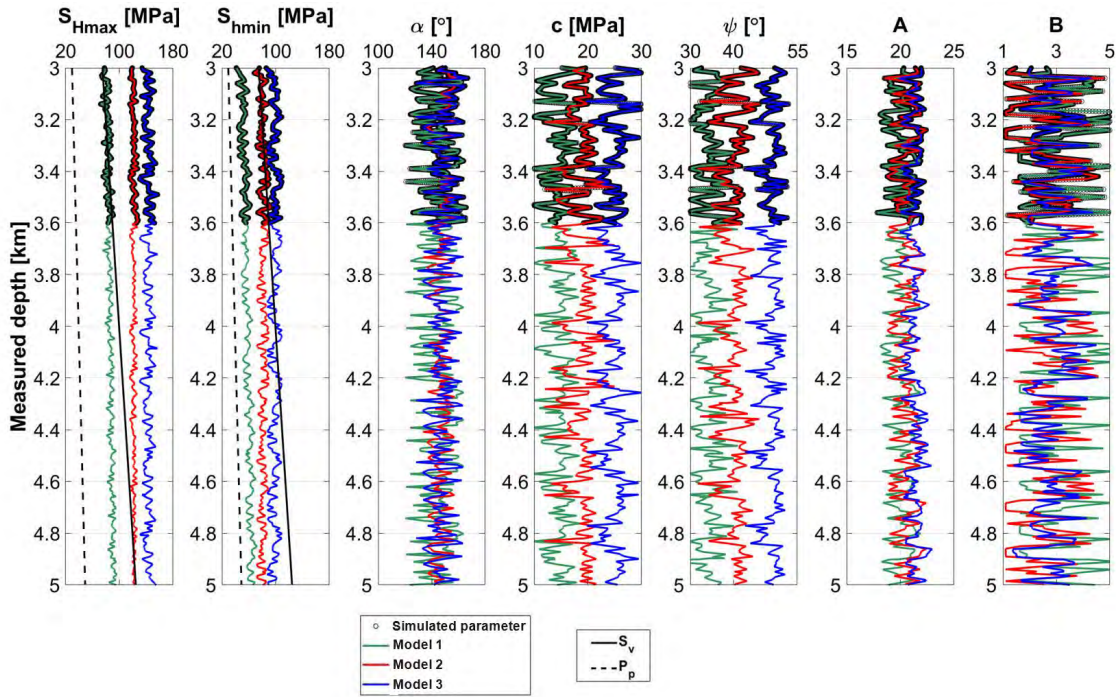


Figure 4.4.: 2nd order calibrated parameter profiles along the section 3 to 3.6 km: (a) S_{Hmax} ; (b) S_{hmin} ; (c) Euler's angle, α ; (d) cohesion, c ; (e) internal friction angle, ψ and the regression constants (f) A and (g) B . The dashed and solid black lines in panels (a) and (b) depict pore pressure, P_p , and vertical principal stress, S_v , respectively. The green, red and blue depth profiles in all the panels refer to models 1, 2 and 3 (0.05 quantile, mean and 0.95 quantile), respectively.

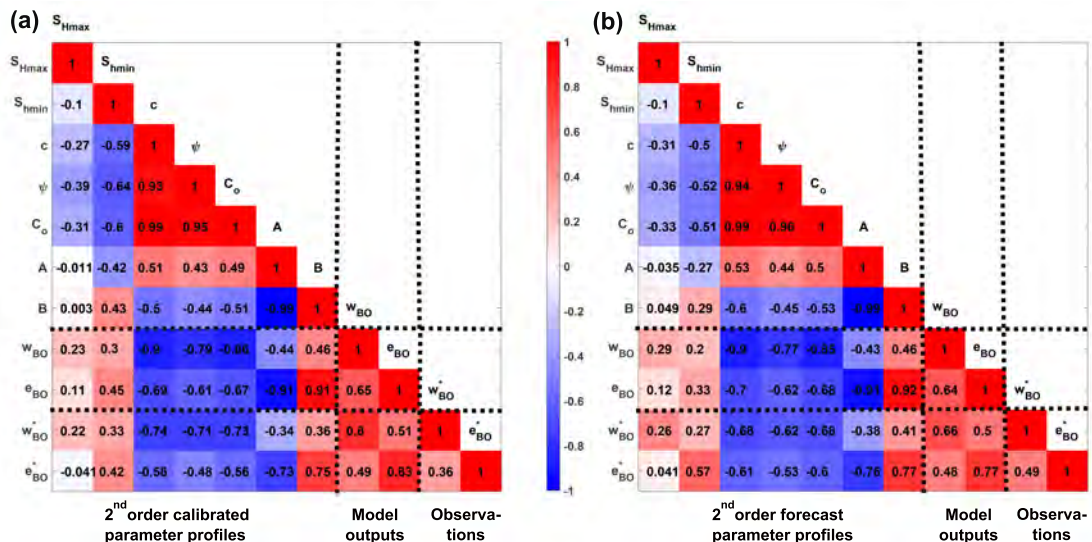


Figure 4.5.: Correlation matrix between (a) 2nd order calibrated parameter profiles (section 3-3.6 km), calculated outputs and corresponding observations; (b) 2nd order prediction (section 3.6-5 km). Results correspond to model 2, closest to the median of S_{Hmax} .

4.3.2.2. Parameters forecast and borehole failure prediction

The three 2nd order calibrated profiles are used as TDSs in DeeSse (Section 4.2.2 and Straubhaar, 2019) for generating the synthetic variability of all model parameters along the 3.6 to 5 km prediction section. As such, the existing correlations and anticorrelations are inherited by the simulated parameter profiles. 1000 equally-likely realizations of the expected variability were generated for each considered model (Fig. 4.4 shows one realization of the generated synthetic profiles for all input parameters) and borehole failure was calculated. The correlation matrix was calculated again (but at the prediction section 3.6-5 km) to (1) discard possible biases in the forecast, and (2) to verify that the correlations and anticorrelations between parameters and outputs were satisfactorily reproduced.

The predicted depth profiles are shown in Fig. 4.6. These compare well to actual measurements not used along the calibration process. As expected, the predicted profiles exhibit the spatial patterns observed along the calibration section (including the gaps in the absence of borehole breakouts), an exception being the DITFs. This negative finding can be easily explained by observing the DITFs pattern inherited by the simulations (Fig. 4.3d). Along the calibration section, the calculated DITFs are mostly above the tensile strength, and negative deviations (i.e., calculated values smaller than the tensile strength) are scarce. Instead, several such negative deviations are found in the observed profile along the prediction section, e.g., at depths between 4 and 4.5 km. Since the pattern indicating such deviations is scarce in the TDS, it is hardly possible that the simulations reproduce it, an exception being the deepest section (4.6-5 km in Fig. 4.6d), where such pattern is inherited by the presented simulations.

Fig. 4.7 shows the cumulative distribution functions (CDFs) of the predicted borehole failure indicators from 3.6 to 5 km compared to the CDF of the corresponding observations. Regardless of the chosen initial parameterization, the observed failure indicators are consistent with our predictions, an exception being the DITFs for the reason stated above. Notably, the predictions also capture approximately the proportion of the borehole length without breakouts (i.e., the initial kinks in panels a and b). These results offer compelling evidence for the accuracy and the robustness of the developed prediction methodology.

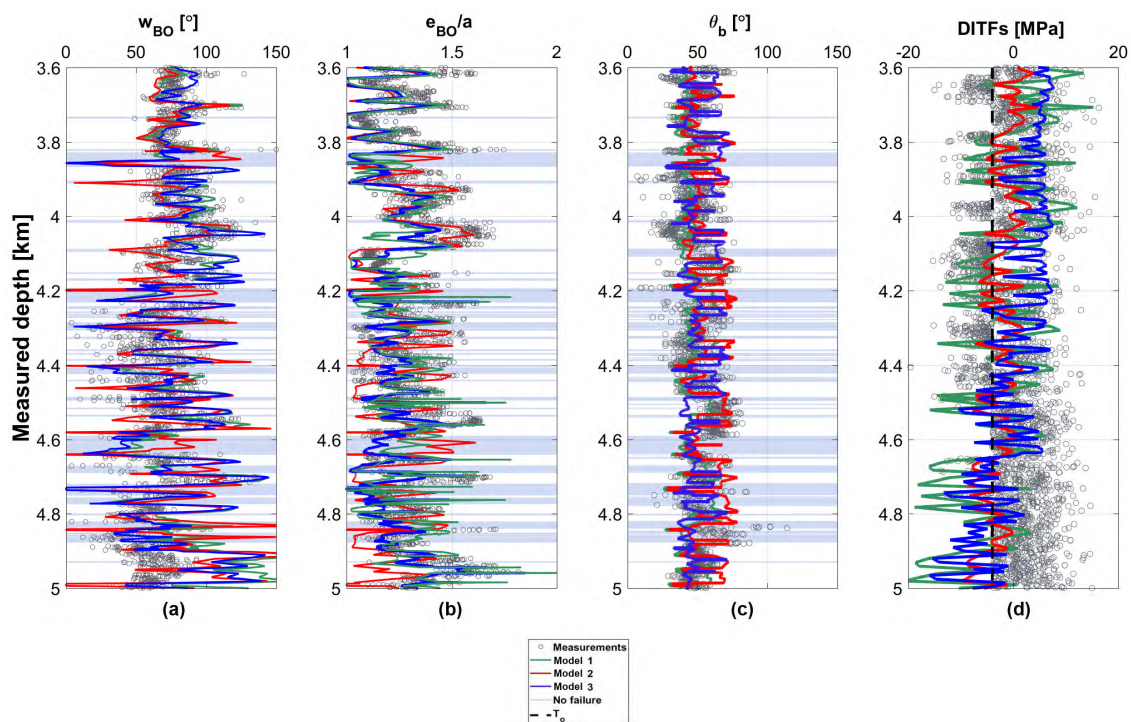


Figure 4.6.: Predicted depth profiles of failure indicators: (a) breakout width; (b) breakout extent; (c) breakout orientation; (d) DITFs. The grey circles depict observations, whereas the light blue horizontal lines correspond to depths where there is no failure. The dashed black line in panel d depicts the tensile strength. Models 1, 2 and 3 correspond to 0.05 quantile, mean and 0.95 quantile models, respectively.

4.4. Discussion

4.4.1. Forecasting calibrated parameters and accounting for variability

The first step required for prediction is to take the calibrated parameters from the calibration section of the borehole and to forecast their value along the borehole trajectory for which prediction is required. The suggested methodology relies on two main assumptions inherent to any extrapolation approach, namely (1) the parameter linear trends (1st order) can be linearly extrapolated to the prediction section, and (2) the patterns contained in the calibrated 2nd order parameter (the training data set, TDS) are representative for the prediction section. This implies that the 2nd order patterns are isotropic, i.e., independent of the borehole direction. As discussed above, the first assumption, i.e., on linear trends, is plausible if no singular disruptive features (lithological changes, large fault zones, etc.) are expected. With regards to the quality of the TDS, the training section in our application is relatively short and contains a limited number of patterns. As a result, the DS algorithm produces sometimes pattern repetitions observable along the prediction section in Fig. 4.4.

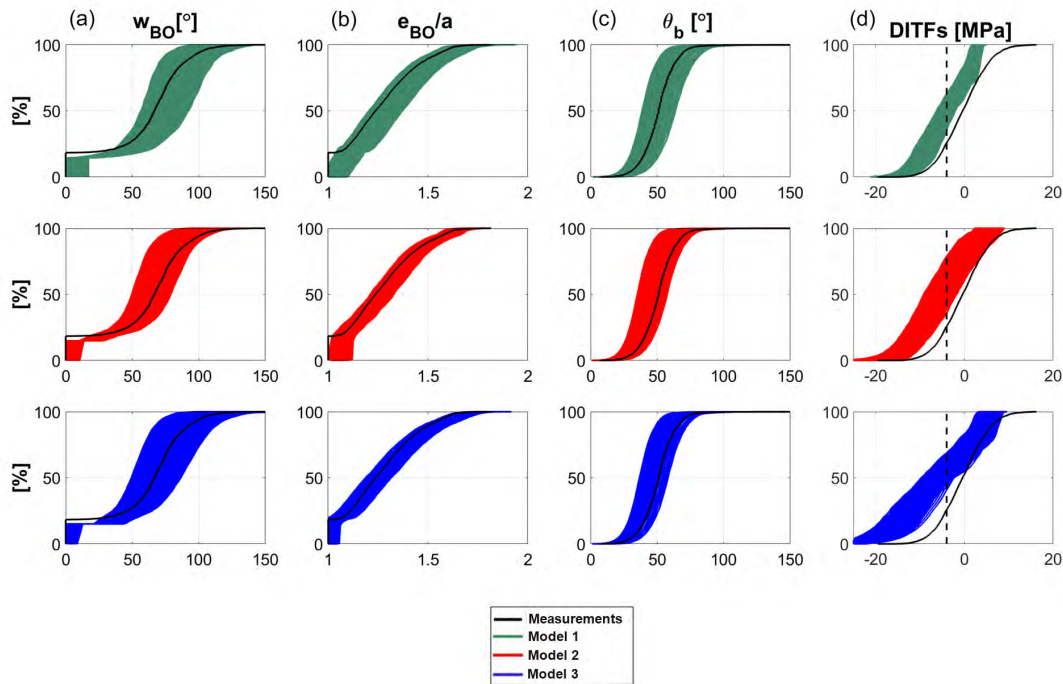


Figure 4.7.: Cumulative distribution functions (CDFs) of predicted (a) breakout width; (b) breakout extent, normalized by borehole radius; (c) breakout orientation and (d) DITFs. 1000 realizations were run for each model using DeeSse. The dashed black line in panel (d) depicts the tensile strength, $T_o = -4$ MPa.

This is a well-known artefact, termed "patching" in the MPS jargon. However, this visually inelegant effect does not affect the statistical properties of the extrapolation and thus does not impact on the usefulness of the prediction to answer questions of practical

interest like how stable will be the borehole ? or what is the chance to exceed a certain failure severity threshold ?. However, due to the stochastic nature of the considered processes, the prediction of the exact position of the failure zones or the exact characteristics of borehole breakouts along the prediction section is simply not possible. In the section directly subsequent to the calibration section, spatial correlation accounted for in the DS-MPS approach leads to consistent prediction for all stochastic realisations (Fig. 4.6), but with increasing distance to the calibration section, the stochastic simulations start to differ in accordance with a finite correlation distance. Beyond the correlation distance, we are not able to capture the failure characteristics in a deterministic manner, but we can assess the statistical characteristics of failure.

4.4.2. Quality of the prediction

The results offer compelling evidence for the robustness and accuracy of both 1st and 2nd order suggested prediction methodology. Indeed, the 1st order predictions capture properly the observations trend. However, they do not capture well borehole sections where breakouts are absent. As breakouts gaps are observed along about 20% of the BS-1 borehole, variability was involved in the 2nd order prediction. The latter converge to a narrow range despite the fact that the calibration leads to a multitude of different solutions (non-uniqueness of the inverse problem) and, notably, capture approximately the proportion of the borehole length without breakouts (Fig. 4.7). The distributions obtained from 1000 stochastic realisations are generally coherent with the observations. Being able to predict the variability distribution of failure indicators open the possibility to assess the probability of exceeding a given failure threshold which is a required information for quantitative risk assessment and thus supports decision making for borehole design and completion.

4.5. Conclusions

This work presents a systematic stochastic methodology to predict borehole failure. To that end, calibration is performed as a prior step to prediction. The calibration methodology is fully described in Dahrabou et al. (2022b). The prediction methodology is applied to failure observations along the crystalline section of the BS-1 borehole in Basel (Switzerland). The calibration of model parameters was carried out against observations along the shallowest section of the borehole (3-3.6 km), whereas predictions were performed along the deepest section (3.6-5 km). The outcomes of the prediction were then compared to actual observations. The main findings of the application are:

- The developed stochastic methodology is robust and accounts for parameter variability, which is a requirement for a meaningful forecasting of the expected range of borehole failure.

- Predictions are accurate despite the wide range of tested model parameters, and reproduce properly the observed trends. In addition, and despite of the inherent parametric uncertainties of any calibrated model, predictions converge to a narrow range of predicted profiles of borehole failure indicators.
- The simulated profiles inherit the correlations and anticorrelations between parameters (and observations) observed after calibration.
- In our application, the calibrated and predicted parametric correlations and anticorrelations along the BS-1 borehole support a crustal model in which the stress variability is largely controlled by slip on natural fractures and not by rock stiffness contrast, as proposed by Valley (2007).

So far, the prediction methodology has been tested on a sub-vertical well. Thus, our work may have undetected limitations especially when deviated boreholes are considered. As a consequence, further work needs to be carried out to identify the main factors affecting the goodness of our methodology.

5. Application of the calibration and prediction approaches to synthetic cases

This chapter is in preparation for publication as:

A. Dahrabou, B. Valley, P. Brunner, and A. Alcolea. Application of the calibration and prediction approaches to synthetic cases, 2022.

Asmae Dahrabou performed the analysis and provided the structure of the main text. Benoît Valley and Andrés Alcolea contributed to the development of the methodology, the discussion of the results and the writing of the manuscript. Philip Brunner and Peter Meier gave general insights on the calibration part.

5.1. Introduction

Wellbore instability is problematic on many levels as it may lead to costly delays caused by blowouts, stuck pipes and irregular cross-sectional geometries entangling well completion. Thus, maintaining a stable wellbore is an important requirement for both oil and gas and geothermal drilling. It has been widely recognized that highly deviated, extended-reach and horizontal wells can offer economic benefits through lower field development costs, higher production rates, and larger recovery factors (Fritz et al., 1991). However, drilling these sophisticated and challenging well trajectories may be prone to mechanical instability problems. Hence, a systematic understanding of the pros and cons offered by current and emerging inclined well drilling technology should be investigated. The most stable trajectory depends largely on the stress regime and the stress anisotropy. Thus, knowing the in-situ stress state is essential for designing the most stable inclined well trajectory. Acknowledging that gravity has a first order effect on the stress state — and thus one principal stress is assumed to be vertical — Anderson (1905) classified three types of earth's in-situ stress regime based on the relative principal stress magnitude: (1) extensional or normal faulting regime ($S_v > S_{Hmax} > S_{hmin}$), (2) strike-slip ($S_{Hmax} > S_v > S_{hmin}$) and (3) compressional or reverse faulting regime ($S_{Hmax} > S_{hmin} > S_v$) (S_v , S_{hmin} and S_{Hmax} correspond to vertical, minimum and maximum horizontal principal stresses, respectively).

Borehole instability is in most of the cases, a direct reflection of these stress states. Hence, much progress has recently been made toward the determination of the magnitude and orientation of in-situ stress in the crust and a number of models have been developed to compute borehole failure in deviated wells. For instance, highly deviated wells are more stable than vertical wells in an reverse faulting region by conventional stability analysis (Last and McLean, 1996). It was also shown that boreholes drilled parallel to the maximum horizontal stress have minimum risk of instability (Russell et al., 2003). On the other hand, Al-ajmi (2006) and Al-Ajmi and Zimmerman (2009) developed a 3-D analytical model to study the behavior of the collapse pressure under different in-situ stress regimes and drilling trajectories and showed that well path optimization is mainly controlled by the relative magnitude of the in-situ stresses. Additionally, they showed that drilling vertical boreholes will minimize the potential borehole instability only when the horizontal in-situ stress is isotropic and that when it is anisotropic, the optimum well path will divert from the vertical direction. Much work on the influence of stress regimes on borehole failure prediction has been also carried out (Zhou et al., 1996; Hassan et al., 1999; Awal et al., 2001; Al-ajmi, 2006; Islam and Skalle, 2010). For instance, Zhou et al. (1996) proposed a theoretical approach to define stable borehole directions by considering different stress patterns. According to Zhou et al. (1996), the calculated stable conditions showed that:

- For normal stress regime: the most stable drilling direction is always parallel to

the azimuth of S_{hmin} and the optimal deviation angle depends on the ratio of the horizontal principal stresses to the vertical stress.

- For strike-slip regime: the deviation angle should always be 90° (horizontal wells), and that the drilling directions with respect to the azimuth of S_{Hmax} are controlled by the stress ratios, $r_H = \frac{S_{Hmax}}{S_v}$ and $r_h = \frac{S_{hmin}}{S_v}$. The higher the ratio r_H , the closer the drilling direction should be to the S_{Hmax} azimuth.

In previous work (Chapters 3 and 4), the main focus was primarily on developing a systematic methodology to jointly evaluate the stress tensor components and orientations, and the rock strength properties (e.g., cohesion, friction) in the shallower section of the well in a robust probabilistic framework and on proposing a stochastic methodology to predict borehole failure severity in the deepest section of the considered well. The calibration and prediction methodologies have been developed and tested on the BS-1 sub-vertical borehole affected by pervasive breakouts (80% of the well presents breakouts, Valley and Evans, 2009a). The observations along the lowest part of the borehole were used as a verification dataset allowing to validate the reliability of the methodology. However, our work may have some undetected limitations especially when conditions between the calibration and the prediction sections are noticeably more different than in the BS-1 case. Consequently, the main objective of this chapter is to identify the main factors affecting the robustness of our calibration-prediction methodology in a broad range of conditions. As real datasets spanning broad range of conditions are not available, synthetic cases were generated, considering different stress regimes, borehole breakouts intensity and more importantly, different borehole trajectories. This approach using synthetic cases allows us to investigate a much broader range of conditions that may be encountered in real field cases. The main questions to answer in this work are as follows:

- Under what conditions the calibration and prediction methodologies (as proposed in Dahrabou et al., 2022a,b) are robust?
- If a model is calibrated on a vertical borehole section, how much can we deviate the well from the vertical and still make a robust and accurate prediction of the borehole failure severity?
- How to quantify the uncertainty associated with the calibrations and predictions?
- Is it always possible to derive conclusive results concerning the optimal borehole trajectory?

Since the same mechanical model is used to generate the synthetic dataset, to calibrate and to predict, our investigation approach does not interrogate the validity of the failure model, but allows focusing on studying the effect of the stress regime, borehole breakouts intensity and wellbore trajectory on the proposed calibration-prediction approach (Chapters 3-4 and its associated uncertainty. First, an illustration of the problematic using a

representation of failure characteristics on stereographical projections is presented then systematic and complete synthetic cases are generated. Second, the parameters of the failure model described in Chapter 3 are calibrated against data from the shallower part of the borehole in the crystalline rock (from 2.6 to 3.6 km depth). Third, the 1st and 2nd order prediction approaches (Chapter 4) are applied in the deepest section of the borehole (on a section of 1 km). Finally, the entire calibration-prediction approach is validated and the predictions uncertainties are quantified by (1) comparing the predictions with the synthetic control data and by (2) defining the appropriate metrics to evaluate the predictions dispersion and shift relative to these synthetic data when deviating the well.

5.2. Methodology

A convenient way for evaluating the relationship between borehole deviation and failure is to represent wellbore failure parameters on a stereographic projection as initially proposed by Peka and Zoback (1995). In this mode of representation, the failure parameters are contoured on a lower hemisphere stereographic projection. The conditions for a vertical hole are presented on the center of the stereographic projection. Instead, deviated well conditions are presented away from the centre of the stereographic projection and conditions for horizontal wells are presented on its edge. In this chapter, this approach is used in combination with the borehole failure width and extent estimation approaches proposed in Chapter 3. The latter are based on an elastic solution for a cylindrical hole to estimate stresses and the empirical relationship developed by Shen (2008) to estimate borehole failure extent. This gives a first insight into the effect of well deviation on failure prediction. However, this allows analysis at a single point and one set of stress conditions. Consequently, a methodology based on synthetic cases is developed in this work in order to evaluate in more detail the borehole failure prediction approach proposed in Chapter 4. The latter involves the six tasks illustrated in Fig. 5.1. The main steps are described in detail in the following subsections and itemized next:

- Step 1: generate synthetic stress and strength depth profiles that account for variability. This synthetic database involves several stress regimes (normal, strike-slip and reverse stress regimes), nine borehole trajectories (Fig. 5.2) and different borehole breakouts intensity. These synthetic scenarios are summarized in Table 5.1.
- Step 2: compute borehole failure (breakout width, w_{BO} , breakout extent, e_{BO} and drilling induced tensile fractures, DITFs) based on the generated synthetic data. These computed borehole failure indicators will be considered as observations in further analyses.
- Step 3: the 1st order calibration (Chapter 3) is carried out to jointly estimate the 1st order trends of the parameters that mainly influence borehole failure (i.e., maximum and minimum principal horizontal stresses, S_{Hmax} , S_{Hmin} , respectively, cohesion, c ,

friction angle, ψ and Shen's regression parameters, A and B Shen (2008)) against the (generated) synthetic observations in the shallower vertical section of the well (from 2.6 to 3.6 km). This 1st order calibration, involving a few parameters (those defining parameter linear trends), is carried out for N different starting points in order to span the entire parameters space and account for non-uniqueness of the solutions.

- Step 4: perform 1st order prediction to assess the accuracy of the prediction methodology proposed in Chapter 4:
 - Extrapolate linearly the calibrated input parameters from Step 3 to a greater depth (the final 1 km section of the well) and compute the corresponding borehole failure indicators. This assumes that there is no severe disruption of the lithological conditions leading to the calibrated trends.
 - Carry out a validation analysis by comparing the predictions with the control data set, i.e., the observations (generated in Step 2) along the deepest section of the well to evaluate the accuracy of the predictions.
- Step 5: perform 2nd order calibration in order to estimate the variability of parameters around their 1st order mean obtained from Step 3. The 2nd order calibration is carried out only for two scenarios presenting different breakouts intensity. It is argued in this chapter that the calibrated parameters deviation from their mean is independent from the stress regime.
- Step 6: perform 2nd order prediction as proposed in Chapter 4:
 - Extrapolate linearly the calibrated input parameters from Step 3 and add synthetic variability generated using DS (Direct Sampling) algorithm as implemented in DeeSse (Straubhaar, 2019).
 - Compute failure in the deepest section of the well and compare the predicted and the generated observations from Step 2 to analyze the consistency and accuracy of the predictions.
- Step 6: quantify the shift relative to the control data and the dispersion of the predictions by defining the appropriate metrics for both the 1st and 2nd order predictions.

5.2.1. Generating synthetic cases

In this chapter, we have been interested in testing the limits of the calibration and prediction methodologies as developed in Chapters 3 and 4. Both proposed methodologies were applied to the BS-1 sub-vertical borehole, which is not appropriate to test the robustness and accuracy of these approaches when the borehole is deviated. To solve this issue, synthetic cases were generated in order to investigate a much broader range of conditions

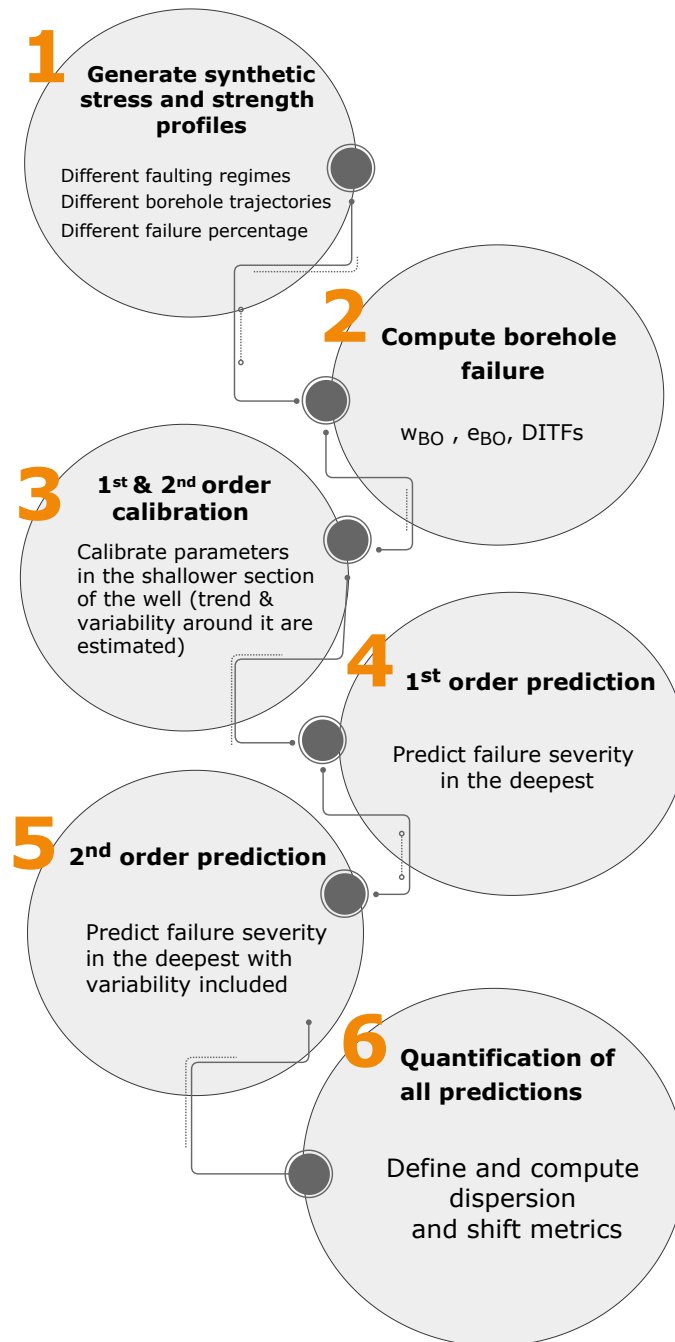


Figure 5.1.: Overview of the main steps of the proposed methodology.

that can be encountered in real field cases. The calibration-prediction approach were then tested on representative synthetic cases with (1) different faulting regimes (normal faulting (NF), strike-slip (SS), thrust faulting (TF), and a mix of NF and SS, which is similar to the stress conditions encountered in BS-1), (2) different percentage of borehole breakouts where scenarios affected by 80% and 30% of breakouts were considered (Table 5.1) and different borehole trajectories (Fig. 5.2). Although these models are synthetic, it is worth underlining that they still consider the particularities of the real field cases as they are inspired by the BS-1 borehole.

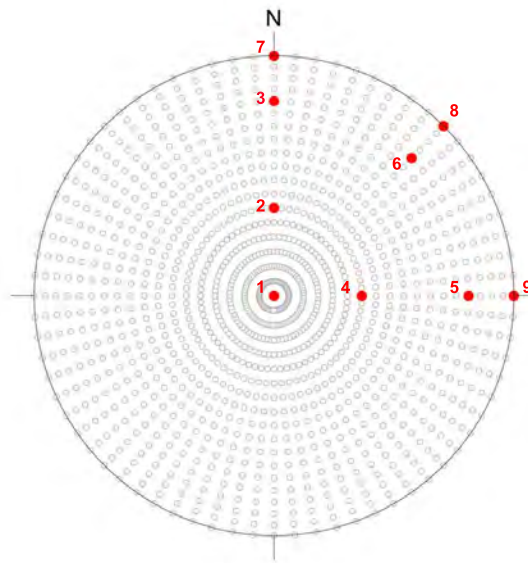
All elements required to generate the synthetic borehole trajectories along the entire well are computed based on the borehole azimuth and deviation provided in Fig. 5.2. The synthetic test boreholes were desurveyed using a balanced tangential method (Walstrom et al., 1972) in order to derive the required correspondences between measured depth (MD) and the true vertical depth (TVD). In addition, the generated stresses and strength depth profiles are accounting for the 2nd order variability derived from analyses that were carried out in Chapter 3, which makes these synthetic data as close as possible to reality. Note that in this chapter, a constant cooling along the entire length of the borehole is assumed in order to avoid adding additional effects that would be very difficult to disentangle in the evaluation of the results. Indeed, as we are mostly interested in studying the impact of stress regimes and borehole deviation, having variations in the cooling leads to another level of complexity that may obfuscate the main objective of this work.

Given a set of initial parameters (e.g., stress orientation, wellbore orientation, Poisson's ratio, thermo-elastic parameters, etc.) in addition to the generated 2nd order stress and strength depth profiles, stresses around the borehole are computed using the analytical solution of Kirsch (Kirsch, 1898; Schmitt et al., 2012). All stress components around the borehole, including the remnant thermal stresses arising from cooling of the borehole wall are accounted for. Note that generating these synthetic cases aims also at coping with the inherent uncertainty on the choice of an appropriate failure criterion. Based on the previous results (Chapter 3), it was recommended to use the Mohr-Coulomb criterion in combination with the Kirsch analytical solution to compute stress. However, the latter has the limitation of not being able to reproduce progressive failure. Thus, it was combined with the empirical relationship proposed by Shen (2008) that we extended in Chapter 3 for complex stress state where borehole trajectory, mud pressure and thermal stresses effect were accounted for. Finally, breakout width, w_{BO} , extent, e_{BO} and drilling induced tensile fractures, DITFs, are computed and used as observations to calibrate against in further analyses.

Note that the stress and cooling profiles are the same for all the synthetic scenarios, whereas strength is different. Indeed, the cooling is set to be constant in such a way that 20% of the borehole is affected by DITFs in all scenarios and the strength was adjusted for each scenario to ensure having boreholes affected by 80% of breakouts in Scenarios 1 to 4 and by 30% of breakouts in Scenarios 5 to 8 (Table 5.1). The reason why different percentage of breakouts were chosen in this study is that our calibration and prediction

Table 5.1.: Description of the generated synthetic scenarios with different faulting regimes, borehole breakouts intensity and borehole trajectories.

Scenarios	Faulting regime	Breakouts	DITFs	Borehole trajectory
Scenario 1	NF-SS	80%	20%	9 trajectories (Fig. 5.2)
Scenario 2	NF			
Scenario 3	SS			
Scenario 4	TF			
Scenario 5	NF-SS	30%	20%	
Scenario 6	NF			
Scenario 7	SS			
Scenario 8	TF			



Trajectory	Borehole dip direction, α [°]	Borehole deviation, i [°]
1	0	0
2	0	30
3	0	70
4	90	30
5	90	70
6	45	70
7	0	90
8	45	90
9	90	90

Figure 5.2.: Stereoplots showing the considered 9 borehole trajectories (red dots). Grey circles depict different borehole trajectories for a borehole dip direction (α) varying from 0 to 360° and a borehole deviation (i) varying from 0 to 90°. The Table shows the considered values of α and i of each trajectory.

methodologies were previously tested only on the BS-1 borehole (Chapters 3-4), which was affected by 80% of pervasive breakouts. This exercise will then help to verify the reliability of the approach implemented in our calibration methodology when considering situations where breakouts occurrence is limited.

5.2.2. Failure models calibration

5.2.2.1. 1st order calibration

At this stage, the 1st order calibration methodology that we proposed in Chapter 3 was used. The main goal is to calibrate the model parameters that are the most influential on borehole stability and cannot be estimated otherwise. They were previously determined by means of sensitivity analysis in Chapter 3. These parameters are the maximum and minimum principal horizontal stresses, S_{Hmax} and S_{Hmin} , cohesion, c , friction angle, ψ , and Shen's parameters, A and B . The chosen 1st order parameterization is summarized in vector \mathcal{M} . In this 1st order calibration, we use simplified profile with depth of these model parameters (Eq. 5.1).

$$p = a \cdot TVD + b \quad (5.1)$$

$$\mathcal{M} = \{a_{S_{Hmax}}, b_{S_{Hmax}}, a_{S_{Hmin}}, b_{S_{Hmin}}, c, \psi, A, B\} \quad (5.2)$$

Where $a_{S_{Hmax}}$, $b_{S_{Hmax}}$, $a_{S_{Hmin}}$, $b_{S_{Hmin}}$ are the slope and the intercept of S_{Hmax} and S_{Hmin} , respectively. Note that in this chapter the maximum horizontal stress orientation is not calibrated because it can be directly inferred from breakout geometry (and is therefore not parameterized). In summary, our stress/strength model is parametrized by 8 parameters (Eq. 5.2). A number of starting points is used in the calibration to guarantee that a global optimum is achieved by the Levenberg-Marquardt algorithm (Alcolea et al., 2000). To that end, 100 initial parameterizations are randomly sampled assuming a uniform distribution. Then a rejection criterion, based on frictional equilibrium (Zoback (2007); Jaeger (2007), Chapter 3) is applied to these initial starting points. Initial sets of parameters not meeting the constraints are rejected and new ones are generated until the target 100 initial coherent parameterizations is achieved.

Assumptions are required for model parameters that are estimated independently and not calibrated. The following equations are used for S_v and P_p (which are mainly inspired by the profiles in the BS-1):

$$S_v[MPa] = 24.9 \cdot TVD[km] \quad (5.3)$$

$$P_p[MPa] = 9.81 \cdot TVD[km] \quad (5.4)$$

Moreover, a hydrostatic mud pressure is assumed corresponding to an equivalent mud

density, $\rho_{mud} = 1.07 \text{ g/cm}^3$. The same values of Young modulus ($E = 65 \text{ GPa}$) and the coefficient of linear expansion ($\alpha = 10^{-5} \text{ K}^{-1}$) as in BS-1 are used in order to have scenarios as close as possible to reality. Additionally, upper and lower bounds of the estimated parameters in PEST (Parameter ESTimation) were defined in order to minimize unwanted and large parameter oscillations. At the end of the calibration process in the shallower section of the well (from 2.6 to 3.6 km), where the borehole is essentially vertical, the well calibrated models based on their final objective function are selected.

5.2.2.2. 2nd order calibration

As fully described in Chapter 3, the 2nd order calibration aims at estimating the deviations of a given parameter from its calibrated mean. As such, the methodology allows to evaluate heterogeneity at any given scale supported by the underlying discretization. The Regularized Pilot Points Method (Alcolea et al., 2006), as implemented in PEST (Doherty, 2015), was used to that end. The generic parameterization now becomes:

$$p = m \cdot TVD + n + \epsilon(MD) \quad (5.5)$$

where m and n are the slope and offset of parameter p , respectively, and ϵ is the perturbation around the mean and is a function of measured depth (MD). The reader is referred to Chapter 3 for a complete description of the approach.

The main objective of performing this 2nd order calibration step is to estimate the variability represented by ϵ and use it as a training image to forecast parameters in the deepest section of the well by using a multi-point statistical approach based on direct sampling technique (DeeSse, Straubhaar, 2019). This step is primordial to be able to carry out 2nd order predictions in the deepest section of the well.

5.2.3. Borehole failure severity prediction

1st and 2nd order predictions were carried out in this chapter. The prediction methodology is fully described in Chapter 4. It is important to differentiate between both of them. This is explained in the next sections.

5.2.3.1. 1st order prediction and quantification indicators

The 1st order calibration is carried out for N starting points in the shallower vertical section of the well (2.6 to 3.6 km MD). At the end of the calibration process, M well calibrated models are selected based on a rejection and filtering criterion as defined in Chapter 3. Then 1st order predictions are performed. This means that the parameter trends calibrated along the shallowest section of the borehole are linearly extrapolated to greater depths and failure is then computed along the deepest section of the borehole using the failure model proposed in Chapter 3. The 1st order prediction step performed

in this chapter is primordial to assess the reliability and the consistency of the predictions with the observations. To that end, two indicators are defined:

- I_s : a shift indicator that measures the difference between the mean of the 1st order predictions and the mean of the observations. The generalized definition of this indicator is as follows:

$$I_s = \frac{\bar{x} - \bar{x}^*}{\bar{x}^*} \quad (5.6)$$

where \bar{x} and \bar{x}^* are the mean of predicted and observed parameter x , respectively (x being either breakout width, extent or DITFs in this chapter).

- I_{1d} : a 1st order dispersion indicator that measures the spread of the 1st order predictions around the mean. In other words, I_{1d} is the standard deviation defined as the square root of sum of squared deviation from the mean divided by the number of predictions.

$$I_{1d} = \sqrt{\frac{\sum_{i=1}^M (x - \bar{x})^2}{M - 1}} \quad (5.7)$$

Where x and \bar{x} correspond to the predicted borehole failure indicators (breakout width, w_{BO} , breakout extent, e_{BO} and DITFs, D) and the corresponding mean, respectively, and M the total number of predictions. The shift indicator, I_s , is a metric to measure how shifted/displaced is the predictions distribution compared to the observations that were generated in the deepest section of the well. Ideally, if the predictions are coherent with the observations, $I_s \approx 0$. Otherwise, if I_s is negative or positive, this means that the predictions either underestimate or overestimate borehole failure, respectively. However, this metric alone is not sufficient because it ignores the dispersion of the predictions. To fill this gap, a 1st order dispersion metric, I_{1d} , is defined. The combination of these two metrics give insight into the influence of stress regimes, borehole trajectory and breakout intensity on the quality of the 1st order predictions. However, it is important to highlight that parameters variability should not be neglected when dealing with rock masses and rock mass failure. To that end, 2nd order predictions are carried out and an appropriate metric to quantify them is also defined.

5.2.3.2. 2nd order prediction and quantification indicator

2nd order prediction deals with the quantification of variability of the predicted variables around the estimated trends. The outcomes of the 1st order calibration performed in the shallowest section of the well were extrapolated to greater depths and stochastic variability that were simulated using Multi-Point Statistical technique in Section 5.2.2.2 were added to these trends. Indeed, 2nd order calibration were performed for only two scenarios (both having 80% and 30% of breakouts in the shallower section of the well) and their outcomes were used as training data sets to simulate variability in the deepest section of the well. Finally, failure is computed in the deepest section of the well (the final 1 km of the borehole for all scenarios). A 2nd order dispersion metric, I_{2d} , is defined as:

$$I_{2d} = \frac{STD - STD^*}{STD^*} \quad (5.8)$$

where STD is the standard deviation of a given predicted borehole indicator (e.g., breakout width, breakout extent or DITFs) and STD^* is the standard deviation of the corresponding observation. This metric measures the dispersion and scattering of the predictions. It gives us also information about the ability of our predictions to reproduce the variability of the observations. Ideally, if the predictions reproduce the variability of observations, $I_{2d} \approx 0$.

5.2.4. Well optimization path

Al-ajmi (2006) showed that well path optimization is mainly controlled by the relative magnitude of the in-situ stresses. The same finding was reported in a number of publications (e.g., Chen et al., 1996; Zhou et al., 1996; Moos et al., 1998). The optimum drilling inclination changes progressively as the intermediate principal in-situ stress, σ_2 , changes from the minimum to the maximum principal stresses, depending on the stress regime. This outlines the existence of a potentially explicit correlation between the optimum drilling inclination and the stresses anisotropy. Al-ajmi (2006) derived a relationship between the optimum drilling inclination, and the field stresses that we will use throughout this chapter to explain some of our predictions results. This relationship is expressed as follows:

$$\gamma = \arcsin(\sqrt{\Phi}) \quad (5.9)$$

where γ is the deviation angle from the maximum principal in-situ stress in the σ_1 - σ_3 plane and Φ is the anisotropic stress ratio defined by:

$$\Phi = \frac{\sigma_2 - \sigma_3}{\sigma_1 - \sigma_3} \quad (5.10)$$

σ_1 , σ_2 and σ_3 being the maximum, intermediate and minimum effective principal stresses, respectively. The stress ratio, Φ , represents the overall anisotropic level of the field stress. $\Phi = 0$ when $\sigma_2 = \sigma_3$ and $\Phi = 1$ when $\sigma_2 = \sigma_1$. In NF and SS-RF stress regimes with isotropic horizontal stress, $\Phi = 0$. In these field stress systems, the optimum well path is parallel to σ_1 . However, when $\Phi = 1$, the optimum well path will be parallel to σ_3 . This is true in RF and NF-SS stress regimes with isotropic horizontal stresses. To be consistent with the findings of Al-ajmi (2006), we define the angle α as the deviation of the borehole from σ_2 , and the angle i and the deviation of the borehole from σ_1 (Fig. 5.3).

The relationship proposed by Al-ajmi (2006) will be used in this chapter in order to explain the shift of predictions that were observed for some specific cases when deviating the borehole.

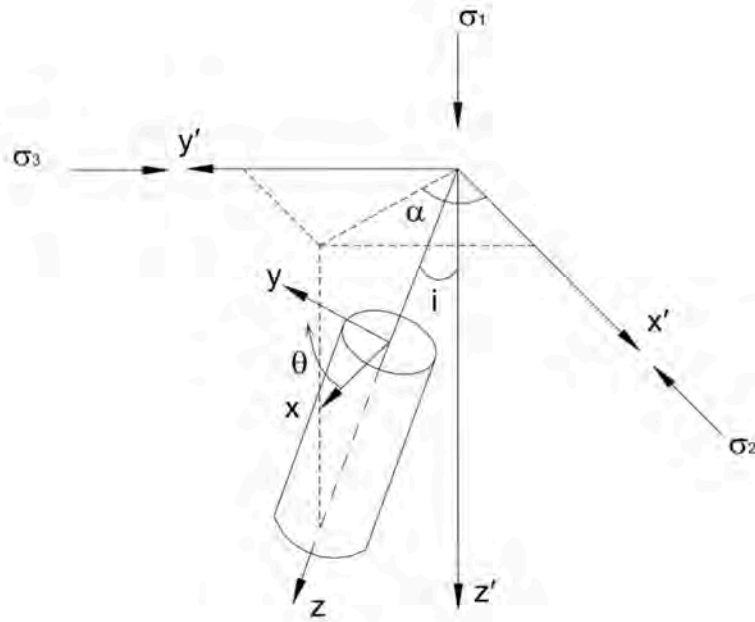


Figure 5.3.: Generalized stress transformation system for a deviated borehole (after Al-ajmi, 2006).

5.3. Results

5.3.1. Illustration of the relationship between borehole deviation and failure using stereographic projections

First the relationship between borehole deviation and failure is illustrated by considering an arbitrary set of parameters generating a moderate breakout in a vertical borehole with a failure width of 41° and a normalised failure extent $\frac{e_{BO}}{a}$ of 1.17 (a being the nominal borehole radius). The parameters for this base case are listed in Table 5.3. The studied stress regime is normal stress conditions with a stress ratio of $\Phi = \frac{\sigma_2 - \sigma_3}{\sigma_1 - \sigma_3} = 0.875$. The data are presented with the maximum horizontal stress S_{Hmax} orientated N-S and the minimum horizontal stress S_{Hmin} orientated E-W in Fig. 5.4. In this case, a borehole deviated toward the North or South is less stable than a vertical hole, while a borehole deviated to the East or West is more stable than the vertical hole. Indeed, when deviating the well to the East or West of 42° or more, breakouts are not forming.

In order to evaluate predictability in this particular case, it is necessary to look for other set of parameters that lead to the same failure characteristics for a vertical hole. To that end, a grid search is firstly performed on strength and stress parameters in order to match the targeted breakout width. In a second step, the parameters of Shen A and B (Shen, 2008) are adjusted in order to match breakout extent. The calibrated set of parameters are presented in Fig. 5.5. They cover a broad range of stress and strength conditions, reflecting the already well described fact that this determination is highly non-unique (Chapter 3).

Table 5.3.: Parameters used for the base case presented in the stereographical projection of Fig. 5.4.

Parameter	Value
S_v	100 MPa
S_{Hmax}	95 MPa
S_{Hmin}	60 MPa
$P_m = P_p$	40 MPa
c	37 MPa
ψ	30 °
UCS	128 MPa
A	15.2
B	2.67

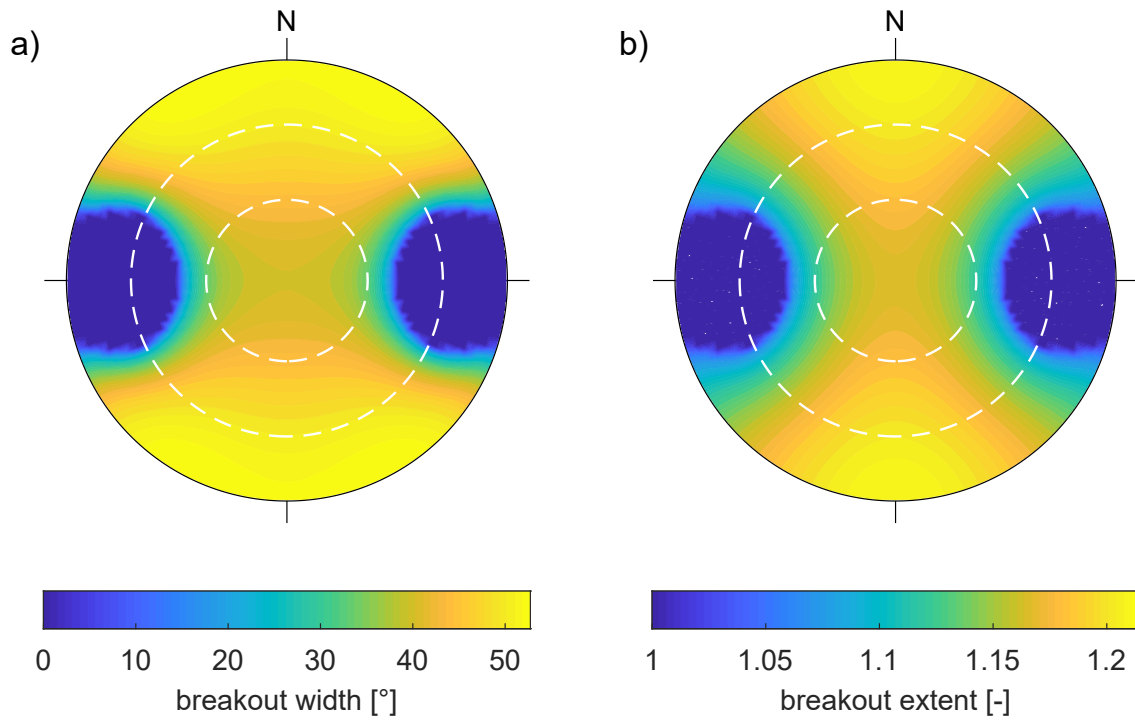


Figure 5.4.: Stereographic projection of (a) breakout width and (b) breakout extent for the parameter set listed in Table 5.3. The white dashed lines represent borehole deviation of 30 and 60°, respectively.

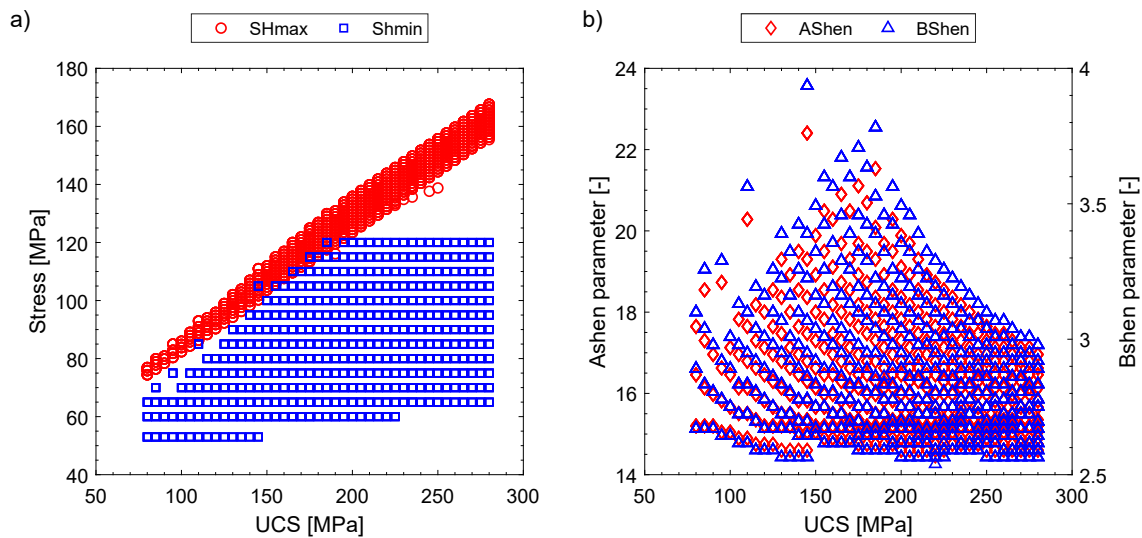


Figure 5.5.: Set of calibrated (a) stresses and (b) Shen's parameters. The parameters are shown in function of the uniaxial compressive strength, UCS. This figure demonstrates that the calibrated solutions are highly non-unique and that our grid search is properly covering a broad spectrum of calibrated parameter sets.

At this stage, one can assess for all these parameters set what would be the computed breakout width and extent for deviated boreholes. First, these results are shown for boreholes deviated to azimuth 0° , 30° , 45° , 60° and 90° (Fig. 5.6). For vertical boreholes, all the models estimate the same width and extent showing that the considered grid search for equivalent solutions is performed properly. However, when the boreholes are deviated, the predictions diverge. In order to visualise this divergence for all borehole orientations, the breadth of the envelop of all models is displayed in a stereographic projection for all predictions (Fig. 5.7). This shows that for deviations beyond $\approx 30^\circ$ divergences are large.

The reason for these divergences is that borehole failure in a vertical borehole is insensitive to the vertical stress magnitude. Since our models are calibrated on a vertical borehole, these calibrations are insensitive to the vertical stress and the stress ratio for the sets of calibrated models varies a lot. When a deviated borehole is considered, the ratio of the vertical stress to horizontal stress matters and thus, if this ratio is not properly calibrated, the predictions are diverging. This is illustrated in Fig. 5.8, where all the calibrated set of parameters are shown according to their stress ratio. The normalised sum of the squared difference with the base case model is computed as an indicator of the quality of the predictions. The normalisation is done with the model having the highest sum of squared difference (the worst model for prediction). This shows that if the stress ratio of the calibrated model is close to the base case, the predictions are very close to the base case, but diverge when the stress ratio is different.

This example illustrates the limitation of calibration on a single breakout in a vertical borehole. Somewhat better results, i.e., less dispersed predictions, are obtained when the

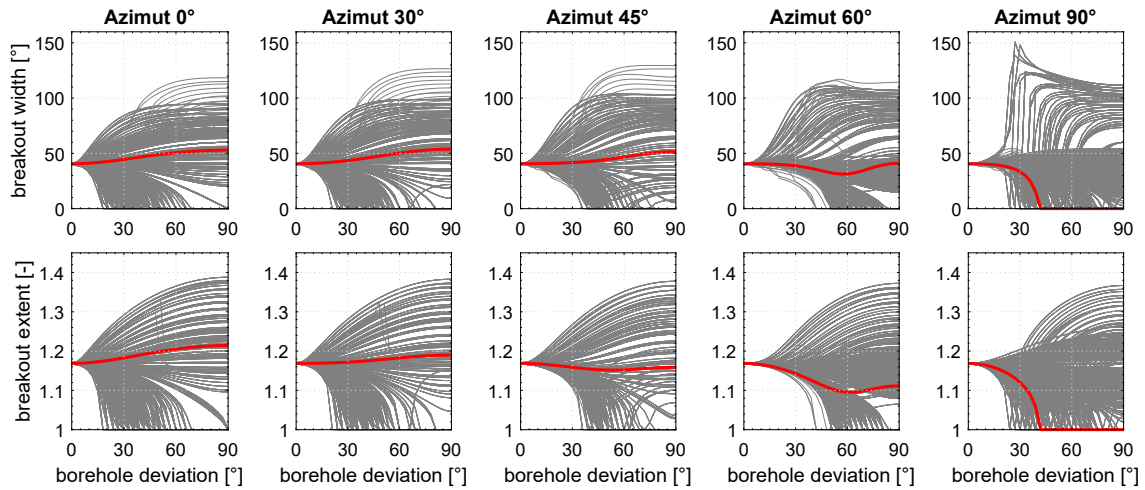


Figure 5.6.: Prediction of breakout width (top) and extent (bottom) for borehole deviation azimuth 0° , 30° , 45° , 60° and 90° . The grey are the prediction for all the calibrated set of parameters. The red line is the prediction with the parameters from the base scenario of Table 5.3.

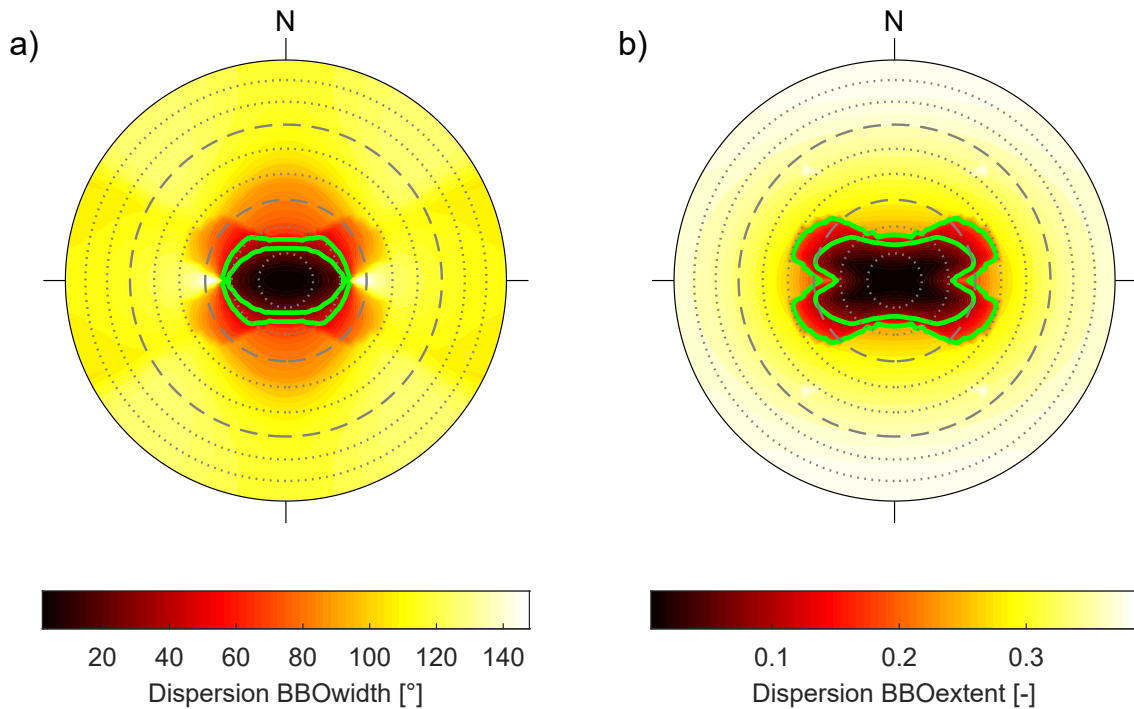


Figure 5.7.: Breadth of the envelop of all calibrated models for (a) breakout width and (b) breakout depth. Green lines are contour lines for breadth envelope of 30° and 50° (width) and 0.1 and 0.2 (extent). Grid for borehole deviation steps of 10° are presented with the dashed line for borehole deviation of 30° and 60° .

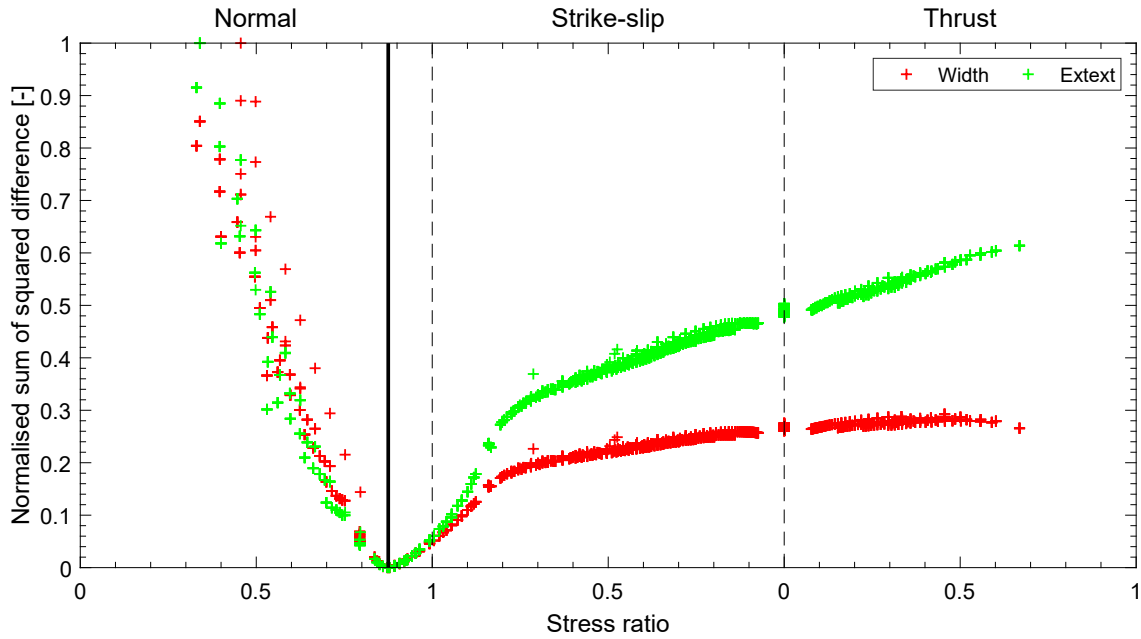


Figure 5.8.: Coherence of the width and extent estimation from calibrated models with the base model depends of their stress ratio $\Phi = \frac{\sigma_2 - \sigma_3}{\sigma_1 - \sigma_3}$. The coherence is computed by the sum of the squared differences with the base model and is normalised by the model with the worst sum of squared differences. The vertical thick black line shows the stress ratio of the base model.

calibration borehole is oblique to all principal stresses and thus sensitive to all stress magnitudes. This adds some information to constrain the stress ratio and helps narrowing the predictions. However, even more information is required to generate calibrated models that are useful for predictions. Calibration including 1st and 2nd order approach on borehole profile brings the additional information necessary for better constrained models. This will be tested systematically with the synthetic data generated in the following section.

5.3.2. Generating synthetic failure data

Using the methodology described in Section 5.2.1 and considering the scenarios of Table 5.1), 72 synthetic cases were generated against which our calibration-prediction methodology is tested. Fig. 5.9 shows two examples amongst the 72 of the generated stresses and strength depth profiles. This is for Scenarios 1 and 5 (sharing the same stress conditions, NF-SS faulting regime, but different strength leading to different failure intensity, Table 5.1) with a borehole dip direction, $\alpha = 0^\circ$ and a borehole deviation, $i = 70^\circ$. In this example, the vertical section where calibration will be performed starts from 2.6 to 3.6 km MD and the deviated section where predictions will be carried out starts from 4.49 to 5.49 km MD. Moreover, one should differentiate between measured depth (MD) and true vertical depth (TVD). In the vertical section of the well, MD and TVD are the same. However, when the well starts deviating, the latter are no more equal as shown

in the double y-axes of Fig. 5.9. It is also important to notice the non-linear profile of the vertical principal stress, S_v , (black solid line, and the pore pressure, P_p (black dashed line) in Fig. 5.9a). The stresses are indeed a linear function of TVD but while representing them in MD, the profiles become non-linear. In this example, the input parameters were generated in such a way that 20% of the two wells (corresponding to both rows in Fig. 5.9 is affected by DITFs and 80% and 30% of their vertical section is affected by breakouts, respectively. The stress profiles for both Scenarios 1 and 5 are the same along their entire length and only strength and cooling are varied to reach the target breakouts and DITFs percentage. Note that the cooling is assumed to be constant because (1) we are mostly interested in studying the impact of stress regime and borehole deviation on predictions (the cooling is equal to -15°C and -35°C for breakouts and DITFs, respectively) and (2) having variations in cooling lead to another level of complexity. Table 5.4 gives the values of the common parameters to all the generated synthetic scenarios. Note that these values were inspired by the BS-1 borehole in order to generate not only synthetic data but also realistic. Based on the generated synthetic stress and strength profiles, borehole failure indicators (i.e., w_{BO} , e_{BO} and DITFs) are computed. An example of computed borehole failure in Scenario 1 and 5 is shown in Fig. 5.10. Depths where failure does not occur have a breakout width, $w_{BO}=0^\circ$ and a breakout extent, e_{BO} equal to the nominal borehole radius.

Table 5.4.: Common input parameters to all the generated synthetic scenarios.

Input parameter	Value
Euler's angles $[\circ]$	$\alpha=0, \beta=0, \gamma=0$
mud density, ρ_{mud} $[g/cm^3]$	1.07
Poisson ratio, ν [-]	0.25
Young modulus, E [GPa]	65
Tensile strength, T_o [MPa]	-4
Linear coefficient of thermal expansion $[K^{-1}]$	10^{-5}
Cooling for breakouts $[\circ\text{C}]$	-15
Cooling for DITFs $[\circ\text{C}]$	-35
Borehole radius, a , from 2.6 to 4.8 km [mm]	125.41
Borehole radius, a , above 4.8 km [mm]	108

5.3.3. 1st order calibration

Model parameters which are the most influential and difficult to constrain were used in the calibration study. The latter are the maximum and minimum horizontal principal stresses, S_{Hmax} and S_{Hmin} , respectively, the cohesion, c , the internal friction angle, ψ and finally Shen's parameters A and B as shown in Chapter 3. In this 1st order calibration, simplified profile with depth of the aforementioned parameters were used (Eq. 5.1). In addition, $N=100$ starting points, that explore the global parameter space, were used in this calibration to guarantee that a global optimum is achieved by the Levenberg-Marquardt algorithm (Alcolea et al., 2000). Then a rejection criterion, based on frictional equilibrium,

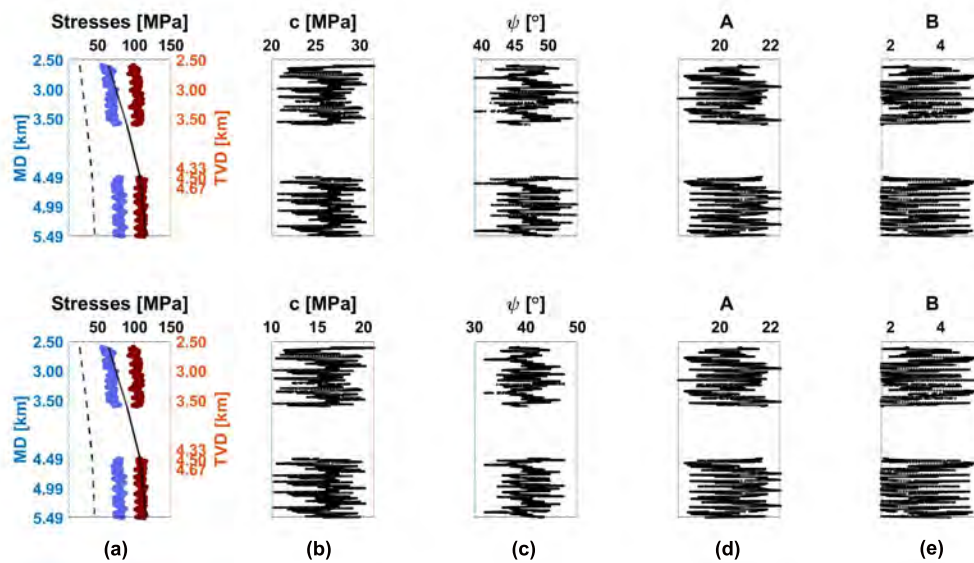


Figure 5.9.: An example of the generated stresses and strength profiles in depth for Scenarios 1 and 5 (NF-SS stress regime) with $\alpha = 0^\circ$ and $\beta = 70^\circ$ (trajectory 3 in Fig. 5.2). The two rows of this figure correspond to Scenarios 1 and 5, respectively. (a) maximum and minimum horizontal principal stresses in orange and blue, respectively, the dashed and solid black lines represent the pore pressure and the vertical principal stress, respectively; (b) cohesion, c ; (c) internal friction angle, ψ ; Shen's regression parameters (d) A and (e) B . Note that in all panels, the blue and orange y-axes correspond to measured depth (MD) and true vertical depth (TVD), respectively.

is applied to the initial starting points as explained in Dahrabou et al. (2022b). Fig. 5.11 shows an example of the 1st order calibration that were performed on Scenario 1 and 5 (NF-SS stress regime and 80% and 30% of breakouts, respectively). Note that 91 filtered calibrated models were selected for Scenario 1, whereas only 40 models were kept for Scenario 5. Indeed, calibrating against observations with limited breakouts (only 30%) results in few models that succeed in reaching an optimal objective function. This may be explained by the lack of robustness of the used approach when considering no failure. The range of both calibrated S_{Hmax} and S_{Hmin} (Fig. 5.11a) shows the non-uniqueness of the solutions, which highlights the inherent parametric uncertainties.

5.3.4. Failure prediction

5.3.4.1. 1st order prediction

The 1st order prediction is primordial to assess the reliability and the precision of the predictions (Chapter 4). In this step, the calibrated parameters are linearly extrapolated to a larger depth and failure is estimated. Fig. 5.12a shows the 1st order predictions that were performed in the deepest section of a vertical well (from 4 to 5 km) ($\alpha=0^\circ$ and $i=0^\circ$). Note that the calibrated stress profiles cover a fairly wide range (Fig. 5.12a) but the

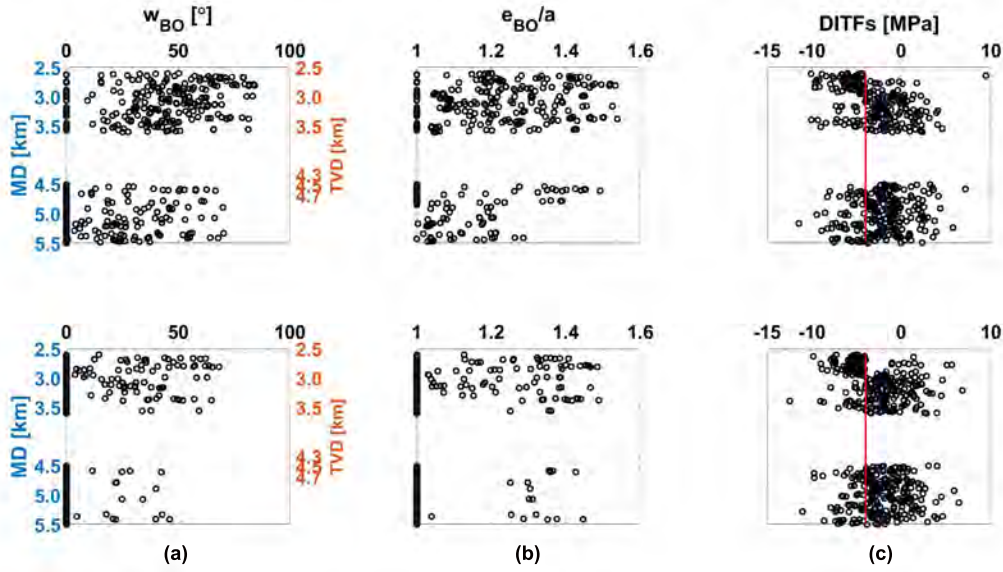


Figure 5.10.: Computed borehole failure based on the generated synthetic profiles of stress and strength in Fig. 5.9. (a) breakout width, w_{BO} ; (b) breakout extent normalized by the nominal borehole radius, e_{BO}/a ; (c) drilling induced tensile fractures, DITFs. The red line in panel (c) depicts tensile strength, $T_o = -4$ MPa and blue and orange y-axes correspond to MD and TVD, respectively.

predictions are not dispersed and coherent with the mean of the synthetic observations. However, when the well is deviating, the predictions start diverging. This is illustrated in Fig. 5.13 where all parameters are similar to the ones used in Fig. 5.12 but with a different borehole trajectory ($\alpha=0^\circ$ and $i=30^\circ$). These results reveal the influence of the borehole trajectory on the quality and reliability of our predictions. This 1st order prediction process were performed for all the generated 72 synthetic scenarios and it was noticed that, despite the stress regime and the percentage of breakouts affecting the borehole, the predictions were consistent with the observations when the borehole is vertical ($\alpha=0^\circ$ and $i=0^\circ$). In the other cases, the predictions are either dispersed and/or their mean is shifted compared to the mean of the observations. We were then interested in quantifying the dispersion of these 1st order predictions and to measure their shift in comparison to observations. To that end, we computed the 1st order shift metric, I_s , and the 1st order dispersion metric, I_{1d} , that were previously defined in Section 5.2.3.1.

5.3.4.2. 1st order predictions shift

The 1st order shift metric, I_s , was computed for the three borehole failure indicators (w_{BO} , e_{BO} and DITFs) as well as d , the difference between the mean of the failure observations in both the shallower (essentially vertical) and the deepest section of the well. Results are itemized next:

- When the borehole is vertical ($\alpha=0^\circ$ and $i=0^\circ$), the 1 order shift of breakout width

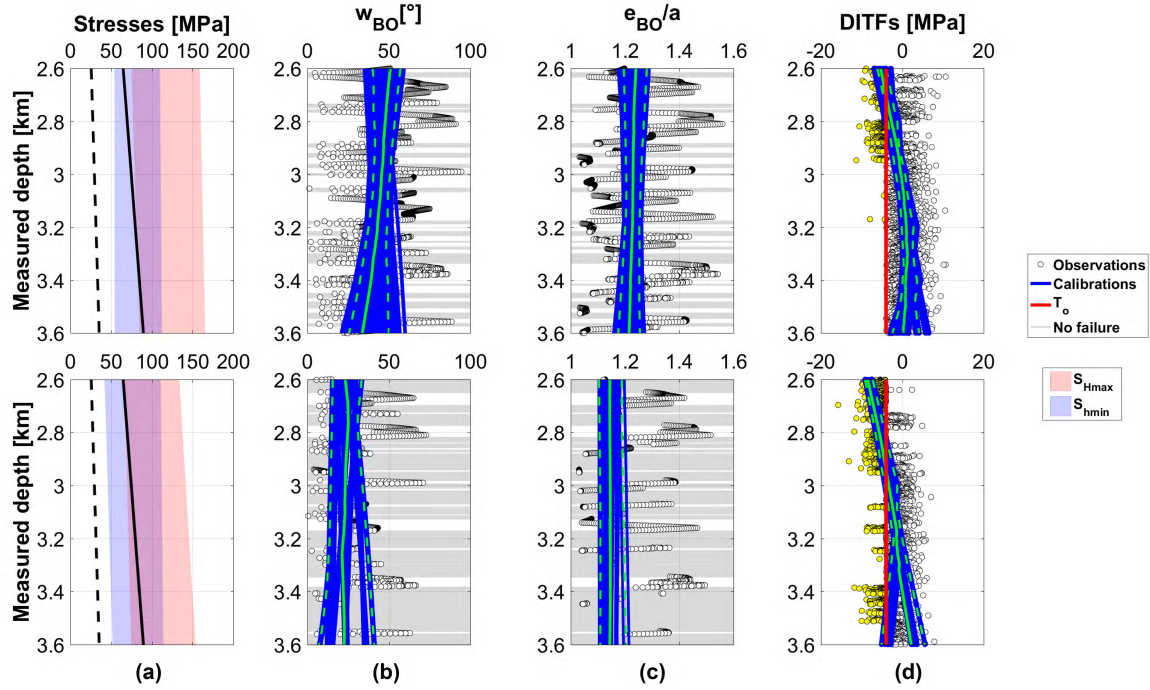


Figure 5.11.: Outputs of the 1st order calibration that was carried out using both Scenario 1 and 5. Note that 'trajectory 1' (Table 5.2) were used for failure computation in this example where $\alpha=0^\circ$ and $i=0^\circ$. (a) range of the well calibrated models of S_{Hmax} (pink) and S_{hmin} (light blue). S_v and pore pressure profiles are depicted by the solid and dashed black lines, respectively; (b) breakout width; (c) normalized breakout extent; (d) DITFs. The black circles correspond to failure synthetic observations while the solid blue lines correspond to the calibrated failure for the analyzed models. The red line in panel (d) depicts the tensile strength, $T_o = -4$ MPa and the yellow dots correspond to depths where DITFs are observed. Finally, the solid lines in green correspond to the mean of the calibrated models, whereas the dashed green lines represent the 5th-95th percentiles. Note that 91 and 40 well calibrated models were selected for Scenario 1 and 5, respectively.

predictions in the deepest is very close to zero ($I_s \approx 0$), meaning that the mean of both the 1st order predictions and the observations in the deepest section of the well are superimposed. This is illustrated in Fig. 5.14 where the first order shift, I_s , is plotted against d , the difference between the mean of the breakout width observations in both the shallower (vertical) and the deepest section of the well. Vertical holes are represented by the dark blue dots (Fig. 5.14) all starting at a shift, $I_s \approx 0$. This observation is valid for all scenarios. This shows that the breakout width predictions are consistent with the observations in the deepest section of the well as they are centered on them.

- When starting to deviate the borehole, predictions start to shift (both mean of the predictions and observations in the deepest are no more superimposed). Predictions tend either to underestimate or overestimate breakout width, depending on (1) the

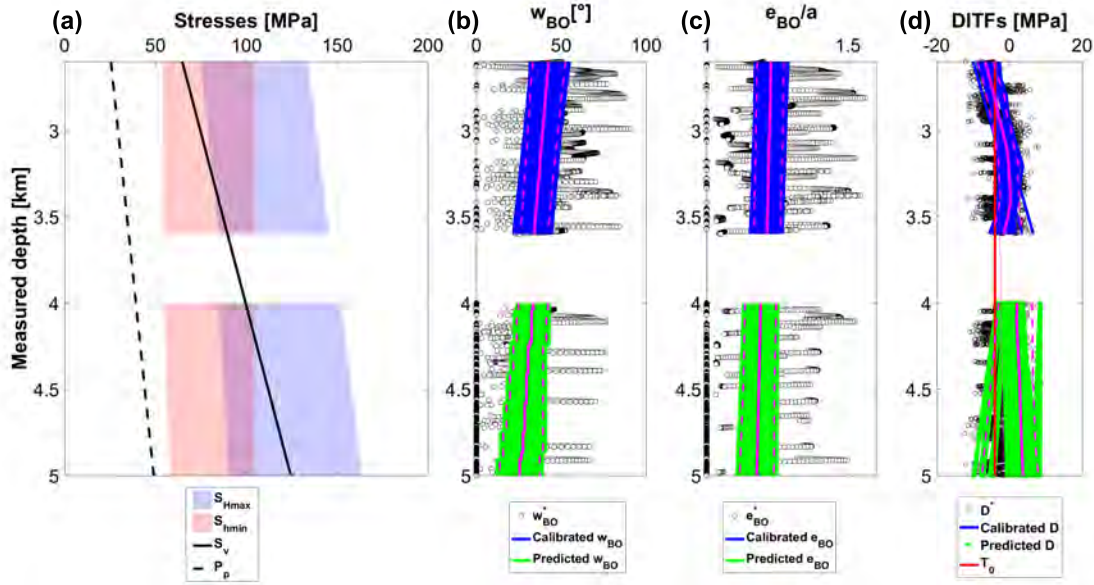


Figure 5.12.: Outputs of the 1st order calibration and prediction that were carried out using Scenario 1 (NF-SS stress regime and 80% of the borehole is affected by breakouts). Note that 'trajectory 1' (Table 5.2) were used for failure computation in this example where $\alpha=0^\circ$ and $i=0^\circ$. (a) range of the 91 well calibrated models of S_{Hmax} (light blue) and S_{Hmin} (pink). S_v and pore pressure profiles are depicted by the solid and dashed black lines, respectively; (b) breakout width; (c) normalized breakout extent; (d) DITFs. The black circles correspond to failure synthetic observations while the solid blue and green lines correspond to the calibrated and predicted failure for the analyzed models, respectively. The red line in panel (d) corresponds to tensile strength, $T_o = -4$ MPa. Finally, the solid lines in magenta correspond to the mean of the 91 calibrated and predicted models, whereas the dashed magenta lines represent the 5th-95th percentiles.

stress anisotropy ratio, Φ , and (2) the difference between the mean of observations in the calibration and prediction sections of the well, noted as d .

- If the vertical section of the well where calibration are carried out is affected by pervasive breakouts (Scenarios 1 to 4), we observe that I_s and d are positively correlated:
 - I_s is low ($0 \leq I_s \leq 9\%$) when d is less than a certain threshold ($0 \leq d \leq 18\%$) (Fig. 5.14a-d). This means that small shifts of predictions are observed when the intensity of breakouts in both the calibration and prediction sections is not considerably different (does not exceed $\approx 18\%$). In simple terms, when calibrating on a vertical section with pervasive breakouts, predictions of the width are slightly shifted if the deepest section has pervasive breakouts as well.
 - I_s is high ($17 \leq I_s \leq 38\%$) when d is higher ($d \geq 40\%$). Simply put, when calibrating on a vertical section with pervasive breakouts, the shift of predictions

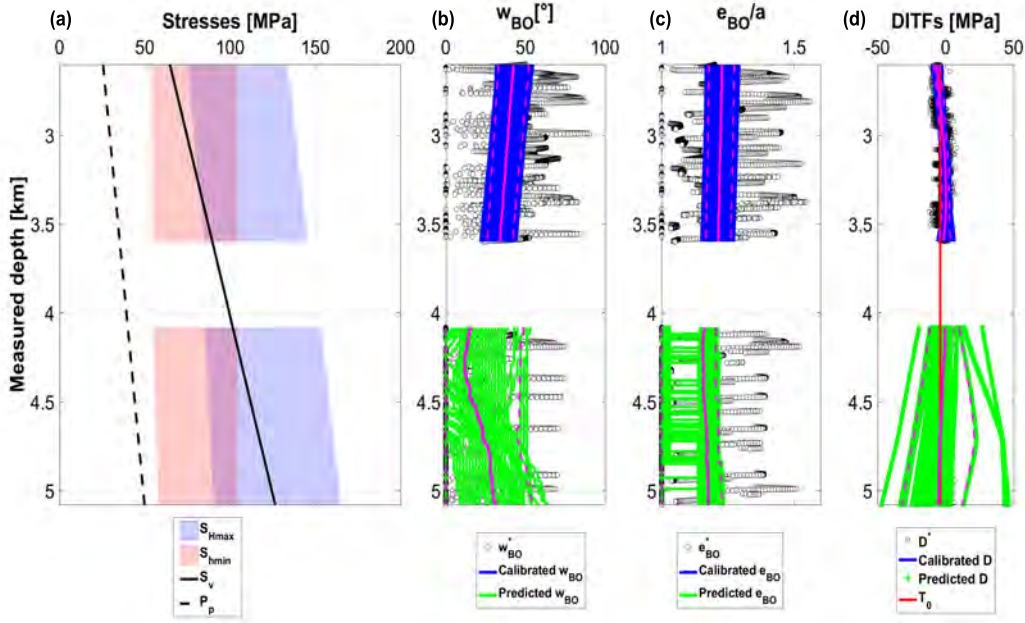


Figure 5.13.: Outputs of the 1st order calibration and prediction that were carried out using Scenario 1 (NF-SS stress regime and 80% of the borehole is affected by breakouts). Note that 'trajectory 2' (Table 5.2) were used for failure computation in this example where $\alpha=0^\circ$ and $i=30^\circ$. See the caption of Fig. 5.12 for further details.

starts to be considerable when limited breakouts are present in the prediction section (Fig. 5.14a-d).

- On the other hand, if the vertical section of the well where calibration is performed is affected by limited breakouts (Scenarios 5 to 8), we observe that I_s and d are correlated:
 - I_s is small ($0 \leq I_s \leq 10\%$) when d is less than a certain threshold ($0 \leq d \leq 18\%$). This means that small shifts of predictions are observed when the intensity of breakouts in both calibration and prediction sections is not considerably different (does not exceed $\approx 18\%$). Similarly, when calibrating on a vertical section with limited breakouts, predictions are slightly shifted if the deepest section has limited breakouts as well.
 - I_s is considerably negative ($-30 \leq I_s \leq -12\%$) when d is negative ($-65 \leq I_s \leq -43\%$) (Fig. 5.14e-h). In simple words, when calibrating on a vertical section with limited breakouts, the shift of predictions is considerably high when 'pervasive' breakouts are present in the prediction section (Fig. 5.14e-h).

The same conclusions were drawn for breakout extent as shown in Fig. 5.15. Indeed, when calibrating on breakout extent in a vertical section, predictions in the deepest are coherent with observations (i.e., $I_s \approx 0$). This is also a valid conclusion for all the studied

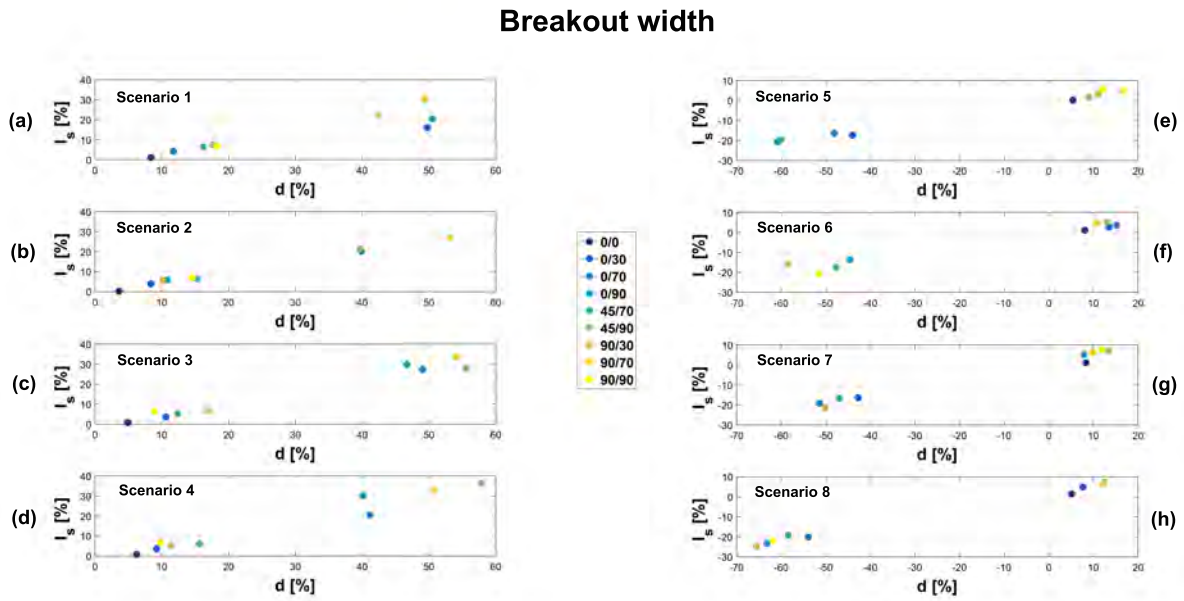


Figure 5.14.: Computed first order shift, I_s , for breakout width Vs. the difference between both the mean of the breakout width measurements in the shallowest and deepest section of the well, d . Panels from (a) to (h) correspond to Scenarios 1 to 8, respectively. The colored dots in all panels correspond to the nine studied borehole trajectories as illustrated in Fig. 5.2.

scenarios, meaning that the stress regime does not influence the shift of the predictions when considering a vertical hole. However, I_s starts to increase when deviating the borehole. When analyzing the results shown in Fig. 5.15, it can be noticed that for all scenarios 1 to 8, the shift is acceptable (less than 10%) when $0 \leq d \leq 18\%$. When d is considerably high (either positively or negatively), the shift of predictions of breakout extent in the deepest is notably high.

The statements above can be summarized as follows:

- When considering a vertical hole, predictions of breakout width and extent are consistent with the observations in the deepest, independently from the stress regime.
- When the well is deviated, 1st order predictions of both breakout width and extent are shifted compared to the mean of the observations in the deepest. This shift is either acceptable or notably high. Indeed, I_s is acceptable when the intensity of breakouts is more or less the same in both sections where calibration and prediction are performed. However, if breakouts are pervasive in the calibration section and limited in the prediction section of the well, predictions tend to overestimate breakout width and extent. Conversely, if breakouts are limited in the calibration section and more pronounced in the prediction section, then predictions underestimate the breakout width and extent, leading to incoherent predictions.

Breakout extent

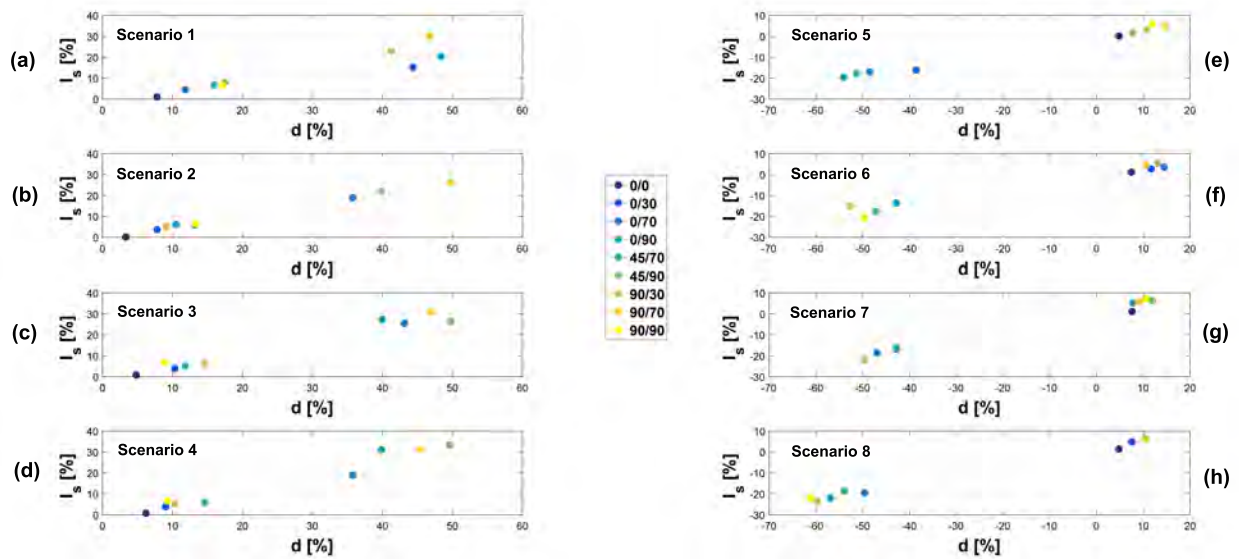


Figure 5.15.: Computed first order shift, I_s , for breakout extent Vs. the difference between both the mean of the breakout extent measurements in the shallowest and deepest section of the well, d . See the caption of Fig. 5.14 for further information.

Concerning the DITFs, predictions are coherent with the observations when the hole is vertical. However, our approach predicts more tensile conditions than observed when the well is deviating as shown in Fig. 5.16. This is valid independently from the considered stress regime, borehole trajectory or breakouts intensity along the well.

5.3.4.3. Explaining the observed shifts

To better understand the conclusions drawn previously, we have been interested in answering the following questions:

- For scenarios 1 to 4 (with 80% of breakouts present in the upper section of the well): why do we observe very limited breakouts in the deepest section only for some specific drilling trajectories? What makes these borehole trajectories distinct from others?
- For scenarios 5 to 8 (with 30% of breakouts present in the upper section of the well): why do we observe more pronounced breakouts in the deepest section only for some specific borehole trajectories? Again, what makes these borehole trajectories different from others?

To answer these two questions, the well optimization path curve as defined by Al-Ajmi and Zimmerman (2006) in Eq. 5.9 was computed for the 8 synthetic scenarios.

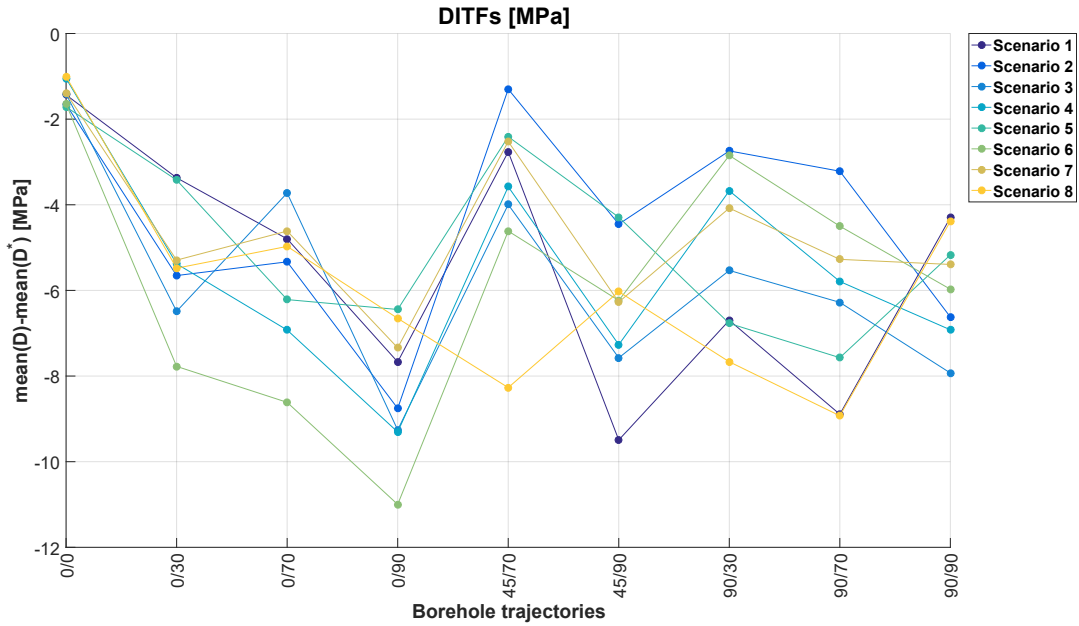


Figure 5.16.: The difference between the mean of predicted and observed DITFs (D and D^* , respectively) in the deepest section of the well, Vs. borehole trajectory. Colors scheme correspond to Scenarios 1 to 8.

Note that when calibrating on the vertical section of each one of the 8 scenarios, M well calibrated models are filtered based on the rejection criterion in Chapter 3. The stress anisotropy ratio, Φ , is computed for each calibrated model, and for each synthetic scenario. It is worth underlining that when the initial models — models to calibrate — are in a certain stress regime, the calibrated models do not necessarily have the same stress regime. Once Φ is computed, the optimum borehole drilling trajectory, γ , is calculated for each calibrated model using Eq. 5.9 (Al-ajmi, 2006). The obtained curves are plotted in Fig. 5.17. Calibrated models with NF, SS and/or TF regime are plotted in red, blue and green respectively. According to Al-ajmi (2006):

- In NF stress regime (red circles), the optimum drilling trajectory is deviated from the vertical by $i = \gamma$ in a direction parallel to the minimum principal horizontal stress, S_{hmin} ($\alpha = 90^\circ$).
- In SS stress regime (blue circles), the most stable borehole is horizontal ($i = 90^\circ$) with a drilling direction, $\alpha = \gamma$.
- In RF stress regime (green circles), the wellbore is the most stable when it is drilled in the direction of the maximum horizontal principal stress ($\alpha = 0^\circ$) with a drilling inclination, $i = 90^\circ - \gamma$, to minimize borehole instability.

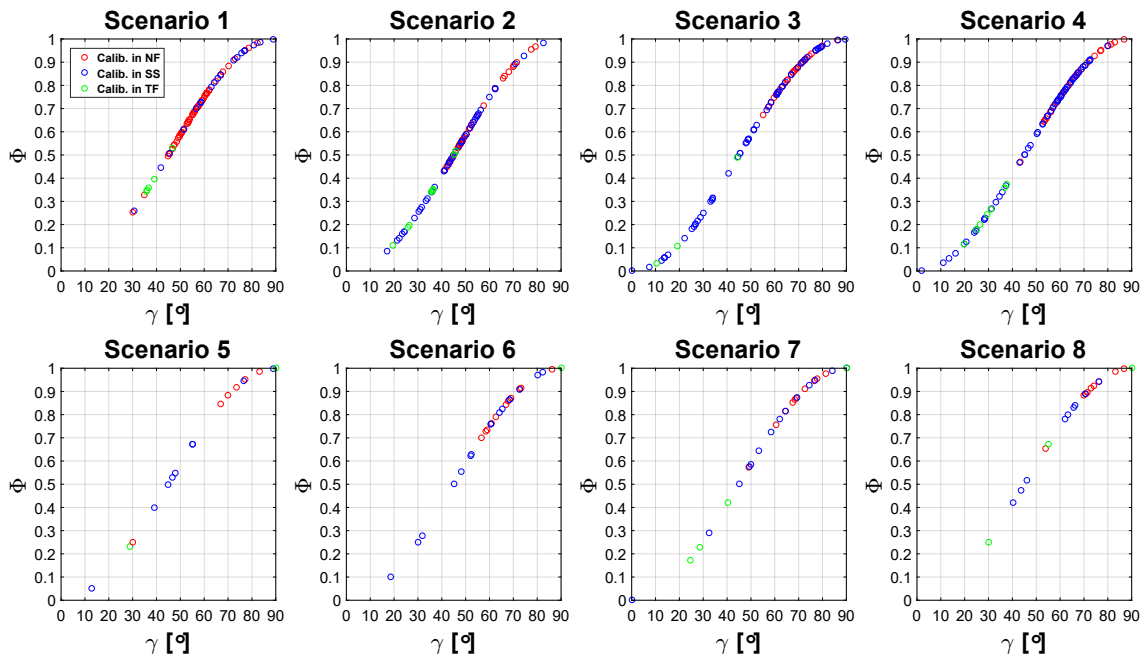


Figure 5.17.: Stress anisotropy function, Φ , Vs. the optimum well path, γ , that ensures the lowest percentage of breakouts as given by Al-ajmi (2006). Φ was computed for all the well calibrated failure models. In all panels, the circles correspond to the well calibrated failure models for each scenario. Each circle is colored depending on which stress regime the calibrated model represents: red, blue and green circles correspond to normal, strike-slip and reverse stress regimes, respectively.

Based on these curves, the most stable borehole trajectories (i.e., with the least breakouts) for Scenarios 1 to 4 are summarized in Table 5.5 and the least stable borehole trajectories for Scenarios 5 to 8 are summarized in Table 5.6.

Table 5.5 summarizes the most favorable drilling trajectories that ensure the lowest intensity of breakouts in the case of scenarios with 80% of breakouts in the upper vertical section of the well (Scenario 1 to 4). These trajectories were extracted from Fig. 5.17. Interestingly, the listed favorable borehole trajectories (based on Eq. 5.9, (Al-ajmi, 2006)) correspond to the drilling trajectories with the highest d and I_s in Fig. 5.14. Indeed, when deviating the borehole to these directions, less breakouts are formed, meaning that the difference between the mean of observations in the vertical and the deepest part is considerable (hence, the high values of d for these trajectories when considering Scenarios 1 to 4). As our failure models were calibrated on a vertical section with pervasive breakouts, predictions are unable to predict very small intensity of breakouts in the deepest, and thus, I_s is high for these borehole trajectories.

Table 5.5.: The most favorable drilling trajectories for Scenarios 1 to 4 based on the optimized well path proposed in Al-ajmi (2006).

Scenario	α [°]	i [°]
Scenario 1	0	30
	0	90
	90	30
	90	70
Scenario 2	0	70
	45	90
	90	70
Scenario 3	0	70
	45	90
	90	70
Scenario 4	0	70
	0	90
	45	90
	90	70

Table 5.6 however summarizes the 'worst' drilling trajectories where breakouts are more pronounced when considering Scenarios with 30% of failure. The listed trajectories correspond to the smallest d and I_s in Fig. 5.15. Indeed, when deviating the borehole to these directions, the percentage of breakouts increases, meaning that the difference between the mean of observations in the vertical and the deepest section is considerably negative. In the same line of arguments, as our failure models were calibrated on a vertical section with limited breakouts, predictions are unable to predict 'pervasive' breakouts in the deepest, and thus, the shift I_s is extremely negative for these borehole trajectories.

5.3.4.4. Dispersion of the 1st order predictions

Computing the shift of the predictions is not enough to decide of their goodness. It is then useful to calculate the dispersion of these 1st order predictions in order to quantify their dispersion. To that end, the 1st order dispersion indicator, noted as I_{1d} , is calculated for all scenarios and for the three borehole failure indicators, w_{BO} , e_{BO} and DITFs as shown in Fig. 5.18. I_{1d} is defined as the standard deviation of the envelop of all predictions. Results show that when considering a vertical hole, the dispersion of the predictions is very small independently from stress regime and the percentage of breakouts affecting the borehole. For instance, $I_{1d} \leq 9^\circ$ when predicting breakout width in a vertical well for all scenarios (Fig. 5.18a and d) and $I_{1d} \leq 0.05$ when predicting breakout extent in a vertical well for all scenarios (Fig. 5.18b and e). This means that in addition to the fact

Table 5.6.: The least favorable drilling trajectories for Scenarios 5 to 8 based on the optimized well path proposed in Al-ajmi (2006).

Scenario	α [°]	i [°]
Scenario 5	0	30
	0	70
	0	90
	54	70
Scenario 6	0	90
	45	70
	90	30
	90	90
Scenario 7	0	30
	0	70
	45	70
	90	30
Scenario 8	0	70
	0	90
	45	70
	90	30
	90	90

the predictions are not shifted when considering vertical holes, they are also not dispersed, which outlines the accuracy of the predictions in this case and their consistency with the observations. However, the dispersion starts to get higher when deviating the well.

The dispersion of the models when predicting the DITFs is quite difficult to explain. Fig. 5.18c-f shows that the dispersion is important but no general trend is noticed. The dispersion is indeed independent from the stress regime but the influence of the borehole trajectory is not clear.

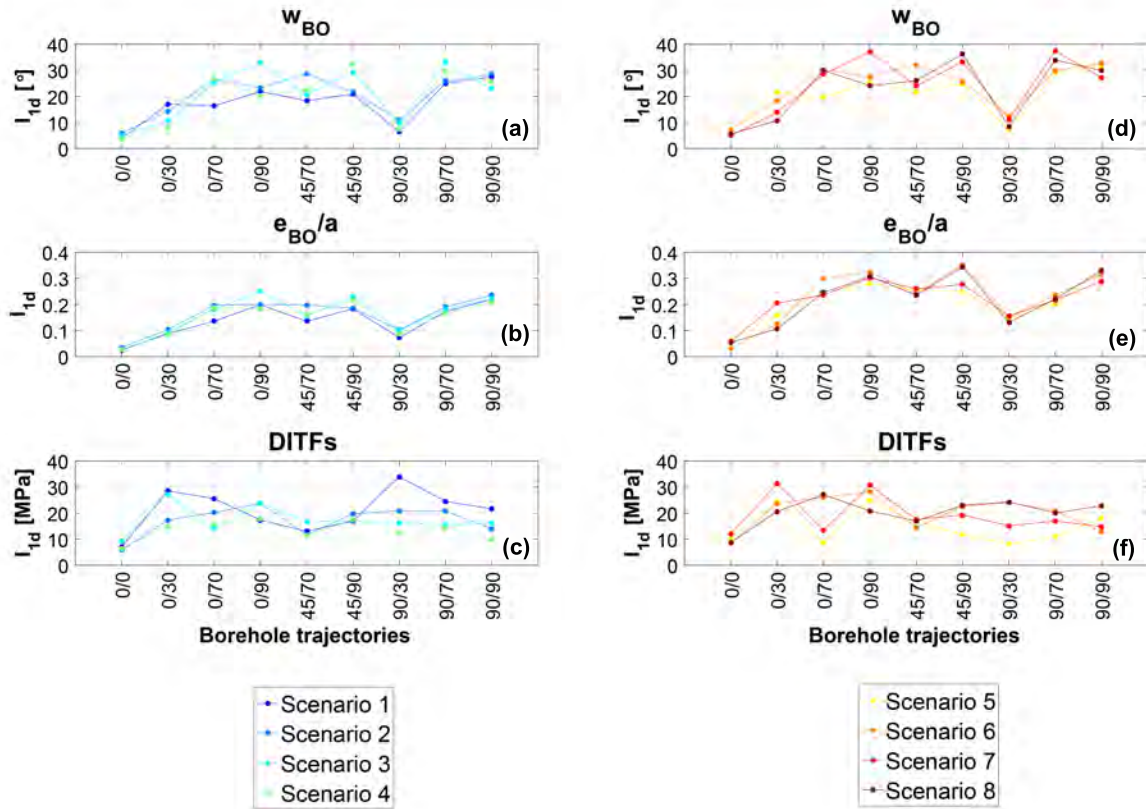


Figure 5.18.: Computed dispersion of the 1st order predictions Vs. borehole trajectory for all scenarios. (a), (b) and (c) correspond to scenarios 1 to 4 with 80% of breakouts present in the upper section of the well and (d), (e) and (f) represent scenarios 5 to 8, with 30% of breakouts in the upper section. The first order dispersion, noted as I_{1d} , is computed for: breakout width, breakout extent and DITFs. Note that scenarios are represented by a color scheme in each panel.

5.3.5. Dispersion of the 2nd order predictions

Local scale variability has been shown to be typically large (Valley, 2007) in crystalline rocks and must be accounted for in meaningful predictions. To fulfill this mission, 2nd order calibration were carried out in the vertical section of the well using the methodology proposed by Dahrabou et al. (2022b). The calibration process was performed only for

scenarios 1 and 5 as they represent different intensity of breakouts. We assume here that the estimated deviations of a given parameter around its calibrated mean (represented by ϵ in Eq. 5.5) does not change noticeably when the stress regime is different. The estimated deviations, ϵ , are then simulated to a greater depth using direct sampling method (DS) as implemented in DeeSse (Straubhaar, 2019), added to the 1st order calibrated depth profiles and then 2nd order predictions are performed. The outcomes of these predictions were quantified by computing a 2nd order dispersion indicator, I_{2d} of Eq. 5.8

Fig. 5.19 shows the calculated 2nd order dispersion indicator, I_{2d} for all scenarios. For a vertical well, the second order dispersion indicator is very small ($I_{2d} \leq 0.1$), meaning that our predictions are able to reproduce the variability in the deepest section of the well. However, when the well is deviating, a general trend is noticed in all panels of Fig. 5.19. This dispersion is more considerable when the well is horizontal ($\alpha=90^\circ$ and $i=90^\circ$). Finally, models predicting DITFs are all dispersed even for a vertical hole, which highlights the uncertainties amongst these predictions.

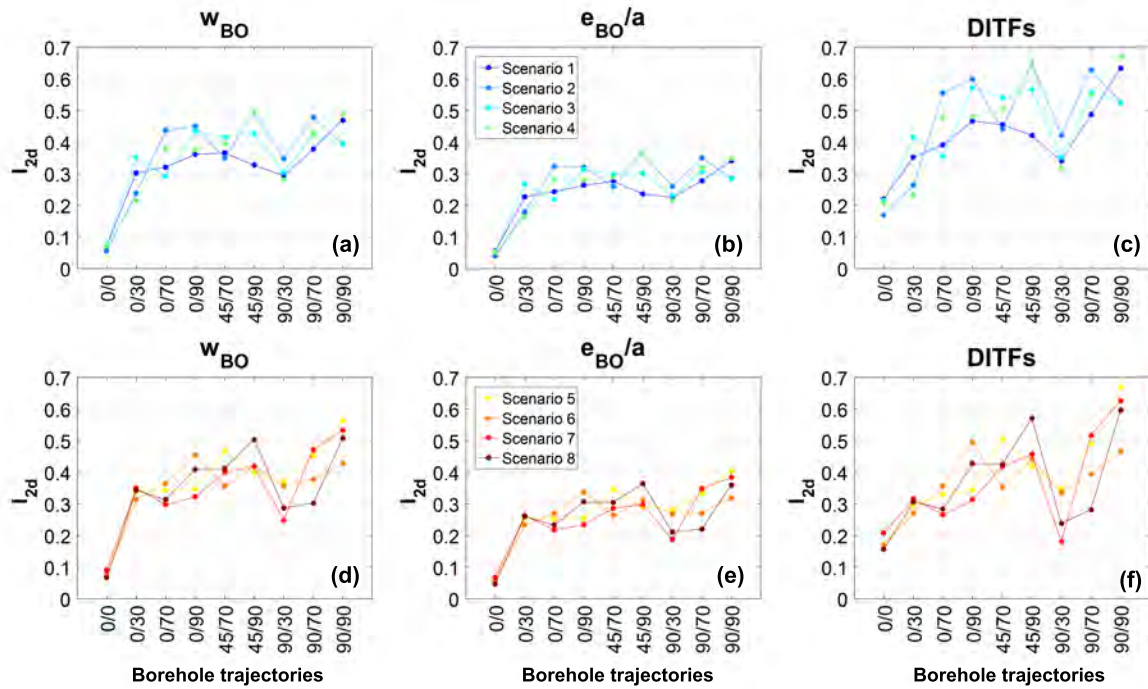


Figure 5.19.: Computed dispersion of the 2nd order predictions Vs. borehole trajectory for all scenarios. (a), (b) and (c) correspond to scenarios 1 to 4 with 80% of breakouts present in the upper section of the well and (d), (e) and (f) represent scenarios 5 to 8, with 30% of breakouts in the upper section. The 2nd order dispersion, noted as I_{2d} , is computed for breakout width, breakout extent and DITFs. Note that scenarios are represented by a color scheme in each panel.

5.4. Discussions

5.4.1. Quality of 1st order calibration

The 1st order calibration performed in the shallowest section (which is essentially vertical) of the studied wells showed satisfying results for all scenarios, confirming as such the efficiency and accuracy of the proposed calibration methodology proposed in Chapter 3 independently from the stress regime. So far, this is a validated conclusion for a vertical borehole, but no indication is available to believe that this will not be as well efficient in a deviated borehole.

A very important point to highlight is the percentage of the well calibrated models in scenarios where 80% and 30% of the boreholes sections are affected by breakouts. In the first case, 91% of the models were coherent and consistent with observations and could be retained as adequately calibrated models, whereas only 40% were found to be well calibrated in the second case. This outlines two interrelated important observations: (1) the calibrations quality is affected by the intensity of breakouts, i.e., when few breakouts are affecting the well, few models are well calibrated based on the filtering criterion we defined in Chapter 3 and (2) the used approach in the calibration methodology to consider depths where failure does not occur has some limitations. Observation (1) certainly follows at least in part from observation (2). In other words, our calibration methodology requires continuous numerical parameters and we represent the absence of breakouts by considering the breakout width being equal to 0° . In reality when no breakout occurs, we do not know what is the "distance to failure". This is illustrated in Fig. 5.20 where the maximum, intermediate and minimum effective principal stresses at the wellbore wall as a function of θ , the angle around the borehole for two different cases with different S_{Hmax} and S_{hmin} are shown. All other parameters are identical for these two examples. The Mohr-Coulomb failure criterion (dashed black line) does not intersect σ_1 in both cases, meaning that there is no breakout in these cases, however it is obvious from Fig. 5.20 that the first case (left) is much closer to failure than the second case (right). In our approach these two situations will however be treated identically: breakout width $w_{BO} = 0^\circ$ will be considered for both cases in our calibration process. Consequently, this will include a bias in the PEST calibrations and sets of parameters leading to situations far from failure may be under represented in our calibrated models. This bias is more severe when few breakouts are present along the considered well. Consequently, further work has to be done to deal with this issue. One can define a penalty function in PEST that accounts for discontinuous or Boolean variables so that PEST algorithm can calibrate on presence/absence of breakouts in addition to the consideration of breakout width when breakouts occurs. This limitation did not seem as important when developing our approach on the Basel data, because in this case breakouts are pervasive and the induced bias is negligible. It appears however from this systematic evaluation using the synthetic cases that this limitation could be problematic when only few breakouts occur on the calibration section.

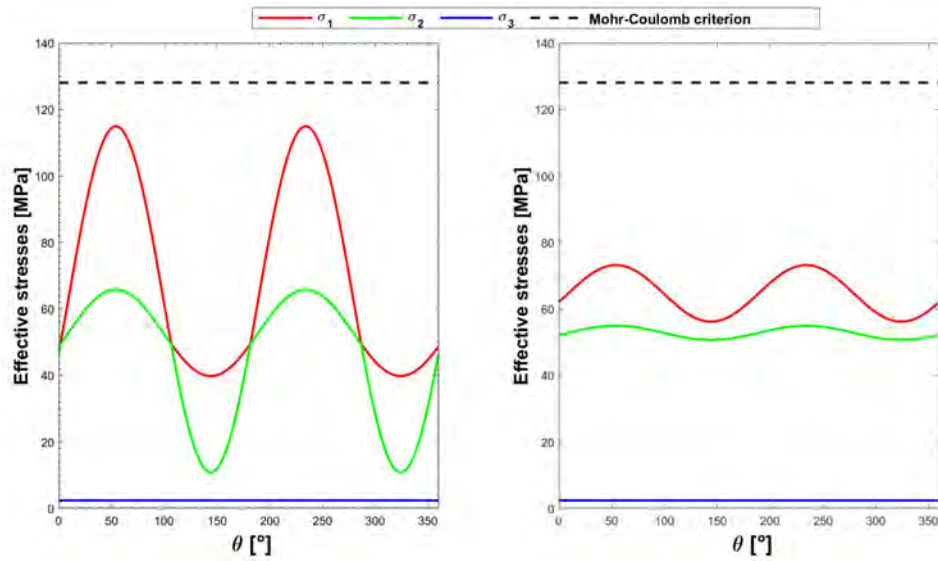


Figure 5.20.: Two examples where breakout do not occur, but with stress conditions and distance to failure significantly different. The effective principal stresses are presented as a function of θ , the angle around the borehole. The maximum, intermediate and minimum effective principal stresses, σ_1 , σ_2 and σ_3 , are plotted in red, green and blue respectively. The dashed black line depicts the yield line computed by using the Mohr-Coulomb failure criterion. On the left, $S_{Hmax}=80$ MPa, $S_{hmin}=54$ MPa and on the right, $S_{Hmax}=70$ MPa, $S_{hmin}=65$ MPa. The rest of the parameters are common to both cases: $UCS=128$ MPa, $S_v=87$ MPa.

5.4.2. Failure predictions quantification

5.4.2.1. Failure prediction in a vertical well

In this chapter, the outcomes of both 1st and 2 order calibration were used to predict failure severity in the deepest section of the well. The main objective is to apply and test our calibration and prediction methodology (Chapters 3-4) on synthetic cases investigating a much broader range of conditions that can be encountered in real field cases (different stress regimes, borehole trajectories and intensity of breakouts). Results show that both 1st and 2nd order predictions were accurate and consistent with observations when the well is vertical. This lends support to previous findings in Chapter 4 where the sub-vertical BS-1 borehole was used and adds additional information: the predictions are reliable in a vertical well independently from the considered stress regime or the breakouts intensity along the borehole. Indeed, the computed shift and dispersion indicators in this case showed very satisfying results, i.e., a 1st order shift, $I_s \approx 0$, 1st order dispersion, $I_{1d} \text{ leq } 9^\circ$ and a 2nd order dispersion, $I_{2d} \leq 0.1$. This means that (1) the mean of predictions is superimposed with the mean of the observations, (2) the envelop of 1st order predictions is narrow and centered on observations and (3) the 2nd order predictions are able to reproduce the variability observed in observations.

5.4.2.2. Failure prediction in a deviated well

We were aware that our calibration and prediction methodology may have some limitations when the well starts deviating. This was firstly illustrated by calibrating parameters against a single breakout at a given depth and performing predictions for different borehole trajectories (stereographic presentation of these results in Fig. 5.7). Results show that when considering a vertical hole, predictions are converging, whereas they diverge when the well is deviating. We argue that this is mainly due to the sensitivity of borehole failure to the vertical stress magnitude. Indeed, the stress anisotropy ratio has a considerable impact on predictions when the well is deviated, and thus if this ratio is not properly calibrated, the predictions diverge.

More complexity were added to our methodology by calibrating and predicting not only at a given depth but along the entire length of the well. The shift, 1st and 2nd order dispersion of predictions were quantified as well. Results show that when deviating the well, the predictions start to shift depending on the (1) stress anisotropy ratio and on (2) the difference of breakouts intensity in calibration and prediction sections. Indeed, when the well is deviating, the shift of predictions is acceptable only if both calibration and prediction sections have approximately the same breakouts intensity (i.e., pervasive-pervasive, limited-limited breakouts). If the intensity of breakouts is markedly different in both sections, the shift becomes notably high, meaning that our predictions are no more consistent and coherent with observations. These findings raised our curiosity of better understanding the reason why intensity of breakouts changes markedly between calibration and prediction sections only for some specific drilling trajectories. Thanks to the relationship between stress anisotropy and the optimum well path derived by Al-ajmi (2006), some important findings were highlighted. Indeed, the drilling trajectories for which breakouts intensity changes from being 'pervasive' in the shallower to 'limited' in the deepest section of the well, are the most favorable borehole trajectories that ensure the least breakouts. Similarly, the trajectories for which breakouts intensity changes from being 'limited' in the upper section and very pronounced in the deepest, coincide with the worst drilling trajectories in terms of stability according to Al-ajmi (2006). This explains the observed high shift of predictions for these specific borehole trajectories.

The 1st and 2nd order dispersion indicators showed that the distribution of predictions gets larger when the well is deviating and that they are no more consistent with observations. These anticipated results may be explained by the fact that when deviating the well, S_v is no more vertical and orientations of the three principal stresses impact calibrations and inevitably predictions. Despite the limitations of our calibration-prediction methodology when applying it to deviated boreholes, our findings do nevertheless suggest that when the angular difference between the calibration and prediction section do not exceed 30°, our estimation of the breakout width are typically precise within a shift of $\approx 10^\circ$ for breakout width and less than 5% for breakout extent, which is deemed to provide useful information for practical well design. Beyond these points, our massive calibrated

approach covers a large number of possibilities leading to diverging predictions. We suggest here to consider carefully the breadth of possibilities and to generate stereographic representation of the of the failure severity pattern for a number of calibrated cases in order to evaluate favourable wellbore trajectories. Thus, our calibration and prediction methodology as proposed in Dahrabou et al. (2022b,a) should be improved by (1) calibrating the ratio between horizontal principal stresses and S_v , (2) adding some available measurements of stresses, i.e., S_{hmin} estimate from XLOTs, to help narrowing the calibrated profiles range and thus reducing the divergence of predictions. We expect that adding this information will have a noticeable impact on the predictions spread and thus will improve the reliability of the predictions.

5.5. Conclusions

In this chapter, we have been interested in testing the limits of our calibration and prediction methodologies as developed in Chapters 3-4. This is mainly because the proposed workflow was applied only to the extensive borehole data set along the crystalline section of the borehole BS-1, in Basel (Switzerland) (Håring et al., 2008; Valley and Evans, 2009a, 2019). This borehole is sub-vertical over its entire length and thus, it is not appropriate to test the robustness and accuracy of our approaches when the borehole is deviated. Also, 80% of this borehole is affected by breakouts and the calibration and prediction methodology was still not applied on a borehole with few breakouts to test its reliability. To fulfill these objectives, synthetic cases were generated in order to investigate a much broader range of conditions that can be encountered in real field cases. Scenarios with different stress regime conditions, borehole trajectories and failure intensity were generated. This led to a variety of scenarios that cover a wide range of possibilities. Our key findings are itemized next:

- Our calibration methodology (Chapter 3) shows accurate results independently from the stress regime but its quality is influenced by the intensity of breakouts that affect the borehole. When few breakouts are present, our calibration methodology is less efficient at finding calibrated set of parameters.
- 1st and 2nd order predictions are accurate and consistent with observations in the case of a vertical well, independently from the stress regime or breakouts intensity.
- 1st order predictions start to shift when the well is deviating. This shift was quantified by defining an appropriate metric. The latter showed that this shift is acceptable or not depending on the (1) stress anisotropy ratio and (2) the difference of breakouts intensity in both calibration and prediction sections.
- Borehole trajectories for which the computed shift was notably high coincide with either the most favorable or the worst drilling trajectories in terms of borehole sta-

bility. This finding was based on the relationship between stress anisotropy and optimum well path derived by Al-ajmi (2006).

- When pervasive breakouts are affecting the calibration section, and few breakouts are formed in the deepest (because the considered borehole trajectory is the most stable according to Al-ajmi (2006)), predictions overestimate failure. Similarly, when few breakouts are present in the calibration section but more pronounced in the deepest (because the considered trajectory is the worst in terms of stability), predictions tend to underestimate failure.
- The shift is however acceptable for practical purposes when the prediction section deviation do not differ from more than 18% of the calibration section.
- When quantifying predictions dispersion by defining the appropriate metrics, results show that 1st order predictions envelop is narrow and that the variability is satisfactorily reproduced in the 2nd order predictions. This finding is valid only for a vertical well independently from the stress regime and the breakouts intensity.
- When the well is deviating, dispersion is markedly increasing, leading to predictions with a spread that increases, when the borehole deviation is increasing as well. This is valid for all stress regimes.

6. Deep Geothermal Well Optimization Workflow (DG-WOW) application

6.1. Introduction

6.1.1. Scope and objectives of the 'DG-WOW' application

The Deep Geothermal Well Optimisation Workflow (DG-WOW) aims at providing decision support tools for optimising deep geothermal well trajectories. The applied outcome of this work is a set of supporting software tools (referred to as the DG-WOW-app) to assist with the application of the workflow. This work being supported by InnoSuisse and the industry, it was important to insure that the knowledge and processes developed in this thesis are transferred to the industry. A software tool with a Graphical User Interface (GUI) is the most efficient way to allow practitioners to apply the workflow and thus enable the knowledge transfer.

In practice, it is important to be able to apply the workflow quickly in order to avoid drill rig downtime. The objective of this workflow is to provide a systematic approach to select the most appropriate drilling direction, which is defined as the one that promotes wellbore stability while intersecting as many as possible potential feed zones. The optimal trajectory of the borehole is critical as it influences the wellbore injectivity and productivity, which in turn will have a decisive impact on the performance of the future geothermal plant. Moreover, the stability of the wellbore is essential to enable zonal isolation and to prevent drilling delays associated with an unstable borehole. Obtaining this result as quickly as possible is important, because it has to be done while the (expensive) drilling equipment is on hold. Thus, the primary objective of this workflow is risk and cost reduction for deep geothermal well drilling operations. It was intent on developing the workflow for the Haute-Sorne project. The phased development plan of the latter imposes the overall structure of the workflow. It starts first with a vertical drilling section along which one can collect and analyse relevant data in order to propose an optimal direction of the subsequent deviated section. This sequence of operation is somewhat specific to the Haute-Sorne project, but the intent is to have a more versatile tool that can be adapted to various projects.

The purpose of this chapter is to present the DG-WOW-app which is the practical translation of the calibration-prediction workflow developed in Chapters 3 and 4 of this thesis. This section is not a user guide of the application, which is the purpose of another document not part of this thesis, but it is an illustration of the practical application of the

workflow. For illustration purposes, the dataset from the Basel deep geothermal borehole, BS-1, were used.

6.1.2. Guiding principles

The context and purpose of the project lead us to follow some guiding principles for this workflow:

Workflow main targets: The first key element of this workflow is to minimize wellbore instabilities and the second element is to maximize intersections with potential feed zones.

Calibration and prediction: The workflow is based on two main phases: a first phase where the reservoir parameters (i.e., stress and strength) are calibrated against data set obtained from the shallower section of the wellbore that will be essentially vertical and a second phase where predictions are performed for potential deepest and deviated wellbore section.

Non-uniqueness of calibration: It was shown previously (Chapter 3) that the studied inverse problem is ill-posed as multiple non-unique parameter sets can reproduce equally the observation data. Thus, a multitude of sets of parameters spanning the space of possibilities should be identified with a systematic calibration approach. The latter will be used in a probabilistic manner in order to predict failure in the deepest section of the well.

Rapidity of the workflow: The decision concerning the optimal borehole trajectory must be taken rapidly in order to limit expensive rig downtime.

Approximate analytical solution: The failure model to be used should be efficient and easy to implement because we need to (1) consider a multitude of solutions and (2) take a rapid decision for optimal borehole trajectory selection. To that end, a simple analytical solution were used to compute borehole failure (closed-form analytical solution of Kirsch (1898)).

Consideration of natural variability: Natural variability in stress and/or strength leads to large variability in borehole conditions. Considering this variability, i.e., estimating the statistical distribution of the parameters, is required for risk assessment. Thus, we developed a two steps approach with not only the general trends being reproduced (1st order characterization) but also the variability around these 1st order trends (2nd order characterization). Such approach is in-line with stress characteristic observations in the earth crust (Zoback, 1992) and related site stress characterisation strategies (Stephansson and Zang, 2012).

6.2. Overview and implementation of the workflow

6.2.1. Workflow overview

The workflow is divided into three main sections:

1. Data pre-processing.
2. Failure models calibration and identification of critically stressed fractures.
3. Failure prediction and evaluation.

Each section is subdivided into many steps. Each step is briefly described in Fig. 6.1. One important step in this application is the data preparation section. The latter is instrumental for the successful execution of the workflow. Indeed, in this section, all the required data are loaded, pre-processed and prepared for the calibration process. The model calibration section is the central part of the workflow and the most critical step. During the calibration process, fundamental parameters for failure prediction (i.e., stress and strength) are estimated. This is also the most time-consuming process. Note that we perform the calibration in two steps: (1) 1st order calibration to determine the linear trends of the parameters of interest and (2) 2nd order calibration to characterize the variability of these parameters around their trends. Finally, the failure prediction section allows to evaluate various drilling scenarios based on the model calibration outputs and to identify the optimal trajectories for which the borehole is stable and intersects the maximum of feed zones. The required initial data for each phase are listed in Fig. 6.2.

6.2.2. DG-WOW-app implementation

The DG-WOW-app in its current form is an operational prototype, i.e., it is fully functional, but could be programmed in a more efficient way. The core of the app is coded in MATLAB. This part guides the user through the entire workflow, reads/writes and executes the files required to interact with other softwares. The core computation of the app, i.e., stress and failure computation around a borehole are also coded in MATLAB.

Some operations are best performed in or by other softwares. This is the case for some logging data handling that is best done within the *WellCADTM* software. It is not required to rebuild such functionality in the app. Only functionality that are not satisfying in *WellCADTM* (e.g., breakout geometry measurements) are implemented in the DG-WOW-app. Reading and writing of *WellCAD* ASCII format is built in the application in order to expedite data transfer.

The calibration sections of the workflow are performed using PEST software (Doherty, 2015). The DG-WOW-app prepares all the required files and executes the calibration process using multiple starting points. It also reads and integrates the calibration outputs. Figures are automatically created in order to illustrate the obtained results.

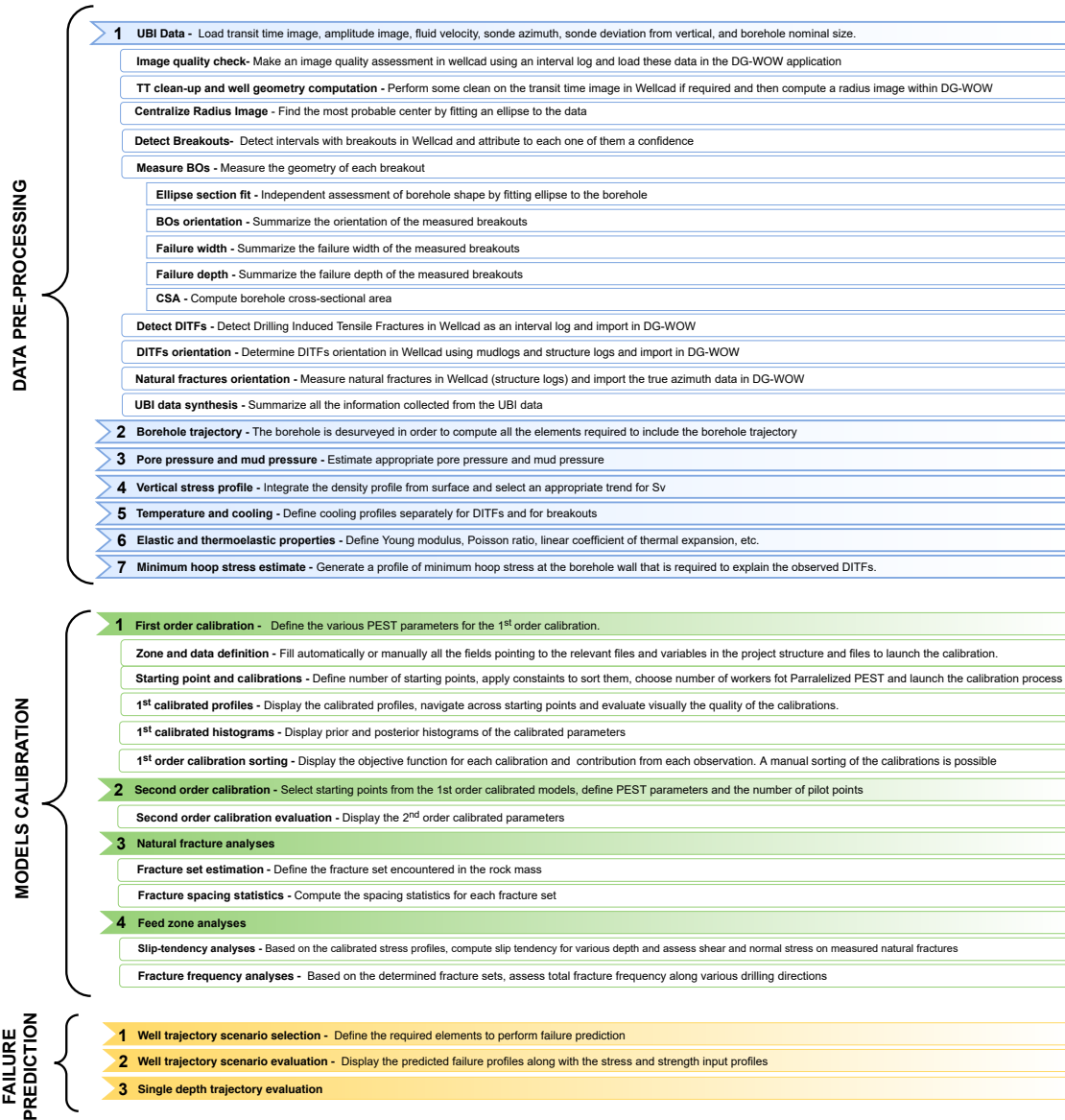


Figure 6.1.: Overview of the entire workflow that were implemented in the 'DG-WOW-app' with a brief description of each step.

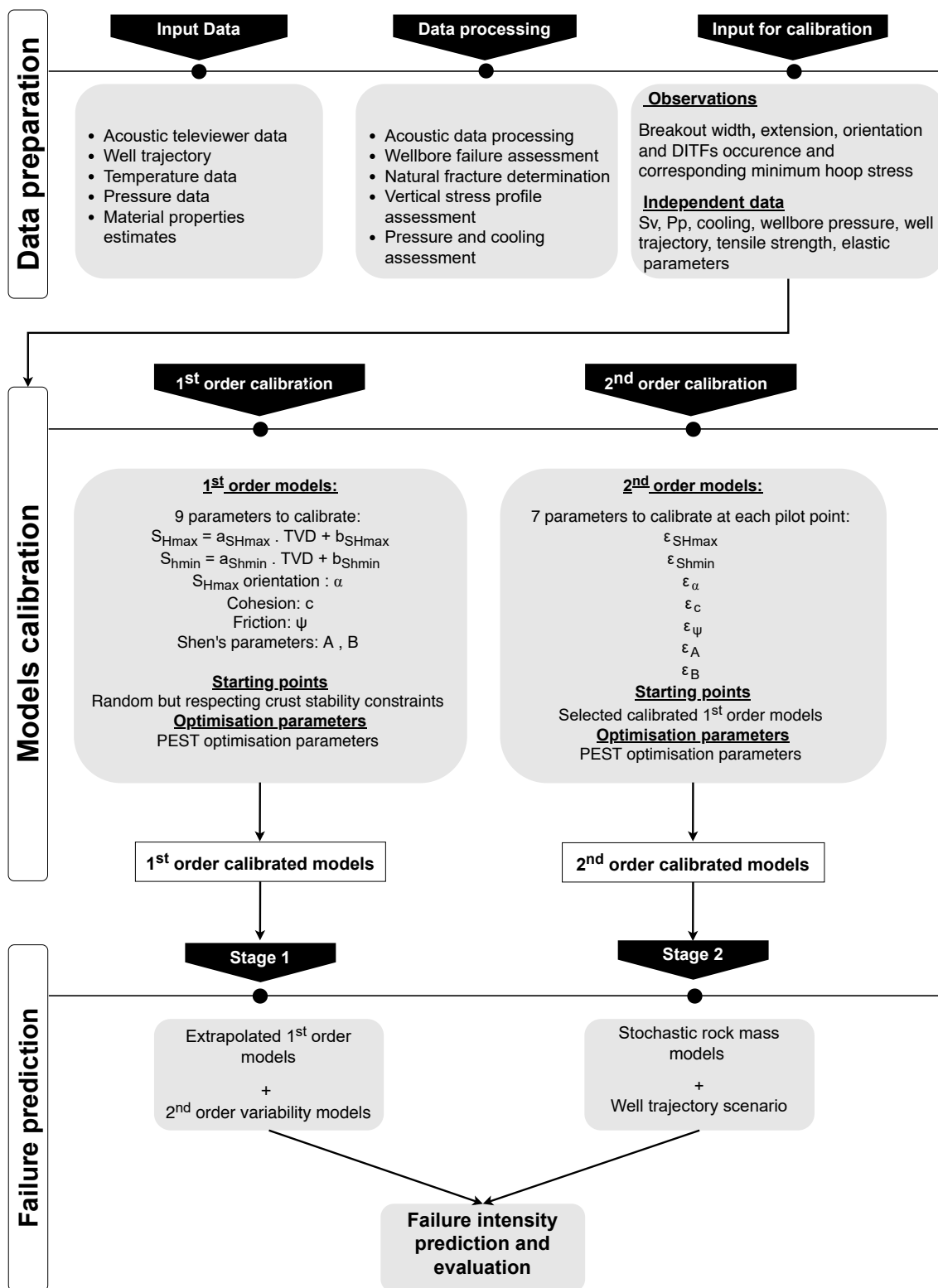


Figure 6.2.: Summary of the main required initial data for each phase of the implemented workflow.

Finally, stochastic realisations are performed using the DeeSse algorithm (Straubhaar, 2019). The required reading/writing/execution functionalities are built in the DG-WOW-app.

6.3. Presentation of the DG-WOW application using the BS-1 borehole data

In this section, we illustrate the functionalities of the DG-WOW-app by showing and describing the most relevant steps to the developed calibration and prediction approaches in Chapters 3 and 4. The extensive data set from the BS-1 borehole were used as a test bed for the developed application. Firstly, note that this GUI is made of a main window with a workflow tree on the left and a main panel (Fig. 6.3). Performing the workflow consists of stepping through each item of this tree. Icons (red cross or green tick mark) indicate if a tree item, i.e., a step in the workflow, has already been completed or not. On the main panel, one can load, process and display data.

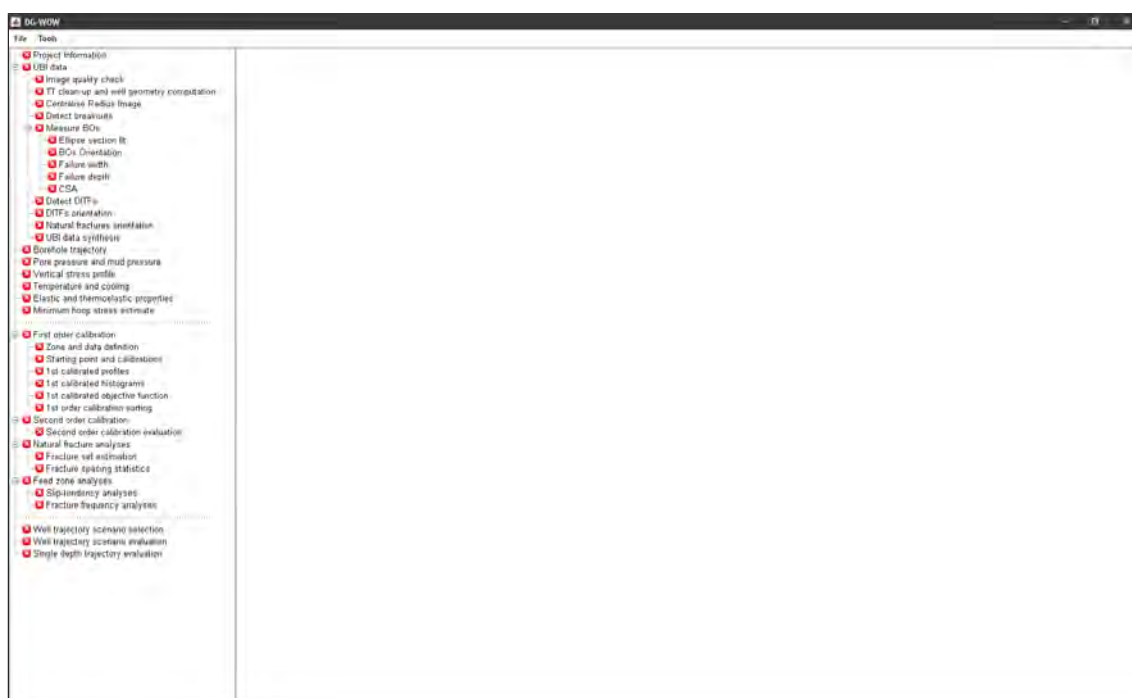


Figure 6.3.: View of the interface of the application consisting in a workflow tree (left) and a main panel to display relevant information for the analyses (large white area in this figure).

6.3.1. Data pre-processing - UBI data synthesis

At this stage all the key information derived from acoustic televiewer logs are uploaded and required data are extracted. Various steps were completed before heading to this stage (i.e., image quality check, transit time clean-up and well geometry computation, detecting breakouts and drilling induced tensile fractures (DITFs), measuring breakouts, etc.). The 'UBI data synthesis' tab offers a synthetic display of all these data. Bringing all the data together in a coherent manner is an important milestone along the workflow. This data set is the base on which depend all subsequent workflow steps. The synthetic

view provided in the DG-WOW-app allows verifying that all the pre-processed data are consistently compiled before moving to the next steps of the workflow. This synthetic view is presented in Fig. 6.4.

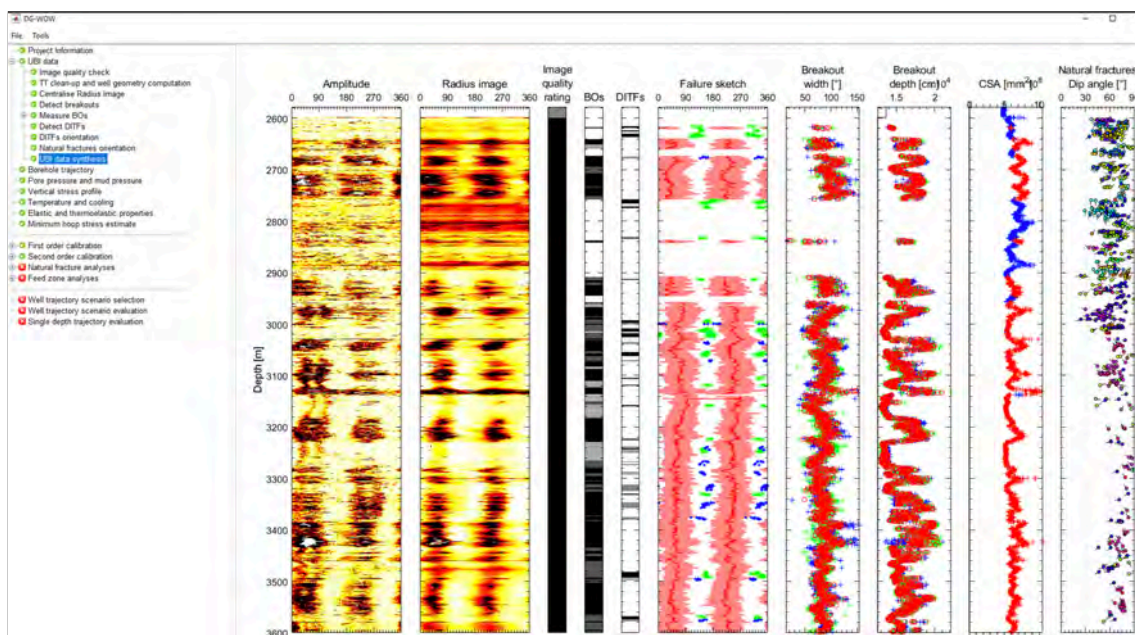


Figure 6.4.: UBI data synthesis panel: from left to right: amplitude image, radius image, image quality rating, breakouts intervals, drilling induced tensile fractures (DITFs) intervals, sketch of stress induced failure, breakout width, breakout extent, cross-sectional area and natural fractures tadpole plot. This example illustrates the failure data of BS-1 borehole between ≈ 2578 m and 3600 m.

6.3.2. Failure models calibration

When all information needed is pre-processed, formatted and compiled by following the first part of the workflow as described in Section 6.3.1 and synthesized in Fig. 6.1, the calibration of failure models (i.e., stress and strength) is initiated. The latter is performed in two phases: 1st and 2nd order calibration. Both phases are performed in a sequence of steps that allow the parametrization of the calibration and the evaluation of its outputs.

6.3.2.1. 1st order calibration

6.3.2.1.1. Zone and data definition: In the first step of the 1st order calibration, the calibration name is created and the PEST specific parameters are defined. Then, the zone of interest and data required to perform the calibration must be defined. On the panel of this step, two main elements are presented (Fig. 6.5):

1. in the upper part of the panel, all the needed data to calibrate are defined either as *static parameters* (white boxes), *observations* that will be used in the calibrations (green boxes) or as *parameters to be estimated* in the calibration process (red boxes).

- in the lower part of the panel, a summary of some key data required for and used in the calibration are displayed.

In the example showed in this panel (Fig. 6.5), we calibrate maximum and minimum principal horizontal stresses (named as ' s_1 ' and ' s_2 ', respectively), Euler's angle (noted as ' a ' in the GUI), cohesion ('coh'), internal friction angle ('fric') and Shen's parameters A ('Ashen') and B ('Bshen'). The aforementioned parameters are calibrated from 3000 to 3600 m (grey shaded area in the lower part of the panel) against four types of observations: breakout width ('BBOwidth'), breakout extent ('BBOext'), breakout orientation ('BBOtheta') and DITFs ('DITFshm'). The rest of the parameters required for the calibration process are defined as static. All the input are automatically populated from the pre-processing step but the user can modify them following his own requirement. The input of each parameter can be constant values, functions of measured depth (MD) or true vertical depth (TVD) or file names (.csv, .mat) pointing to relevant data.

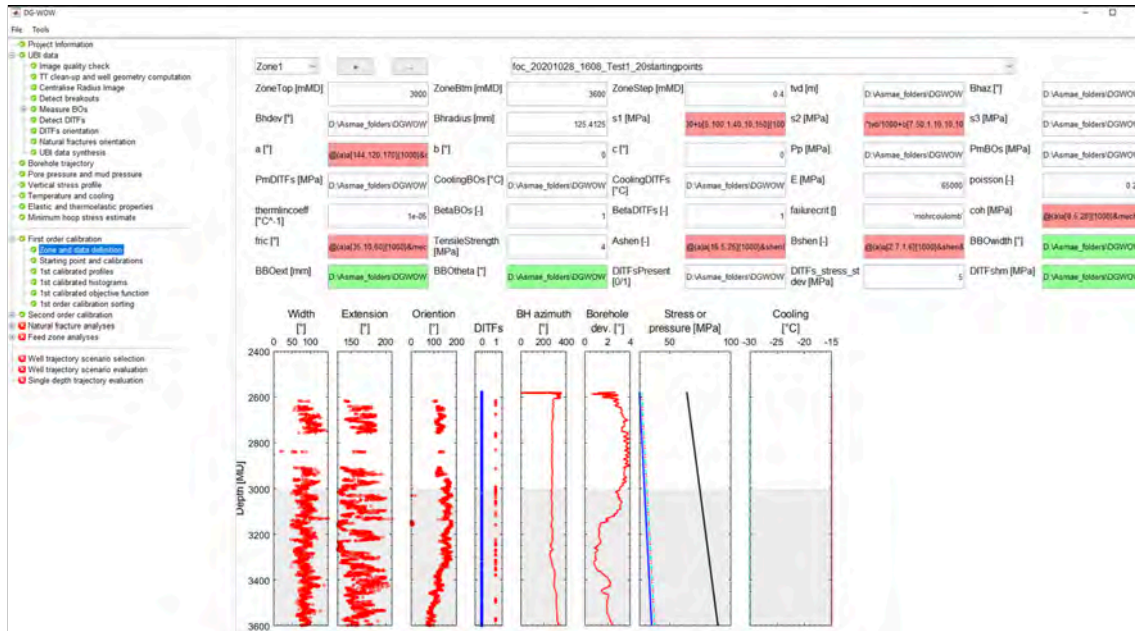


Figure 6.5.: Definition of the zones where calibration will be performed and required data of each zone such as *static parameters* (white boxes), *observations* (green boxes) and *parameters to be estimated* (red boxes). The shaded grey area in the lower part of the panel depicts the zone of calibration.

6.3.2.1.2. Starting points and calibrations: The 1st order calibrations are initiated from a set of starting point in order to cover the space of all possible calibrated parameter set. The number of starting points and their range need to be defined. In the example presented in Fig. 6.6, 20 starting points were used. They are automatically generated by random draw from uniform distributions within the bounds described in the "Zone and data definition" tab (Fig. 6.5). The detailed process of generating the prior distribution of the input parameters is fully described in Chapter 3. These starting points are then

validated against constraints (Section 3.5.1). If a starting point does not meet these constraints, it is eliminated and new random draws and validations are made until the target number of valid starting points are met. This process leads to starting points that do not necessarily follow a uniform distribution. This is illustrated in the histograms shown in Fig. 6.6. Note that the calibrations can be performed using PEST (preferred method) or a MATLAB routine (quicker but experimental and less robust). In order to speed up PEST calculations, one can use parallel computations. To that end, the number of workers has to be defined in the `nworkers` field. The appropriate number of workers will depend on the used machine's characteristics. Once the starting points are generated and their distribution is constrained, the calibration process can be launched ('Start calibration' button).



Figure 6.6.: An example of prior distributions (displayed as histograms) of the input parameters to be calibrated for 20 starting points. From left to right: slope and offset of S_{Hmax} , noted as $s1_a$ and $s1_b$ respectively; slope and offset of S_{Hmin} , noted as $s2_a$ and $s2_b$ respectively; Euler's angle, a_a , cohesion, coh_a , friction, $fric_a$, and Shen's regression parameters, $Ashen_a$ and $Bshen_a$. Lower and upper bounds for each parameter are defined by the user and displayed next to each parameter's name.

6.3.2.1.3. 1st calibrated profiles This panel shows the calibrated depth profiles of stresses and the corresponding borehole failure (breakout width, extent, orientation and DITFs). Fig. 6.7 shows the calibrated depth profiles of stresses (green and red linear profiles depict S_{Hmin} and S_{Hmax} , respectively), breakout width, breakout extent, breakout orientation and DITFs (represented by the grey profiles). This allows evaluating visually the quality of the calibrations as it is possible to navigate across starting points: one can

select a starting point and display the corresponding calibrated profiles as shown in black in Fig. 6.7.

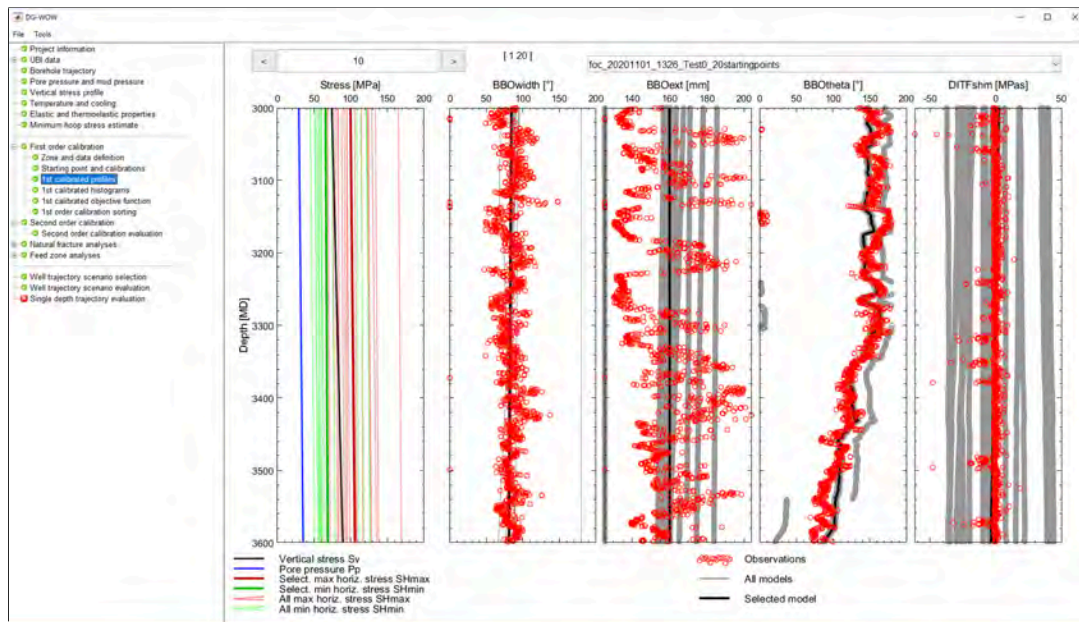


Figure 6.7.: Outputs of the 1st order calibration of 20 starting points. From left to right: calibrated depth profiles of stresses (green and red linear profiles depict S_{hmin} and S_{Hmax} respectively), calibrated breakout width, breakout extent, breakout orientation and DITFs (represented by the grey profiles). Finally, the red circles represent the failure observations of BS-1 used to carry out the 1st order calibration from 3000 to 3600 m. Note that in the upper part of this panel, one can select one starting point to visualize its corresponding calibrated stresses and failure profiles (black profiles).

6.3.2.1.4. 1st calibrated histograms In this tab, both the prior and posterior distributions of the initial and calibrated input parameters, respectively, are displayed as histograms as illustrated in Fig. 6.8. In this example, we chose the 10th starting point as it gives satisfying and consistent calibration results (Fig. 6.7). The calibrated parameters corresponding to this starting point are represented by red lines in Fig. 6.8:

- $S_{Hmax}[\text{MPa}] = 10.1 \cdot \text{TVD}[\text{km}] + 69.8$
- $S_{hmin}[\text{MPa}] = 5 \cdot \text{TVD}[\text{km}] + 51.1$
- $\alpha[^\circ] = 151.1$
- cohesion, $c[\text{MPa}] = 27$
- Friction, $\psi[^\circ] = 35.2$
- Shen's parameters $A = 8.5$ and $B = 2.1$

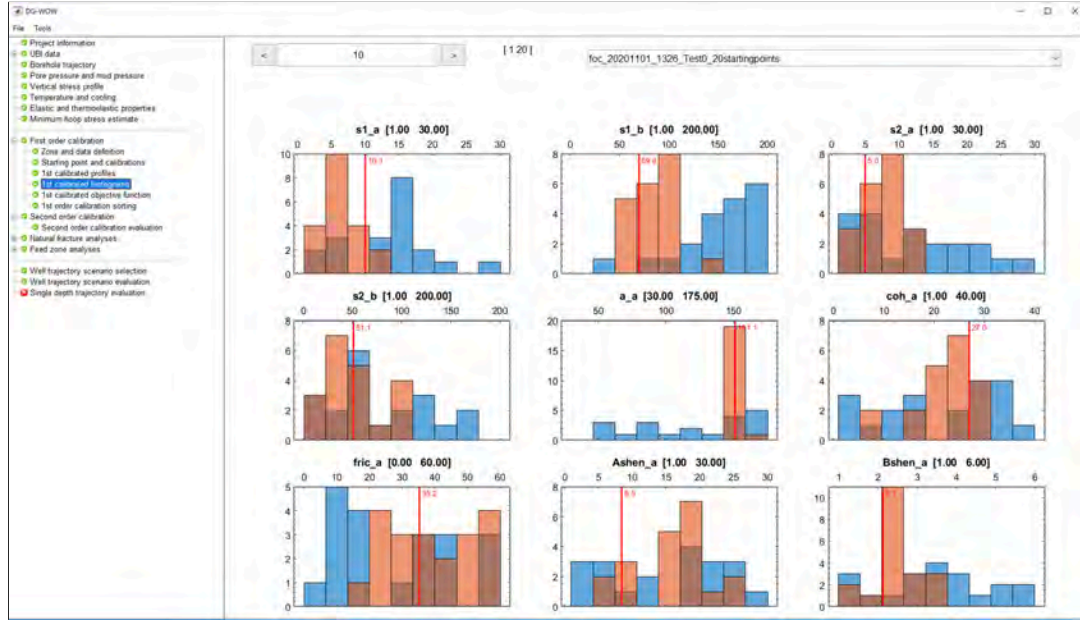


Figure 6.8.: Prior (blue) and posterior (orange) distributions of initial and calibrated input parameters respectively presented in the form of histograms. The red vertical lines correspond to the selected calibrated model. In this example, we selected the 10th starting point.

6.3.2.2. 2nd order calibration

The 2nd order calibration starts with a panel in which all inputs are collected (Fig. 6.9). At this stage, multiple second order calibrations can be run in parallel. The needed information include the PEST parameters and all the required *static parameters* (white boxes), *observations* (green boxes) and *parameters to be estimated* (red boxes) (Fig. 6.9). All the parameters are generated automatically by loading them from the outputs of the 1st order calibration. An important parameter to define in the 2nd order analyses is the number of pilot points. This will influence the quality of the calibration, i.e., more pilot points will allow to capture shorter wavelength variability. This will also have a large impact on the computation's time. When all the parameters are defined, calibrations can be run. The 2nd order characterization is carried out by estimating optimum parameters values at a set of pilot points (common to all parameter type, and is discussed in detail in Chapter 3 Section 3.5.1.1). In the example illustrated in Fig. 6.9, we chose 60 pilot points to be regularly spaced in the studied depth interval [3-3.6 km]. The pilot point discretization is common to all strength and stress parameters profiles, which leads to an overall parameterization involving 420 pilot points.

PEST PARAMETERS INPUT		2nd ORDER CALIBRATION PARAMETERS		npilotpoints		60	
nopmax	10	ZoneName []	Zone1	ZoneTop [mMD]			3000
ini_marq	10	ZoneBem [mMD]	3599	ZoneStep [mMD]			0.4
fac_marq_upd	5	hd [m]	D:\Asmaa_Itidens\DGWOW\Projects\Folder\BS1\...	Bhaiz []			D:\Asmaa_Itidens\DGWOW\Projects\Folder\BS1\...
phratsuf	0.4	Bhdev []	D:\Asmaa_Itidens\DGWOW\Projects\Folder\BS1\...	Bhradius [mm]			129.4125
phredlam	0.02	s1 [MPa]	7.2874e+1000+66.048	s2 [MPa]			9.72527e+1000+32.223
numlam	7	s3 [MPa]	D:\Asmaa_Itidens\DGWOW\Projects\Folder\BS1\...	a []			-11.8
relparmax	10	b []	0	c []			0
facpamax	10	Pp [MPa]	D:\Asmaa_Itidens\DGWOW\Projects\Folder\BS1\...	PmBOs [MPa]			D:\Asmaa_Itidens\DGWOW\Projects\Folder\BS1\...
facorig	1e-05	PmDITFs [MPa]	D:\Asmaa_Itidens\DGWOW\Projects\Folder\BS1\...	CoolingBOs [°C]			D:\Asmaa_Itidens\DGWOW\Projects\Folder\BS1\...
phredshh	0.1	CoolingDITFs [°C]	D:\Asmaa_Itidens\DGWOW\Projects\Folder\BS1\...	E [MPa]			55000
phredstp	0.01	poisson []	0.25	thermcoeff [°C ⁻¹]			1e-05
rphstp	4	BetaBOs []	1	BetaDITFs []			1
rphnored	4	failurecrit []	inshccolomb	coh [MPa]			13.6831
relparstp	0.01	tlc []	33.2825	TensileStrength [MPa]			4
rrelpar	4	Ashen []	15.6784	Bshen []			2.3056
		BBOwidth []	D:\Asmaa_Itidens\DGWOW\Projects\Folder\BS1\...	BBOext [mm]			D:\Asmaa_Itidens\DGWOW\Projects\Folder\BS1\...
		BBOtheta []	D:\Asmaa_Itidens\DGWOW\Projects\Folder\BS1\...	DITFsPresent [0/1]			D:\Asmaa_Itidens\DGWOW\Projects\Folder\BS1\...
		DITFs_stress_stddev [MPa]	5	DITFshn [MPa]			D:\Asmaa_Itidens\DGWOW\Projects\Folder\BS1\...

Figure 6.9.: Required parameters to perform the 2nd order calibration process. On the left, the PEST parameters are input by the user (we refer the interested reader to the PEST manual for a full description of each parameter (Doherty, 2015)). On the right, the *static parameters* (white boxes), *observations* (green boxes) and *parameters to be estimated* (red boxes) are generated automatically by loading them from the results of the 1st order calibration.

6.3.2.2.1. Second order calibration evaluation When the 2nd order calibration is completed, the outputs of the calibration are displayed in this window and can be evaluated visually (Fig. 6.10). The latter displays the 2nd order calibrated profiles of principal horizontal stresses, S_{Hmax} and S_{Hmin} in addition to Euler's angle α , cohesion, internal friction and Shen's parameters A and B . The corresponding borehole failure (in black as shown in Fig. 6.10d-g) fits well with the available failure BS1 observations from 3 to 3.6 km.

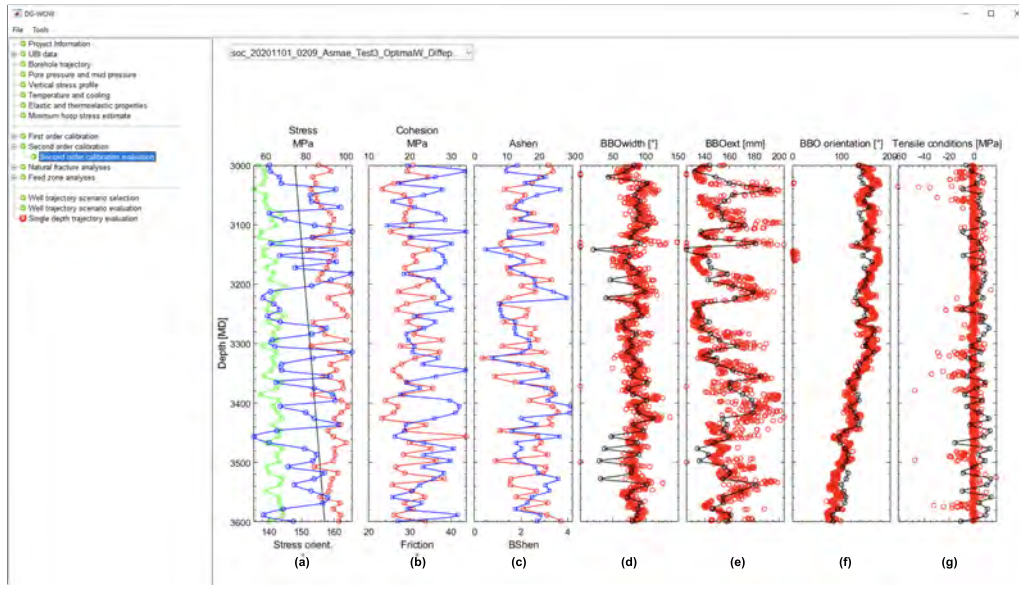


Figure 6.10.: Evaluation of the outputs of the 2nd order calibration. (a) calibrated depth profiles of stresses (S_{Hmax} in red and S_{Hmin} in green) and breakout orientation (blue); (b) calibrated cohesion (red) and friction (blue); (c) Shen's parameters A (red) and B (blue). Panels from (d) to (g) show the calibrated (black circles) and observed (red circles) breakout width, extent, orientation and DITFs, respectively. Finally, the black line in panel (a) depicts the vertical principal stress, S_v .

6.3.2.3. Natural fractures analyses

Further processing is performed here on the natural fractures. The first step is to cluster the fracture data in fractures sets based on their orientation. This is best done using external software (e.g., Dips from rocscience). Then the fractures sets can be imported and displayed in the DG-WOW-app (Fig. 6.11). After loading the data, they are presented in the form of tadpole plots and stereographic projection with a colour scheme per fracture set as illustrated in Fig. 6.11. When the fracture sets are identified, fracture spacing statistics can be performed on each one of them. In this step, the true spacing (spacing in the direction perpendicular to the fracture planes) statistics for each set is automatically computed. Each set's true spacing distribution is represented by a boxplot and the mean and median are displayed (Fig. 6.14). This information is required for subsequent quantitative spacing analyses.

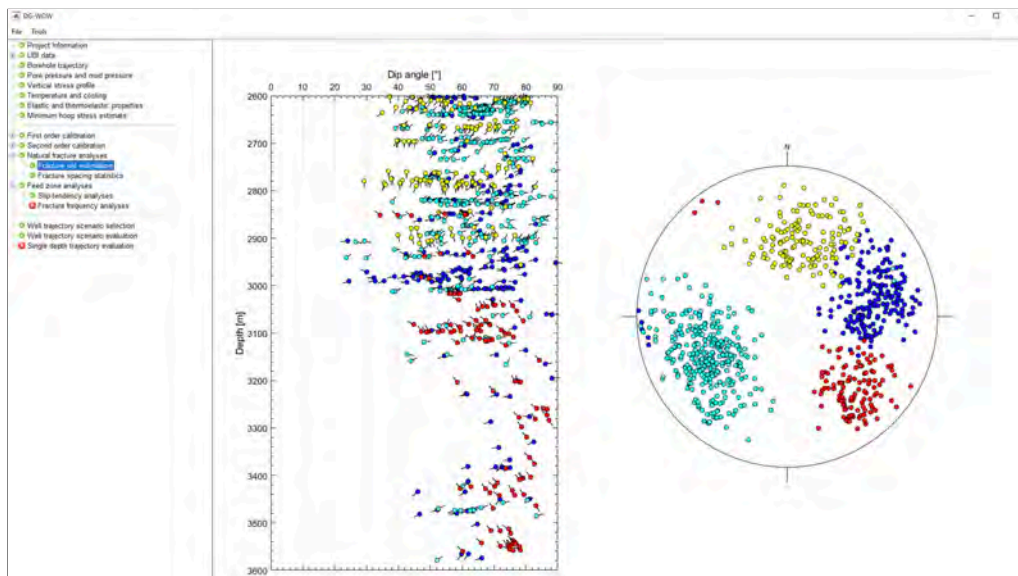


Figure 6.11.: Screenshot displaying the fractures sets in BS-1 in the form of tadpole plot (left) and stereographic projection (right) with a color scheme for each fracture set. In this example, 4 fracture sets were determined.

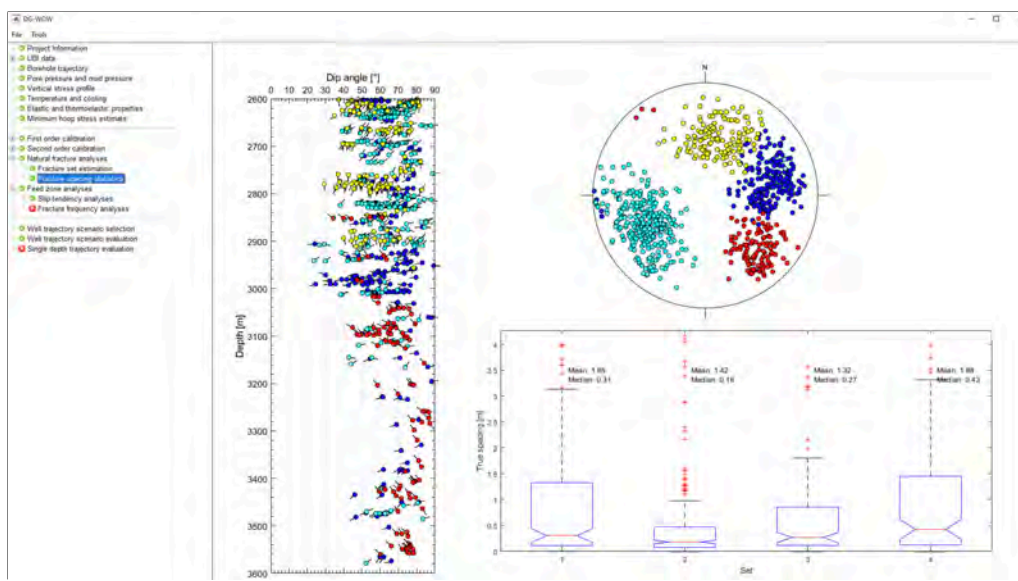


Figure 6.12.: Screenshot of the GUI where fracture true spacing statistics are performed. Each set's true spacing distribution is represented by a boxplot and the mean and median are displayed.

6.3.2.3.1. Feedzones analyses: Two feedzone analyses are performed:

1. The computation of slip and dilation tendency of the fractures. Fracture with high slip and dilation tendency are believed to be the most favorable fracture for flow.
2. Total fracture spacing computation in function of the main fracture sets and the drilling directions.

These two analyses allow to select optimal drilling direction in terms of feed zones and the results are presented in the workflow items Slip-tendency analyses (Fig. 6.13) and Fracture frequency analyses (Fig. 6.14), respectively.

6.3.2.3.2. Slip-tendency analyses The relationship between stress and fractures is crucial and it is believed to play a major role in fracture transmissivity. It is usually assumed that critically stressed fractures are the most transmissive (Barton et al., 1995; Zhang and Sanderson, 1996). The latter are evaluated by computing both slip and dilation tendency. The slip and dilation tendency analyses are presented in the form of stereographic projection (Fig. 6.13). The required input for these analyses is the stress state (magnitudes and orientations) and pore pressure. These inputs are given in the top of the panel. The objective is to load stress values from the calibrations. The natural fracture poles are overlaid on top of the slip and dilation computations and thus it is possible to assess which fractures are the most critical. In addition a Mohr diagram is displayed, presenting the effective stress state as Mohr circles as well as the normal and shear stress on the fractures.

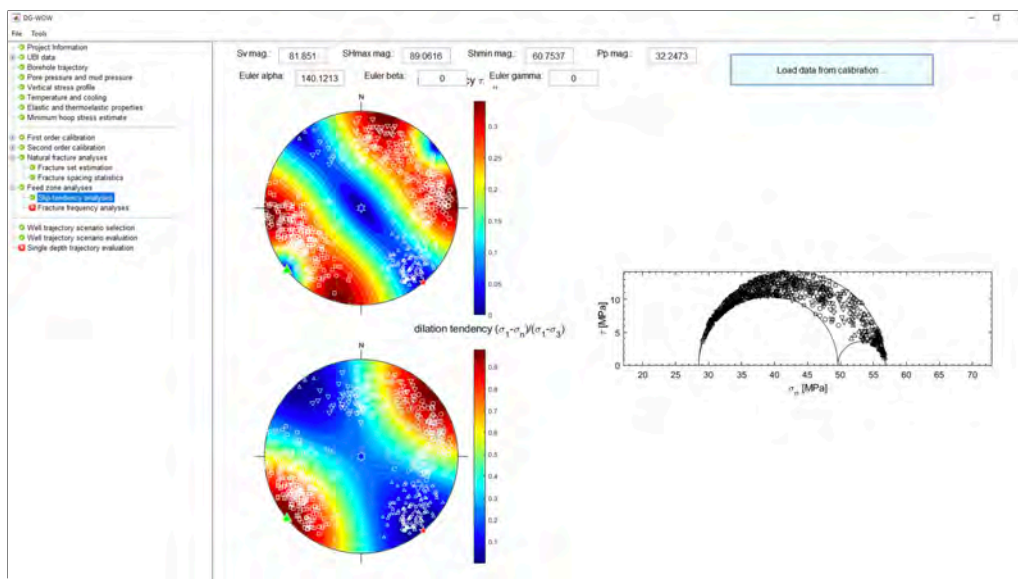


Figure 6.13.: Screenshot illustrating slip tendency analyses performed on the natural fractures in BS-1.

6.3.2.3.3. Fracture frequency analyses An other aspect that controls the borehole injectivity or productivity is its connection to the natural fracture network. A borehole intersecting many fractures has more chance to be well connected to the network and thus to have a profitable injectivity and productivity index. The number of intersections of a borehole with a fracture set depends on the fracture spacing, the fracture orientation and the borehole orientation. When multiple fracture sets are present, the fracturing intensity along the well is a combination of the contribution of each fracture set.

In our analyses, we consider the characteristics and statistics of each fracture set and compute a resulting fracture intensity for any borehole orientation and represent these computation on a stereographic projection Fig. 6.14.

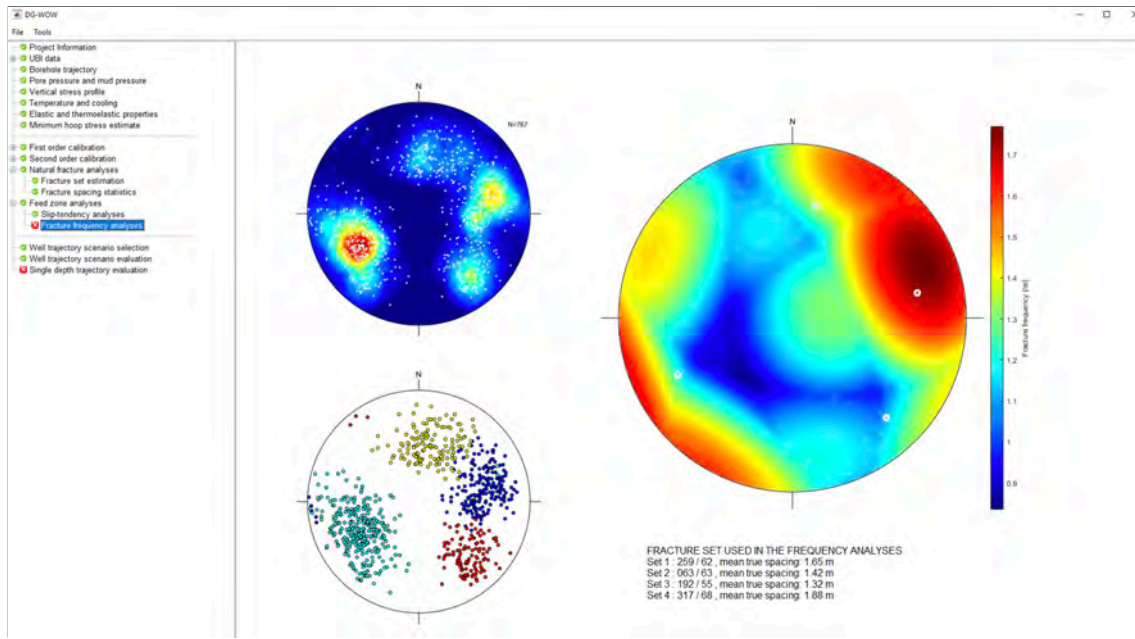


Figure 6.14.: Example of total fracture frequency analyses as a function of drilling directions performed in the BS-1.

6.3.3. Failure severity prediction

6.3.3.1. Well trajectory scenario selection

In order to perform failure prediction, the following elements are needed:

1. A borehole trajectory and section along which the failure should be predicted.
2. A 1st order calibrated stress and strength model that can be extrapolated to the true vertical depth level where failure should be predicted.
3. Optionally a 2nd order stress and strength model can be used to add stochastic variability to the predictions.

The main panel of the "Well trajectory scenario selection" tab allows to define these elements (Fig. 6.15). On the top of the panel, one can select the 1st and 2nd order models from which stress and strength will be extracted. One can also choose whether or not add a stochastic variability mimicking the results obtained in the 2nd order calibration by using them as a training image for DeeSse algorithm (The used approach is fully described in Chapter 4, Section 4.2.2). The borehole trajectory, diameter, the initial depth, the end depth, and the step at which the prediction should be performed are defined by the user. The loaded trajectory, and the selected section are displayed along with the borehole and section used in the calibrations (Fig. 6.15).

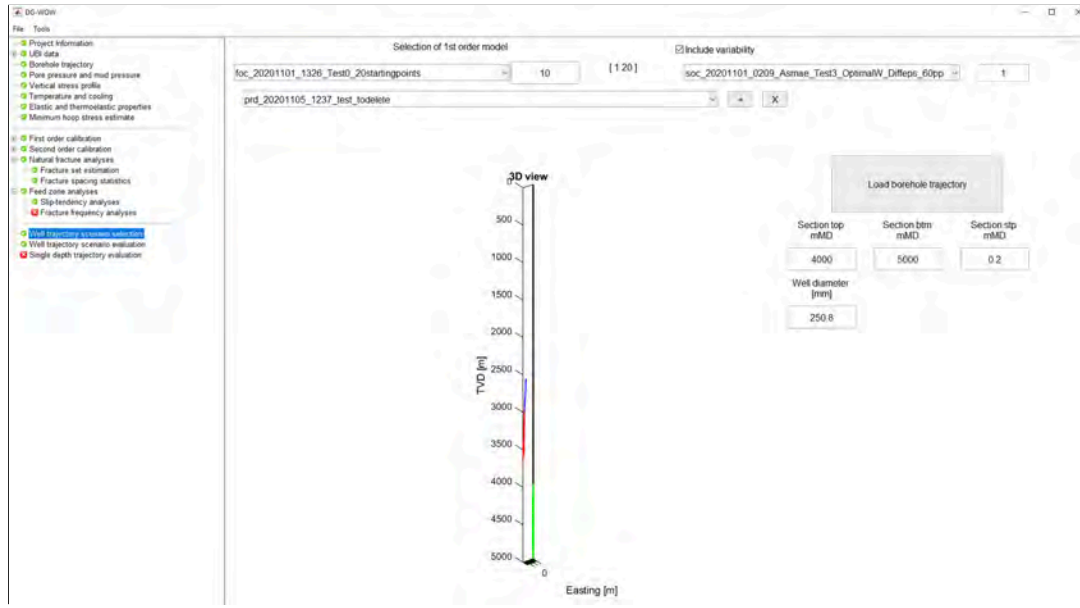


Figure 6.15.: 3D view of the borehole trajectory and sections along which calibrations (red section) and prediction (green section) were performed.

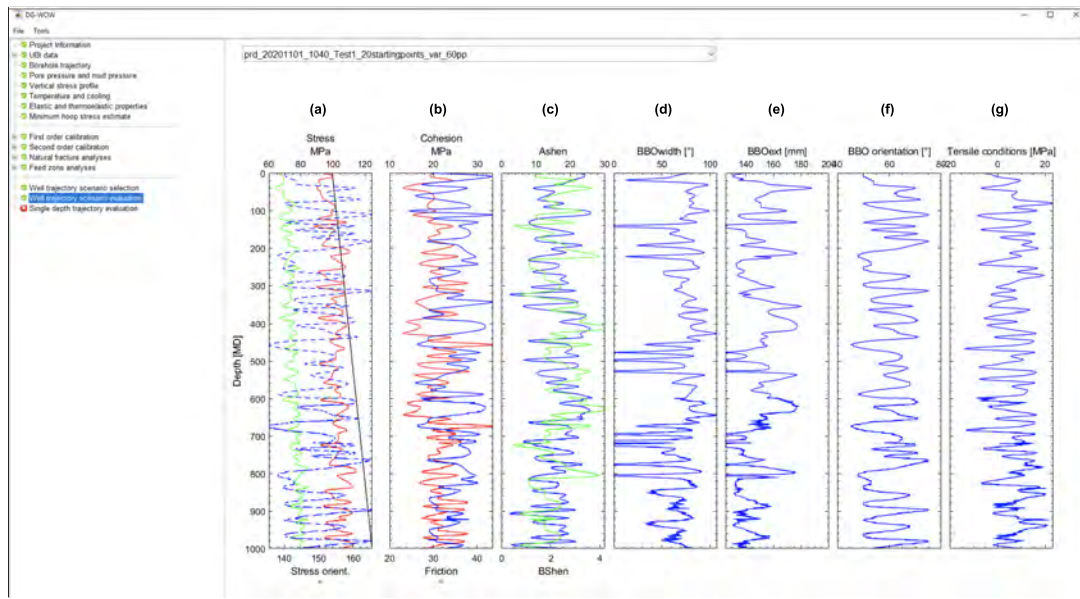


Figure 6.16.: Predicted failure severity from 4000 to 5000 m. (a) forecast stresses, using DeeSse multivariate simulations, (S_{Hmax} [MPa], S_{Hmin} [MPa], and stress orientation [°] are displayed in red, green and blue, respectively; (b) forecast cohesion [MPa] (red) and friction angle [°] (blue); (c) forecast Shen's parameters A (green) and B (blue); (d) predicted breakout width; (e) predicted breakout extent; (f) breakout orientation and (g) DITFs.

6.3.3.2. Well trajectory scenario evaluation

When the simulations are completed, this final tab allows to display the predicted failure profiles along with the forecast stress and strength profiles as shown in Fig. 6.16. Indeed,

Fig. 6.16a-c displays the forecast 2nd order profiles of horizontal stresses, Euler's angle, α , cohesion, friction and Shen's parameters using DeeSse multivariate simulations. These predictions were performed from 4 to 5 km. The corresponding prediction borehole failure is depicted by Fig. 6.16d-g.

6.4. Summary and outlook

A complete workflow was developed and implemented as a software application to provide a systematic approach to select the most appropriate drilling direction. The latter is defined as the one that promotes wellbore stability while intersecting as many as possible potential feed zones. The workflow is divided in three main phases: (1) Data pre-processing, (2) failure models calibration in the shallowest section of the well and identification of critically stresses fractures and finally (3) failure severity prediction in the deepest section of the well. The longer phase is the data pre-processing where all required data are loaded and pre-processed to enable the optimal drilling direction selection. The model calibration section is the central part of the workflow and the most critical one as it allows to estimate fundamental parameters for failure prediction like stress and strength. The failure prediction section allows then to evaluate various drilling scenario based on the model calibration outputs. In this chapter, we used the BS-1 borehole as a test bed to validate the developed workflow. The outputs of both calibration and prediction are consistent and coherent with the results shown in Chapters 3 and 4 and reproduce satisfactorily the BS-1 observations. The importance of this software tool is to provide a complete, intuitive and easy-to-use interface and immediate visual feedback that may help deciding of an optimal drilling trajectory. It must however be considered as a prototype and will need further testing and developments including:

- Adding a section to help the user adding available estimates of stresses (e.g., estimate of S_{hmin} interpreted from XLOTs) in order to reduce the spread of calibrations and predictions uncertainties.
- A section to consider the effect of mud weight will be required. Indeed, it is very important to assess the impact of mud pressure on calibrations and predictions. This highly affects the selection of an optimal borehole trajectory that promotes stability of the borehole. For instance, one could compute a safe mud weight window for each calibrated failure model in order to reduce the range of the non-unique solutions and discard more models that lead to unstable conditions. This may also be performed for different borehole deviation and dip directions.
- A section to quantify predictions uncertainties, their dispersion and their quality may be useful for risk assessment. For instance, one may add a section in the GUI to compute the shift and dispersion indicators defined in Chapter 5 in order to get a general insight into the goodness of the predictions and their reliability.

- Summarizing potential optimal borehole trajectories that promote borehole stability and intersect as many as possible feed zones is necessary to help the user quickly decide of an optimal well path. For instance, a section may be added with a summary of well calibrated models, the corresponding computed safe mud weight window, the critically stressed fractures and the corresponding shift and dispersion indicators to quantify the goodness and reliability of predictions. Having all of these elements in one panel may help in the selection of an optimal drilling trajectory in a timely manner. It may even be helpful if one can classify these optimal borehole trajectories by defining a metric in order to discard 'similar' trajectories and keep only representative ones. One may use some classification methods like the so-called hierarchical clustering, also known as hierarchical cluster analysis, which is an algorithm that groups similar objects into groups called clusters.

7. Application of the workflow to two real test cases

7.1. Introduction

The methodology presented in this thesis for calibrating key geomechanical elements of the reservoir, and proposing predictions of borehole stability from these calibrations was developed using Basel data (Chapter 3 and 4). Its applicability and limitations were tested on synthetic data (Chapter 5), and the methodology was then implemented in an application to facilitate its deployment (Chapter 6). This application provides a complete, intuitive and easy-to-use interface and immediate visual feedback that may help deciding of an optimal drilling trajectory. It is important to expose the application to more data sets and real case studies. To that end, the entire workflow is applied to newly acquired data set from Bedretto by Geo-Energie Suisse, and to the Soultz-sous-Forêts project.

In this chapter, we do not propose a careful and detailed estimation of all parameters but our focus is mainly placed on testing our approach in real application conditions, where a quick decision of an optimal drilling trajectory has to be made in order to minimize costly drill rig time. The purpose of this chapter is then to test the DG-WOW-app on real case studies and conditions to test (1) its versatility and resilience and (2) the calibration-prediction workflow developed in Chapter 3 and 4 of this thesis.

First, a brief description of both sites is presented. Then, the DG-WOW-app is tested on both datasets by going through all the steps of the workflow. For the sake of brevity, results of all the steps are not presented here but only the most relevant ones to test the proposed calibration-prediction methodology.

7.2. Brief site description

7.2.1. CB-1 borehole (Bedretto)

Researchers from the Swiss Competence Center for Energy Research (SCCER-SoE) and the Department of Earth Sciences of ETH Zurich, supported by the Swiss federal office of Energy, have established the "Bedretto Underground Laboratory for Geoenergies" (BULG) in the Bedretto Tunnel within the Gotthard massif in the Central Swiss Alps. The main purpose of the conducted large-scale in-situ experiments in the BULG is to improve the understanding of hydromechanical processes linked to the creation of a deep geothermal reservoir and to develop effective and safe hydraulic stimulation approaches that increase

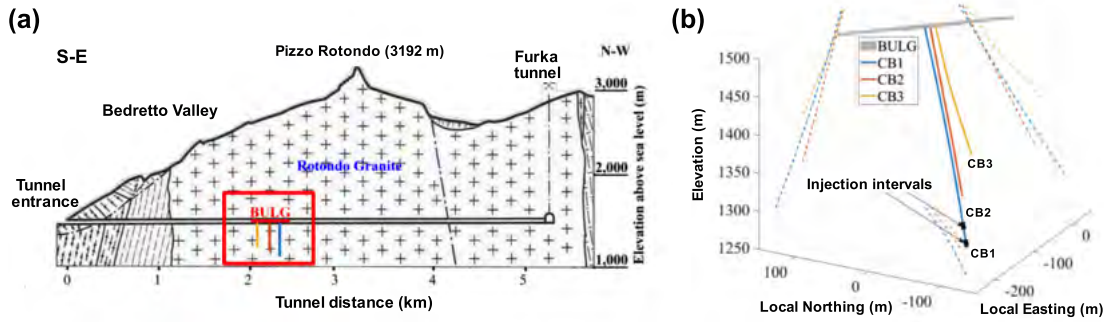


Figure 7.1.: (a) Geological cross-section of the Bedretto tunnel. The red rectangle represents the section where the BULG is located. (b) A 3D visualization of the existing CB boreholes in the BULG. Stimulation intervals in CB1 are depicted by black bars. Source: This figure taken from Shakas et al. (2020).

rock mass conductivity at a controlled risk of induced seismicity (Gis, 2020). The BULG is located in a 100 m long cavern at distances between 2000 and 2100 m from the southern entrance of the Bedretto tunnel that connects the Tessin with the Furka tunnel (Keller and Schneider, 1982). Above the tunnel lies the Pizzo Rotondo, the highest mountain (3192 m) of the Saint-Gotthard Massif (Fig. 7.1a), providing about 1000 m overburden depth at the level of the BULG. This offers ideal conditions to perform these in-situ experiments and gives the opportunity to pursue the research conducted in laboratories at universities and in other rock laboratories, e.g., at Grimsel, on a bigger scale. The BULG is located in relatively homogeneous Rotondo granite dissected by NESW-striking steep faults (Gis, 2020). Details on the geological characterisation of the BULG and the Bedretto tunnel can be found in (Meier, 2017; Jordan, 2019). Additionally, the BULG offers a geological environment that mimics a realistic EGS reservoir with the exception of the temperature conditions. It is also fully contained below the water table and the hydraulic fractures that intersect the drilled boreholes are water filled, which gives considerable outflow of several liters per minute (Shakas et al., 2020).

During the initial characterization phase, three boreholes have been drilled in the BULG (CB1: 302 m and 45°, CB2 222 m and 50°, CB3: 190 m and 40° dip). A geological cross-section of the tunnel is shown in Fig. 7.1a. Geo-Energie Swiss (GES) performed an initial test stimulation in CB1 based on borehole acoustic and optical logging results (Shakas et al., 2020). The stimulation intervals are denoted with black bars in Fig. 7.1b. Throughout this chapter, only CB1 borehole is considered.

As a first step, the World Stress Map can be used to determine the regional stress field in the Swiss Central Alps (Heidbach et al.). The general trend of S_{Hmax} in the Swiss Alps is in NW direction. As there is no stress measurement points around the BULG, one can only extrapolate the closest information but should consider this information with caution. This leads to the expectation of a NW-SE trend for S_{Hmax} and a strike-slip or normal faulting regime (Bröker, 2019). These observations were confirmed by Kastrup et al. (2004) and Ma et al. (2020). Stress measurements have been conducted in multiple

boreholes in BULG using classic hydraulic fracturing and these results are still in the process of being interpreted, integrated and published. They indicate a normal faulting and/or strike-slip stress regime and that the rock mass is almost critically-stressed. The slip tendency of the mapped fractures/faults is analyzed based on the measured stress condition. This highlights the E-W fractures as the most favorably-oriented set, followed by tunnel-parallel, tunnel-perpendicular, and N-S sets (Ma, 2019).

The estimated stress components at the level of the lab as well as other relevant parameters are as follows (David et al., 2020):

- The principal vertical stress: $S_v = 26.5$ MPa.
- The minimum principal horizontal stress, $S_{hmin} \in [13 \text{ to } 16]$ MPa.
- The maximum principal horizontal stress, $S_{Hmax} \in [0.8 \cdot S_v \text{ to } 1 \cdot S_v]$.
- Based on the orientation of the created tensile fractures, the estimated azimuth of S_{Hmax} is 100° (WNW-ESE).
- The pore pressure is significantly under-hydrostatic, $P_p \in [3 \text{ to } 6]$ MPa, which indicates tunnel drainage effects.
- Tensile strength, $T_o = 4$ MPa. [Geo-Energie Suisse, personal communication]
- Poisson ratio, $\nu = 0.37$.
- Young modulus, $E = 46$ GPa.

7.2.2. GPK3 borehole (Soulz-sous-Forêt)

The data analysed in this study stem from one of the three deep wells drilled to 5 km at the Soultz-sous-Forêts geothermal project site, located in the Rhine Graben north of Strasbourg, France. This well, called GPK3, was drilled in 2002 as a deviated borehole and reached a total true vertical depth of about 5 km. For more information about the geological setting of Soultz, the reader is referred to Dezayes et al. (2003). UBI logs were run in the granitic section of GPK3 and GPK4 to total depth (TD) (Dezayes et al., 2005). Both boreholes are sub-vertical in the upper 2-3 km and penetrate granite at 1.4 km. Their separation in the uppermost kilometer of granite to 2.4 km is less than 20 m. Only GPK3 borehole was studied in this thesis. The granite section in GPK3 was drilled with a 12-1/4 inch bit to 4514 m TVD and then with 8-1/2 inch to total depth.

About 10% of the logged borehole lengths are affected by breakouts, 10% by A-DITFs, and 7% by E-DITFs. According to Valley and Evans (2007), taking an average of all estimates from GPK3 and GPK4 (another deviated borehole drilled closely to GPK3) by weighting each value by the length of borehole considered in the study yields a mean orientation for S_{Hmax} at the Soultz site from 1.4 km to 5 km depth of $169^\circ \pm 14^\circ$.

Valley and Evans (2007) report on analyses conducted by Evans et al. (1992) to estimate the pore pressure:

$$P_p[MPa] = 0.9 + 9.8 \cdot z[km] \quad (7.1)$$

Through the integration and analyses of density log from the Soultz-sous-Forêts project and from measurements conducted in the Rhine Graben, Valley and Evans (2007) estimated the vertical profile in the granite to be expressed by the following linear trend:

$$S_v[MPa] = -1.30 + 25.50 \cdot z[km] \quad (7.2)$$

Moreover, limited casing-shoe pressure behaviours during massive injection in GPK1, GPK3 and GPK4 were interpreted to be controlled by the magnitude of the minimum horizontal stress, S_{hmin} , resulting in a best fit linear trend as follows:

$$S_{hmin}[MPa] = -1.78 + 14.06 \cdot z[km] \quad (7.3)$$

Analysis of stress-induced wellbore failure in the form of breakouts and drilling induced tensile fractures to estimate some constraints on S_{Hmax} were performed by Valley and Evans (2007). When considering an estimate of the minimum horizontal principal stress, S_{hmin} , the wellbore failure observations impose constraints on the magnitude of S_{Hmax} as well as its direction. This suggests the following:

$$-1.17 + 22.95 \cdot z[km] \leq S_{Hmax} < -1.37 + 26.78 \cdot z[km] \quad (7.4)$$

The S_{Hmax} magnitude is the most uncertain stress component. The analyses did not rely on the breakout geometry (e.g., breakout width) considerations but on the distribution of failure type with depth, taking advantage of the observation that tensile failure occurs mostly in the upper part of the well and breakouts in the lower section. These analyses include an estimation of the thermo-elastic stress component, but available data are limited to support the estimation of thermal perturbation while drilling.

7.3. UBI data synthesis

The first steps consist in adding all relevant data into the application. Details on these steps are given in Chapter 6 and include checking image quality, cleaning-up transit time, computing well geometry, detecting breakouts and DITFs, measuring breakouts, computing minimum hoop stress associated to the absence/presence of DITFs, etc. The DG-WOW-app was used to derive all key information from acoustic televiewer logs in order to extract the required data to perform the subsequent steps in the GUI on both CB1 and GPK3 boreholes. Fig. 7.2 and 7.3 give a summary of the UBI data of CB1 and GPK3 boreholes, respectively. Failure data were displayed between ~ 2 m MD and 295 m MD for CB1 borehole and between ~ 1445 m MD and 5110 m MD for GPK3.

Graphically, it can be noticed that CB1 has no breakouts except for the middle section

between ~ 150 m MD and 210 m MD and no DITFs are observed along the entire well length. Breakout width is moderate with a width angle ranging mostly between 20° and 40° . The absence of DITFs is expected in the CB1 drilling conditions with very limited cooling if any (we consider cooling for breakouts, $\Delta T_{BO}=0^\circ\text{C}$ and cooling for DITFs, $\Delta T_D \in [-3^\circ\text{C}, -0.9^\circ\text{C}]$). Drilling from underground implies although short mud columns while drilling and thus small internal well pressure that do not favorize formation of drilling induced tension fractures. Breakout orientation is $\theta_b \sim 143^\circ$.

In GPK3 no high-confidence breakouts are identified above 3000 m MD. Below 3000 m MD, breakouts are sparsely distributed until ~ 3670 m TVD when the density increases markedly. However, DITFs dominate above 3000 m MD. Axial DITFs in GPK3 above 3257 m MD depth indicate a mean S_{Hmax} direction of $N167^\circ$. Below 3257 m MD in GPK3, the numerous breakouts indicate an S_{Hmax} orientation of $N162^\circ$.

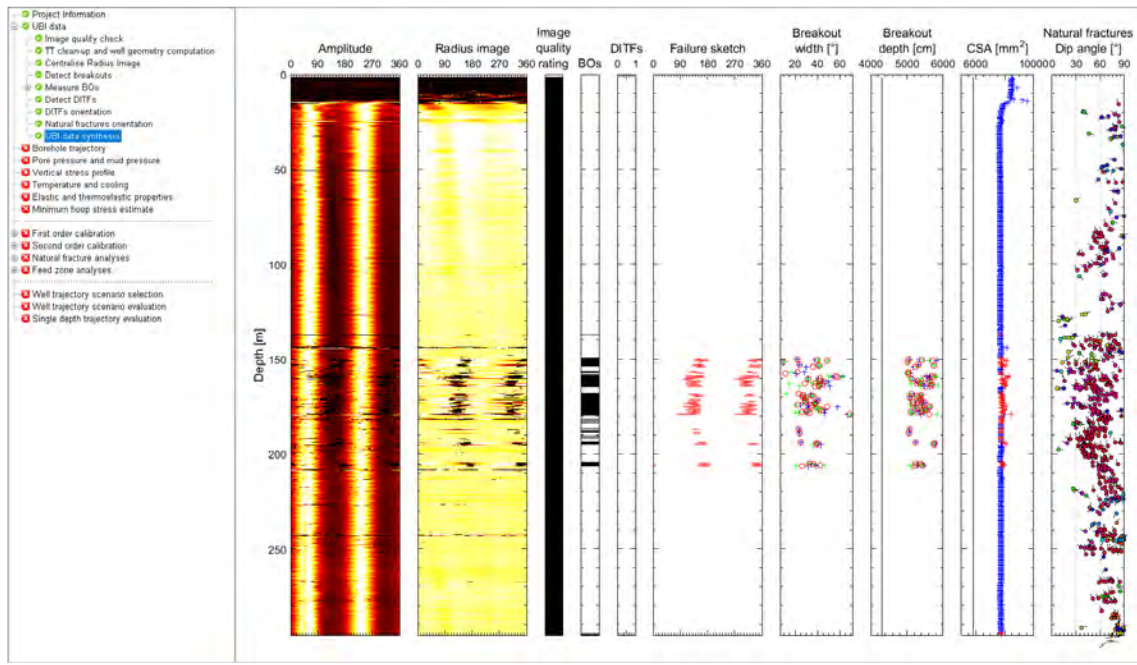


Figure 7.2.: Screenshot of the CB1 UBI data synthesis panel. From left to right: amplitude image, radius image, image quality rating, breakouts intervals, drilling induced tensile fractures (DITFs) intervals, sketch of stress induced failure, breakout width, breakout extent, cross-sectional area and natural fractures tadpole plot. This example illustrates the failure data of CB1 borehole between ~ 2 m MD and 295 m MD.

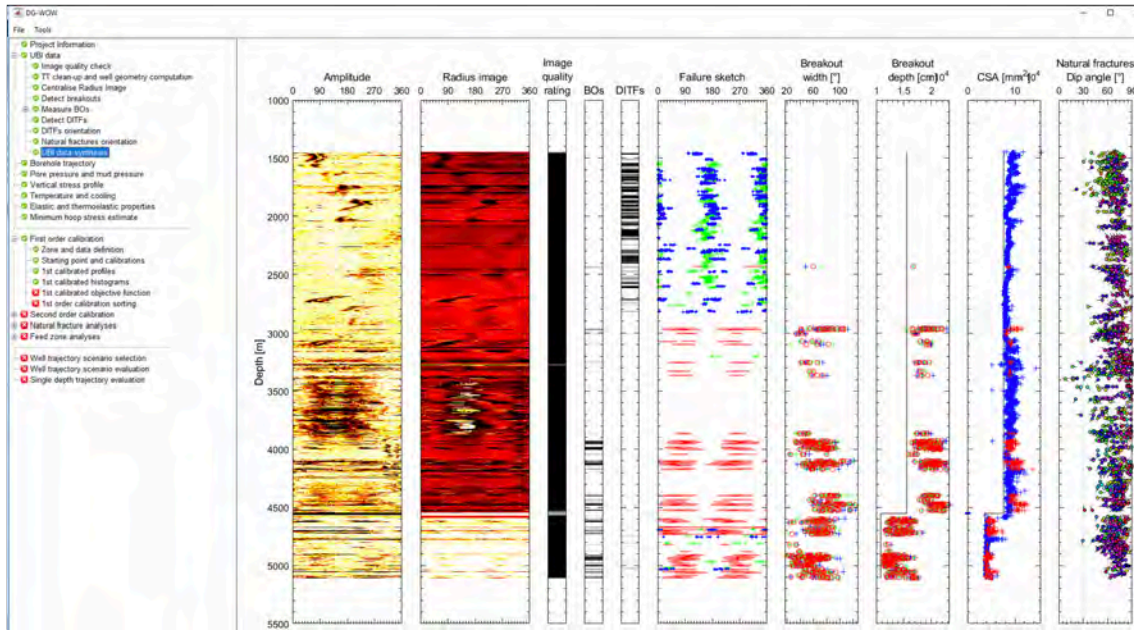


Figure 7.3.: Screenshot of the UBI data synthesis panel. This example illustrates the failure data of GPK3 borehole between ~ 1445 m MD and 5110 m MD. See the caption of Fig. 7.2 for further details.

7.4. Failure models calibration

After pre-processing all needed information, the calibration of failure models (i.e., stress and strength) was carried out for both CB1 and GPK3 boreholes. The calibration process is performed in two phases: 1st and 2nd order calibration as it is fully described in the previous Chapters 3 and 4.

7.4.1. 1st order calibration

The GUI displays a summary of the key data required for performing the calibration process (Figs. 7.4-7.5). The parameters to calibrate are represented by the red boxes (i.e., slope and intercept of both S_{Hmax} and S_{hmin} , Euler's angle, α , cohesion, friction angle and Shen's parameters (Shen, 2008)). The calibration for both boreholes was run against four types of measurements (represented by green boxes): breakout width, breakout extent, breakout orientation and DITFs. The remaining parameters are defined as static. The grey shaded areas in both figures depict the zones where calibrations were performed. For illustration purposes, calibrations were run between 135 and 210 m MD for CB1, which is the most affected section by breakouts and between 1445 m MD and 5110 m MD for GPK3, where no breakouts are identified above 3000 m MD. This exercise will give us insight into the applicability of our calibration-prediction methodology.

As explained in Chapter 3, the proposed calibration methodology takes into account the presence or absence of DITFs by generating a profile of the minimum hoop stress at the borehole wall that is required to explain the observed DITFs. In order to generate this



Figure 7.4.: Screenshot of the "Data and Zone Definition" panel of the DG-WOW-app when testing it on the CB1 borehole. One zone was defined in this example where calibration will be performed as well as the required data such as *static parameters* (white boxes), *observations* (green boxes) and *parameters to be estimated* (red boxes). The shaded grey area in the lower part of the panel depicts the zone of calibration (135-210 m MD in this example).

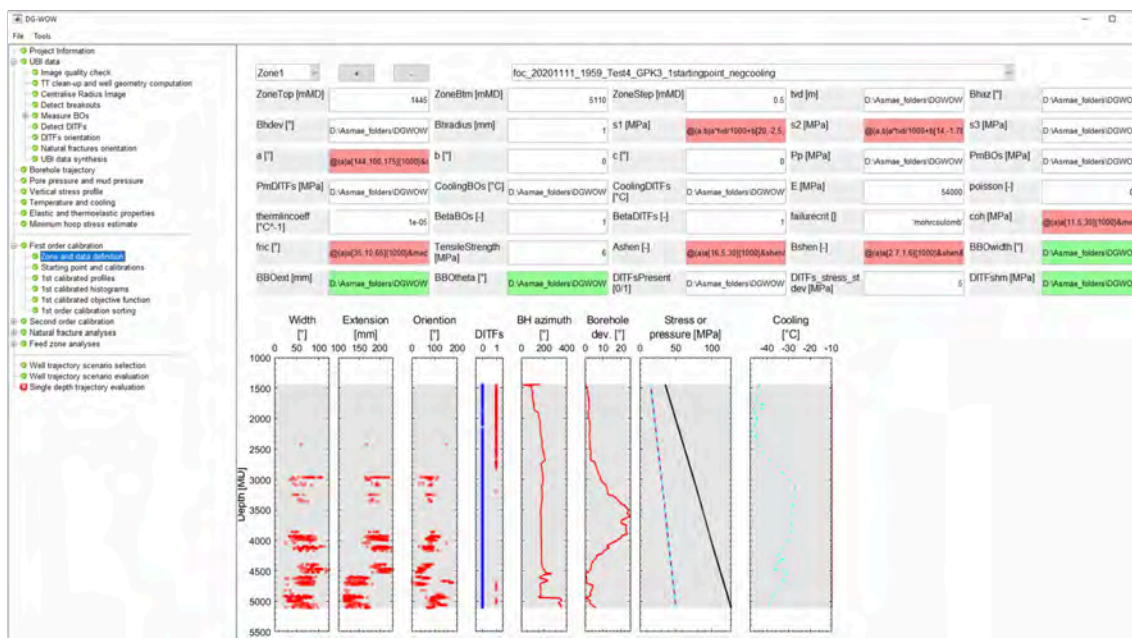


Figure 7.5.: Screenshot of the "Data and Zone Definition" panel of the DG-WOW-app when testing it on the GPK3 borehole. The 1st order calibration section is between 1445 m MD and 5110 m MD. See the caption of Fig. 7.4 for further details.

profile, the required input are the position of the interval where DITFs are observed, the tensile strength of the rock and a best-guess estimate of the standard deviation capturing the minimum hoop stress variability. After generating this profile, the number of starting points must be defined for the 1st order calibration. For illustration purposes, only 10 and 20 starting points were used for GPK3 and CB1, respectively. They are automatically generated by random draw from uniform distributions within the bounds described in Figs. 7.4-7.5. Finally, the calibration process is launched and the calibrated depth profiles of stresses and the corresponding borehole failure (breakout width, extent, orientation and DITFs) are displayed in Figs. 7.6-7.7 for CB1 and GPK3, respectively.

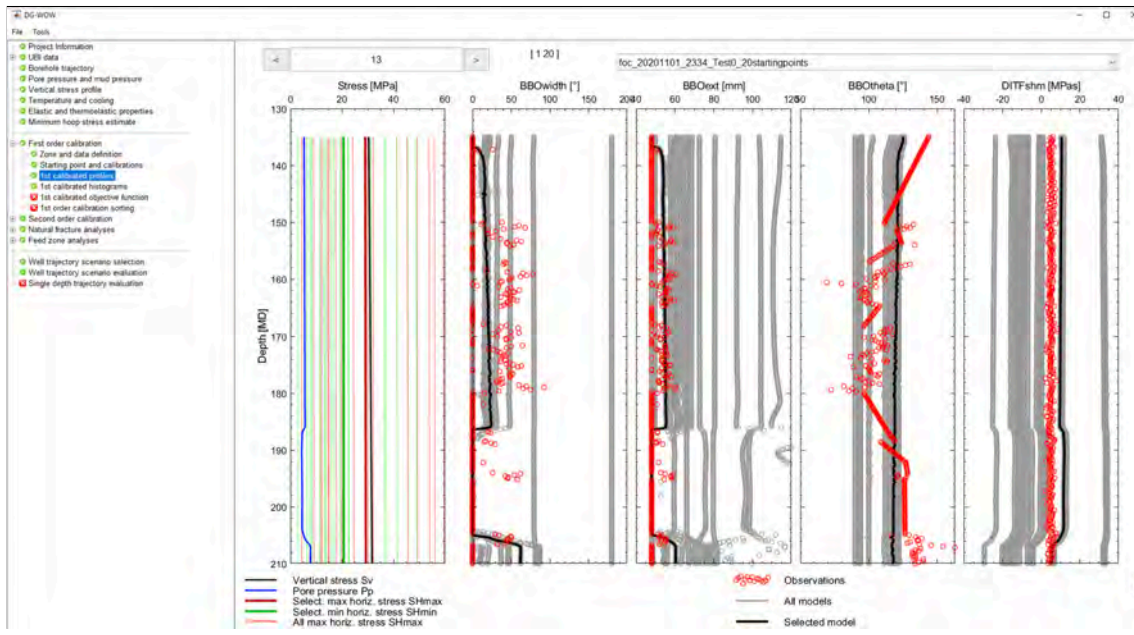


Figure 7.6.: Screenshot of the '1st order calibrated profiles' tab summarizing the outputs of the 1st order calibration carried out using 20 starting points for CB1 borehole. From left to right: calibrated depth profiles of stresses (green and red linear profiles in the first panel depict S_{Hmin} and S_{Hmax} , respectively), breakout width, breakout extent, breakout orientation and DITFs. Calibrated models are shown in grey and CB1 observations in red circles. The black profiles in all panels depict the corresponding calibrated profiles of the 13th starting point that is the most consistent with observations.

The corresponding calibrated parameters are shown in Figs.7.8-7.9 for CB1 and GPK3, respectively. Both prior and posterior distributions of the initial and calibrated input parameters, respectively, are displayed in the form of histograms. Note that for the sake of time efficiency, we did not perform a massive calibration approach with many starting points but a limited number of these initial points were used with the objective of identifying at least a couple of well calibrated scenarios of each case study and select the best one to carry on with 2nd order calibration. The 13th and 3rd first order calibrated models were selected for CB1 and GPK3, respectively, as they show the most satisfying results. Ta-

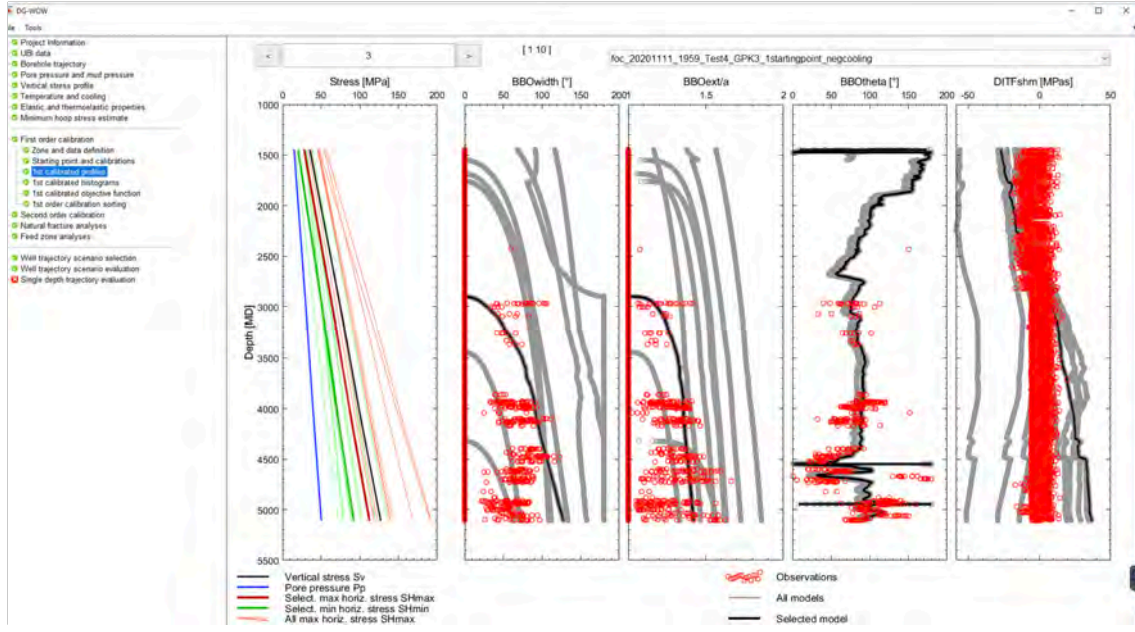


Figure 7.7.: Screenshot of the '1st order calibrated profiles' tab summarizing the outputs of the 1st order calibration carried out using 10 starting points for GPK3 borehole. See the caption of Fig. 7.6 for further information.

ble 7.1 summarizes the calibrated parameters values of the selected well calibrated models for both boreholes.

Table 7.1.: Parameters values of the well calibrated 13th and 3rd models of CB1 and GPK3, respectively.

	CB1	GPK3
a_{SHmax} [MPa/km]	5.2	26.8
b_{SHmax} [MPa]	23.1	8.6
a_{SHmin} [MPa/km]	1.1	20.5
b_{SHmin} [MPa]	19.4	0.3
α [°]	94.4	175
c [MPa]	20	23.4
ψ [°]	33.1	32.2
A [-]	22.9	17.1
B [-]	3.9	4

The outcomes of the 1st order calibration that were performed against CB1 observations in the depth section 135-210 m MD are dispersed and only few calibrated failure models show consistency with the observations (graphical inspection led to 4 well calibrated models out of 20). This may be due to the fact that not sufficient starting points required to ensure that the parameters space is entirely spanned are generated. However, the selected well calibrated model shows coherency and consistency with the mean of the observations (Fig. 7.6). Note that the posterior stresses distributions as shown in Fig. 7.8 are narrowed even if calibrations were performed using only 20 starting points. Similarly, the calibrated

models for GPK3 are quite scattered and only one model is consistent with the observations. This is also due to the same reason mentioned above and massive calibrations should be performed in order to span a wide range of possibilities. However, when considering only the well calibrated models, results are almost satisfying for GPK3 borehole and are consistent with the literature (Valley and Evans, 2007), but with a small discrepancy in the estimate of S_{hmin} . This can be fixed by adding the best estimate of S_{hmin} that was already determined by means of injections tests (Valley and Evans, 2007). However, for CB1, it is difficult to draw conclusions as only one model is well calibrated. We can only comment on the consistency of the breakout orientation value with (David et al., 2020).

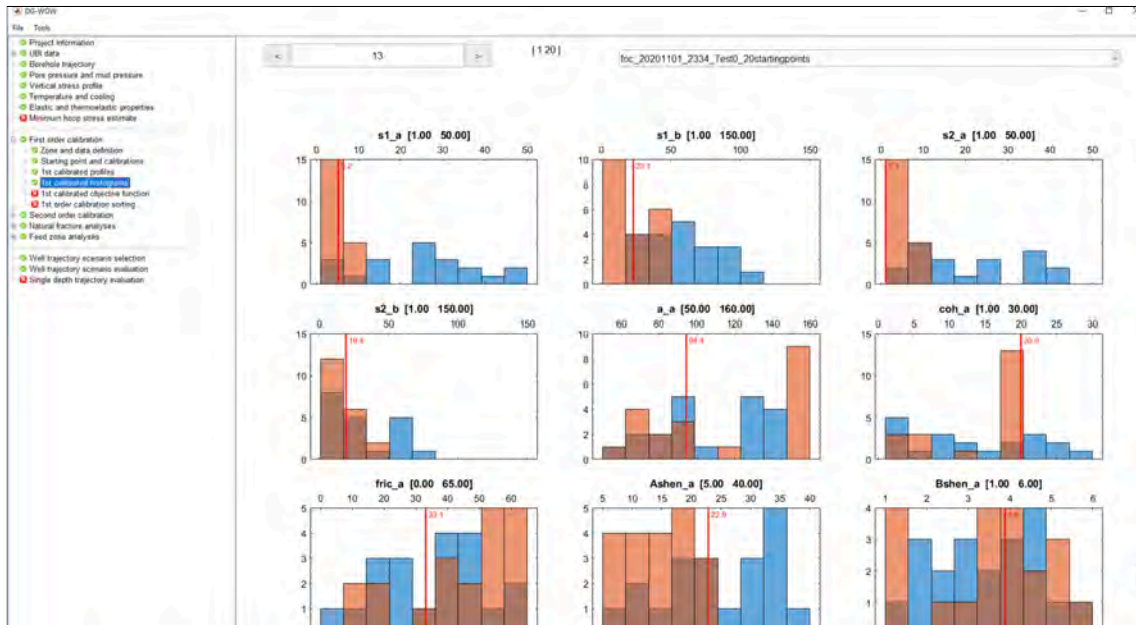


Figure 7.8.: Screenshot of the '1st order calibrated histograms' tab showing prior and posterior parameters histograms for CB1. Prior (blue) and posterior (orange) distributions of initial and calibrated input parameters, respectively, presented in the form of histograms. The red vertical lines correspond to the selected calibrated model. In this example, we selected the 13th starting point.

7.4.2. 2nd order calibration

At this stage, the needed information including PEST parameters and all the required parameters for the 2nd order calibration are defined. The 1st order well calibrated models (13th and 3rd starting points for CB1 and GPK3, respectively) were selected as starting points for the 2nd order calibration. Then 100 and 120 pilot points were chosen to perform calibration in CB1 and GPK3, respectively. The pilot point discretization is common to all strength and stress parameters profiles, which leads to an overall parameterization involving 900 and 1080 pilot points for CB1 and GPK3, respectively. Results are displayed in Figs. 7.10-7.11 for CB1 and GPK3, respectively. The outcomes of the 2nd order calibration carried out in CB1 are satisfying especially, an exception being the DITFs. The

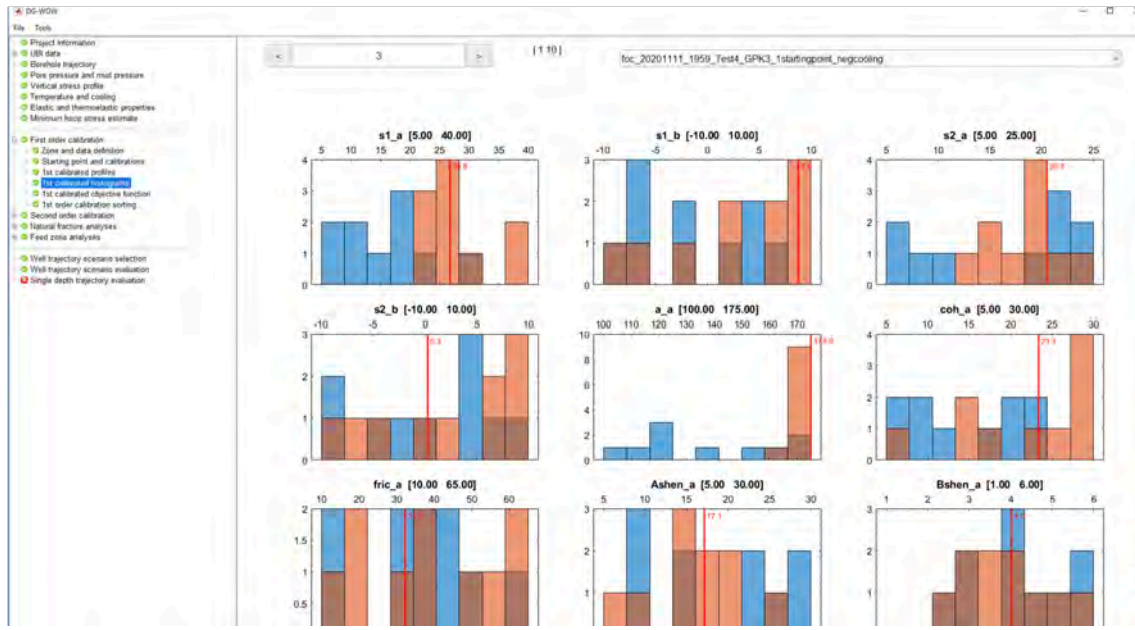


Figure 7.9.: Screenshot of the '1st order calibrated histograms' tab showing prior and posterior parameters histograms for GPK3. The red vertical lines correspond to the selected 3rd calibrated model. See the caption of Fig. 7.8 for further information.

corresponding stress profiles have a mean of ~ 18 MPa and ~ 28 MPa for S_{Hmax} and S_{Hmin} , respectively. The corresponding stress ratio $\frac{S_{Hmax}}{S_v} = 0.93$, which is consistent with the literature (David et al., 2020). However, the 2nd order calibration that was performed in GPK3 borehole show some discrepancies starting from 2700 m MD for both breakout width and breakout extent. This may be due to (1) the number and/or the location of pilots points and (2) to the assigned calibration weights to theses depths and more likely to (3) our approach to calibrate on the absence of breakouts.

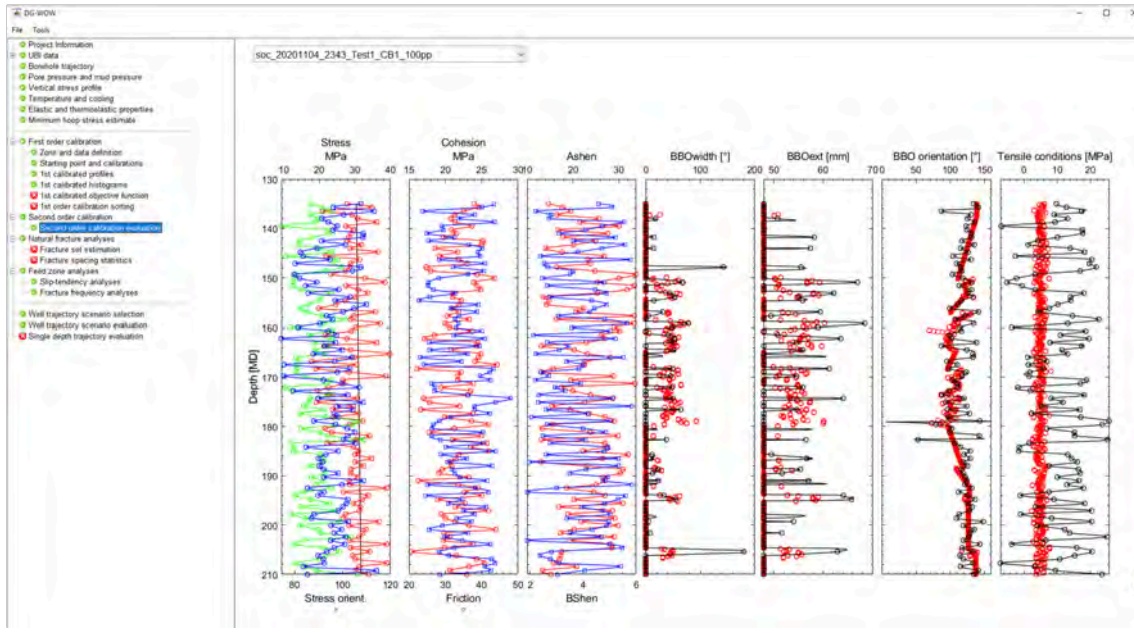


Figure 7.10.: Evaluation of the outputs of the 2nd order calibration performed for CB1 borehole. From left to right: calibrated depth profiles of stresses (S_{Hmax} in red and S_{Hmin} in green) and breakout orientation (blue); calibrated cohesion (red) and friction (blue); Shen's parameters A (red) and B (blue). Observations and calibration are shown in red and grey circles, respectively. Finally, the black line in the first panel depicts the vertical principal stress, S_v .

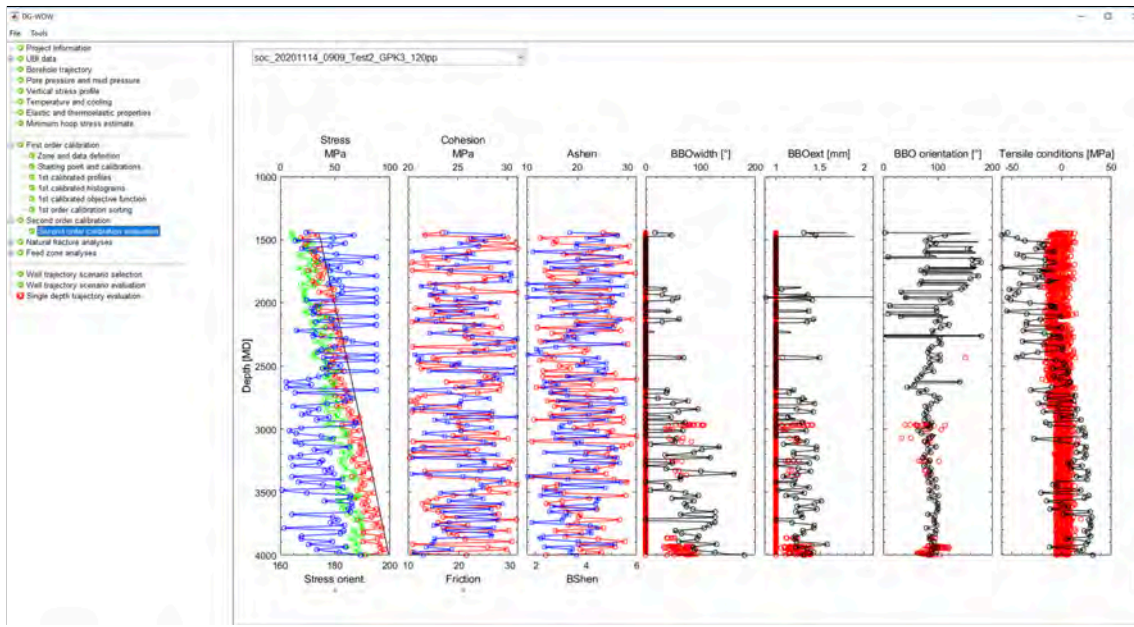


Figure 7.11.: Evaluation of the outputs of the 2nd order calibration performed for GPK3 borehole. See the caption of Fig. 7.10 for further information.

7.5. Natural fractures analyses

The first step is to cluster the fracture data in fractures sets based on their orientation. This is illustrated in the form of tadpole plots and stereographic projection with a color scheme per fracture set in Fig. 7.12 and 7.13 for CB1 and GPK3, respectively. The second step is performing fracture spacing statistics on each one of the estimated fracture set. In this step, the true spacing statistics for each set is automatically computed. Each set's true spacing distribution is represented by a boxplot and the mean and median are displayed (Fig. 7.12 and 7.13). This information is required for subsequent quantitative spacing analyses. Based on this analysis, 4 and 7 fracture sets are determined for CB1 and GPK3, respectively. The computed true spacing distribution for CB-1 varies from 0.34 m to 3.33 m, whereas in GPK3 borehole, it is the spacing is more important as it varies from 1.4 to 92.

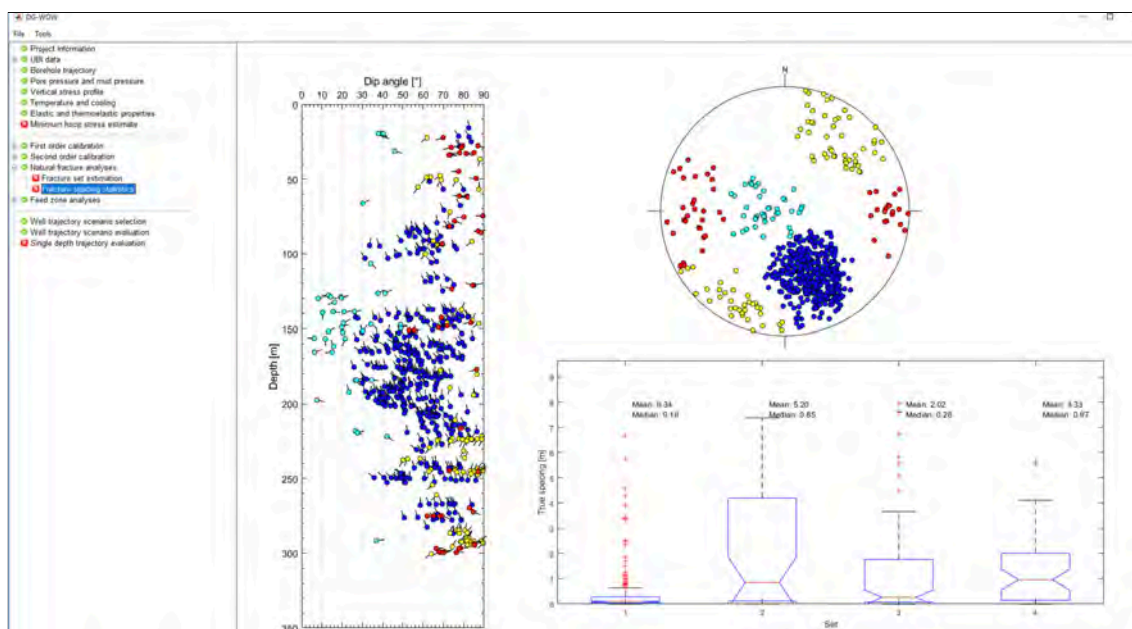


Figure 7.12.: Screenshot displaying the fractures sets in CB-1 in the form of tadpole plot (left) and stereographic projection (right) with a color scheme for each fracture set. In this example, 4 fracture sets were determined.

Feedzone analyses are then performed by computing slip dilation tendency of fractures and the total fracture spacing. Additionally, the characteristics and statistics of each fracture set are considered and a resulting fracture intensity for any borehole orientation is computed. The outcomes of these analyses are presented using a stereographic projection as shown in Figs. 7.14-7.15.

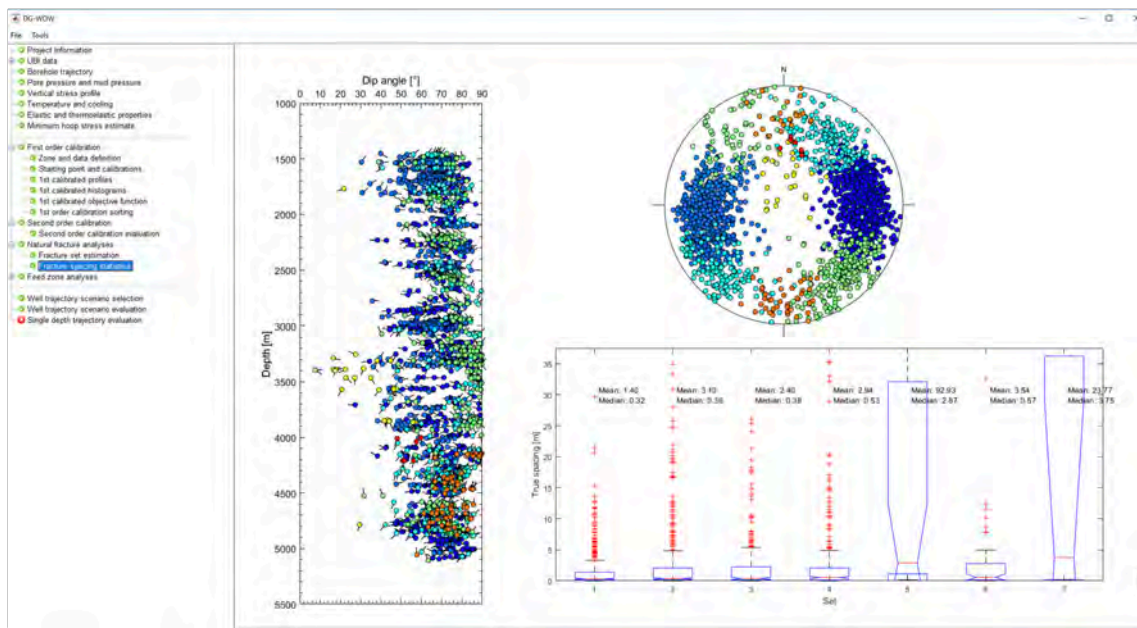


Figure 7.13.: Screenshot displaying the fractures sets in GPK3 in the form of tadpole plot (left) and stereographic projection (right) with a color scheme for each fracture set. In this example, 7 fracture sets were determined.

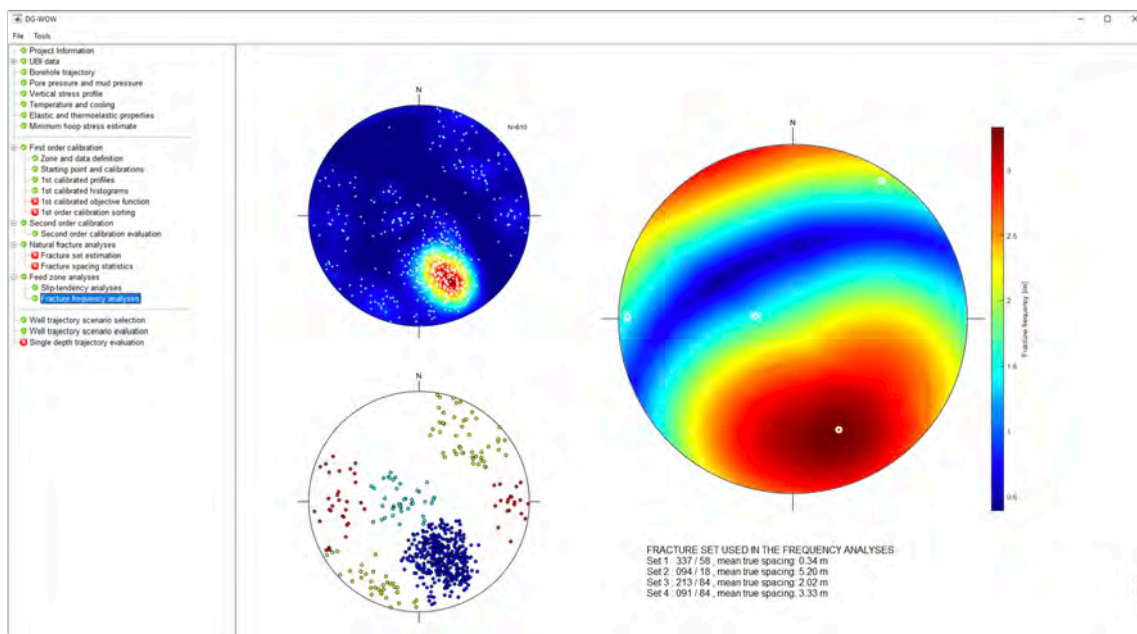


Figure 7.14.: Total fracture frequency analyses in function of drilling directions in the CB1 borehole.

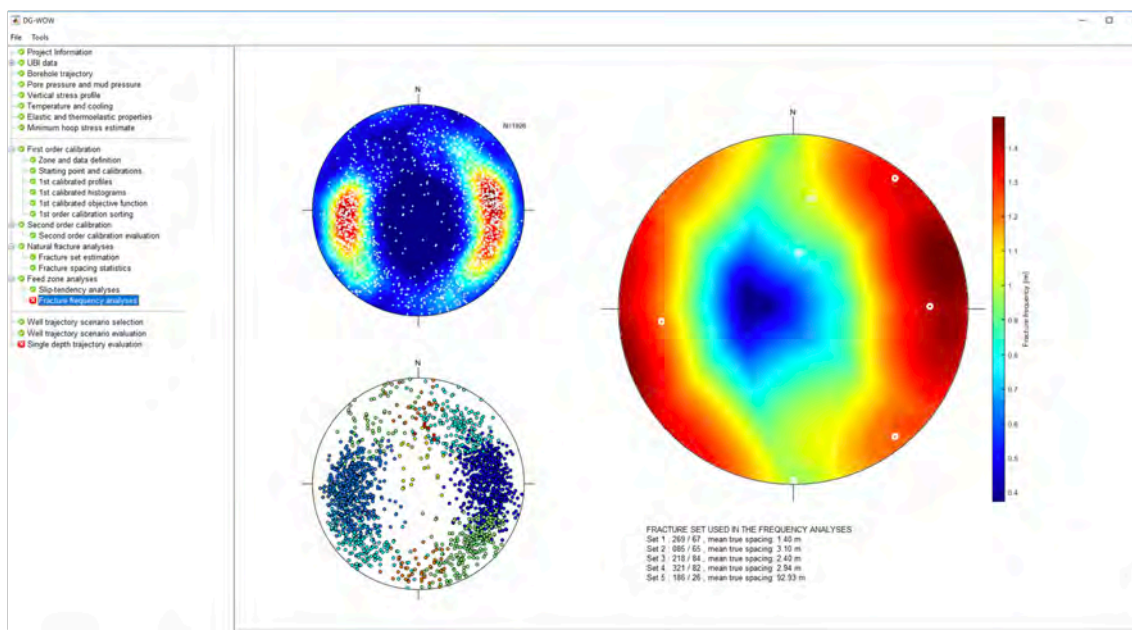


Figure 7.15.:]

Total fracture frequency analyses in function of drilling directions in the GPK3 borehole.

7.6. Failure severity prediction

In order to perform predictions in both CB1 and GPK3, two borehole trajectories were defined for illustration purposes (a vertical hole and a hole deviated by 70° from the vertical). The trajectories are the ones along which the failure should be predicted. Then the 1st order well calibrated stress and strength models (13th model for CB1 and 3rd model for GPK3) were extrapolated to the true vertical depth level where failure should be predicted. Finally, failure is predicted in both defined sections (shown in green in Figs. 7.16-7.17). Results of the performed 1st order prediction are shown in Figs. 7.16-7.17. Indeed, predictions were carried out in the deepest section of the CB-1 borehole (200 to 300 m MD) using the only one well calibrated model obtained in Section 7.4.1. Failure predictions range from 0 to 50° for breakout width, 100 to 125 mm for breakout extent and stable tensile conditions (Fig. 7.16). However, when deviating the borehole to 70° , the borehole is stable and no breakouts occur (Fig. 7.20).

2nd order predictions can also be performed by choosing the appropriate stochastic variability. The methodology is described in detail in Chapter 4. Results are shown in Fig. 7.22 and 7.23. These results show that our prediction methodology is able to account for parameters variability in depth and that the application is flexible to perform predictions for different borehole trajectories. However, conclusions cannot be drawn about the reliability of these predictions because only one model was well calibrated and thus only one prediction is carried out in the deepest.

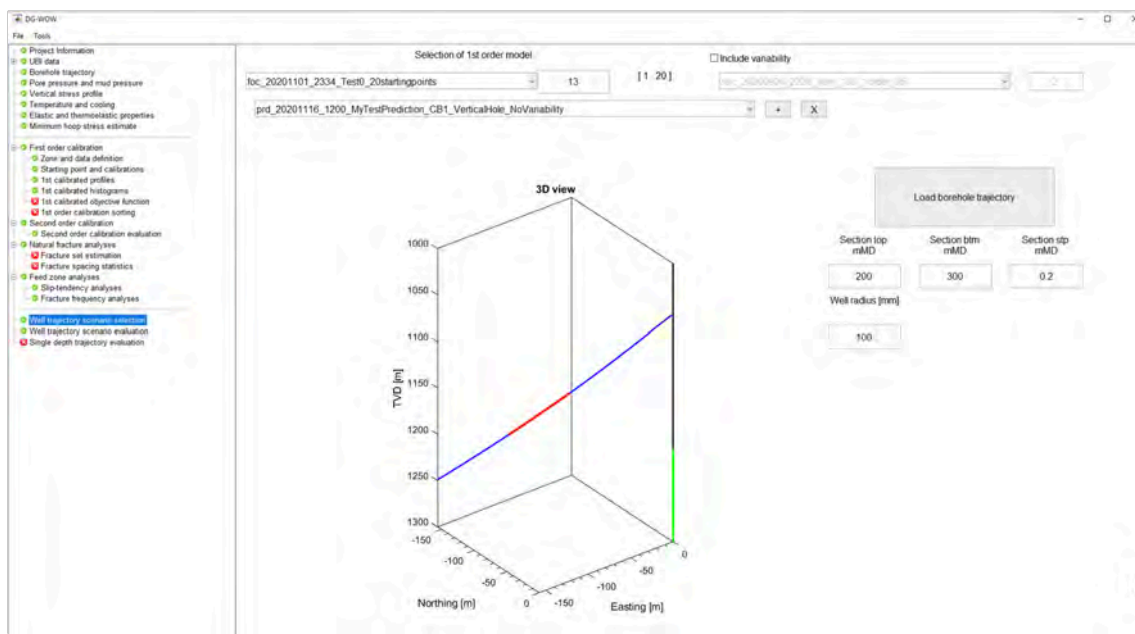


Figure 7.16.: 3D view of the CB1 borehole trajectory and sections along which calibration (red section) and prediction (green section) were carried out. Note that the borehole trajectory along which the failure should be predicted in this example is vertical.

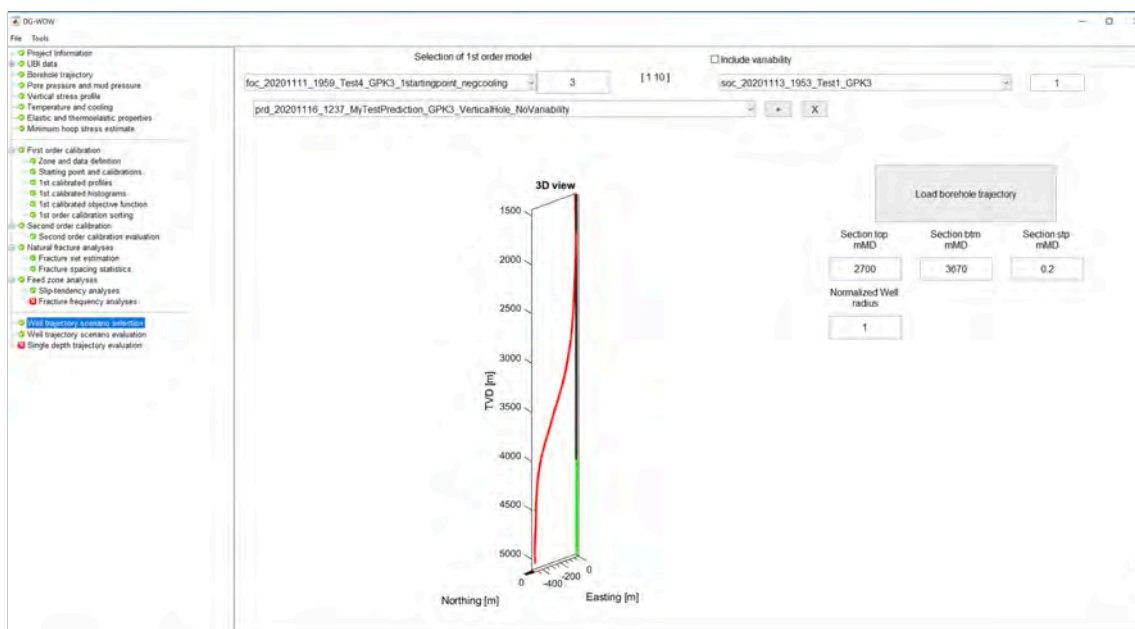


Figure 7.17.: 3D view of the GPK3 borehole trajectory. Note that the borehole trajectory along which the failure should be predicted in this example is vertical. See the caption of Fig. 7.16 for further information.

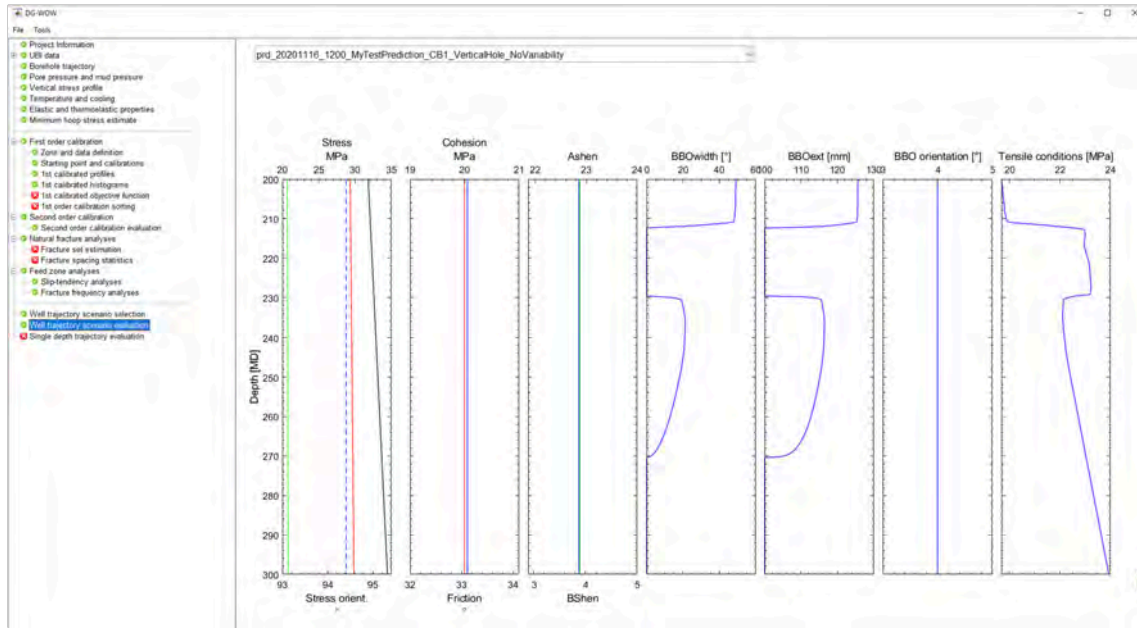


Figure 7.18.: Predicted failure severity from 200 to 300 m MD for CB1 borehole. (a) forecast stresses using DeeSse multivariate simulations (S_{Hmax} [MPa], S_{hmin} [MPa], and stress orientation [°] are in red, green and blue respectively; (b) cohesion [MPa] (red) and friction [°] (blue); (c) Shen’s parameters A (green) and B (blue); (d) predicted breakout width; (e) breakout extent; (f) breakout orientation and (g) DITFs. Note that this 1st order prediction was performed on a vertical hole.

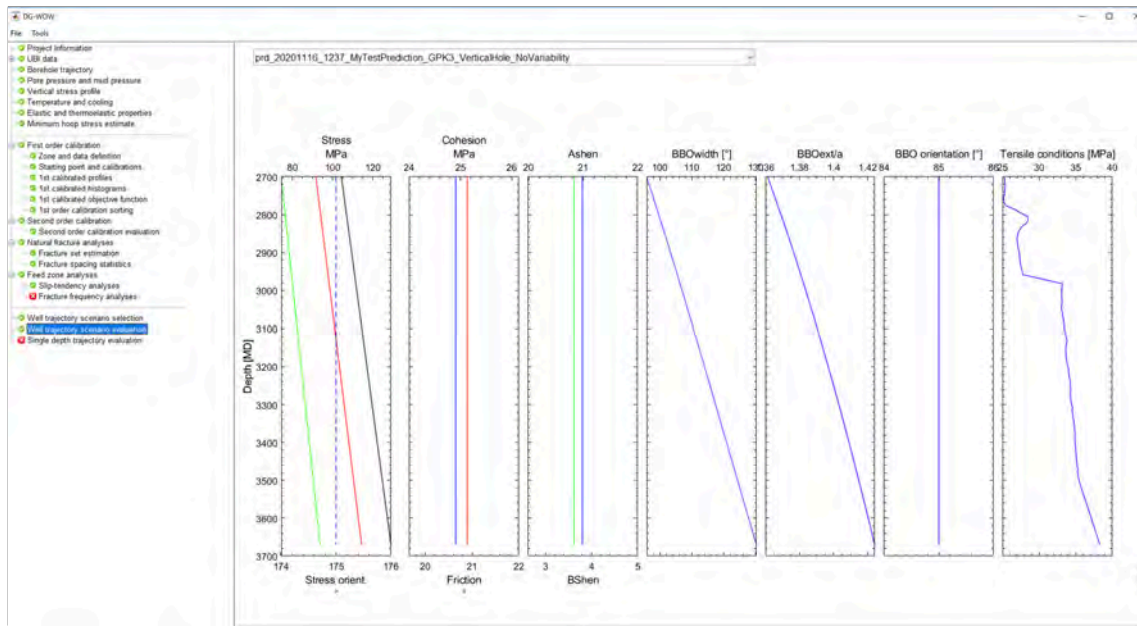


Figure 7.19.: Predicted failure severity from 2700 to 3700 m MD for GPK3 borehole. See the caption of Fig. 7.18 for further information. Note that this 1st order prediction was performed on a vertical hole.

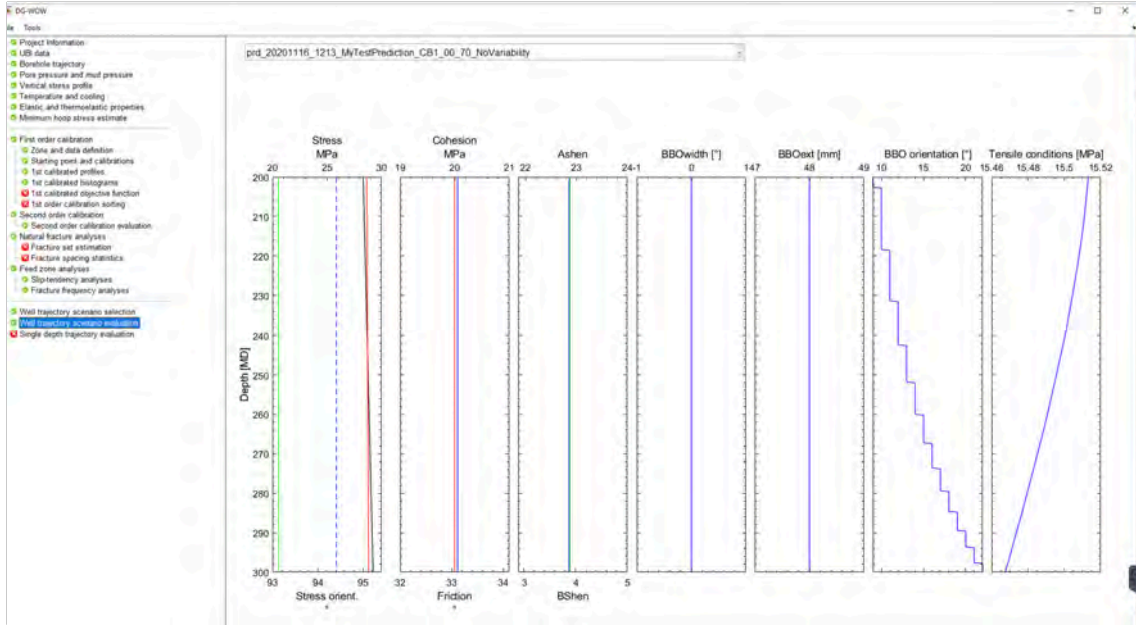


Figure 7.20.: Predicted failure severity from 200 to 300 m MD for CB1 borehole. See the caption of Fig. 7.18 for further information. Note that this 1st order prediction was performed on a borehole deviation of 70°.

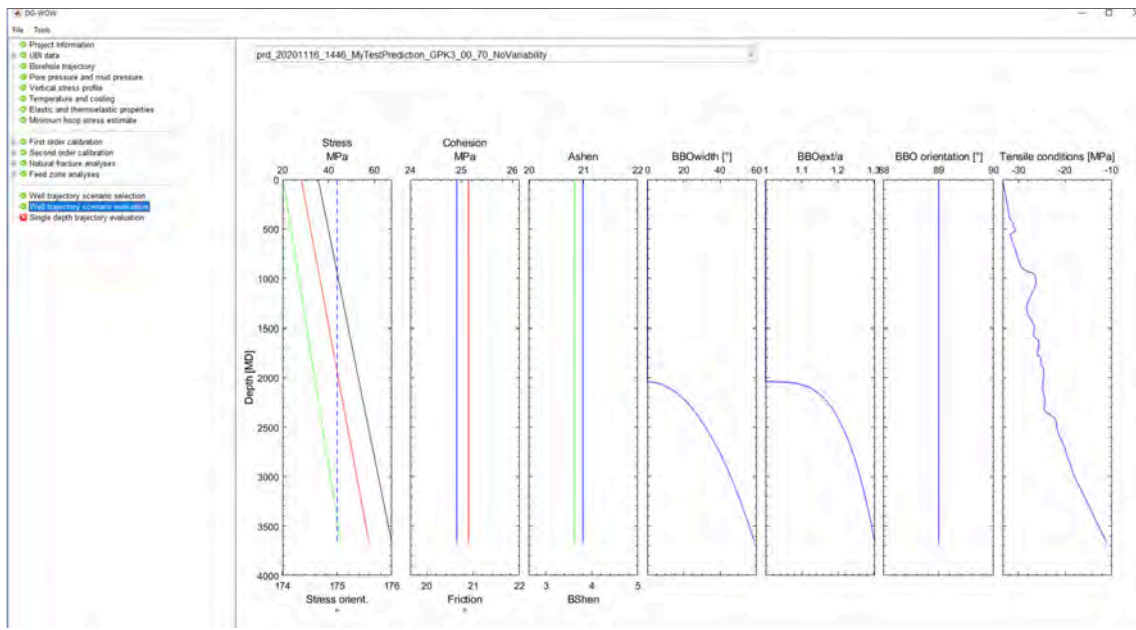


Figure 7.21.: Predicted failure severity from 2700 to 3700 m MD for GPK3 borehole. See the caption of Fig. 7.18 for further information. Note that this 1st order prediction was performed on a borehole deviation of 70°.

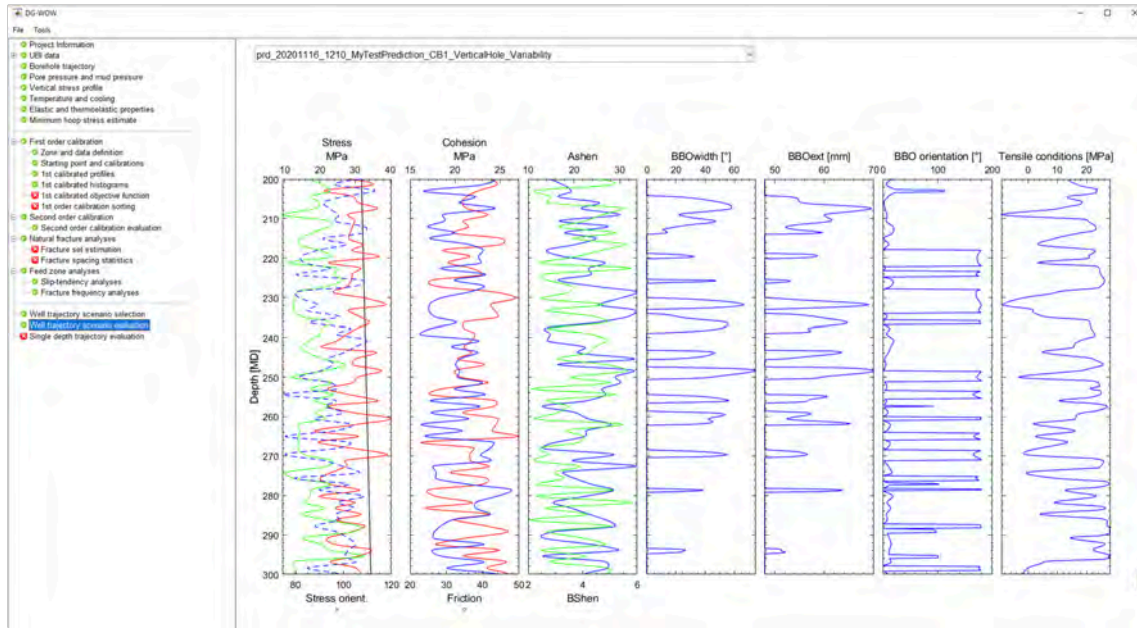


Figure 7.22.: Predicted failure severity from 200 to 300 m MD for CB1 when accounting for stochastic variability. (a) forecast stresses using DeeSse multivariate simulations (S_{Hmax} [MPa], S_{Hmin} [MPa], and stress orientation [°] are in red, green and blue respectively; (b) forecast cohesion [MPa] (red) and friction [°] (blue); (c) Shen’s parameters A (green) and B (blue); (d) predicted breakout width; (e) breakout extent; (f) breakout orientation and (g) DITFs. The considered hole for this study is vertical.

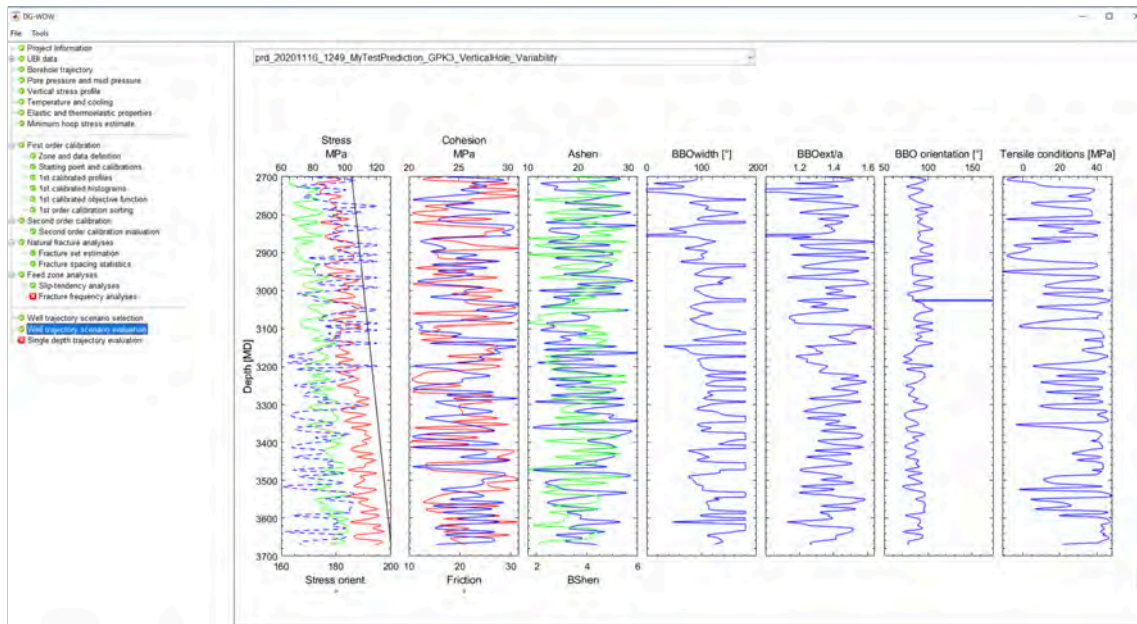


Figure 7.23.: Predicted failure severity from 2700 to 3700 m MD for GPK3 when accounting for stochastic variability. See the caption of Fig. 7.22 for further information. The considered hole for this study is vertical.

7.7. Summary

The main objective of this chapter is to test the applicability limits of our calibration and prediction methodology as proposed in Dahrabou et al. (2022b,a) against available observations from two real cases: CB-1 and GPK3 boreholes. Data from both boreholes were pre-processed, formatted and compiled. 1st and 2nd order calibrations were then carried out in order to estimate depth trends of stresses and strength and to characterize their variability around their mean. Unfortunately, we could not draw clear conclusions about the reliability of our predictions and calibrations. This may be due to one or more of the following reasons:

1. The starting points were not sufficient to perform the calibration and prediction study.
2. The locations and the number of pilot points were not optimal.
3. The defined initial ranges for stresses and strength in the CB1 case should be modified. Indeed, as CB1 is newly drilled, there were no much precise information about geomechanical parameters.
4. The calibrations may be biased as our method to calibrate when no breakouts occur is still not optimal.

All of the possible reasons above can explain the poor quality of the results. Although performance was not ideal, we still believe that the DG-WOW-app is resilient when applying it to different data sets and is able to provide an immediate visual feedback. Further analysis should be done carefully on each case study in order to generate more extensive calibrated parameter sets and evaluate the robustness of the approach. These analysis are part of to recommended future work.

8. Conclusions and outlook

This dissertation presents a novel, complete and efficient methodology to jointly estimate wellbore failure parameter sets that reproduce the observations of cross-sectional borehole geometry in the shallower section of the well and to predict borehole failure severity in the deepest in a robust probabilistic framework. The suggested calibration and prediction methodologies have been tested on a number of synthetic and real cases. This workflow was also brought into practice by developing a set of versatile supporting software tool to quickly define the optimal borehole direction at a specific point during the drilling operations of deep geothermal wells. In the following, we first summarize the main results and then propose a few directions for future research.

Summary of main contributions

Chapter 3: A systematic methodology to calibrate wellbore failure models and estimate wellbore cross-sectional geometry

In this first paper, a systematic and an efficient methodology is proposed to estimate jointly wellbore failure parameter sets (stress and strength) that reproduce the observations of cross-sectional borehole geometry. The performance of this methodology is explored using the extensive data set of the BS-1 borehole (from the Basel Deep Heat Mining project). Traditionally, breakout extent is usually disregarded as it is difficult to simulate but this paper sheds new light not only on breakout width, breakout orientation and the presence/absence of DITFs but also on breakout extent. The latter's characterisation is crucial towards proper well completion, e.g., to guarantee effective packer sealing. In this paper, it was investigated computationally feasible alternatives to carry out this characterization. The direct use of failure criteria with Kirsch solution (Kirsch, 1898) for breakout extent computation was found to be inappropriate because progressive failure is neglected. Consequently, we used Kirsch solution with an empirical approach proposed by Shen (2008) were used throughout this paper as it is shown to reproduce accurately the failure observations of the Basel borehole and is computationally affordable. We needed to extend this criterion to make it applicable to a broader range of conditions than initially included by Shen (2008). To that end, we defined an apparent wellbore strength accounting for the strengthening effect of σ_2 and σ_3 , that can be adjusted to any failure criterion. Thereafter, emphasis was placed on sensitivity analyses to identify parameters with large impact on model outputs, i.e., those to be calibrated, and to bracket parameter ranges, thus reducing prior uncertainties and computational effort. It was concluded

that stress (i.e., maximum and minimum principal horizontal stresses), strength (cohesion and friction angle), and Shens parameters are the most influential parameters on borehole failure.

The parameterization of the problem depends on the desired characterization. Indeed, throughout this paper, the difference between a 1st and a 2nd order characterisation was explicitly highlighted. The former aims at estimating depth trends of the wellbore failure driving parameters (i.e., stress and strength) and the latter aims at estimating the deviations of a given parameter from its estimated mean trend (1st order characterization), which enables the analysis of variability at all scales. To that end, we used the regularized pilot points method (RPPM, Alcolea et al., 2006), originally devised by De Marsily (1984), as implemented in the free parameter estimation software PEST (Doherty, 2015). A number of starting points is used in the 1st order calibration to guarantee that a global optimum is achieved by the Levenberg-Marquardt algorithm (Alcolea et al., 2000). Results show the non-uniqueness of the solutions which outlines that the problem is ill-posed. A prior and posterior rejection criteria were then defined to constrain prior distributions based on frictional equilibrium and to filter calibrations. The reduction of parametric uncertainties was handled by (1) using singular value decomposition (SVD) and regularisation (Doherty, 2015) And (2) including available measurements (e.g. estimate of S_{hmin} from XLOT). Results show that the range of calibrated parameters is reduced drastically, which shows the importance of collecting such data.

Dealing with the inherent uncertainty on the choice of a failure criterion is another explored item in this paper. This is coped by means of sensitivity analysis, whose results allow to validate or discard failure models. The obtained results are an evidence of the goodness of the Mohr-Coulomb failure criterion as it leads to profiles consistent with the literature (Valley and Evans, 2019). Last but not least, the derived parameters stress/strength are all plausible and coherent with those in the literature (Valley and Evans, 2019) and the outcomes of both 1st and 2nd order calibration show consistency and the goodness of fit is striking.

Chapter 4: A computational stochastic methodology to predict failure severity in deep geothermal boreholes

Chapter 3 and 4 present an overall calibration-prediction methodology. Calibration of stress and strength parameters of the proposed failure model is made against existing data, typically collected along the shallower section of the well. Then, in this chapter, the methodology was extended to failure prediction where stochastic forecasts of different boreholes trajectories can be carried out in the deepest section of the well. The singularity of these forecasts is their ability to account for (1) all available information, (2) the inherent variability and uncertainty of model parameters and (3) existing dependencies/correlations between parameters. In order to test the applicability and accuracy of this methodology, it was applied to predict failure in the deepest part of the BS-1 well and predictions

were compared with actual observations. In this work, not only a 1st order prediction is proposed but also a 2nd order prediction that deals with the quantification of variability of the predicted variables around the estimated trends. This is mainly because local scale variability has been shown to be typically large in crystalline rocks (Valley, 2007) and thus should not be neglected. Results show that the predictions are homogeneous and coherent with the mean profile of the available observations, which gives a first evidence of the accuracy and reliability of the proposed methodology.

In this chapter, existing correlations between parameters were investigated and accounted for by using a direct sampling multi-point statistical approach as implemented in DeeSse. Results show that the correlations and anti-correlations between the studied parameters were well captured in the prediction section, which has further strengthened our confidence in the proposed methodology. Additionally, the DS-MPS approach leads to consistent predictions for all stochastic realisations. However, it was shown that it is not possible to predict the exact position of breakouts but it is possible to assess the statistical characteristic of failure.

The proposed approach has the merit to provide the complete stress tensor along continuous profile in the crust. This gives a unique opportunity to evaluate stress heterogeneity and their source in the crystalline basement. The absence of correlation between S_{Hmax} and S_{hmin} supports the hypothesis that stress heterogeneity is controlled by slip on fractures (Shamir and Zoback, 1992; Valley, 2007). It discards the idea that stress heterogeneities are controlled by stiffness contrast, as for example due to lithological changes or alteration, because in such case, S_{Hmax} and S_{hmin} would be correlated to some extent.

Chapter 5: Application of the calibration and prediction approaches to synthetic cases

The main objective of this chapter is to test the limits of the calibration and prediction methodology as proposed in Dahrabou et al. (2022b,a). So far, the proposed workflow was applied only to the extensive borehole data set along the crystalline section of the borehole BS-1 (Basel, Switzerland). The latter is sub-vertical, 80% of its entire length is affected by breakouts and normal to strike slip stress regime conditions are encountered. 1st and 2nd order calibration and prediction that were carried out for this specific case showed striking results but we are aware that this work may have undetected limitations especially when deviated boreholes are considered and/or the breakouts intensity is considerably different. As a consequence, further work is carried out in this chapter to identify the main factors affecting the robustness of our methodology. To that end, synthetic cases with different stress regime conditions, borehole trajectories and different failure intensity were generated in order to investigate a much broader range of conditions than those encountered in real field data sets. This led to a variety of scenarios that cover a wide range of possibilities. Firstly, results confirmed the previous findings in Dahrabou et al. (2022b,a) when considering a vertical well, not only for the NF-SS stress regime (as it

was firstly studied) but this was valid independently from the considered stress regime. Different intensity of breakouts occurrence, however, affects the quality of the calibrations, meaning that when calibrations are carried out for a multitude of starting points in the vertical section of a well affected by pervasive breakouts, only few calibrated models are discarded. Conversely, when few breakouts are observed in the calibration section, only few calibrated models are retained. This is mainly due to the used approach to deal with depths where failure does not occur.

Concerning predictions, results show that they are accurate and consistent with observations in the case of a vertical well, independently from the stress regime or breakouts intensity. However, the 1st order predictions start to shift when the well is deviating. This shift was quantified by defining an appropriate metric. The latter showed that this shift is either acceptable or not depending on two main factors: (1) stress anisotropy ratio and (2) the difference of breakouts intensity in both calibration and prediction sections. Indeed, borehole trajectories for which the computed shift was notably high coincide with either the most favorable or the worst drilling trajectories in terms of borehole stability. This finding was based on the relationship between stress anisotropy and optimum well path derived by Al-ajmi (2006). On the other hand, when pervasive breakouts are affecting the calibration section, and few breakouts are formed in the deepest section of the well (because the considered borehole trajectory is the most stable according to Al-ajmi (2006)), predictions overestimate failure. Similarly, when few breakouts are present in the calibration section but more pronounced in the deepest section of the well (because the considered trajectory is the worst in terms of stability), predictions tend to underestimate failure. Finally, when quantifying predictions dispersion by defining the appropriate metrics, results show that 1st order predictions envelop is narrow and that the variability is satisfactorily reproduced in the 2nd order predictions. This finding is valid only for a vertical well independently from the stress regime and the breakouts intensity. However, when the well is deviating, dispersion is markedly increasing, leading to predictions with a spread that increases, when the borehole deviation is increasing as well. This is valid for all stress regimes.

This poor performance of the calibration and prediction methodology as proposed in Dahrabou et al. (2022b,a), was not surprising because (1) our approach to account for the absence of failure in our model is not optimal and when few breakouts are affecting the well, the calibrated stresses are somehow biased, (2) the ratio between the principal horizontal and the vertical stresses is not calibrated and thus its impact when the well is deviated is not accounted for. Finally, a potential solution to reduce the spread of predictions is to add available measurements of stresses, i.e., S_{hmin} from XLOTs.

Chapter 6: Deep Geothermal Well Optimization Workflow (DG-WOW) application

In this chapter, the practical translation of the entire developed workflow is presented in the form of a supporting tool software (DG-WOW-app). In practice, it is indeed important to be able to apply the proposed workflow in this thesis quickly in order to select an optimal drilling trajectory while the (expensive) drilling equipment is on hold. The optimal drilling direction is defined as the one that promotes wellbore stability while intersecting as many as possible potential feed zones. The workflow is divided into three main phases: (1) data pre-processing, (2) failure models calibration and identification of critically stresses fractures and (3) failure severity prediction.

Assessing borehole stability is essential to enable zonal isolation and to prevent drilling delays associated with an unstable borehole. This sequence of operation is somewhat specific to the Haute-Sorne project, but the intent is to have a more versatile tool that can be adapted to various projects. In this chapter, the resilience of the developed application was tested on the BS-1 borehole data. Results show consistency and coherence with the outcomes of Chapter 3 and 4 and reproduce satisfactorily the BS-1 observations. The importance of this software tool is its ability to provide a complete, intuitive and easy-to-use interface and immediate visual feedback that may help deciding of an optimal drilling trajectory. It must however be considered as a prototype and will need further testing on other real case studies and developments.

Chapter 7: Application of the calibration and prediction approaches to real case studies

The proposed calibration and prediction methodology in Chapters 3 and 4 were developed and tested only on the data set from the Basel geothermal borehole, BS-1, and its applicability limits were also tested against a systematic study with synthetic cases as fully described in Chapter 5. However, it is very important to apply the developed workflow to other real cases that present different conditions from BS-1. In this chapter, two real cases were studied: CB1 (Bedretto) and GPK3 (Soultz-Sous-Forêt) boreholes. Note that our focus was more placed on presenting an approach in real application conditions, where a decision of an optimal drilling direction must be made in a short period of time to minimize costly drill rig time. The objective of this chapter is then to apply the DG-WOW-app to real case studies and conditions and to test (1) its versatility and resilience and (2) the calibration-prediction workflow developed in Chapter 3 and 4 of this thesis. Data from both boreholes were pre-processed, formatted and compiled. Then, 1st and 2nd order calibrations were carried out in order to estimate depth trends of stresses and strength and to characterize their variability around these trends. Results show that only few models were well calibrated. This is due to the fact that only few starting points were used and thus, the parameters space was not entirely spanned. However, when considering only the well filtered models, results were approximately satisfying for GPK3 borehole and

are consistent with the literature, but with a small discrepancy in the estimate of S_{hmin} . This can be fixed by adding the best estimate of S_{hmin} that was already determined by means of injections tests. However, for CB1, conclusions are difficult to draw because only one model was well calibrated. Consequently, further tests must be performed. Despite this, the DG-WOW-app is resilient when applying it to different data sets and is able to provide an immediate visual feedback. The identification of critically stresses fractures and the prediction of failure severity in the deepest section of the well were performed in a timely manner.

Perspectives for future research

The previous results raise some questions and promising directions for possible future research. We discuss below some clues and ideas that could be followed to answer these questions.

Estimation of breakout width and DITFs using Boolean variables

The computation of breakout width, w_{BO} , consists of evaluating a given failure criterion at the borehole wall using the stresses calculated by the Kirsch closed-form solution. The arc, measured as angle, along which the failure criterion is met, provides an estimate of w_{BO} . When estimating breakout width along the section of a well, breakouts are either present or absent. In the first case, our failure model estimates the magnitude of the width but in the second case, the width is assumed to be equal to zero. This is problematic as explained in detail in Chapter 7. This computational limitation leads to biased calibrations using PEST. This bias is markedly severe when few breakouts are considered along the considered well. As a consequence, further work should be done to deal with this issue. It would be useful to define a penalty function in PEST that accounts for discontinuous or Boolean variables so that PEST algorithm can calibrate on presence/absence of breakouts in addition to the consideration of breakout width when breakouts occur.

Similarly, the approach used in this thesis to estimate drilling induced tensile fractures, DITFs, is not robust. Indeed, the acquired DITFs data give information only about the presence and/or absence of DITFs along the considered borehole. We developed an approach to generate realistic values to transform the DITFs variables from being discrete to continuous but some discrepancies were observed in the outcomes of the calibration and prediction studies that were carried out. To solve this issue, one can also define a penalty function in PEST to deal with the presence/absence of the DITFs. To deal with these limitations, new development in model calibration including the estimation of discrete variables could be integrated in order to better represent the absence of breakouts, and the presence or absence of DITFs. For instance, ensemble-based Kalman methods could be considered as they have been used to handle discrete parameter estimation using proper parameterization techniques (Liu and Oliver, 2005; Hu et al., 2013; Lam et al., 2020).

Pilot points and calibration weights

A subjective and less pragmatic approach was used in this work consisting of placing pilot points on regular intervals. Few tests were run with different number pilot points along the section of BS-1 borehole but not in a systematic manner. Thus, a key question, still unsolved, is the optimal number and location of pilot points. Obviously, the density of pilot points should be larger at areas where a finer characterization is needed. One can use an alternative proposed by Alcolea et al. (2006); Hendricks-Franssen and Franssen (2001) which is less pragmatic and subjective and consists of placing pilot points randomly; or according to adjoint sensitivity to identify the most sensitive/informative sections of the data sets (LaVenue and Pickens, 1992). Another suggestion is to place pilot points where important maxima-minima are observed with higher calibration weights in order to account for severe variability.

Sensitivity to parameters controlling thermal stresses

Sensitivity to parameters controlling thermal stresses (i.e., Young Modulus, E , the coefficient of linear expansion, α and the Poisson ratio, ν) was not studied in this thesis. This was justified by the fact that the thermal stresses are small compared to the mechanical stress when considering borehole breakouts. This is valid for the cases that were studied in this work. However, thermal stresses are often necessary to consider for explaining DITFs. The estimation of the relevant cooling magnitude occurring during drilling is also subject to uncertainties. One may consider them as additional calibration parameters.

Reducing uncertainties

It was shown previously the key role of adding additional measurements to reduce uncertainties and thus narrow the spread of calibrations. One may also study the sensitivity of the calibration and prediction to this added information and especially the impact of adding more than one measurement on predictions spread. Another suggestion is to add more complexity to the calibration methodology by adding the possibility of calibrating the anisotropy ratio between horizontal and vertical stresses.

Effect of mud pressure on calibration and prediction

So far, the effect of mud pressure on the quality of calibration and prediction was not studied. It was assumed to be constant as its profile did not change considerably in the BS-1 borehole, but this may be different in other real case studies. Thus, its impact on the selection of an optimum drilling trajectory should not be neglected. In future analysis, it may be helpful to compute a mud weight window for each calibrated model in the deepest section of the well (where prediction should be carried out) in order to discard models that do not predict a safe one that promotes less breakouts and tensile conditions. This will help tremendously in reducing the uncertainties amongst the calibrations and predictions.

Moreover, this safe mud weight window can be calculated for different drilling trajectories to help decide of an optimal one.

Some improvements for the DG-WOW-app and the model's rapidity

The developed DG-WOW-app must be considered as a prototype and will need further testing and developments. Indeed, a section to add estimates of stresses (e.g., estimate of S_{hmih} interpreted from XLOTs) should added in order to help the user reducing the spread of calibrations and predictions uncertainties. It can be also useful to visualize stress at the borehole wall for a given depth. Indeed, this was developed separately from this GUI but it is not integrated in the final version of this application. As suggested previously, assessing the impact of mud pressure on calibrations and predictions is very important. This will help deciding of an optimal borehole trajectory that promotes stability of the borehole. For each calibrated failure model, one can compute a safe mud weight window in order to reduce the range of the non-unique solutions. This may be performed for different borehole deviation and dip directions. Moreover, it may be helpful to add the possibility to choose a given failure criterion to carry out the calibration and prediction study. In this work, it was shown that the Mohr-Coulomb is the most reliable failure criterion as it resulted in consistent results with the literature, but this conclusion was drawn for the BS-1 borehole. For more versatility, one may add a section to quantify predictions uncertainties. For instance, the defined metrics in Chapter 5 may be implemented in the GUI so that the user may have a general idea about the goodness of the predictions. Finally, and more importantly, calibrations are time-consuming, which prevents the user from running massive tests. We already looked for potential solutions using MATLAB but with no success. One option to explore is to convert the developed codes to another efficient and computationally affordable language such as Python.

Bibliography

High temperature instruments and methods developed for supercritical geothermal reservoir characterisation and exploitation the hiti project. *Geothermics*, 49:90 – 98, 2014.

Hydraulic stimulation and fluid circulation experiments in underground laboratories: Stepping up the scale towards engineered geothermal systems. *Geomechanics for Energy and the Environment*, 24:100175, 2020.

M. J. Afshari Moein, M. Somogyvári, B. Valley, M. Jalali, S. Loew, and P. Bayer. Fracture Network Characterization Using StressBased Tomography. *Journal of Geophysical Research: Solid Earth*, 123(11):9324–9340, Nov. 2018. doi: 10.1029/2018JB016438.

H. Akaike. A new look at the statistical model identification. *IEEE transactions on automatic control*, 19(6):716–723, 1974.

H. Akaike et al. On entropy maximization principle. 1977.

A. Al-ajmi. *Wellbore stability analysis based on a new true-triaxial failure criterion*. PhD thesis, 2006.

A. Al-Ajmi and R. Zimmerman. Stability analysis of deviated boreholes using the mogi-coulomb failure criterion, with applications to some oil and gas reservoirs. In *Proceedings of the IADC/SPE Asia Pacific Drilling Technology Conference 2006 - Meeting the Value Challenge: Performance, Deliverability and Cost*, pages 537–550, 2006.

A. Al-Ajmi and R. Zimmerman. A new well path optimization model for increased mechanical borehole stability. *Journal of Petroleum Science and Engineering*, 69(1-2):53–62, Nov. 2009. doi: 10.1016/j.petrol.2009.05.018.

A. M. Al-Ajmi and R. W. Zimmerman. The relation between the mogi and the coulomb failure criteria. *International Journal of Rock Mechanics and Mining Sciences*, 2005.

A. E. Aladejare and Y. Wang. Evaluation of rock property variability. *Georisk: Assessment and Management of Risk for Engineered Systems and Geohazards*, 11(1):22–41, Jan. 2017. doi: 10.1080/17499518.2016.1207784.

A. Alcolea, J. Carrera, A. Medina, et al. A hybrid marquardt-simulated annealing method for solving the groundwater inverse problem. *IAHS Publication*, pages 157–163, 2000.

- A. Alcolea, J. Carrera, and A. Medina. Pilot points method incorporating prior information for solving the groundwater flow inverse problem. *Advances in Water Resources*, 29:1678–1689, 11 2006. doi: 10.1016/j.advwatres.2005.12.009.
- A. Alcolea, U. Kuhlmann, P. Marschall, A. Lisjak, G. Grasselli, O. Mahabadi, R. de La Vaissière, H. Leung, and H. Shao. A pragmatic approach to abstract the excavation damaged zone around tunnels of a geological radioactive waste repository: application to the hg-a experiment in mont terri. *Geological Society, London, Special Publications*, 06 2016. doi: 10.1144/SP443.8.
- A. Alcolea, P. Meier, V. Vilarrasa, S. Olivella, and J. Carrera. *Induced Seismicity Assessment of the Hydraulic Stimulations in Borehole PX2 at Pohang (South Korea) using Coupled Hydromechanical Modelling*. 2020.
- E. M. Anderson. The dynamics of faulting. *Transactions of the Edinburgh Geological Society*, 8(3):387–402, 1905.
- J. Andersson, C. Martin, and H. Stille. The Äspö Pillar Stability Experiment: Part II—Rock mass response to coupled excavation-induced and thermal-induced stresses. *International Journal of Rock Mechanics and Mining Sciences*, 46(5):879–895, 2009a.
- J. Andersson, D. Martin, and H. Stille. The Äspö pillar stability experiment: Part ii rock mass response to coupled excavation-induced and thermal-induced stresses. *International Journal of Rock Mechanics and Mining Sciences*, 46:879–895, 07 2009b. doi: 10.1016/j.ijrmms.2009.03.002.
- M. R. Awal, M. S. Khan, M. A. Mohiuddin, A. Abdurraheem, and M. Azeemuddin. A new approach to borehole trajectory optimisation for increased hole stability, Jan 2001.
- J. Azzola, B. Valley, J. Schmittbuhl, and A. Genter. Stress characterization and temporal evolution of borehole failure at the Rittershoffen geothermal project. *Solid Earth*, 10(4):1155–1180, July 2019.
- N. Barth, C. Boulton, B. Carpenter, G. Batt, and V. Toy. Slip localization on the southern alpine fault, new zealand. *Tectonics*, 32(3):620–640, 2013.
- C. Barton, M. Zoback, and K. Burns. In situ stress orientation and magnitude at the Fenton Geothermal Site, New Mexico, determined from wellbore breakouts. *Geophysical Research Letters*, 15(5):467–470, 1988a. doi: 10.1029/GL015i005p00467.
- C. Barton, M. Zoback, and K. Burns. In-situ stress orientation and magnitude at the Fenton geothermal site, New Mexico, determined from wellbore breakouts. *Geophysical Research Letters*, 15(5):467–470, 1988b.
- C. Barton, M. Zoback, and D. Moos. Fluid flow along potentially active faults in crystalline rock. *Geology*, 23(8):683–686, 1995.

- N. Barton. The shear strength of rock and rock joints. *International Journal of Rock Mechanics and Mining Sciences and Geomechanics Abstracts*, 13:255–279, 09 1976. doi: 10.1016/0148-9062(76)90003-6.
- J. Bell and D. Gough. Northeast-southwest compressive stress in alberta evidence from oil wells. *Earth and Planetary Science Letters*, 45(2):475 – 482, 1979.
- R. Bertani. Geothermal power generation in the world 2005–2010 update report. *Geothermics*, 41:1–29, 2012.
- M. Biot. The theory of elasticity and consolidation for a porous anisotropic solid. *Journal of Applied Physics*, 26:182 – 185, 03 1955. doi: 10.1063/1.1721956.
- M. Biot and D. Willis. The elastic coefficients of the theory of consolidation. *Journal of Applied Mechanics*, 24:594–601, 01 1957.
- M. A. Biot. General theory of three dimensional consolidation. *Journal of Applied Physics*, 12(2):155–164, 1941. doi: 10.1063/1.1712886.
- G. Blöcher, T. Reinsch, J. Hennings, H. Milsch, S. Regenspurg, J. Kummerow, H. Francke, S. Kranz, A. Saadat, G. Zimmermann, and E. Huenges. Hydraulic history and current state of the deep geothermal reservoir groSS schönebeck. *Geothermics*, 63, 08 2015. doi: 10.1016/j.geothermics.2015.07.008.
- G. Borm, B. Engeser, B. Hoffers, H. Kutter, and C. Lempp. Borehole instabilities in the KTB main borehole. 102, 1997.
- W. Brace and R. Martin. A test of the law of effective stress for crystalline rocks of low porosity. *International Journal of Rock Mechanics and Mining Sciences and Geomechanics Abstracts*, 5(5):415 – 426, 1968.
- R. Braun. Analyse gebirgsmechanischer versagenszustände beim geothermieprojekt basel. *Report to Geopower Basel AG for Swiss Deep Heat Mining Project Basel. Dr. Roland Braun. Consultancy in rock mechanics, Basel, Switzerland, 2007.*
- K. Breede, K. Dzebisashvili, and G. Falcone. Overcoming challenges in the classification of deep geothermal potential. *Geothermal Energy Science*, 3(1):19–39, 2015. doi: 10.5194/gtes-3-19-2015.
- K. Bröker. In-situ stress and rock mass characterization via mini-frac tests at the Bedretto Underground Laboratory. page 105, 2019.
- D. Brown. Review of fenton hill hdr test results. Technical report, Los Alamos National Lab., NM (United States), 1997.
- M. Brudy and M. Zoback. Compressive and tensile failure of boreholes arbitrarily-inclined to principal stress axes: Application to the ktb boreholes, germany. *International Journal*

of *Rock Mechanics and Mining Sciences and Geomechanics Abstracts*, 30(7):1035 – 1038, 1993.

P. Burgherr, S. Hirschberg, and S. Wiemer. *Energy from the Earth. Deep Geothermal as Resource for the Future?* 01 2015.

J. Carrera and S. Neuman. Estimation of aquifer parameters under transient and steady state conditions: 2. uniqueness, stability, and solution algorithms. *Water Resources Research*, 22:211–227, 02 1986. doi: 10.1029/WR022i002p00211.

C. Chang, M. D. Zoback, and A. Khaksar. Empirical relations between rock strength and physical properties in sedimentary rocks. *Journal of Petroleum Science and Engineering*, 51(3):223 – 237, 2006.

X. Chen, C. P. Tan, and C. M. Haberfield. Wellbore stability analysis guidelines for practical well design, Jan 1996.

L. B. Colmenares and M. D. Zoback. A statistical evaluation of intact rock failure criteria constrained by polyaxial test data for five different rocks. *International Journal of Rock Mechanics and Mining Sciences*, 39(6):695–729, 2002.

M. Coulomb. Essai sur une application des regles des maximis et minimis a quelques problemes de statique relatifs, a la architecture. *Memoires de mathematique et de physique, presentes a l'Academie Royale des Sciences, par divers Savans, & lus dans les Assemblies. Annee 1773*, pages 343–382, 1776.

CREGE. Géothermie: Température élevée et grande profondeur. https://crege.ch/index.php?menu=geo&page=geoth_ht, 2010.

R. G. Cummings and G. E. Morris. Economic modeling of electricity production from hot dry rock geothermal reservoirs: methodology and analyses. final report. 9 1979. doi: 10.2172/5716131.

R. Cuss, E. Rutter, and R. Holloway. Experimental observations of the mechanics of borehole failure in porous sandstone. *International Journal of Rock Mechanics and Mining Sciences*, 40(5):747 – 761, 2003.

A. Dahrabou, B. Valley, P. Meier, P. Brunner, and A. Alcolea. A computational stochastic methodology to predict failure severity in deep geothermal boreholes. 2022a.

A. Dahrabou, B. Valley, P. Meier, P. Brunner, J. Doherty, and A. Alcolea. A systematic methodology to calibrate wellbore failure models and estimate wellbore cross-sectional geometry. *International Journal of Rock Mechanics and Mining Sciences*, 2022b. doi: <https://doi.org/10.1016/j.ijrmms.2021.104935>.

C. David, M. Nejati, and D. Geremia. On petrophysical and geomechanical properties of bedretto granite. Technical report, Zurich, 2020.

- G. De Marsily. *Spatial Variability of Properties in Porous Media: A Stochastic Approach*, pages 719–769. 01 1984. doi: 10.1007/978-94-009-6175-3_15.
- N. Deichmann and D. Giardini. Earthquakes Induced by the stimulation of an enhanced geothermal system below Basel (Switzerland). *Seismological Research Letters*, 80(5):784–798, 2009. doi: 10.1785/gssrl.80.5.784.
- C. Dezayes, A. Genter, G. Homeier, M. Degouy, and G. Stein. Geological study of gpk3 hfr borehole (soulz-sous-forêts, france). Technical report, 2003.
- C. Dezayes, S. Gentier, and A. Genter. Deep Geothermal Energy in Western Europe: The Soultz Project. Technical Report RP-54227-FR, BRGM, Orléans, France, 2005.
- M. S. Diederichs. The 2003 canadian geotechnical colloquium: Mechanistic interpretation and practical application of damage and spalling prediction criteria for deep tunnelling. *Canadian Geotechnical Journal*, 44(9):1082–1116, 2007. doi: 10.1139/T07-033.
- M. S. Diederichs, P. K. Kaiser, and E. Eberhardt. Damage initiation and propagation in hard rock during tunnelling and the influence of near-face stress rotation. *International Journal of Rock Mechanics and Mining Sciences*, 41(5):785–812, 2004. doi: 10.1016/j.ijrmms.2004.02.003.
- J. Doherty. Ground water model calibration using pilot points and regularization. *Ground water*, 41:170–7, 03 2003. doi: 10.1111/j.1745-6584.2003.tb02580.x.
- J. Doherty. *Calibration and Uncertainty Analysis for Complex Environmental Models*. Blurb, Incorporated, 2015.
- J. Doherty, D. Hayes, and C. Muffels. Pest home page. URL <https://pesthhomepage.org/>.
- D. Duchane. The history of hdr research and development. Technical report, Los Alamos National Lab., NM (United States), 1998.
- N. Dutler. *Seismo-Hydromechanical interaction during in-situ hydraulic fracturing experiments*. PhD thesis, University of Neuchâtel, Apr. 2020.
- A. W. Edwards. The history of likelihood. *International Statistical Review/Revue Internationale de Statistique*, pages 9–15, 1974.
- K. F. Evans, T. Kohl, R. J. Hopkirk, and L. Rybach. Modelling of energy production from Hot Dry Rock systems. Technical report, Bundesamt für Bildung und Wissenschaft, 1992.
- K. F. Evans, H. Moriya, H. Niitsuma, R. H. Jones, W. S. Phillips, A. Genter, J. Sausse, R. Jung, and R. Baria. Microseismicity and permeability enhancement of hydrogeologic structures during massive fluid injections into granite at 3 km depth at the Soultz HDR site. *Geophysical Journal International*, 160(1):388–412, 2005. doi: 10.1111/j.1365-246X.2004.02474.x.

- M. P. Evans K.F. *Hydrojacking and hydrofracturing tests in a fissile schist in South-west Switzerland: In-situ stress characterisation in difficult rock*. 1995.
- R. Ewy. Wellbore-stability predictions by use of a modified lade criterion. *SPE Drilling Completion*, 14:85–91, 06 1999. doi: 10.2118/56862-PA.
- F. Fernández-Ibáñez, D. Castillo, D. Wyborn, and D. Hindle. Benefits of ht-hostile environments on wellbore stability: a case study from geothermal fields in central australia. 2009.
- R. D. Fritz, M. K. Horn, and S. D. Joshi. *Geological Aspects of Horizontal Drilling*. American Association of Petroleum Geologists, 01 1991. doi: 10.1306/CE33529.
- A. Genter, L. Guillou-Frottier, J.-L. Feybesse, N. Nicol, C. Dezayes, and S. Schwartz. Typology of potential hot fractured rock resources in europe. *Geothermics*, 32:701–710, 08 2003. doi: 10.1016/S0375-6505(03)00065-8.
- A. Genter, K. Evans, N. Cuenot, D. Fritsch, and B. Sanjuan. Contribution of the exploration of deep crystalline fractured reservoir of soultz to the knowledge of enhanced geothermal systems (egs). *Comptes Rendus Geoscience*, 342(7):502 – 516, 2010.
- B. Goldstein, G. Hiriart, R. Bertani, C. Bromley, L. Gutiérrez-Negrín, E. Huenges, H. Muraoka, A. Ragnarsson, J. Tester, and V. Zui. Geothermal energy. in ipcc special report on renewable energy sources and climate change mitigation, 2011.
- A. Gutjahr and J. Wilson. Co-kriging for stochastic flow models. *Transport in Porous Media*, 4(6):585–598, 1989.
- J. Hadamard. Sur les problèmes aux dérivées partielles et leur signification physique. *Princeton university bulletin*, pages 49–52, 1902.
- B. Haimson. True triaxial stresses and the brittle fracture of rock. *pure and applied geophysics*, 163(5):1101–1130, Jun 2006. doi: 10.1007/s00024-006-0065-7.
- V. Hajiabdolmajid, P. K. Kaiser, and C. D. Martin. Modelling brittle failure of rock. *International Journal of Rock Mechanics and Mining Sciences*, 39(6):731–741, Sept. 2002. doi: 10.1016/S1365-1609(02)00051-5.
- A. H. Hale, F. K. Mody, and D. P. Salisbury. The influence of chemical potential on wellbore stability. *SPE Drilling & Completion*, 8(03):207–216, Sep 1993. doi: 10.2118/23885-PA.
- E. J. Hannan. The estimation of the order of an arma process. *The Annals of Statistics*, pages 1071–1081, 1980.
- M. E. Harr. Reliability-based design in civil engineering. new york, n.y., mcgraw-hill. 1987.

- M. E. Harr. Probabilistic estimates for multivariate analyses. *Applied Mathematical Modelling*, 13(5):313–318, 1989.
- S. Hassan, T. Klimentos, M. Badri, M. Sengul, and A. Zeid. Optimizing drilling performance by wellbore stability evaluation and directional drilling practices, Jan 1999.
- O. Heidbach, M. Rajabi, K. Reiter, M. Ziegler, and W. Team. World stress map database release 2016 v. 1.1. gfz data services. doi: 10.5880/WSM.2016.001.
- J. Helton, J. Johnson, W. Oberkampf, and C. Storlie. A sampling-based computational strategy for the representation of epistemic uncertainty in model predictions with evidence theory. *Computer Methods in Applied Mechanics and Engineering*, 196(37-40):3980–3998, 2007. doi: 10.1016/j.cma.2006.10.049.
- Hendricks-Franssen and H.-J. Franssen. Inverse stochastic modelling of groundwater flow and mass transport /. 08 2001.
- Y. Hiramatsu and Y. Oka. Determination of the stress in rock unaffected by boreholes or drifts, from measured strains or deformations. *International Journal of Rock Mechanics and Mining Sciences and Geomechanics Abstracts*, 5(4):337 – 353, 1968.
- E. Hoek. When is a rock engineering design acceptable. (September):1–25, 1991.
- E. Hoek and C. D. Martin. Fracture initiation and propagation in intact rock A review. *Journal of Rock Mechanics and Geotechnical Engineering*, 6(4):287–300, Aug. 2014. doi: 10.1016/j.jrmge.2014.06.001.
- K. Holliger. Upper-crustal seismic velocity heterogeneity as derived from a variety of P-wave sonic logs. *Geophysical Journal International*, 125(3):813–829, June 1996. doi: 10.1111/j.1365-246X.1996.tb06025.x.
- H. Houston. *Deep Earthquakes*, pages 329–354. 12 2015. doi: 10.1016/B978-0-444-53802-4.00079-8.
- L. Y. Hu, Y. Zhao, Y. Liu, C. Scheepens, and A. Bouchard. Updating multipoint simulations using the ensemble Kalman filter. *Computers and Geosciences*, 51:7–15, 2013. doi: 10.1016/j.cageo.2012.08.020.
- M. O. Häring, U. Schanz, F. Ladner, and B. C. Dyer. Characterisation of the Basel 1 enhanced geothermal system. *Geothermics*, 37(5):469–495, Oct. 2008. doi: 10.1016/j.geothermics.2008.06.002.
- Y. Iio. Frictional coefficient on faults in a seismogenic region inferred from earthquake mechanism solutions. *Journal of Geophysical Research: Solid Earth*, 102(B3):5403–5412, 1997. doi: 10.1029/96JB03593.
- M. Islam and P. Skalle. In-situ stress pattern and its impact on stable drilling operation a sensitivity analysis. 04 2010.

- Jaeger. *Fundamentals of Rock Mechanics*_Jaeger&Cook&Zimmerman, 2007.
- C. Jaupart, S. Labrosse, and J. Marechal. *Temperatures, Heat and Energy in the Mantle of the Earth*, volume 7, pages 253–303. 12 2007. doi: 10.1016/B978-044452748-6.00114-0.
- D. Jordan. Geological characterization of the bedretto underground laboratory for geoenergies. Master’s thesis, ETH Zurich, Zurich, 2019.
- B. Kaeser, A. Kalt, and J. Borel. The crystalline basement drilled at the basel-1 geothermal site, a preliminary petrologicalgeochemical study. *Report to Geopower Basel AG for Swiss Deep Heat Mining Project Basel. Institut de Géologie et d’Hydrogéologie, Université de Neuchâtel, Switzerland, 2007.*
- R. Kashyap. Optimal choice of ar and ma parts in autoregressive moving average models. *IEEE Transactions on Pattern Analysis and Machine Intelligence*, PAMI-4:99–104, 1982.
- U. Kastrup, M. L. Zoback, N. Deichmann, K. F. Evans, D. Giardini, and A. J. Michael. Stress field variations in the Swiss Alps and the northern Alpine foreland derived from inversion of fault plane solutions. *Journal of Geophysical Research: Solid Earth*, 109(B1), 2004. doi: 10.1029/2003jb002550.
- F. Keller and T. Schneider. Geologie und geotechnik-geology und geotechnics of the furka-base-tunnel. *Schweiz. Ing. Architekt*, 100(24):512–520, 1982.
- G. King. Hydraulic fracturing 101: What every representative, environmentalist, regulator, reporter, investor, university researcher, neighbor and engineer should know about estimating frac risk and improving frac performance in unconventional gas and oil wells. *Society of Petroleum Engineers - SPE Hydraulic Fracturing Technology Conference 2012*, 01 2012. doi: 10.2118/152596-MS.
- G. Kirsch. Die theorie der elastizitat und die bedurfnisse der festigkeitslehre. *Zeitschrift der Vereins deutscher Ingenieure*, 42:797–807, 1898.
- P. K. Kitanidis and E. G. Vomvoris. A geostatistical approach to the inverse problem in groundwater modeling (steady state) and one-dimensional simulations. *Water Resources Research*, 19(3):677–690, 1983. doi: 10.1029/WR019i003p00677.
- T. Kraft and N. Deichmann. High-precision relocation and focal mechanism of the injection-induced seismicity at the Basel EGS. *Geothermics*, June 2014. doi: 10.1016/j.geothermics.2014.05.014.
- D. G. Krige. *A Statistical Approach to Some Mine Valuation and Allied Problems on the Witwatersrand*. publisher not identified, 1951.
- S. Kwon, L. Xie, S. Park, K.-I. Kim, K.-B. Min, K. Y. Kim, L. Zhuang, J. Choi, H. Kim, and T. Lee. Correction to: Characterization of 4.2-km-deep fractured granodiorite cores

from pohang geothermal reservoir, korea. *Rock Mechanics and Rock Engineering*, 53, 07 2019. doi: 10.1007/s00603-019-01925-2.

S. Lacasse and F. Nadim. Uncertainties in characterising soil properties. 1996.

D.-T. Lam, P. Renard, J. Straubhaar, and J. Kerrou. Multiresolution approach to condition categorical multiplepoint realizations to dynamic data with iterative ensemble smoothing. *Water Resources Research*, 56, 02 2020. doi: 10.1029/2019WR025875.

N. C. Last and M. R. McLean. Assessing the impact of trajectory on wells drilled in an overthrust region. *Journal of Petroleum Technology*, 48(07):620–626, Jul 1996. doi: 10.2118/30465-JPT.

A. M. LaVenue and J. F. Pickens. Application of a coupled adjoint sensitivity and kriging approach to calibrate a groundwater flow model. *Water Resources Research*, 28(6):1543–1569, 1992. doi: 10.1029/92WR00208.

W. Lin, K. Yamamoto, H. Ito, H. Masago, and Y. Kawamura. Estimation of Minimum Principal Stress from an Extended Leak-off Test Onboard the Chikyu Drilling Vessel and Suggestions for Future Test Procedures. *Scientific Drilling*, 6:43–47, July 2008. doi: 10.2204/iodp.sd.6.06.2008.

N. Liu and D. S. Oliver. Ensemble Kalman filter for automatic history matching of geologic facies. *Journal of Petroleum Science and Engineering*, 47(3-4):147–161, 2005. doi: 10.1016/j.petrol.2005.03.006.

S. Luthi. *Geological Well Logs: Their Use in Reservoir Modeling*. 01 2001. doi: 10.1007/978-3-662-04627-2.

X. Ma. Geologic and in situ stress characterization of the Bedretto Underground Laboratory (BUL), an EGS test bed in the Swiss Alps. In *AGU Fall Meeting Abstracts*, pages H14D–02, Dec. 2019.

X. Ma, N. Gholizadeh Doonechaly, M. Hertrich, V. Gischig, and G. Klee. Preliminary in situ stress and fractures characterization in the bedretto underground laboratory, swiss alps: implications on hydraulic stimulation. In S. A. da Fontoura, R. J. Rocca, and J. Pavón Mendoza, editors, *Rock Mechanics for Natural Resources and Infrastructure Development - Full Papers Proceedings of the 14th International Congress on Rock Mechanics and Rock Engineering (ISRM 2019), September 13-18, 2019, Foz do Iguassu, Brazil*, volume 6 of *Proceedings in Earth and Geosciences*, pages 1559 – 1567, London, 2020. CRC Press.

G. Mariethoz, P. Renard, and J. Straubhaar. The direct sampling method to perform multiple-point geostatistical simulations. *Water Resources Research - WATER RESOURCES*, 46, 11 2010. doi: 10.1029/2008WR007621.

- D. W. Marquardt. An algorithm for least-squares estimation of nonlinear parameters. *Journal of the Society for Industrial and Applied Mathematics*, 11(2):431–441, 1963.
- P. Marschall, S. Giger, R. De La Vassière, H. Shao, H. Leung, C. Nussbaum, T. Trick, B. Lanyon, R. Senger, A. Lisjak, and A. Alcolea. Hydro-mechanical evolution of the edz as transport path for radionuclides and gas: insights from the mont terri rock laboratory (switzerland). *Swiss Journal of Geosciences*, 110(1):173–194, Apr 2017. doi: 10.1007/s00015-016-0246-z.
- C. D. Martin and B. Stimpson. The effect of sample disturbance on laboratory properties of lac du bonnet granite. *Canadian Geotechnical Journal*, 31(5):692–702, 1994. doi: 10.1139/t94-081.
- C. D. Martin, P. K. Kaiser, and D. R. McCreath. Hoek Brown parameters for predicting the depth of brittle failure around tunnels. 151(705):136–151, 1999.
- D. Martin. Seventeenth canadian geotechnical colloquium: The effect of cohesion loss and stress path on brittle rock strength. *Canadian Geotechnical Journal - CAN GEOTECH J*, 34:698–725, 10 1997. doi: 10.1139/cgj-34-5-698.
- D. Martin, P. Kaiser, and R. Christiansson. Stress, instability and design of underground excavations. *International Journal of Rock Mechanics and Mining Sciences*, 40:1027–1047, 10 2003. doi: 10.1016/S1365-1609(03)00110-2.
- L. Mastin, B. Heinemann, A. Krammer, K. Fuchs, and M. Zoback. Stress orientation in the ktb pilot hole determined from wellbore breakouts. *Sci. drilling 2 (1991) S. 1-12.*, 1991.
- G. Matheron. Principles of geostatistics. *Economic Geology*, 58(8):1246–1266, 12 1963. doi: 10.2113/gsecongeo.58.8.1246.
- A. Medina and J. Carrera. Geostatistical inversion of coupled problems: dealing with computational burden and different types of data. *Journal of Hydrology*, 281(4):251–264, 2003.
- M. Meier. Geological characterisation of an underground research facility in the bedretto tunnel. Master’s thesis, ETH Zurich, Zurich, 2017.
- P. Meier, A. Alcolea, and F. Bethmann. *Lessons Learned from Basel: New EGS Projects in Switzerland Using Multistage Stimulation and a Probabilistic Traffic Light System for the Reduction of Seismic Risk*. 2015.
- P. M. Meier, A. Medina, and J. Carrera. Geostatistical inversion of cross-hole pumping tests for identifying preferential flow channel within a shear zone. *Ground Water*, 39(1): 10, 2001.

- K. Mogi. Fracture and flow of rocks under high triaxial compression. *Journal of Geophysical Research (1896-1977)*, 76(5):1255–1269, 1971. doi: 10.1029/JB076i005p01255.
- O. Mohr. Welche umstände bedingen die elastizitätsgrenze und den bruch eines materials. *Zeitschrift des Vereins Deutscher Ingenieure*, 46(1524-1530):1572–1577, 1900.
- D. Moos, P. Peska, M. Zoback, et al. Predicting the stability of horizontal wells and multilateralsthe role of in situ stress and rock properties. In *SPE International conference on horizontal well technology*, pages 119–130, 1998.
- D. Moos, P. Peska, T. Finkbeiner, and M. Zoback. Comprehensive wellbore stability analysis utilizing quantitative risk assessment. *Journal of Petroleum Science and Engineering*, 38(3):97 – 109, 2003.
- A. Mortensen, K. Grönvold, . Guðmundsson, B. Steingrímsson, and . Egilson. Quenched silicic glass from well kj-39 in krafla, north-eastern iceland. 01 2010.
- S. Ottesen, R. H. Zheng, and R. C. McCann. Borehole stability assessment using quantitative risk analysis, Jan 1999.
- K. Panthi. *Methodology for analyzing uncertainty*, page 11. 01 2006.
- P. Papanastasiou and A. Zervos. Wellbore stability analysis: From linear elasticity to postbifurcation modeling. *International Journal of Geomechanics*, 4(1):2–12, 2004. doi: 10.1061/(ASCE)1532-3641(2004)4:1(2).
- R. Parri and F. Lazzeri. 19 - larderello: 100years of geothermal power plant evolution in italy. In R. DiPippo, editor, *Geothermal Power Generation*, pages 537 – 590. Woodhead Publishing, 2016.
- P. Peška and M. D. Zoback. Compressive and tensile failure of inclined well bores and determination of in situ stress and rock strength. *Journal of Geophysical Research*, 100(B7):12791, 1995. doi: 10.1029/95JB00319.
- P. Peka and M. D. Zoback. Compressive and tensile failure of inclined well bores and determination of in situ stress and rock strength. *Journal of Geophysical Research: Solid Earth*, 100(B7), 1995.
- R. Pine and A. Batchelor. Downward migration of shearing in jointed rock during hydraulic injections. *International Journal of Rock Mechanics and Mining Sciences and Geomechanics Abstracts*, 21(5):249 – 263, 1984.
- R. Potter, E. Robinson, and M. Smith. Method of extracting heat from dry geothermal reservoirs, Jan. 22 1974. US Patent 3,786,858.
- J. Ramírez, A. Alcolea, A. Medina, J. Hidalgo, and L. Slooten. Inverse problem in hydrogeology. *Hydrogeology Journal*, 13:206–222, 03 2005. doi: 10.1007/s10040-004-0404-7.

- P. A. Reasenber and R. W. Simpson. Response of regional seismicity to the static stress change produced by the loma prieta earthquake. *Science*, 255(5052):1687–1690, 1992.
- H. Richards, R. Parker, A. Green, R. Jones, J. Nicholls, D. Nicol, M. Randall, S. Richards, R. Stewart, and J. Willis-Richards. The performance and characteristics of the experimental hot dry rock geothermal reservoir at rosemanowes, cornwall (19851988). *Geothermics*, 23(2):73 – 109, 1994.
- J. Rissanen. Modeling by shortest data description. *Automatica*, 14(5):465 – 471, 1978.
- Y. Rubin and G. Dagan. Stochastic identification of transmissivity and effective recharge in steady groundwater flow: 1. theory. *Water Resources Research*, 23(7):1185–1192, 1987. doi: 10.1029/WR023i007p01185.
- F. Rummel and J. Baumgärtner. Hydraulic fracturing stress measurements in the gpk1 borehole, soultz-sous-forêts. *Geothermal Science and Technology*, 3:119–148, 01 1991.
- K. Russell, C. Ayan, N. Hart, J. Rodriguez, H. Scholey, C. Sugden, and J. Davidson. Predicting and preventing wellbore instability using the latest drilling and logging technologies: Tullich field development, north sea. 10 2003. doi: 10.2523/84269-MS.
- D. P. Sahara, M. Schoenball, E. Gerolymatou, and T. Kohl. Analysis of borehole breakout development using continuum damage mechanics. *International Journal of Rock Mechanics and Mining Sciences*, 97:134–143, Sept. 2017. doi: 10.1016/j.ijrmms.2017.04.005.
- E. Sarris and P. Papanastasiou. Modeling of hydraulic fracturing in a poroelastic cohesive formation. *International Journal of Geomechanics*, 12(2):160–167, 2012. doi: 10.1061/(ASCE)GM.1943-5622.0000121.
- D. R. Schmitt, C. A. Currie, and L. Zhang. Crustal stress determination from boreholes and rock cores: Fundamental principles. *Tectonophysics*, 580(Supplement C):1–26, Dec. 2012. doi: 10.1016/j.tecto.2012.08.029.
- M. Schoenball and N. C. Davatzes. Quantifying the heterogeneity of the tectonic stress field using borehole data. *Journal of Geophysical Research: Solid Earth*, 122, 2017. doi: 10.1002/2017JB014370.
- R. Schulz. Institut für Geowissenschaftliche Gemeinschaftsaufgaben Hannover Nutzung petrothermaler Technik Vorschlag für eine Definition für die Anwendung des EEG. 2008.
- G. Schwarz. Estimating the Dimension of a Model. *Annals Statist.*, 6:461–464, 1978.
- N. B. Setiawan and R. W. Zimmerman. A unified methodology for computing the stresses around an arbitrarily-shaped hole in isotropic or anisotropic materials. *International Journal of Solids and Structures*, 199:131–143, 2020. doi: 10.1016/j.ijsolstr.2020.03.022.

- A. Shakas, H. Maurer, P.-L. Giertzuch, M. Hertrich, D. Giardini, F. Serbeto, and P. Meier. Permeability enhancement from a hydraulic stimulation imaged with ground penetrating radar. *Geophysical Research Letters*, 47:e2020GL088783, 2020. doi: 10.1029/2020GL088783.
- G. Shamir and M. D. Zoback. Stress orientation profile to 3.5 km depth near the san andreas fault at cajon pass, california. *Journal of Geophysical Research: Solid Earth*, 97 (B4):5059–5080, 1992. doi: 10.1029/91JB02959.
- B. Shen. Borehole Breakouts and In Situ Stresses. *First Southern Hemisphere International Rock Mechanics Symposium*, pages 407–418, 2008.
- B. Shen and O. Stephansson. Modification of the g-criterion for crack propagation subjected to compression. *Engineering Fracture Mechanics*, 47(2):177 – 189, 1994.
- B. Shen, O. S. Stephansson, and M. Rinne. Simulation of borehole breakouts using fracod(2d). *Oil Gas Science and Technology-revue De L Institut Francais Du Petrole - OIL GAS SCI TECHNOL*, 57:579–590, 09 2002. doi: 10.2516/ogst:2002039.
- I. Song and B. C. Haimson. Polyaxial strength criteria and their use in estimating in situ stress magnitudes from borehole breakout dimensions. *International Journal of Rock Mechanics and Mining Sciences*, 34(3):116.e1 – 116.e16, 1997.
- O. Stephansson and A. Zang. ISRM Suggested Methods for Rock Stress Estimation Part 5: Establishing a Model for the In Situ Stress at a Given Site. *Rock Mechanics and Rock Engineering*, 45(6):955–969, 2012. doi: 10.1007/s00603-012-0270-x.
- G. Stephens and B. Voight. Hydraulic fracturing theory for conditions of thermal stress. *International Journal of Rock Mechanics and Mining Sciences and Geomechanics Abstracts*, 19(6):279 – 284, 1982.
- J. Straubhaar. *DeeSse users guide. The Centre for Hydrogeology and Geothermics (CHYN), University of Neuchâtel, Neuchâtel, Switzerland.* 2019.
- J. Straubhaar, P. Renard, and T. Chugunova. Multiple-point statistics using multi-resolution images. *Stochastic Environmental Research and Risk Assessment*, 34(2):251–273, Feb 2020. doi: 10.1007/s00477-020-01770-8.
- R. P. Sutton, S. A. Cox, and R. D. Barree. Shale gas plays: A performance perspective, Jan 2010.
- A. Suvorov and A. Selvadurai. The biot coefficient for an elasto-plastic material. *International Journal of Engineering Science*, 145:103166, 2019.
- X. Tan and H. Konietzky. Numerical study of variation in biot’s coefficient with respect to microstructure of rocks. *Tectonophysics*, 610:159171, 01 2014. doi: 10.1016/j.tecto.2013.11.014.

- X. Tan, H. Konietzky, and T. Frühwirt. Experimental and numerical study on evolution of biots coefficient during failure process for brittle rocks. *Rock mechanics and rock engineering*, 48(3):1289–1296, 2015.
- W. Tanikawa and T. Shimamoto. Comparison of klinkenberg-corrected gas permeability and water permeability in sedimentary rocks. *International Journal of Rock Mechanics and Mining Sciences*, 46:229–238, 12 2009. doi: 10.1016/j.ijrmms.2008.03.004.
- T. Terakawa, S. Miller, and N. Deichmann. High fluid pressure and triggered earthquakes in the enhanced geothermal system in Basel, Switzerland. *J. Geophys. Res.*, 117(B7): B07305, July 2012. doi: 10.1029/2011jb008980.
- K. Terzaghi et al. *Erdbaumechanik auf bodenphysikalischer grundlage*. 1925.
- J. W. Tester, D. W. Brown, and R. M. Potter. Hot dry rock geothermal energy— a new energy agenda for the twenty-first century. Technical report, United States, 1989.
- J. W. Tester, B. J. Anderson, A. Batchelor, D. Blackwell, R. DiPippo, E. Drake, J. Garnish, B. Livesay, M. Moore, K. Nichols, et al. The future of geothermal energy. *Massachusetts Institute of Technology*, 358, 2006.
- A. N. Tikhonov. Regularization of incorrectly posed problems. *Soviet Mathematics Doklady*, 1963.
- B. Valley. *The relation between natural fracturing and stress heterogeneities in deep-seated crystalline rocks at Soultz-sous-Forêts (France)*. PhD thesis, 01 2007.
- B. Valley and K. Evans. Stress state at soultz-sous-forêts to 5 km depth from wellbore failure and hydraulic observations. 01 2007.
- B. Valley and K. Evans. Stress orientation to 5 km depth in the basement below Basel (Switzerland) from borehole failure analysis. *Swiss Journal of Geosciences*, 102(3):467–480, Dec. 2009a. doi: 10.1007/s00015-009-1335-z.
- B. Valley and K. Evans. Stress Heterogeneity in the Granite of the Soultz EGS Reservoir Inferred from Analysis of Wellbore Failure. In *Proceedings World Geothermal Congress 2010*, 2010.
- B. Valley and K. Evans. Preliminary assessment of the scaling relationships of in-situ stress orientation variations indicated by wellbore failure data. In L. Alejano, . Peruchó, C. Olalla, and R. Jiménez, editors, *EUROCK 2014: Rock Engineering and Rock Mechanics: Structures in and on Rock Masses*. CRC Press, 2014a.
- B. Valley and K. Evans. Preliminary assessment of the scaling relationships of in-situ stress orientation variations indicated by wellbore failure data. In L. Alejano, . Peruchó, C. Olalla, and R. Jiménez, editors, *EUROCK 2014: Rock Engineering and Rock Mechanics: Structures in and on Rock Masses*. CRC Press, 2014b.

B. Valley and K. F. Evans. Stress orientation to 5 km depth in the basement below Basel (Switzerland) from borehole failure analysis. *Swiss Journal of Geosciences*, 102(3):467–480, 2009b. doi: 10.1007/s00015-009-1335-z.

B. Valley and K. F. Evans. Stress magnitudes in the Basel enhanced geothermal system. *International Journal of Rock Mechanics and Mining Sciences*, 118(April):1–20, 2019. doi: 10.1016/j.ijrmms.2019.03.008.

B. Valley, P. Kaiser, and D. Duff. Consideration of uncertainty in modelling the behaviour of underground excavations. pages 423–436, 01 2010.

B. Valley, M. Jalali, M. Ziegler, and K. Evans. Constraining DFN characteristics for deep geothermal projects by considering the effects of fractures on stress variability. In *Proceedings of the 1st International Conference on Discrete Fracture Network Engineering*, 2014.

J. E. Walstrom, R. P. Harvey, and H. D. Eddy. A Comparison of Various Directional Survey Models and an Approach To Model Error Analysis. *Journal of Petroleum Technology*, 24(08):935–943, Aug. 1972. doi: 10.2118/3379-PA.

G. Walton, K. Kalenchuk, C. Hume, and M. Diederichs. Borehole Breakout Analysis to Determine the In-Situ Stress State in Hard Rock. In *ARMA 2015, 49th US Rock Mechanics / Geomechanics Symposium*, 2015.

D. Wyborn, L. De Graaf, S. Davidson, and S. Hann. Development of australia’s first hot fractured rock (hfr) underground heat exchanger, cooper basin, south australia. 2004.

J. Zemanek, E. Glenn, L. Norton, and R. Caldwell. Formation evaluation by inspection with the borehole televiewer. *Geophysics*, 35(2):254–269, 1970.

X. Zhang and D. J. Sanderson. Numerical modelling of the effects of fault slip on fluid flow around extensional faults. *Journal of Structural Geology*, 18(1):109–119, Jan. 1996. doi: 10.1016/0191-8141(95)00086-S.

S. Zhou, R. Hillis, and M. Sandiford. On the mechanical stability of inclined wellbores. *SPE Drilling Completions*, 11:67–73, 06 1996.

M. Ziegler, B. Valley, and K. F. Evans. Fault orientations inferred from analysis of a microseismic cluster dataset of the Basel EGS reservoir agree well with borehole fracture data. In *Abstract Volume 13th Swiss Geoscience Meeting, Basel, 20th/21st November 2015: 7. Geothermal Energy, CO2 Sequestration and Shale Gas*, pages 219–219. Swiss Academy of Sciences, 2015.

R. Zimmerman. Coupling in poroelasticity and thermoelasticity. *International Journal of Rock Mechanics and Mining Sciences - INT J ROCK MECH MINING SCI*, 37:79–87, 01 2000. doi: 10.1016/S1365-1609(99)00094-5.

M. D. Zoback. *Reservoir Geomechanics*. Cambridge University Press, 2007. doi: 10.1017/CBO9780511586477.

M. D. Zoback, C. A. Barton, M. Brudy, D. A. Castillo, T. Finkbeiner, B. R. Grollmund, D. B. Moos, P. Peska, C. D. Ward, and D. J. Wiprut. Determination of stress orientation and magnitude in deep wells. *International Journal of Rock Mechanics and Mining Sciences*, 40(7):1049–1076, Oct. 2003. doi: 10.1016/j.ijrmms.2003.07.001.

M. L. Zoback. First- and second-order patterns of stress in the lithosphere: The World Stress Map Project. *Journal of Geophysical Research: Solid Earth*, 97, 1992.

Appendices

A. Stresses transformation to a local borehole Cartesian coordinate system

This section contains the necessary mathematical background that we have used to compute the stress around a wellbore arbitrarily oriented to the principal stress directions. The general approach was presented in (Peška and Zoback, 1995) and initially developed by (Hiramatsu and Oka, 1968). We have been interested in developing that solution here again because it is of key importance for most of the work done on wellbore failure analysis. Let the far-field stress be expressed by means of the principal stresses S_1 , S_2 , and S_3 . Then the stress state is fully described by the tensor \mathbf{S}_{lmn} and three angles α , β , γ :

$$\mathbf{S}_{lmn} = \begin{pmatrix} S_1 & 0 & 0 \\ 0 & S_2 & 0 \\ 0 & 0 & S_3 \end{pmatrix} \quad (\text{A.1})$$

where $S_1 > S_2 > S_3$ are the principal stress magnitudes. The angles α , β , γ are called Euler angles. They define the orientations of the principal stresses axes $(\vec{l}, \vec{m}, \vec{n})$ with respect to the geographic coordinate system $(\vec{x}, \vec{y}, \vec{z})$, with \vec{x} pointing to the North, \vec{y} pointing to the East and \vec{z} pointing downward.

Euler angles α , β , γ define a sequence of three rotations that must be used in order to rotate principal stresses axes $(\vec{l}, \vec{m}, \vec{n})$ to the geographic coordinate system $(\vec{x}, \vec{y}, \vec{z})$. During this rotations sequence, $(\vec{x}, \vec{y}, \vec{z})$ is rotated through two intermediate systems $(\vec{x}_1, \vec{y}_1, \vec{z}_1)$ and $(\vec{x}_2, \vec{y}_2, \vec{z}_2)$. The first rotation is the positive rotation α (counterclockwise) with respect to the axis \vec{z} ($\alpha \in [0^\circ \ 360^\circ]$) using the matrix \mathbf{R}_z (Eq. A.2). After this rotation, we get to the first intermediate axis $(\vec{x}_1, \vec{y}_1, \vec{z}_1)$ where $\vec{z}_1 = \vec{z}$. Then, comes a positive rotation β around \vec{y}_1 ($\beta \in [-90^\circ \ 90^\circ]$) using the matrix \mathbf{R}_{y_1} (Eq. A.3). We obtain then the second intermediate coordinate system $(\vec{x}_2, \vec{y}_2, \vec{z}_2)$ where $\vec{y}_2 = \vec{y}_1$. Finally, the positive rotation γ around \vec{x}_2 ($\gamma \in [0^\circ \ 360^\circ]$) by applying the matrix \mathbf{R}_{x_2} (Eq. A.4) which gives us a final coordinate system that coincides with the principal stresses axes $(\vec{l}, \vec{m}, \vec{n})$ (Fig. A.1).

$$\mathbf{R}_z = \begin{pmatrix} \cos \alpha & \sin \alpha & 0 \\ -\sin \alpha & \cos \alpha & 0 \\ 0 & 0 & 1 \end{pmatrix} \quad (\text{A.2})$$

$$\mathbf{R}_{y_1} = \begin{pmatrix} \cos \beta & 0 & -\sin \beta \\ 0 & 1 & 0 \\ \sin \beta & 0 & \cos \beta \end{pmatrix} \quad (\text{A.3})$$

$$\mathbf{R}_{x_2} = \begin{pmatrix} 1 & 0 & 0 \\ 0 & \cos \gamma & \sin \gamma \\ 0 & -\sin \gamma & \cos \gamma \end{pmatrix} \quad (\text{A.4})$$

Mathematically, this transformation is expressed as:

$$\mathbf{S}_{xyz} = \mathbf{R}_{lmn}^T \mathbf{S}_{lmn} \mathbf{R}_{lmn} \quad (\text{A.5})$$

where \mathbf{S}_{xyz} is the stress state in the referential coordinate system and \mathbf{R}_{lmn} is the product of three rotations that make use of Euler angles.

$$\mathbf{R}_{lmn} = \mathbf{R}_z \mathbf{R}_{y_1} \mathbf{R}_{x_2} \quad (\text{A.6})$$

$$\mathbf{R}_{lmn} = \begin{pmatrix} \cos \alpha \cos \beta & \sin \alpha \cos \beta & -\sin \beta \\ \cos \alpha \sin \beta \sin \gamma - \sin \alpha \cos \gamma & \sin \alpha \sin \beta \sin \gamma + \cos \alpha \cos \gamma & \cos \beta \sin \gamma \\ \cos \alpha \sin \beta \cos \gamma + \sin \alpha \sin \gamma & \sin \alpha \sin \beta \cos \gamma - \cos \alpha \sin \gamma & \cos \beta \cos \gamma \end{pmatrix} \quad (\text{A.7})$$

A borehole coordinates system is defined $(\vec{u}, \vec{v}, \vec{w})$ (Fig. A.2) in order to describe the state of stress around a borehole. \vec{w} runs along the borehole axis pointing downwards, \vec{v} is a horizontal axis in the plane perpendicular to the borehole axis \vec{w} and \vec{u} comes out of the screwdriver rule. The borehole coordinate system is defined by two angles: (1) the borehole dip direction δ comprised in the interval $[0^\circ \ 360^\circ[$ and (2) the inclination of the borehole with respect to verticality ψ while $\psi \in [0^\circ \ 90^\circ]$. The natural state of stress in the borehole coordinates system \mathbf{S}_{uvw} is given as following:

$$\mathbf{S}_{uvw} = \mathbf{R}_{uvw} \mathbf{S}_{xyz} \mathbf{R}_{uvw}^T \quad (\text{A.8})$$

where:

$$\mathbf{S}_{uvw} = \begin{pmatrix} S_u & S_{uv} & S_{uw} \\ S_{vu} & S_v & S_{vw} \\ S_{wu} & S_{wv} & S_w \end{pmatrix} \quad (\text{A.9})$$

\mathbf{R}_{uvw} is the direction cosine of $(\vec{u}, \vec{v}, \vec{w})$ relative to $(\vec{x}, \vec{y}, \vec{z})$, which can be expressed as the product of two rotation matrices \mathbf{R}_δ (counterclockwise rotation of δ around \vec{z}) and \mathbf{R}_ψ , (counterclockwise rotation of ψ around \vec{y} (pointing to the East)):

$$\mathbf{R}_\delta = \begin{pmatrix} \cos \delta & \sin \delta & 0 \\ -\sin \delta & \cos \delta & 0 \\ 0 & 0 & -1 \end{pmatrix} \quad (\text{A.10})$$

$$\mathbf{R}_\psi = \begin{pmatrix} -\cos \psi & 0 & -\sin \psi \\ 0 & -1 & 0 \\ \sin \psi & 0 & -\cos \psi \end{pmatrix} \quad (\text{A.11})$$

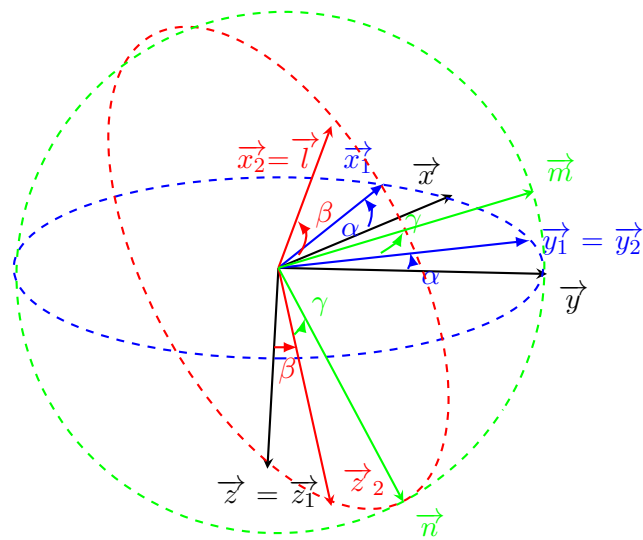


Figure A.1.: A sequence of three rotations to rotate the geographical system coordinate $(\vec{x}, \vec{y}, \vec{z})$ shown in black to the principal stresses coordinate system $(\vec{l}, \vec{m}, \vec{n})$ shown in green. This sequence rotates through two intermediate coordinate systems $(\vec{x}_1, \vec{y}_1, \vec{z}_1)$ (in blue) and $(\vec{x}_2, \vec{y}_2, \vec{z}_2)$ (in red). The first rotation α is around \vec{z} , the second is β around \vec{y}_1 and the last one is γ around \vec{x}_2 .

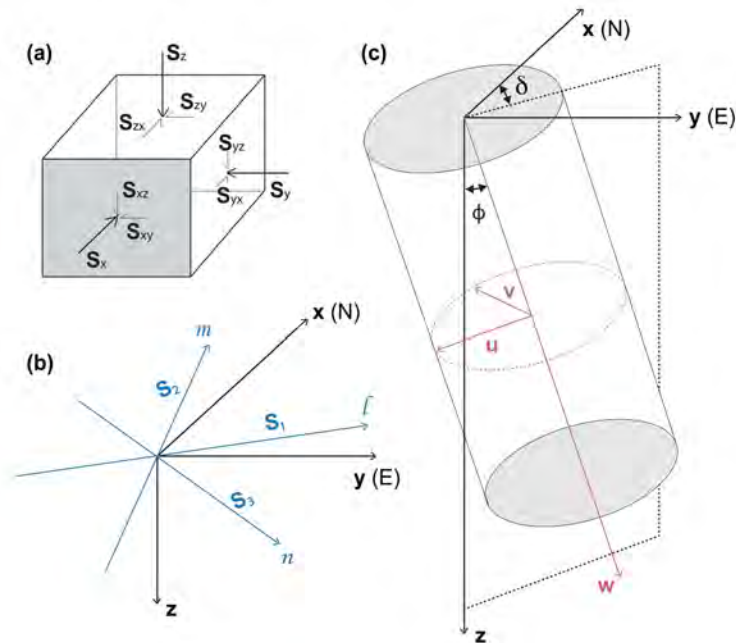


Figure A.2.: (a) Definition of stress tensor in arbitrary cartesian coordinates system. (b) reference geographical coordinates system $(\vec{x}, \vec{y}, \vec{z})$ (in black) where \vec{x} is oriented towards the North, \vec{y} to the East and \vec{z} pointing downward and the principal stress coordinates system $(\vec{l}, \vec{m}, \vec{n})$ (in blue). The latter coincides with the far-field stresses S_1, S_2, S_3 . (c) borehole coordinates system $(\vec{u}, \vec{v}, \vec{w})$. δ and ψ are the borehole dip direction and the borehole inclination respectively. All systems of coordinates are positive orthonormal base

$$\mathbf{R}_{uvw} = \mathbf{R}_\psi \mathbf{R}_\delta = \begin{pmatrix} -\cos \delta \cos \psi & -\sin \delta \cos \psi & \sin \psi \\ \sin \delta & -\cos \delta & 0 \\ \cos \delta \sin \psi & \sin \delta \sin \psi & \cos \psi \end{pmatrix} \quad (\text{A.12})$$

Combining both Eq. A.5 and Eq. A.9 gives us a direct expression between the principal stresses coordinate system $(\vec{l}, \vec{m}, \vec{n})$ and the borehole coordinate system $(\vec{u}, \vec{v}, \vec{w})$:

$$\mathbf{S}_{uvw} = \mathbf{R}_{uvw} \mathbf{R}_{lmn}^T \mathbf{S}_{lmn} \mathbf{R}_{lmn} \mathbf{R}_{uvw}^T \quad (\text{A.13})$$

B. Stress perturbation induced by a cylindrical opening (Kirsch solution)

When a volume of rock is excavated, for example by drilling it, the state of stress around the excavation is modified. The equations that describe the elastic stresses around the hole in an infinite plate in one directional tension are generally referred to as the Kirsch solution (Kirsch, 1898) and are one of the most useful solutions in rock mechanics. This solution is often used to approximate the stress redistribution around deep boreholes and tunnels. The total stress around a filled borehole of radius a , in cylindrical coordinates (r, θ, w) , and with an internal fluid at a pressure P_w , is given by Kirsch equations as following:

$$\mathbf{S}_{r\theta w} = \begin{pmatrix} S_{rr} & S_{r\theta} & S_{rw} \\ S_{\theta r} & S_{\theta\theta} & S_{\theta w} \\ S_{wr} & S_{w\theta} & S_{ww} \end{pmatrix} \quad (\text{B.1})$$

where:

$$S_{rr} = \left(1 - \frac{a^2}{r^2}\right) \left(\frac{S_u + S_v}{2}\right) + \left(1 + \frac{3a^4}{r^4} - \frac{4a^2}{r^2}\right) \left(\frac{S_u - S_v}{2}\right) \cos 2\theta + \left(1 + \frac{3a^4}{r^4} - \frac{4a^2}{r^2}\right) S_{uv} \sin 2\theta + P_w \left(\frac{a^2}{r^2}\right) + S_r^{\Delta T} \quad (\text{B.2})$$

$$S_{\theta\theta} = \left(1 + \frac{a^2}{r^2}\right) \left(\frac{S_u + S_v}{2}\right) - \left(1 + \frac{3a^4}{r^4}\right) \left(\frac{S_u - S_v}{2}\right) \cos 2\theta - \left(1 + \frac{3a^4}{r^4}\right) S_{uv} \sin 2\theta - P_w \left(\frac{a^2}{r^2}\right) + S_\theta^{\Delta T} \quad (\text{B.3})$$

$$S_{ww} = S_z - 4\nu \frac{a^2}{r^2} \left(\frac{S_u - S_v}{2}\right) \cos 2\theta - 4\nu \frac{a^2}{r^2} S_{uv} \sin 2\theta + S_w^{\Delta T} \quad (\text{B.4})$$

$$S_{r\theta} = - \left(1 - \frac{3a^4}{r^4} + \frac{2a^2}{r^2}\right) \left(\frac{S_u - S_v}{2}\right) \sin 2\theta + \left(1 - \frac{3a^4}{r^4} + \frac{2a^2}{r^2}\right) S_{uv} \cos 2\theta \quad (\text{B.5})$$

$$S_{rw} = \left(1 - \frac{a^2}{r^2}\right) (S_{vw} \sin \theta + S_{uw} \cos \theta) \quad (\text{B.6})$$

$$S_{\theta w} = \left(1 + \frac{a^2}{r^2}\right) (S_{vw} \cos \theta - S_{uw} \sin \theta) \quad (\text{B.7})$$

ν is the Poisson's ratio. The subscripts (u,v,w) refer to the total stresses given in the local borehole coordinate system as in Eq. A.9. $S_r^{\Delta T}$, $S_\theta^{\Delta T}$, $S_w^{\Delta T}$ are thermo-elastic stress components estimated by Eqs. 3.1 and 3.2.

C. Overview of the minimization algorithm implemented in PEST

We perform our calibration using PEST (Parameter ESTimation), a widely used code in environmental modelling to calibrate models and to determine uncertainty associated with parameters and predictions. PEST uses a nonlinear estimation technique known as the Levenberg-Marquardt (LM) method also known as the damped least-squares (DLS) method. It is used to solve non-linear least squares problems. This algorithm is used in many software applications for solving generic curve-fitting problems. For linear models, optimization is achieved in one step. However, for non-linear problems, parameter estimation is an iterative process. The Gaussian-Marquardt-Levenberg algorithm adjusts parameter values based on the derivatives of the observations with respect to the parameters (i.e., sensitivity or Jacobian matrix) (Doherty, 2015).

Let us assume that the user has a specified model f . The Levenberg Marquardt algorithm performs a curve fitting on a given data set, by finding the optimum function parameters b that minimizes the sum of the squares of the deviations:

$$S(b) = \min\left(\sum_{i=1}^m (y_i - f(x_i, b))^2\right) \quad (\text{C.1})$$

where y_i are the target values, f , the output of the user's model, x_i , input values and b are the estimated parameters.

Let us assume that we have a model, X , and input parameters, b , such as principal stresses, S_{Hmax} , S_{hmin} , S_v . The action of the model (X) on the inputs in (b) produces a set of outputs (c) (w_{BO} , e_{BO} , θ_b and D in our case). Conceptually, the inputs react with each parameter to produce results. This can be formulated in the following equation (Doherty, 2015):

$$Xb = c \quad (\text{C.2})$$

In Eq. (C.2), X is an ($m \times n$) matrix containing the inputs excitations, b is a vector of order n , which, we assume, holds the system parameters and c is a vector of order m containing values that describe the system's response to a set of excitations X .

$$X_{p1}b_1 + X_{p2}b_2 + \dots + X_{pn}b_n = c_p \quad (\text{C.3})$$

where X_{pi} is the element of X corresponding to the p^{th} row and i^{th} column. As X has m rows, there are m such equations.

The objective function is based on the best set of linear combinations of the parameters b , as affected by the model inputs X , compared to the observations c :

$$\psi = (c - Xb)^t(c - Xb) \quad (C.4)$$

ψ is the objective function to minimize, c contains the set of laboratory or field measurements; the "t" superscript indicates the matrix transpose operation. It can be shown (Doherty, 2015) that the vector b which minimizes ψ of Eq. C.4 is given by:

$$b = (X^t X)^{-1} X^t c \quad (C.5)$$

The vector b expressed in Eq. C.5 is the "best linear unbiased" estimator of the set of true system parameters appearing in Eq. C.1.

Moreover, two different types of regularization are available in PEST: Singular Value Decomposition (SVD) and Tikhonov regularization (Doherty, 2015). SVD is a method to reduce the process matrices into a smaller number of parameters called subset or "super parameters". This method reduces the null space by dropping parameters that do not affect model outputs. This leads to a computationally less expensive calibration problem. On the other hand, Tikhonov regularization is based on the assumption that the objective function of the inverse problem has two components: one is based on hard knowledge and the other is based on soft knowledge (Doherty, 2003). Detailed discussion of mathematical formulation of regularizations is beyond the scope of this study, but more details can be found in Doherty (2003, 2015).

Curriculum Vitae

Asmae Dahrabou

Date of Birth 23.05.1992
Place of Birth Jerada, Morocco



SUMMARY

A highly motivated Reservoir Engineer with a strong knowledge in Computer Science. Excellent verbal and written communication skills and an ability to relate to a wide range of individuals in different languages, to work abroad, and in a multicultural environment. I obtained my first degree in Advanced Maths and Physics in Morocco and pursued my Reservoir Engineering and Petroleum Geosciences studies in France. My Master's thesis was about developing a mathematical and physical model to determine the optimal length of horizontal wells in reservoir engineering. I worked under the supervision of Prof. M. Souhar at LEMTA (Laboratoire d'Energétique et de Mécanique Théorique et Appliquée). In 2015, I worked on a research project at CEREGE (Marseille, France) and BRGM (Orléans, France) based on an application to CO_2 storage uncertainty analysis under the supervision of Prof. Sophie Viseur and Dr. Pascal Audigane. Since 2016, I am working in the research group of Prof. Benoît Valley at CHYN (University of Neuchâtel) on the DG-WOW (Deep Geothermal Well Optimization Workflow) project. I completed my PhD study in December 2020.

EDUCATION

2016 - 2020 **Doctorat ès sciences - géothermie PhD** at Unine (Switzerland)
PhD thesis at the research group of Prof. Benoît Valley in collaboration with Geo-Energie Suisse AG based in Zürich

2014 - 2015 **Master of Science** at ENSG, Nancy (France)
Reservoir Engineering And Petroleum Geosciences

2012 - 2014 **Master's degree** at ENSEM, Nancy (France)
Mechanical and Electrical Engineering

2010 - 2012 **Bachelor's degree** at Lycée Technique, Beni Mellal (Morocco)
Advanced Maths, Physics and Engineering Science

2009 - 2010 **Baccalaureate** at Lycée Hassan II, Beni Mellal (Morocco)
Maths and Physics, with "mention très bien"

WORK EXPERIENCE

8.2021 - 11.2021 **Sales Engineer** at Stensborg, Roskilde (Denmark)
Nanoscience and Nanotechnology

6.2018 - 6.2019 **Co-Founder** at Berberka

- 6.2015 - 9.2015 **Engineer Intern** at BRGM, Orléans (France)
Topological comparisons of fluvial reservoir rock volumes using Betti numbers: application to CO₂ storage uncertainty analysis
- 4.2015 - 6.2015 **Junior Researcher** at CEREGE, Marseille (France)
- 9.2014 - 3.2015 **Master thesis** at LEMTA, Nancy (France)
Horizontal wells in the reservoir engineering: optimal length
- 6.2013 - 9.2013 **Research Student** at LEMTA, Nancy (France)
- 9.2012 - 9.2020 **Private tutor:** Teaching Bachelor's and Master's students Mathematics, Physics, Earth science, French and English

DIPLOMAS

- 12.2020 Doctorat ès sciences - géothermie PhD
- 09.2015 Master in Reservoir Engineering and Petroleum Geosciences
- 09.2015 Master's degree in Mechanical and Electrical Engineering
- 09.2012 Bachelor's degree in Mathematics, Physics and Computer Science
- 09.2010 Baccalaureate diploma in Maths, Physics and Engineering Science

In this PhD project, a workflow allowing a fast decision-making process for selecting an optimal well trajectory for Enhanced Geothermal System (EGS) projects is developed. Firstly, the deep geothermal borehole is drilled vertically. Secondly, based on logging data which are costly, the direction in which the strongly deviated borehole section will be drilled needs to be determined in order to optimize borehole stability and to intersect the highest number of fractures that are oriented favorably for stimulation. The workflow applies to crystalline rock and includes an uncertainty and risk assessment framework.